Dissertation zur Erlangung des Doktorgrades der Fakultät für Chemie und Pharmazie der Ludwig-Maximilians-Universität München

Structure-Function Relationships in Lead-Free Perovskite-Inspired Semiconductors

Andreas Weis

aus

Bozen, Italien

2023

Erklärung

Diese Dissertation wurde im Sinne von § 7 der Promotionsordnung vom 28. November 2011 von Herrn Professor Dr. Thomas Bein betreut.

Eidesstattliche Versicherung

Diese Dissertation wurde eigenständig und ohne unerlaubte Hilfe bearbeitet.

München, den 19.09.2023 . . . . . .

Andreas Weis

Dissertation eingereicht am: 18.07.2023

1. Gutachter: Prof. Dr. Thomas Bein

2. Gutachter: Prof. Dr. Achim Hartschuh

Mündliche Prüfung am: 13.09.2023

List of Abbreviations

β-MPA	β-methylphenylethylammonium
JV	current-voltage
J_{sc}	short circuit current density
V_{oc}	open circuit voltage
2D	two-dimensional
3AMPY	3-(aminomethyl)pyridinium
4AMP	4-(aminomethyl)piperidinium
4FPEA	4-fluorophenethylammonium
AE2T	5,5'-diylbis(aminoethyl)-[2,2'-bithiophene]
AFM	atomic force microscopy
APP	4-aminopiperidinium
BA	butylammonium
BDA	1,4-butyldiammonium
c-SnO_2	compact tin oxide
CASI	$\mathrm{Cu_xAg_{1-x}SbI_4}$
CB	conduction band
CBM	conduction band minimum
CHD	1,4-cyclohexandiamine
CLB	chlorobenzene
DFE	defect formation energy
DFT	density functional theory
DIPE	diisopropylether
DJ	Dion-Jacobson
DMF	dimethylformamide
DMSO	dimethyl sulfoxide
DOS	density of states
DSSC	dye-sensitized solar cells

EBE	exciton binding energy
EDX	energy dispersive X-ray spectroscopy
EPR	electron paramagnetic resonance
EQE	external quantum efficiency
ETL	electron transport layer
EtOH	ethanol
FF	fill factor
FLIM	fluorescence-lifetime imaging microscopy
FTO	fluorine-doped tin oxide
FWHM	full width half maximum
GBL	γ-butyrolactone
GIWAXS	grazing incidence wide angle X-ray scattering
HOIP	hybrid organic-inorganic perovskite
HOMO	highest occupied molecular orbital
HSE	Heyd-Scuseria-Ernzerhof
HTL	hole transport layer
IBA	4-iodobutylammonium
IoT	internet of things
IPA	isopropanol
iPA	isopentylammonium
IQE	internal quantum efficiency
ITO	indium-doped tin oxide
LED	light emitting diode
LiTFSI	bis(trifluoromethane)sulfonimide lithium salt
LSDA	localized spin-density approximation
MA	methylammonium
MASI	methylammonium antimony iodide
MeOH	methanol
mp-TiO_2	mesoporous titanium dioxide
MPP	maximum power point
NMP	N-Methyl-2-pyrrolidone
OC	organic cation
OCA	octylammonium
OM	optical microscopy
OPTP	optical-pump terahertz-probe spectroscopy
PA	propylammonium

PBE	Perdew-Burke-Ernzerhof
PCE	power conversion efficiency
PEA	phenylethylammonium
PES	photoelectron spectroscopy
PL	photoluminescence
PSE	periodic system of elements
PTAA	poly(triaryl amine)
PV	photovoltaic
QE	quantum efficiency
QFL	quasi Fermi level
RH	relative humidity
RP	Ruddlesden-Popper
RT	room temperature
SEM	scanning electron microscopy
SI	Supporting Information
SOC	spin-orbit coupling
spiro-OMeTAD	2,2',7,7'-tetrakis[N,N-di(4-methoxyphenyl)amino]-9,9'-spirobifluorene
SQ	Shockley-Queisser
TBP	*tert*-butylpyridine
THTO	tetrahydrothiophene 1-oxide
TIL	thermodynamic ionization level
TRMC	time-resolved microwave conductivity
TU	thiourea
UPS	ultraviolet photoelectron spectroscopy
UV	ultraviolet
UV-Vis	ultraviolet–visible spectroscopy
VB	valence band
VBM	valence band maximum
vdW	van der Waals
XPS	X-ray photoelectron spectroscopy
XRD	X-ray diffraction
XRF	X-ray fluorescence
ZFS	zero field splitting

Abstract

Hybrid organic-inorganic lead-based perovskites employed in thin-film solar cells have been at the forefront of photovoltaic research interest in the last decade as cheap, earth-abundant and highly efficient absorber materials. Nonetheless, many factors still hamper their large-scale application, with the most prominent problems being an inherent low stability and proneness to decomposition under regular operating conditions like humidity and heat. This is aggravated by the pronounced toxicity of lead halides, which are degradation products and precursors likewise. Because of this reason, a lot of research in recent years was focused on replacing lead with isovalent cations to retain the favorable properties while eliminating the detrimental toxicity and stability issues. To achieve this, it is common to preserve the octahedral halide coordination of the central metal atoms, which on the other hand leads to strongly structure-dependent functionality.

In this thesis, we first demonstrate the synthesis of a stable lead-free perovskite-like material based on corner-sharing antimony-iodide octahedra, namely layered $\mathrm{MA_3Sb_2I_9}$. We show a facile synthetic strategy based on increasing the interatomic distance of the metal precursor by employing acetate salts to circumvent the formation of the thermodynamically favored but photovoltaically unpropitious "dimer" phase. A much improved photovoltaic performance, lowered exciton binding energy and lowered band gap is shown by means of density-functional theory (DFT) calculations, optical analysis and initial device implementations.

Moreover, to further boost the optical properties, we alloyed antimony in the same octahedral framework with tin cations in heterovalent oxidation states, strongly enhancing the stability of tin in such structures, which was shown to be a major challenge. We additionally observe a great increase in optical absorption, which we then dissect through experimental and theoretical studies with the help of X-ray photoelectron spectroscopy, DFT and optical analysis. Lastly, we were ably to assign the individual contributions to heteroatom band-to-band transitions from Sb to Sn and intervalence transitions (i.e. charge transfer between metal centers differing in oxidation state) in the closely coupled $\mathrm{Sn(II)/Sn(IV)}$ clusters.

In the next chapter, studies on a system based on $\mathrm{Cu_xAg_{1-x}Sb_{1-y}Bi_yI_3}$ are discussed. While the octahedral antimony-halide coordination is retained here as shown before, the perovskite framework is abandoned completely. This leads to a structure based on the $\mathrm{CdCl_2}$ prototype with a crystallographic $\mathrm{Cu/Ag/Sb/Bi}$ disorder, which on the other hand gives way to a very widely tunable phase. Through DFT calculations we furthermore analyze a wide range of compositions and postulate the stability of a phase with the formula

$Cu_{1-x}Ag_xSbI_4$. Furthermore, via defect formation calculations and optical fitting procedures, combining an excitonic absorption model with an exponential disorder tail, we reveal deep defect levels arising from Ag point defects in the band gap. These measurements combined with the calculations also show a constant band gap throughout and an improvement in stability and side phase formation upon Cu/Ag alloying, confirmed by photoelectron spectroscopy. We furthermore demonstrate control of the photovoltaic performance, which is connected to a much improved morphology, a reduced band gap by minor Bi incorporation and more homogeneous emission behavior with an optimal ratio of 40% Cu/Ag. Moreover, a striking increase in photocurrent is shown through external quantum efficiency measurements when decreasing the light intensity, indicating promise for indoor photovoltaic energy conversion.

In the following project, a novel double perovskite system $Cs_2NaFeCl_6$ based on Na and Fe as central atoms in the octahedral halide cavities is studied. The incorporation of iron leads to spin-polarized character through an unpaired spin system, which is shown by electron paramagnetic resonance measurements on high-quality single crystals and theoretical DFT calculations. We perform low-temperature photoluminescence and UV-Vis measurements on these crystals to illustrate thermochromism and exitonic states with low binding energies.

Concluding, the dimensional reduction of another double perovskite with the formula $(4FPEA)_4AgBiX_8$ (X = Cl, Br, I) is shown, where the iodide phase is stabilized with the help of a strongly templating 4-fluorophenylethylammonium spacer. This leads to a change in band gap nature from indirect to direct, highlighted by DFT calculations. Highly oriented thin films are synthesized and analyzed with temperature-dependent photoluminescence and optical-pump terahertz-probe spectroscopy. This reveals strongly localized-charge carrier behavior through exciton-phonon-coupling and defect-mediated polaron formation.

Contents

Introduction 1

1.1 SEMICONDUCTORS

Nowadays, we live in the Age of Information, characterized by an economy which is based to a large extent on *knowledge, information and the technology of their processing including the technology of management and the management of technology*.[1,2] Technology on the other hand derives from the greek word τεχνολογία, roughly translating to *systematic treatment*.[3] In fact, one could argue that one of the stepping stones enabling the advent of modern information technology was the systematic discovery and study of a special class of materials, namely semiconductors. Although immensely important work in the understanding of conduction in solid state materials was carried out in the late 19th century, the first occurrence of the term *"Halbleiter"* was in the Ph.D. thesis of Josef Weiss in 1910.[4] Nonetheless, it took until the 1940s to transcend general skepticism even from famed scientists like Gudden and Pauli[4] against the existence of semiconductors with the invention of the first germanium-based transistor in 1947 at Bell Labs by Bardeen, Brattain and Shockley.[5] Since then, semiconductors have been at the heart of the arguably most important and impactful inventions of the last 100 years, with the most important being the integrated circuit, which forms the basis of nearly every electronic device nowadays. These discoveries have made it possible to massively reduce the size of digital computers, as compared in Figure 1.1. Here, the Atanasoff-Berry computer in Figure 1.1a consisted of more than 300 vacuum tubes and had a calculation capability of one operation per 15 seconds, which is eclipsed by modern machines with 150 billion operations in the same time.[6]

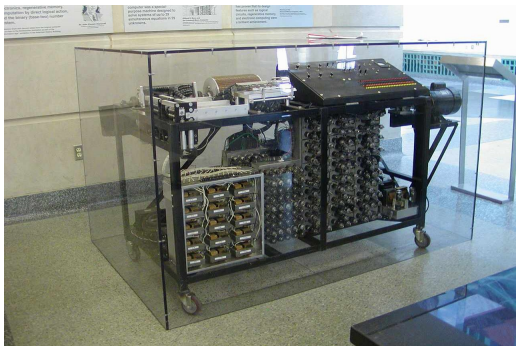

(a) Photograph of the first automatic electronic digital "Atanasoff-Berry" computer from 1942.[6]

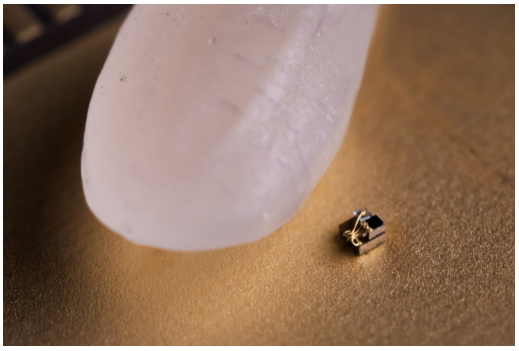

(b) Photograph of the smallest computer in the world in 2018 compared to a grain of rice.[7]

Figure 1.1: Comparison of the first digital to the world-record smallest computer.

Nowadays, multiple companies race to produce even smaller chips, with multiple reports already suggesting the commercial application of technology nodes of only $3\,\mathrm{nm}$.[8,9]

1.1.1 Band theory

As mentioned before, the discovery and understanding of semiconductors was tightly connected to the emergence of solid state physics, in itself catalyzed by the theories of quantum mechanics and X-ray crystallography. With the discovery of X-ray diffraction by crystals in 1912 by Max von Laue it was proven that crystals were composed of periodic arrays of atoms.[10,11] In quantum mechanics, a particle or bound state can only occupy discrete energy levels or orbitals, according to a theory developed by Bohr, Schrödinger and Heisenberg in the first quarter of the 20th century.[12] In molecules, the orbitals of constituents overlap to form new energetic states. With the periodic array of atoms in crystals on the other hand, it was shown that electrons can occupy every energy level in a broad range, the energy bands. These are formed by the hybridization of individual atomic orbitals, of which there are very large numbers in a macroscopic solid (about 10^{22}), leading to only small differences in energies which then can be seen as a continuum or band. Here, only valence electrons are generally responsible for this effect, as the inner orbitals don't overlap strongly.

In metals, these mobile valence electrons could be explained by a simple model by Arnold Sommerfeld in 1927, namely the "Free electron model".[11] This is based on the kinetic Drude theory of electrons combined with Fermi-Dirac statistics and is able to explain effects in metals like heat capacity, electrical conductivity and magnetic susceptibility.[11] Nonetheless, to distinguish different transport behavior, one has to consider the interaction of the outer electron states with the ionic core. Through Bragg reflection of electron

waves by the ionic core potential, two standing waves are formed with different potential energy.[11] This leads to gaps in the energy levels, commonly known as band gaps. The formation of bands starting from atomic energy levels is shown in Figure 1.2a and the characterization of solids by their band structure and electronic occupation can be seen in Figure 1.2b.

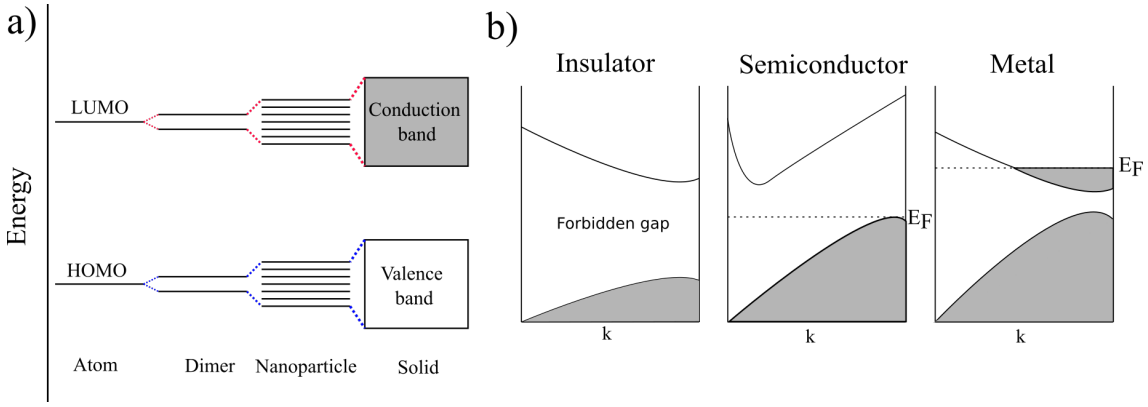

Figure 1.2: a) Illustration of the transition from discrete states in atoms to periodic bands in solids and b) band structure schematic with occupied states (grey) for the cases of an insulator, semiconductor and metal, respectively. E_F refers to the Fermi energy and k to the k-vector.

In general, a perfect solid behaves insulating if the energy bands are either completely filled (valence band) or empty (conduction band), with a high energy band gap ($\geq 3\,\mathrm{eV}$), where as a consequence the application of an electric field does not induce electrons to move at all. In a semiconductor, the valence band is filled with conduction bands that are either slightly filled or empty and separated by a low energy band gap ($\leq 3\,\mathrm{eV}$). At absolute zero, they act insulating because of this. In a metal, bands overlap and are partly filled.[11] The Fermi level E_F defines the highest energy level an electron can occupy at $0\,\mathrm{K}$.

1.1.2 Carriers and Doping

A unique property of semiconductors is their ability to operate as insulating or conducting material by excitation of an electron. Upon this process, a small number of electrons is moving with a parabolic dispersion relation in a band, with an effective mass that is defined by the curvature of the frontier valence band (VB) and conduction band (CB) and consequently its mobility. Furthermore, as the electron is excited, a newly formed vacancy in the VB is defined as hole and also moves in an electric or magnetic field with a positive charge $+e$. In a perfect intrinsic semiconductor, the number of holes and electrons is equal

and thus no majority carrier is present. Upon heteroatom doping, for example with group III and V elements in silicon, the carrier concentration can be influenced and a p- or n-doped material is obtained, with electron acceptor and donor properties, respectively.[13] If these are connected, a directed current flow is obtained, immensely important in all kinds of semiconductor devices like diodes, solar cells, transistors and more. This is defined as p-n junction and is shown schematically in Figure 1.3.

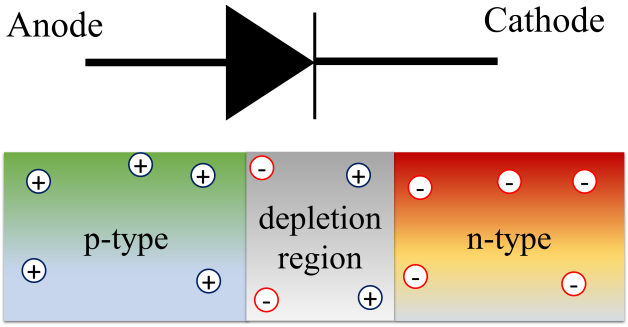

Figure 1.3: Illustration of a p-n junction acting as diode with majority carriers, p-n type regions and depletion region at the contact.

1.1.3 Optical Transitions

A very important characteristic of band gaps in semiconductors is their transition nature. This can generally be divided into direct and indirect band gaps, depending if the highest point of the valence band edge is at the same point in the k-space in the Brillouin zone as the lowest point of the conduction band edge. This is illustrated in Figure 1.4a.

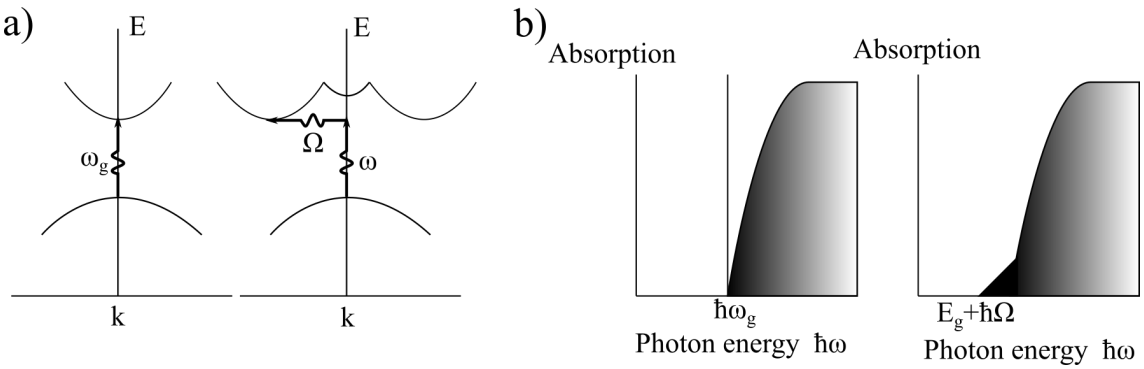

Figure 1.4: a) Schematic direct and indirect band transition and b) direct and indirect absorption processes at 0 K.

A semiconductor can be excited with a photon, a quantum of electromagnetic radiation. Fundamentally, the photon momentum is much smaller than the crystal momentum, causing an excited electron to conserve its momentum after photon absorption.[14] The absorption coefficient is then related to the transition probability and the density of states of the perturbed frontier bands. In a direct semiconductor, all transitions are allowed if they conserve the momentum and thus the transition probability is independent of the photon energy.[14] In an indirect semiconductor on the other hand, the transition to the bandgap requires a change in energy *and* momentum, which is obtained from a phonon interaction, i.e. a quantum of lattice vibrations.[11,14] The characteristic absorption spectra for both cases can be seen in Figure 1.4b. These effects are very important for devices like light emitting diode (LED) and solar cells, where the transition mechanism determines for example how probable an emission is through radiative recombination of electron and holes is. Obviously, through the required coupling with a phonon, the emission process is much slower in indirect semiconductors and therefore most LEDs materials are based on direct band gap semiconductors. In solar cells, an indirect material like the commonly used silicon has to be fabricated as rather thick film to absorb all irradiated light because of the smaller absorption coefficient in comparison to direct semiconductors like CIGS or perovskites, which can be employed as thin films.[15]

1.1.4 Photovoltaics

With the global energy economy in dire straits, photovoltaic energy harvesting has become one of the most important sources of renewable and non-CO_2-emitting energy, based on the conversion of the energy of the sun into electricity. The photovoltaic effect is a less extreme version of the photoelectric effect, demonstrated famously by Einstein in 1905.[16,17] In the photoelectric effect, energetic ultraviolet light can expel an electron from a metal into vacuum (Figure 1.5).

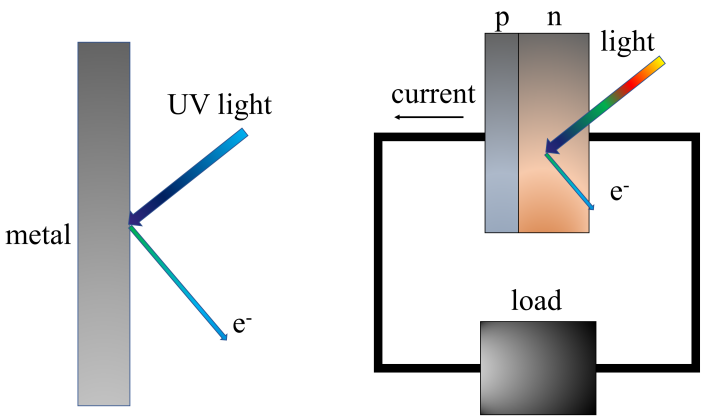

Figure 1.5: Illustration of the photoelectric effect (left) and the photovoltaic effect (right) in a closed circuit with p-n junction and a load.

In a photovoltaic cell, excited electrons in a semiconductor are ideally not allowed to relax and are rather extracted into an external circuit. This is accomplished via an inherent asymmetry as discussed in section 1.1.2 with a p-n junction for example. A potential difference or electromotive force is created through this excess energy of the excited electron, driving the current through the load.[16]

The so-called active layer is composed of a semiconductor material with a band gap in the usual range between $1.0\,\mathrm{eV}$ to $2.5\,\mathrm{eV}$ (ca. $1240\,\mathrm{nm}$ to $500\,\mathrm{nm}$), in order to extract the most energy from the solar spectrum. The theoretical maximum efficiency one can obtain from a single p-n junction solar cell with exclusively radiative recombination is approximately 30% and illustrated in Figure 1.6, which is also known as Shockley-Queisser limit.[18]

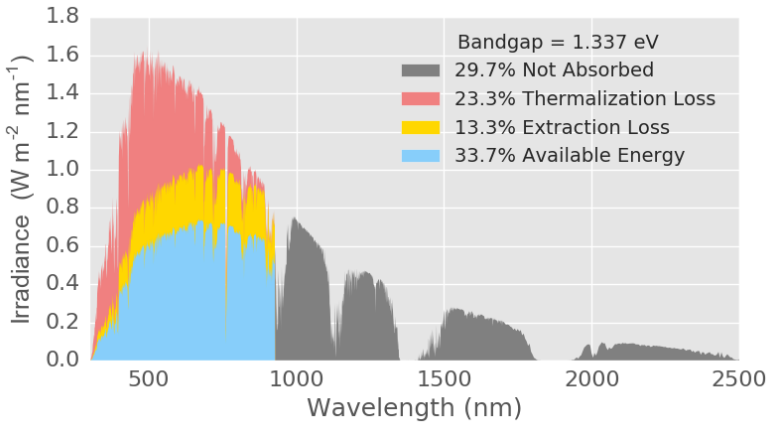

Figure 1.6: Air mass 1.5 spectrum (grey) with theoretical maximum efficiency extracted by a solar cell with a band gap of $1.337\,\mathrm{eV}$ and with typical losses highlighted in red, yellow and cyan.[19]

To understand this efficiency limit, fundamental aspects of the semiconductor are highly important. First of all, the voltage created by the p-n junction is theoretically limited by the magnitude of the semiconductor band gap, but is in fact also influenced by radiative recombination, i.e. the recombination of an electron and hole with photon emission. Furthermore, this value also defines that no light with an energy smaller than the band gap is absorbed (grey in Figure 1.6). Then, Shockley and Queisser assume thermalization losses, namely that energy of carriers above the band gap is lost and turned into heat, a big factor in reducing the theoretical maximum efficiency (red in Figure 1.6). Lastly, the electrical work to extract the carriers also reduces the efficiency (yellow in Figure 1.6).[16,20] These limitations are based on assumptions that can be influenced negatively by different factors like additional recombination mechanisms through crystal and electronic defects or phonon coupling, short carrier lifetimes and limited mobility. Nonetheless, concepts including sunlight concentration, tandem solar cells, intermediate band solar cells and more could and have surpassed the Shockley-Queisser (SQ) limit already.[21–23]

1.2 THE RISE OF PEROVSKITE SOLAR CELLS

With the interest in photovoltaic energy conversion steadily increasing, many new techniques and materials were studied and engineered in recent years to replace or support commercial silicon solar cells. This is due to the fact that silicon solar cells have a very high energetic production cost (minimum of $120\,\mathrm{kW\,h\,kg^{-1}}$)[24] to generate crystalline silicon, which is needed to achieve high performance.[25] Two of the most prominent examples for novel photovoltaic technologies are organic and perovskite solar cells.[26,27]
In particular, perovskite solar cells have been at the center of one of the most remarkable success stories in solar cell research history, as can be seen in the NREL (National Renewable Energy Laboratory) research cell chart in Figure 1.7, where the maximum certified research solar cell efficiencies for different materials and techniques are depicted.

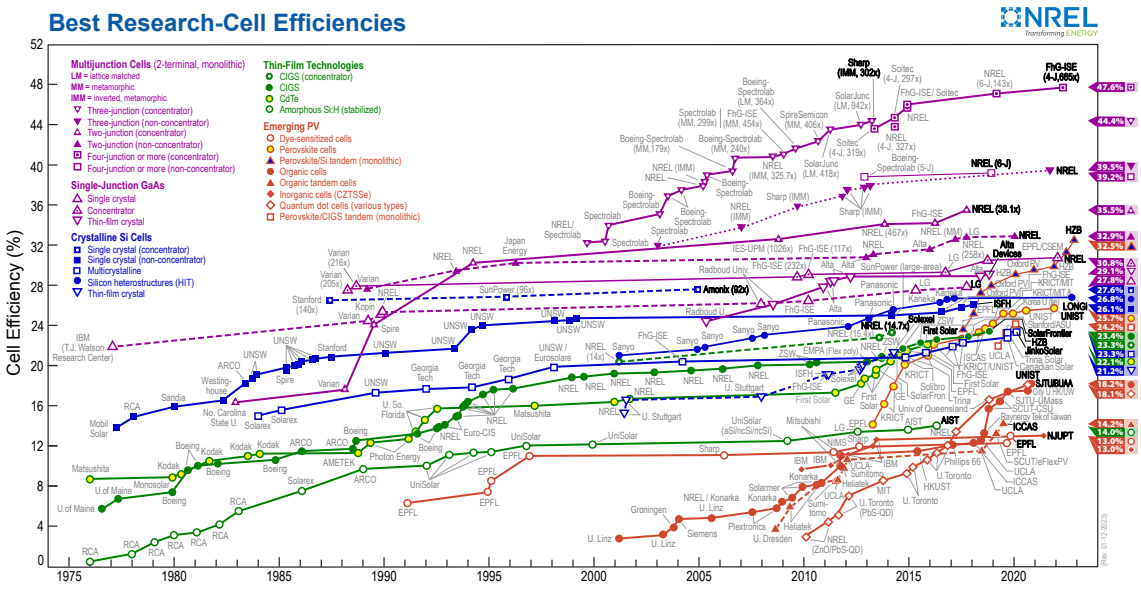

Figure 1.7: Best research cell efficiency chart from NREL.[28] Different emerging and consolidated photovoltaic technologies are marked in the legend.

Perovskite solar are shown as yellow-filled red circles with yellow borders and it can be seen that the unprecedented rise of efficiency from around 10% to an impressive 25.6% happened in only 10 years.[29–31] Furthermore, these remarkable devices could be fabricated through a low-temperature solution-based synthesis approach based on an active layer material consisting of cheap and abundant elements.

1.2.1 Understanding the Origin: Dye-Sensitized Solar Cells

To understand the steps that led to the development of perovskite solar cells, it is helpful to look back at a special type of photovoltaic device, described in 2001 by a seminal paper of Michael Grätzel, namely dye-sensitized solar cells (DSSC).[32] The main advantage of these kind of devices are low-cost fabrication and control at the molecular level. The basic working principle is shown schematically in Figure 1.8, where an electron transfer sensitizer, a molecular dye, injects charge carriers into a semiconductor/electrolyte junction with a wide band gap, e.g. TiO_2.[32–34]

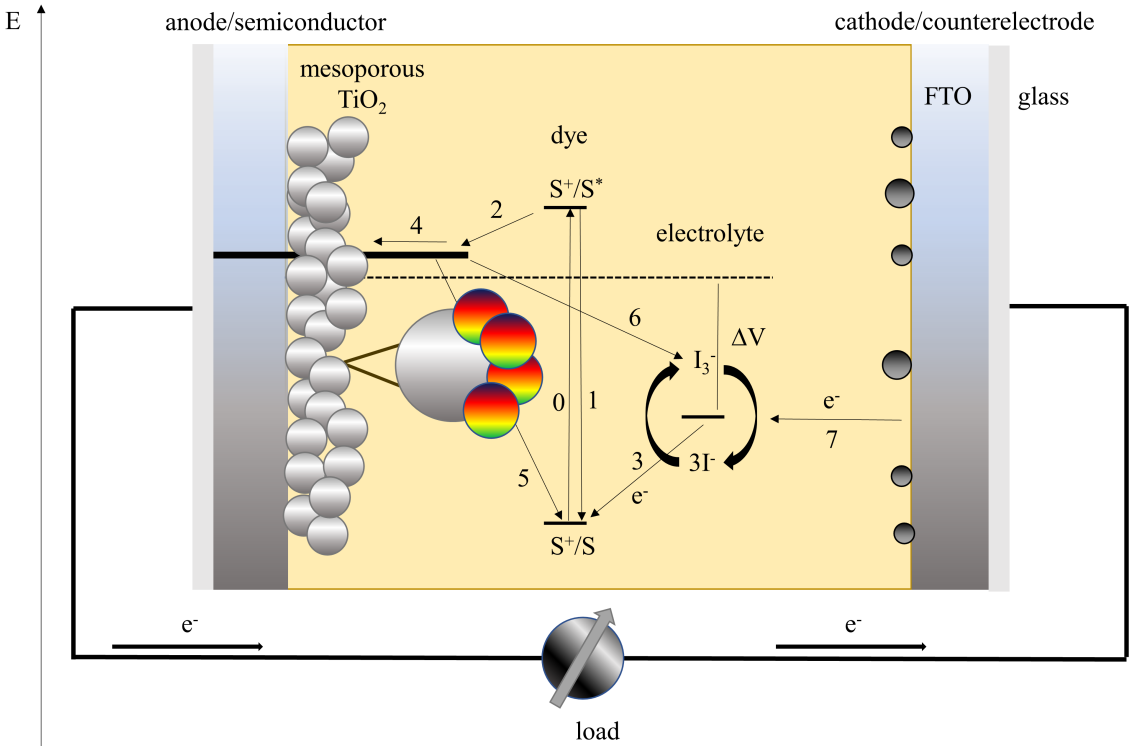

Figure 1.8: Schematic depiction of a DSSC with energy level diagram demonstrating the carrier transport processes shown with numbers (see text).

Here, a mesoporous layer of titania nanoparticles is deposited on a conducting oxide, for example fluorine-doped tin oxide (FTO). On this wide band gap semiconductor ($\approx 3.1\,\mathrm{eV}$) a molecular dye which acts as charge-transfer material can be found. When exciting this dye with light, an electron is injected into the CB of the $\mathrm{TiO_2}$ and the dye is oxidized (0,2 in Figure 1.8).[34] This is then reduced again via an electrolyte commonly based on an $\mathrm{I^-/I_3^-}$ redox system (3), which is governed by the equilibrium reaction between iodide and triiodide.[35] This prevents immediate recombination from the CB to the excited dye (5). At the platinum/electrode interface, the electrolyte system is restored again (7). The voltage of the cell is defined by the difference between the Fermi level of the mesoporous layer and the redox potential of the electrolyte.[34]

In genereal, DSSC technologies have been a paradigm shift in solar cell research, enabling short energy payback times, cheap fabrication, light weights and most of all widely tunable devices.[36,37] Despite their still comparably low power output, they are very promising for low-energy applications, e. g. in a bigger internet of things (IoT) scheme.[38] In 2009, Kojima et al. demonstrated organometal halide perovskites for the first time as new sensitizer material for DSSC cells, which turned out to be a watershed moment in third generation photovoltaics research (including concepts to overcome the SQ limit).[39]

1.2.2 Perovskites and What Makes Them Efficient

The name perovskite derives from the mineral $CaTiO_3$ named after Russian mineralogist Lev Perovski and is used for structures with the general composition ABX_3, where A and B are positively charged cations and X is an anion bound to both cations.[40,41] The ideal unit cell is cubic, but can also be orthorhombic, tetragonal or trigonal in many cases through symmetry losses.[42] Here, the B cation is coordinated by 6 X anions, forming an octahedron and A is 12-fold coordinated in a cuboctahedron. In the hybrid organic-inorganic perovskite (HOIP) $MAPbI_3$, MA (methylammonium, $(CH_3NH_3)^+$) acts as the A cation, while Pb^{2+} is the central octahedral cation B surrounded by I^-. The crystal structure and the electronic band structure for the case of $MAPbI_3$ is shown in Figure 1.9.[43]

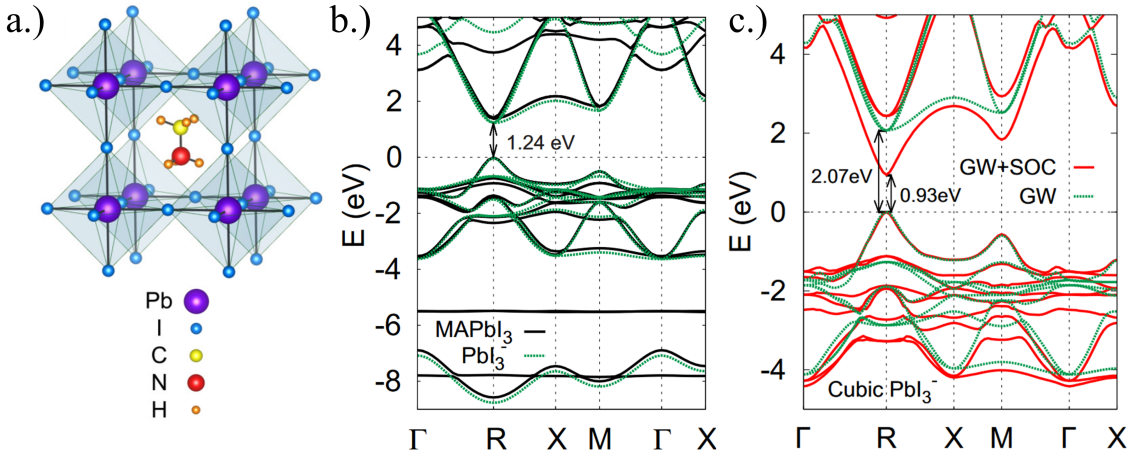

Figure 1.9: a) Crystal structure of cubic $MAPbI_3$, b) PBE band structures of $MAPbI_3$ (black) and PbI_3^- (green and c) quasiparticle band structure of PbI_3^- without spin-orbit coupling corrections (green) and with spin-orbit coupling (red).[43] Reproduced with permission. Copyright 2016, American Physical Society.

It can be seen with the bandstructures shown in Figure 1.9b and 1.9c that this material exhibits a direct bandgap of around $1.2\,eV$, which is very close to the optimal value to maximize a single-junction solar cell efficiency as defined by the SQ limit.[43] Furthermore, this value is strongly influenced by the choice of the A cation and the tilting of the $(PbI_6)^{4-}$ octahedra, making it widely tunable.[44] Additionally, the curvatures of the VB and CB are very high (Figure 1.9c), indicating low effective masses, which was shown in conjunction with low exciton binding energies,[45] where the exciton binding energy refers to the energy needed to split a bound quasiparticle of a hole and electron into free carriers. Together, this enables very favorable charge carrier transport properties and a high fraction of free carriers at room temperature, as the thermal energy needed to split

the exciton fully is mostly available. We also note that the main electronic structure at the band edges is dominated by the $(PbI_3)^-$ framework (Figure 1.9b). The organic A cation does not dictate the main electronic processes but rather acts as a templating agent to distort and/or compress the structure, which in turn influences the electronic structure massively in terms of band curvature and gap.[46]
Since their first use in DSSCs with efficiencies rapidly climbing,[39,47] lead-based perovskite materials were soon employed successfully as stand-alone active layer in solar cells because of the aforementioned properties. Here, the device structure was similar as in DSSCs as shown in a landmark publication in 2012 with some distinct differences that paved the way for novel solar cell architectures (Figure 1.10).[48]

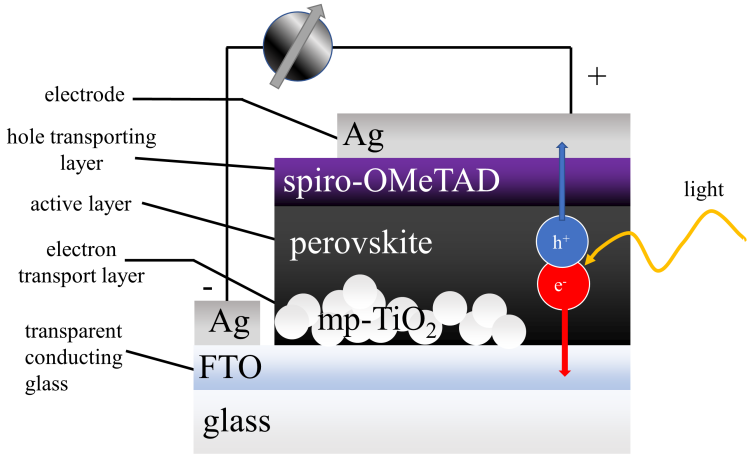

Figure 1.10: Model p-i-n solar cell architecture for a lead-based perovskite material with contacts, load and individual layers.

As discussed before, an asymmetry has to exist in solar cells to achieve directed current flow. Here, the perovskite acts as an "intrinsic semiconductor" that is very robust to accidental doping, with the electron (TiO_2) and hole transporting layers (spiro-OMeTAD) defining the p-n direction, resulting in a model p-i-n diode.[49] This architecture coupled with the optical characteristics of the perovskite, i.e. a high absorption coefficient and direct transition, enables the fabrication of extremely thin devices, as the thickness of the perovskite layer to achieve the maximum SQ efficiency is only around $200\,\mathrm{nm}$.[50]
Furthermore, the active perovskite layer can be fabricated easily and efficiently via a solvent-based spin-coating process starting from the inexpensive halide salts in organic solvents with a successive annealing step at comparably low temperatures, of around $100\,^\circ\mathrm{C}$.[51] Detrimentally, this production method usually introduces interruptions in the crystal lattices and irregularities in the fabricated thin film, leading to electronic perturbations in the materials.[52] Here, another unique property of lead-based perovskites prevents significant efficiency losses: their pronounced defect tolerance.[53,54] This is illustrated

schematically in Figure 1.11.

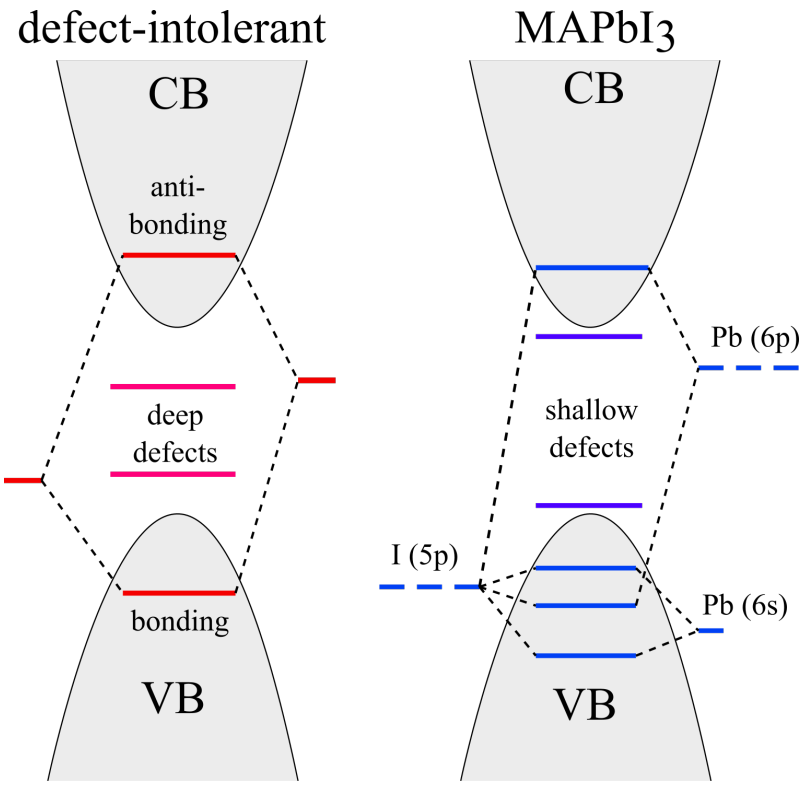

Figure 1.11: Illustration of a system with deep defect levels (left) and the bonding situation in $MAPbI_3$, where the orbitals lead to shallow defect states.

Usually, electronic states that are created by these crystallization faults can be found either close to the energetic levels of the frontier bands (shallow defects), influencing the carrier mobility, and deep in the band gap (deep defects), which can significantly reduce the voltage of the as-fabricated device through unwanted recombination centers.[53–55] Nonetheless, in lead-based HOIPs, studies suggested that the photocarriers are large polarons (quasiparticles which are formed by polarization of the crystal lattice through carriers), which shield the carriers from scattering with other carriers and defect states, thus increasing the lifetime of excited species.[56,57]

1.2.3 Stability Issues and Toxicity

In general, perovskite-based materials have shown to be inexpensive, easy to fabricate, defect tolerant, astoundingly efficient and tunable in the choice of all constituents. Nonetheless, there are still significant problems and challenges hindering the commercial application of these kinds of HOIP materials: first and foremost, lead halides are toxic for humans, cancerogenic and easily absorbable through the skin.[58] Additionally, in the 2011

RoHS2 directive, lead was prohibited at over 0.1% concentration in common working materials by the European Union.[59,60] The toxicity of lead is so pronounced that only a few µg can be extremely harmful for the nervous system and hence it should be completely avoided to introduce such compounds into the ecosystem to avoid circulation as seen in Figure 1.12.[61,62]

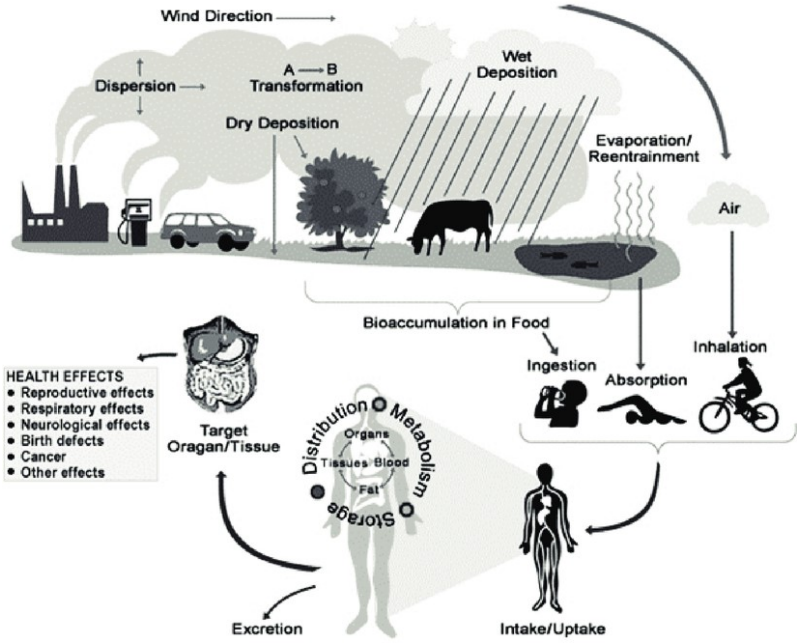

Figure 1.12: Lead circulation in the ecosystem and impact on the environment and human health.[62]

What aggravates this problem even more is an inherent instability of common lead based perovskite systems in real-world operating conditions.[63] Humidity, heat, phase instability and ion migration of especially I^- ions induces performance loss and degradation of a HOIP system like $MAPbI_3$ into MAI and PbI_2.[63–66]

1.3 PEROVSKITE-INSPIRED MATERIALS

As discussed before, the octahedral $(PbI_6)^{4-}$ motif determines the electronic characteristics that made perovskites so successful and efficient in the first place. Hence, a common strategy to circumvent the use of lead and retain at least some of the properties of perovskites is the implementation of elements with an *isoelectronic* (same electron configuration), *isovalent* (same valence electrons) character into a roughly *isostructural* (same crystal structure) framework. Pb has the electron configuration $[Xe]6s^24f^{14}5d^{10}6p^2$ and in the oxidized $2+$ state $[Xe]6s^24f^{14}5d^{10}$, where the energetically highest lying occupied

orbital is $6s^2$ (see Figure 1.11). These orbitals in conjunction with the unoccupied $6p$ orbitals have been identified as root cause for the unique properties like the defect tolerance, low band gap and transport properties.[67] The easiest way to achieve this replacement is to look at the neighbouring elements in the periodic system of elements (PSE), namely Ge^{2+} ($[Ar]3d^{10}4s^2$), Sn^{2+} ($[Kr]4d^{10}5s^2$), Sb^{3+} ($[Kr]4d^{10}5s^2$) and finally, the isoelectronic Bi^{3+} ($[Xe]6s^24f^{14}5d^{10}$).

1.3.1 Structural Aspects

Before considering derivative perovskite materials, it is useful to understand and analyze the influence of the constituents on the structure and vice versa. An important fact to regard is the so-called tolerance factor, which predicts if a regular perovskite structure is obtained at all and what unit cell it adopts, depending on a ratio of the ionic radii $t = R_{AX}/\sqrt{2}R_{BX}$.[68,69] The influence on the crystal structure and octahedral orientation is shown schematically in Figure 1.13.

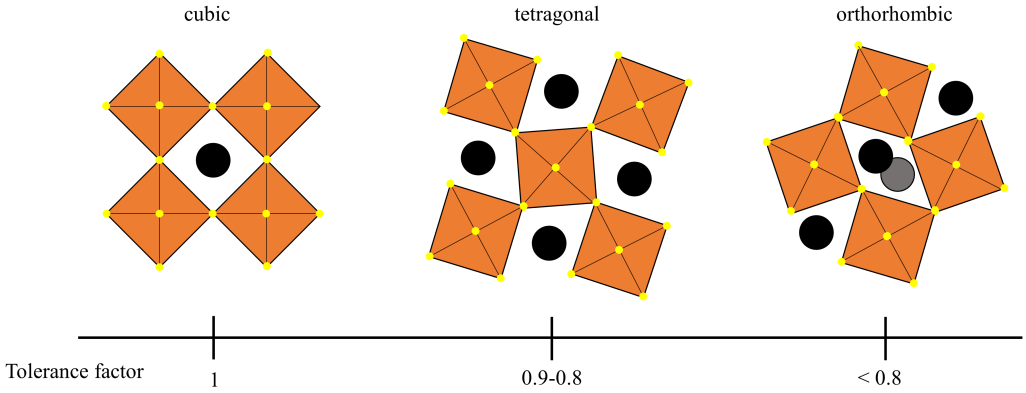

Figure 1.13: Schematic visualization of the influence of the Goldschmidt tolerance factor on the unit cell and octahedral positioning in perovskite structures.

This phenomenon is also very important in lead-based perovskites, where, for example, a phase duality in $FAPbI_3$ between a yellow, hexagonal structure and a black, trigonal structure determines whether it works successfully as solar cell or not.[70,71] By ion alloying, for example with Rb, Cs, Br etc., the tolerance factor can be tuned and the favorable crystal structure can be stabilized.[69–72] Moreover, as expected, unit cell modification and octahedral positioning induces changes in the electronic structure as seen in Figure 1.14.[73,74]

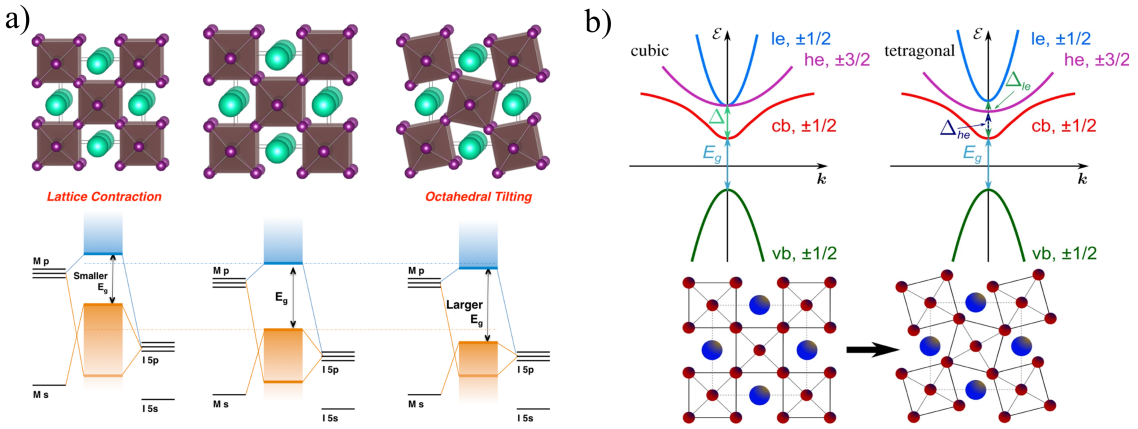

Figure 1.14: a) Influence of lattice contractions and octahedral tilting on the band gap of perovskite materials[74] and b) illustration of the change in band structure upon transition from cubic to tetragonal lattice.[73] le and he refer to large and heavy electrons, respectively. Reproduced with permission. Copyright 2017, American Chemical Society and 2022, Nature Publishing Group.

Here, for example through enlargement of the lattice or octahedral distortion, the band gap can be increased (Figure 1.14a). Also, through the symmetry reduction from cubic to tetragonal, the degenerated spin band above the conduction band (light electrons (le) and heavy electrons (he)) is separated.[73]

Looking beyond the same conformations (as expected with divalent ions of the same PSE group), introduction of trivalent ions like Sb and Bi drastically changes the obtained structure (depicted in Figure 1.15).

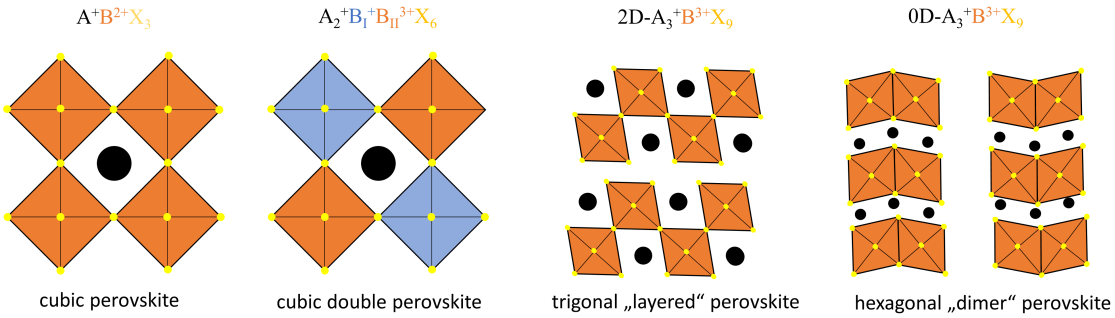

Figure 1.15: Illustration of perovskite-derived structures with trivalent B cation. From left to right: regular perovskite, double perovskite, layered "defect" perovskite and dimer "defect" perovskite.

One approach is to split the cations into two oxidation states by adding a monovalent cation like Ag to Bi to sum up to $(+II)_2$. This results in so-called double perovskite structures $A_2B_IB_{II}X_6$ with alternating $(B_IX_6)^{5-}/(B_{II}X_6)^{3-}$ octahedra.[75,76]

When avoiding this and sticking with a single trivalent cation, the so called "defect" perovskite structures with stoichiometry $A_3B_2X_9$ can be obtained.[77,78] Here, two poly-

morphs can be distinguished: one layered structure with corner-sharing octahedra which can be seen as a regular perovskite structure with every 3rd octahedral layer removed ($AB_{2/3}X_3$) and a non-perovskite dimer structure with fused bioctahedra.
From this foundation, immense combinatorial possibilities open up, especially when considering further techniques like dimensional reduction by introduction of organic spacer molecules between the slabs.[79–82] This has even been shown to induce such drastic changes as shifting of the band gap nature from indirect to direct in some materials.[80,83] A more detailed depth discussion about the electronic consequences will be carried out in the following sections.

1.3.2 Group IV Elements as Substitutes: Perovskite-Type

With the Group IV elements Sn and Ge, the same crystal structure of the archetypical $MAPbI_3$ can be obtained because of their divalent oxidation state as cations. The corresponding band structures with Cs as A cation can be seen in Figure 1.16.[84]

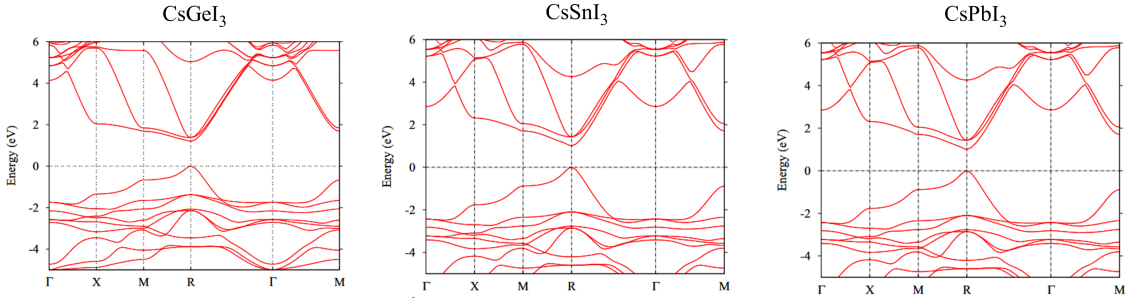

Figure 1.16: Electronic band structures calculated with the quasiparticle GW method and spin-orbit coupling for $CsGeI_3$, $CsSnI_3$ and $CsPbI_3$.[84] Reproduced with permission. Copyright 2016, American Physical Society.

Interestingly, replacement with germanium and tin leads to almost identical band structures with slightly changing band gaps. $CsSnI_3$ has the lowest band gap with $1.0\,eV$, then $CsGeI_3$ exhibits a band gap of $1.2\,eV$ and finally $CsPbI_3$ with $1.3\,eV$.[84] While germanium-based perovskite materials still underperform at around 7%, the tin-based compounds have shown efficiencies of up to 13.2% already.[85,86] The main bottlenecks with these materials are pronounced instability and proneness to oxidation to the tetravalent state.[87,88] Furthermore, the diffusion lengths in tin perovskites seem to be shorter than in lead-based analogs, making it hard to produce well-absorbing thick films without losing charge carriers.[86] This has been attributed to self-doping via oxidative reactions, inducing unwanted recombination.[89] Nonetheless, the voltage values in devices of such

materials are already high, hinting at a great potential for tin-based perovskites if the stability can be enhanced, for which manifold strategies are currently being studied.[90,91]

1.3.3 Group V Elements as Substitutes: Double Perovskites

Because of the instability of the aforementioned materials and the still relevant toxicity of tin,[92] recent research looked one group further in the PSE towards Bi and Sb in the double perovskite form. The most prominent example for double $(I/III)_{II}$ substitution in the perovskite lattice is $CsAgBiBr_6$.[93,94] Many interesting properties like long carrier lifetimes of up to 1 µs, very high stability and easy processability were demonstrated early on, but the PCE still has not surpassed about 3%.[95–97] The reasons become apparent when the band structure is observed (Figure 1.17a).

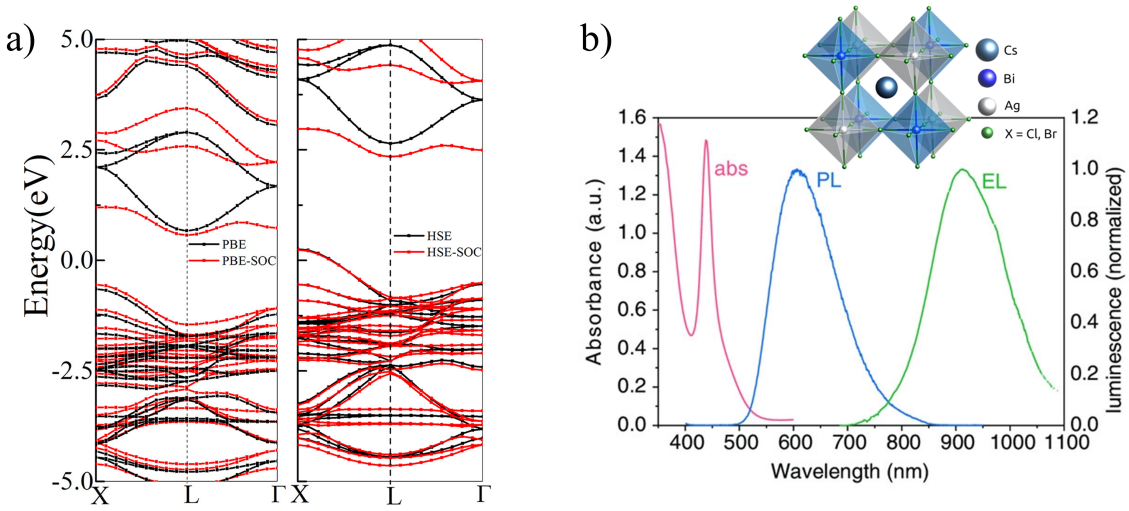

Figure 1.17: a) Electronic band structures of $Cs_2AgBiBr_6$, calculated with PBE and HSE, with and without spin orbit coupling. b) Absorption curve, photoluminescence and electroluminescence spectra for a $Cs_2AgBiBr_6$ thin film and solar cell device (EL). Inset: Model of the crystal structure.[98,99] Reproduced with permission. Copyright 2022, Elsevier B.V.

First of all, the band gap is quite large (> 2 eV) and indirect, creating the need for thick absorber layers and theoretically limiting the efficiency in solar cells to 10% through the SQ limit.[98] Accessing the iodide version would possibly circumvent this, but was only shown to be accessible via dimensional reduction, e.g. in $[AE2T]_2AgBiI_8$ (5,5'-diylbis(aminoethyl)-[2,2'-bithiophene] (AE2T)).[100] Additionally, the photoluminescence spectrum is strongly redshifted as seen in Figure 1.17b, as is the electroluminescence, which is tied to the voltage limit.[99] The PL emission is tied to many effects, namely disorder through A/B cation mixing, electron-phonon coupling and color

centers (point defects of trapped carriers), which are all unfavorable for photovoltaic applications.[101–103] Furthermore, low contact selectivity was shown,[104] further reducing the efficiency for photovoltaic energy conversion. Approaches to capitalize and improve on this material are focused on band gap reduction and device engineering.[105,106]

1.3.4 Group V Elements as Substitutes: Defect Perovskites

As discussed before, if only one group V element like Bi and Sb is substituted for lead, the so-called defect-ordered perovskites of the stoichiometry $A_3B_2X_9$ are obtained. This class of materials offers some more advantages compared to double perovskites like $Cs_2AgBiBr_6$ including easier fabrication, lower band gaps and lower exciton binding energies.[107] The phase duality has great electronic impact here, as shown in the band structures for $Cs_3Sb_2I_9$ in Figure 1.18a.

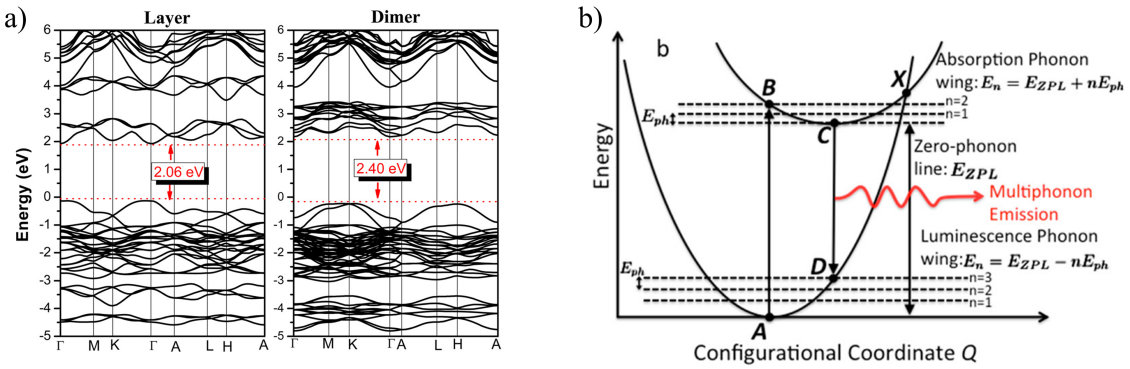

Figure 1.18: a) Electronic band structures of $Cs_3Sb_2I_9$ in the dimer and layered form, calculated with HSE, and b) configuration coordinate model illustrating the phonon-coupled recombination and absorption mechanism in $Cs_3Sb_2I_9$.[77,108] Reproduced with permission. Copyright 2017, American Chemical Society.

Firstly, the size of the band gap is reduced significantly in the layered form with the corner sharing octahedra compared to the dimer one with the face-sharing octahedra. Nonetheless, both polymorphs exhibit rather flat valence bands, which indicates holes with large effective masses and therefore unfavorable transport properties.[77] Interestingly, the dimer form was shown to be more efficient in devices generally, which is counter intuitive when observing the band structures. The PCE record for dimer $MA_3Sb_2I_9$ lies at 2.77% and for layered $MA_3Sb_2I_9$ at 1.8%.[107,109] This is attributed to a very important and detrimental effect in many lead-free perovskite devices: electron-phonon coupling (shown in Figure 1.18b).[110] Here, these interactions of lattice vibrations with charge carriers lead to small polarons, which trap carriers and produce self-trapped excitons, which then recombine

with the help of a phonon (upper band: self-trapped excitons, lower band: valence band in Figure 1.18).[108,110]

1.3.5 Group V Elements as Substitutes: Non-Perovskites

Lastly, as shown with the dimer defect perovskite structures, non-perovskite structures based on ns^2 cations can also be efficient in photovoltaic cells. This has been demonstrated extensively with numerous other structures, like pnictogen halides with the structural formula $A_a^{+I}B_b^{+III}X_{a+3b}^{-I}$ (B = Bi/Sb) or chalcogen halides $B^{+III}Ch^{-II}X^{-I}$ (X = Br/I; Ch = O/S/Se).[111,112] Pnictogen halides consist of side-sharing $(AX_6)^{5-}$/$(BX_6)^{3-}$ octahedra, responsible for the frontier electronic structure as seen in most perovskite and perovskite-derived materials. $A_a^{+I}B_b^{+III}X_{a+3b}$ can adopt two different structures: a structure in a rhombohedral unit cell as seen in Figure 1.19a with $(AX_6)^{5-}$ and $(BX_6)^{3-}$ octahedral slabs separated by also octahedrally coordinated A cations on different lattice positions, and a cubic "defect-spinel" structure with all cations on the same lattice positions as seen in Figure 1.19b.[111,113,114]

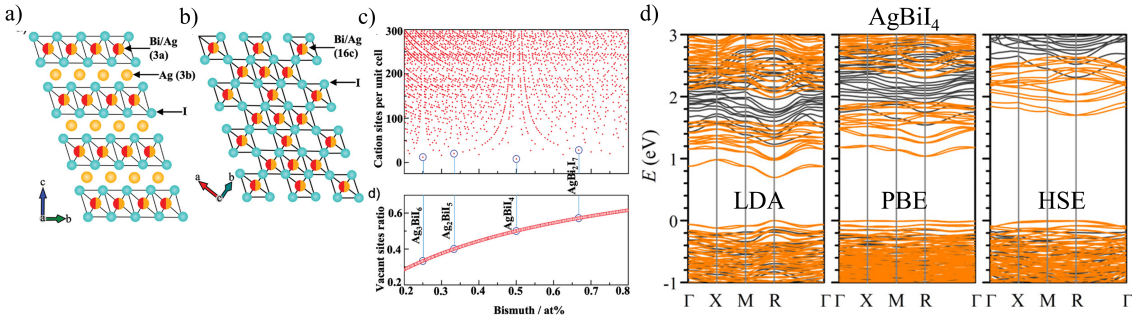

Figure 1.19: a) $CdCl_2$-type crystal structure of $Ag_aBi_bX_{a+3b}$, b) cubic defect-spinel phase of $Ag_aBi_bX_{a+3b}$, c) illustration of the phase width with stable stoichiometries and d) band structures with model $AgBiI_4$ calculated with the LDA/PBE/HSE methods with (orange) and without (grey) spin-orbit coupling.[111,113,114] Reproduced with permission. Copyright 2017, Wiley-VCH Verlag GmbH and Co. KGaA and 2016, American Chemical Society.

In general, this class of materials can be simplified as consisting completely of $(AX_6)^{5-}$, $(BX_6)^{3-}$ and vacant octahedra $(\Delta X_6)^{6-}$.[111] This enables a very large phase width as shown in Figure 1.19c, especially when considering that the A and B cations can be alloyed widely, shown extensively for Cu/Ag and Bi/Sb.[115–118] The band structures of the prototpye $AgBiI_4$ system are shown in Figure 1.19d, demonstrating a low and direct band gap in the range of 1.7 eV, which was shown to lead to very high absorption coefficients near the optimal range for single-junction solar cells.[113,114] These materials exhibited promising efficiencies of 4.3% for Ag_3BiI_6 and 5.4% for a sulfur doped-variant.[113,119]

A factor hampering the device performance is the intrinsic high concentration of mostly deep-lying defects, probably resulting from the stoichiometric and structural disorder of these materials and the short carrier lifetime.[111] Furthermore, the charge carrier mobility is low, owing to the mostly flat bands at the band edges (Figure 1.19c).[114] Lastly, the band alignment with commonly used electron and hole transporting layers is still not optimal, further reducing the efficiency, which could be, e.g., improved by alloying with sulfur.[119]

1.3.6 Intrinsic Challenges and Application Space

Multiple difficulties still stand in the way of completely replacing lead as central atom for perovskite solar cells. This ranges from chemical and physical instability to unfavorable defect properties, pronounced exciton-phonon coupling, large band gaps and more. Nonetheless, the facile processability and very wide phase width and tunability leads to a plethora of new materials, also beyond the use as highly efficient solar cells.[120]
Here, for example, the defect perovskite $Cs_3Bi_2Br_9$ has been successfully employed as efficient blue phosphor, as was the perovskite-type $Bi : Cs_2SnCl_6$.[121,122] Alternatively, the double perovskite $Cs_2AgBiBr_6$ was shown to be a robust and efficient semiconductor for photocatalysis, as was $MA_3Bi_2I_9$.[123,124] $Cs_2AgBiBr_6$, moreover, outperformed lead-based perovskites in X-ray detection applications because of its heavy Bi cation and pronounced stability.[125] The layered defect perovskite $Cs_3Sb_2I_9$ was demonstrated to operate in an artificial synaptic memory device exactly because of its high electronic-ionic coupling which was a drawback for solar cells.[126] Finally, the non-perovskite Cu_2AgBiI_6 proved to be a highly efficient photovoltaic absorber if used in an indoor setting, i.e. with a significantly lower light intensity and reduced spectrum, matching better with the higher band gap.[115,127,128]

1.4 OUTLINE OF THIS THESIS

In this work, the synthesis, properties and application potential of multiple lead-free "perovskite-inspired" materials were investigated. Here, perovskite-inspired is referring not only to a related crystal structure, but rather a way of designing and tuning solution-processed halide materials to unravel novel semiconductors for a range of device implementations.

In Chapter 3, an easy synthetic strategy to access the layered polymorph of $MA_3Sb_2I_9$ instead of the thermodynamically favored dimer structure is presented. This is accomplished via replacing the usual halide precursors with acetate salts, increasing the interatomic distance of Sb-Sb, thus leading to a phase-pure layered structure with reduced band gap, exciton binding energy and higher photovoltaic performance.

In Chapter 4, the same approach is expanded with the addition of tin salts in various oxidation states, dramatically boosting the absorption capability of the thin films. This absorption increase is studied thoroughly and traced back to a heterovalent oxidation state of the tin cations, stabilizing themselves in close mixed-valent clusters and adding a broad intervalence absorption contribution in the process.

In Chapter 5, the thin film synthesis and characterization of novel lead-free material $Cu_xAg_{1-x}Sb_{1-y}Bi_yI_3$ is shown. We demonstrate a composition of 1:1:4 and highlight the presence of deep Ag/Cu point defects in the band gap. Nonetheless, we manage to improve the morphology by incorporation of Cu and Bi. These effects are shown to be the root cause for performance improvement in solar cells, which is overall boosted even further when working with low light intensity.

In Chapter 6, a unique double perovskite based on a Na/Fe pair is studied. By means of theoretical and experimental methods, an unpaired spin system of 5/2 with a spin-polarized electronic structure is shown. Through low temperature optical measurements, thermochromism and excitonic behavior is demonstrated.

In Chapter 7, a fluorinated spacer cation is employed to dimensionally reduce the archetype photovoltaic double perovskite $Cs_2AgBiBr_6$, demonstrating the stabilization of a lower band gap iodide phase with a direct band gap due to band folding and revealing ultrafast charge carrier localization in such systems.

1.5 REFERENCES

[1] M. Castells, *City* **1997**, *2*, 6–16.

[2] M. Castells, *Media Studies: a reader* **2010**, *2*, 152.

[3] S. Liddell, Jones. 1980. A Greek-English Lexicon, **1980**.

[4] G. Busch, *European Journal of Physics* **1989**, *10*, 254.

[5] M. Riordan, L. Hoddeson, C. Herring, *Reviews of Modern Physics* **1999**, *71*, S336.

[6] Picture of the Atanasoff-Berry computer, https://www.thoughtco.com/john-atanasoff-and-clifford-berry-inventors-4078350, Accessed: 2023-03-09.

[7] Picture of the worlds smallest computer, https://news.umich.edu/u-m-researchers-create-worlds-smallest-computer, Accessed: 2023-03-09.

[8] Samsung Announces Chip Production Using 3nm Technology, https://news.samsung.com/global/samsung-begins-chip-production-using-3nm-process-technology-with-gaa-architecture, Accessed: 2023-03-09.

[9] 3nm Technology report by Taiwanese company TSMC, https://www.tsmc.com/english/dedicatedFoundry/technology/logic, Accessed: 2023-03-09.

[10] M. Eckert, Max von Laue and the discovery of X-ray diffraction in 1912, **2012**.

[11] C. Kittel, P. McEuen, *Introduction to solid state physics*, John Wiley & Sons, **2018**.

[12] D. Ter Haar, *The Old Quantum Theory: The Commonwealth and International Library: Selected Readings in Physics*, Elsevier, **2016**.

[13] U. K. Mishra, J. Singh, *Semiconductor device physics and design*, *Vol. 83*, Springer, **2008**.

[14] J. I. Pankove, *Optical processes in semiconductors*, Courier Corporation, **1975**.

[15] L. Khriachtchev, *Silicon Nanophotonics: Basic Principles, Present Status, and Perspectives*, CRC Press, **2016**.

[16] J. A. Nelson, *The physics of solar cells*, World Scientific Publishing Company, **2003**.

[17] A. Pais, *Reviews of modern physics* **1979**, *51*, 863.

[18] W. Shockley, H. J. Queisser, *Journal of applied physics* **1961**, *32*, 510–519.

[19] M. Chuang, Shockley Queisser limit, https://github.com/marcus-cmc/Shockley-Queisser-limit, **2017**.

[20] P. Würfel, U. Würfel, *Physics of solar cells: from basic principles to advanced concepts*, John Wiley & Sons, **2016**.

[21] A. Al-Ashouri, E. Köhnen, B. Li, A. Magomedov, H. Hempel, P. Caprioglio, J. A. Marquez, A. B. Morales Vilches, E. Kasparavicius, J. A. Smith, et al., *Science* **2020**, *370*, 1300–1309.

[22] A. Luque, A. Marti, C. Stanley, *Nature Photonics* **2012**, *6*, 146–152.

[23] Y. Xing, P. Han, S. Wang, P. Liang, S. Lou, Y. Zhang, S. Hu, H. Zhu, C. Zhao, Y. Mi, *Renewable and Sustainable Energy Reviews* **2015**, *51*, 1697–1708.

[24] S. Pizzini, *Solar energy materials and solar cells* **2010**, *94*, 1528–1533.

[25] T. Saga, *npg asia materials* **2010**, *2*, 96–102.

[26] H. Hoppe, N. S. Sariciftci, *Journal of materials research* **2004**, *19*, 1924–1945.

[27] M. A. Green, A. Ho-Baillie, H. J. Snaith, *Nature photonics* **2014**, *8*, 506–514.

[28] Best Research-Cell Efficiency Chart, https://www.nrel.gov/pv/cell-efficiency.html, Accessed: 2023-03-13.

[29] P. Gao, M. Grätzel, M. K. Nazeeruddin, *Energy & Environmental Science* **2014**, *7*, 2448–2463.

[30] J. Jeong, M. Kim, J. Seo, H. Lu, P. Ahlawat, A. Mishra, Y. Yang, M. A. Hope, F. T. Eickemeyer, M. Kim, Y. J. Yoon, I. W. Choi, B. P. Darwich, S. J. Choi, Y. Jo, J. H. Lee, B. Walker, S. M. Zakeeruddin, L. Emsley, U. Rothlisberger, A. Hagfeldt, D. S. Kim, M. Grätzel, J. Y. Kim, *Nature* **2021**, *592*, 381–385.

[31] H. Min, D. Y. Lee, J. Kim, G. Kim, K. S. Lee, J. Kim, M. J. Paik, Y. K. Kim, K. S. Kim, M. G. Kim, et al., *Nature* **2021**, *598*, 444–450.

[32] M. Grätzel, *nature* **2001**, *414*, 338–344.

[33] M. Grätzel, *Journal of photochemistry and photobiology C: Photochemistry Reviews* **2003**, *4*, 145–153.

[34] A. Hagfeldt, G. Boschloo, L. Sun, L. Kloo, H. Pettersson, *Chemical reviews* **2010**, *110*, 6595–6663.

[35] G. Boschloo, A. Hagfeldt, *Accounts of chemical research* **2009**, *42*, 1819–1826.

[36] P. V. Kamat, *The Journal of Physical Chemistry Letters* **2013**, *4*, 3733–3734.

[37] M. K. Nazeeruddin, E. Baranoff, M. Grätzel, *Solar energy* **2011**, *85*, 1172–1178.

[38] D. Devadiga, M. Selvakumar, P. Shetty, M. Santosh, *Journal of Electronic Materials* **2021**, *50*, 3187–3206.

[39] A. Kojima, K. Teshima, Y. Shirai, T. Miyasaka, *Journal of the american chemical society* **2009**, *131*, 6050–6051.

[40] N. Wiberg, *Lehrbuch der Anorganischen Chemie*, De Gruyter, Berlin, Boston, **2008**.

[41] H.-R. Wenk, A. Bulakh, *Minerals: their constitution and origin*, Cambridge University Press, **2016**.

[42] A. Navrotsky, *Chemistry of Materials* **1998**, *10*, 2787–2793.

[43] W. Gao, X. Gao, T. A. Abtew, Y.-Y. Sun, S. Zhang, P. Zhang, *Physical Review B* **2016**, *93*, 085202.

[44] A. Amat, E. Mosconi, E. Ronca, C. Quarti, P. Umari, M. K. Nazeeruddin, M. Gratzel, F. De Angelis, *Nano letters* **2014**, *14*, 3608–3616.

[45] K. Galkowski, A. Mitioglu, A. Miyata, P. Plochocka, O. Portugall, G. E. Eperon, J. T.-W. Wang, T. Stergiopoulos, S. D. Stranks, H. J. Snaith, et al., *Energy & Environmental Science* **2016**, *9*, 962–970.

[46] C. Motta, F. El-Mellouhi, S. Kais, N. Tabet, F. Alharbi, S. Sanvito, *Nature communications* **2015**, *6*, 7026.

[47] J.-H. Im, C.-R. Lee, J.-W. Lee, S.-W. Park, N.-G. Park, *Nanoscale* **2011**, *3*, 4088–4093.

[48] M. M. Lee, J. Teuscher, T. Miyasaka, T. N. Murakami, H. J. Snaith, *Science* **2012**, *338*, 643–647.

[49] K. Miyano, N. Tripathi, M. Yanagida, Y. Shirai, *Accounts of chemical research* **2016**, *49*, 303–310.

[50] W. E. Sha, X. Ren, L. Chen, W. C. Choy, *Applied Physics Letters* **2015**, *106*, 221104.

[51] P. Roy, N. K. Sinha, S. Tiwari, A. Khare, *Solar Energy* **2020**, *198*, 665–688.

[52] N.-G. Park, K. Zhu, *Nature Reviews Materials* **2020**, *5*, 333–350.

[53] G.-W. Kim, A. Petrozza, *Advanced Energy Materials* **2020**, *10*, 2001959.

[54] K. X. Steirer, P. Schulz, G. Teeter, V. Stevanovic, M. Yang, K. Zhu, J. J. Berry, *ACS Energy Letters* **2016**, *1*, 360–366.

[55] W.-J. Yin, T. Shi, Y. Yan, *Applied Physics Letters* **2014**, *104*, 063903.

[56] K. Miyata, X.-Y. Zhu, *Nature materials* **2018**, *17*, 379–381.

[57] K. Miyata, T. L. Atallah, X.-Y. Zhu, *Science Advances* **2017**, *3*, e1701469.

[58] G. Flora, D. Gupta, A. Tiwari, *Interdisciplinary toxicology* **2012**, *5*, 47–58.

[59] A. Abate, *Joule* **2017**, *1*, 659–664.

[60] E. Council, *Off. J. Eur. Union* **2003**, *37*, 19–23.

[61] E. van der Voet, R. Salminen, M. Eckelman, T. Norgate, G. Mudd, R. Hisschier, J. Spijker, M. Vijver, O. Selinus, L. Posthuma, et al., *Environmental challenges of anthropogenic metals flows and cycles*, United Nations Environment Programme, **2013**.

[62] A. Ara, J. A. Usmani, et al., *Interdisciplinary toxicology* **2015**, *8*, 55–64.

[63] M. Wu, N. Haji Ladi, Z. Yi, H. Li, Y. Shen, M. Wang, *Energy Technology* **2020**, *8*, 1900744.

[64] B. Conings, J. Drijkoningen, N. Gauquelin, A. Babayigit, J. D'Haen, L. D'Olieslaeger, A. Ethirajan, J. Verbeeck, J. Manca, E. Mosconi, et al., *Advanced Energy Materials* **2015**, *5*, 1500477.

[65] A. H. Slavney, R. W. Smaha, I. C. Smith, A. Jaffe, D. Umeyama, H. I. Karunadasa, *Inorganic chemistry* **2017**, *56*, 46–55.

[66] Y. Zhou, Y. Zhao, *Energy & environmental science* **2019**, *12*, 1495–1511.

[67] A. M. Ganose, C. N. Savory, D. O. Scanlon, *Chemical Communications* **2017**, *53*, 20–44.

[68] G. Kieslich, S. Sun, A. K. Cheetham, *Chemical science* **2015**, *6*, 3430–3433.

[69] Y. Fu, M. P. Hautzinger, Z. Luo, F. Wang, D. Pan, M. M. Aristov, I. A. Guzei, A. Pan, X. Zhu, S. Jin, *ACS central science* **2019**, *5*, 1377–1386.

[70] Z. Song, A. Abate, S. C. Watthage, G. K. Liyanage, A. B. Phillips, U. Steiner, M. Graetzel, M. J. Heben, *Advanced Energy Materials* **2016**, *6*, 1600846.

[71] Y. H. Park, I. Jeong, S. Bae, H. J. Son, P. Lee, J. Lee, C.-H. Lee, M. J. Ko, *Advanced Functional Materials* **2017**, *27*, 1605988.

[72] H. Chen, Y. Chen, T. Zhang, X. Liu, X. Wang, Y. Zhao, *Small Structures* **2021**, *2*, 2000130.

[73] E. Kirstein, D. R. Yakovlev, M. M. Glazov, E. A. Zhukov, D. Kudlacik, I. V. Kalitukha, V. F. Sapega, G. S. Dimitriev, M. A. Semina, M. O. Nestoklon, et al., *Nature Communications* **2022**, *13*, 3062.

[74] R. Prasanna, A. Gold-Parker, T. Leijtens, B. Conings, A. Babayigit, H.-G. Boyen, M. F. Toney, M. D. McGehee, *Journal of the American Chemical Society* **2017**, *139*, 11117–11124.

[75] N. K. Tailor, A. Listorti, S. Colella, S. Satapathi, *Advanced Materials Technologies* **2023**, *8*, 2200442.

[76] C. Wu, Q. Zhang, Y. Liu, W. Luo, X. Guo, Z. Huang, H. Ting, W. Sun, X. Zhong, S. Wei, et al., *Advanced Science* **2018**, *5*, 1700759.

[77] B. Saparov, F. Hong, J.-P. Sun, H.-S. Duan, W. Meng, S. Cameron, I. G. Hill, Y. Yan, D. B. Mitzi, *Chemistry of Materials* **2015**, *27*, 5622–5632.

[78] B. Chabot, E. Parthe, *Acta Crystallographica Section B: Structural Crystallography and Crystal Chemistry* **1978**, *34*, 645–648.

[79] R. Bakthavatsalam, M. P. Haris, S. R. Shaikh, A. Lohar, A. Mohanty, D. Moghe, S. Sharma, C. Biswas, S. S. K. Raavi, R. G. Gonnade, et al., *The Journal of Physical Chemistry C* **2019**, *124*, 1888–1897.

[80] B. A. Connor, L. Leppert, M. D. Smith, J. B. Neaton, H. I. Karunadasa, *Journal of the American Chemical Society* **2018**, *140*, 5235–5240.

[81] A. H. Proppe, A. Johnston, S. Teale, A. Mahata, R. Quintero-Bermudez, E. H. Jung, L. Grater, T. Cui, T. Filleter, C.-Y. Kim, et al., *Nature communications* **2021**, *12*, 3472.

[82] H. Tsai, W. Nie, J.-C. Blancon, C. C. Stoumpos, R. Asadpour, B. Harutyunyan, A. J. Neukirch, R. Verduzco, J. J. Crochet, S. Tretiak, et al., *Nature* **2016**, *536*, 312–316.

[83] E. T. McClure, A. P. McCormick, P. M. Woodward, *Inorganic Chemistry* **2020**, *59*, 6010–6017.

[84] L.-y. Huang, W. R. Lambrecht, *Physical Review B* **2016**, *93*, 195211.

[85] R. Chiara, M. Morana, L. Malavasi, *ChemPlusChem* **2021**, *86*, 879–888.

[86] T. Wu, X. Liu, X. Luo, X. Lin, D. Cui, Y. Wang, H. Segawa, Y. Zhang, L. Han, *Joule* **2021**, *5*, 863–886.

[87] H. Yao, F. Zhou, Z. Li, Z. Ci, L. Ding, Z. Jin, *Advanced Science* **2020**, *7*, 1903540.

[88] M. Chen, M.-G. Ju, H. F. Garces, A. D. Carl, L. K. Ono, Z. Hawash, Y. Zhang, T. Shen, Y. Qi, R. L. Grimm, et al., *Nature communications* **2019**, *10*, 16.

[89] N. K. Noel, S. D. Stranks, A. Abate, C. Wehrenfennig, S. Guarnera, A.-A. Haghighirad, A. Sadhanala, G. E. Eperon, S. K. Pathak, M. B. Johnston, et al., *Energy & Environmental Science* **2014**, *7*, 3061–3068.

[90] Q. Zhang, S. Liu, M. He, W. Zheng, Q. Wan, M. Liu, X. Liao, W. Zhan, C. Yuan, J. Liu, et al., *Angewandte Chemie International Edition* **2022**, *61*, e202205463.

[91] X. Zhang, S. Wang, W. Zhu, Z. Cao, A. Wang, F. Hao, *Advanced Functional Materials* **2022**, *32*, 2108832.

[92] K. Winship, *Adverse drug reactions and acute poisoning reviews* **1988**, *7*, 19–38.

[93] A. H. Slavney, T. Hu, A. M. Lindenberg, H. I. Karunadasa, *Journal of the American Chemical Society* **2016**, *138*, 2138–2141.

[94] E. T. McClure, M. R. Ball, W. Windl, P. M. Woodward, *Chemistry of Materials* **2016**, *28*, 1348–1354.

[95] A. H. Slavney, T. Hu, A. M. Lindenberg, H. I. Karunadasa, *Journal of the American chemical society* **2016**, *138*, 2138–2141.

[96] R. L. Hoye, L. Eyre, F. Wei, F. Brivio, A. Sadhanala, S. Sun, W. Li, K. H. Zhang, J. L. MacManus-Driscoll, P. D. Bristowe, et al., *Advanced Materials Interfaces* **2018**, *5*, 1800464.

[97] E. Greul, M. L. Petrus, A. Binek, P. Docampo, T. Bein, *Journal of Materials Chemistry A* **2017**, *5*, 19972–19981.

[98] J. Su, T. Mou, J. Wen, B. Wang, *The Journal of Physical Chemistry C* **2020**, *124*, 5371–5377.

[99] W. Tress, M. T. Sirtl, *Solar RRL* **2022**, *6*, 2100770.

[100] M. K. Jana, S. M. Janke, D. J. Dirkes, S. Dovletgeldi, C. Liu, X. Qin, K. Gundogdu, W. You, V. Blum, D. B. Mitzi, *J Am Chem Soc* **2019**, *141*, 7955–7964.

[101] J. Yang, P. Zhang, S.-H. Wei, *The journal of physical chemistry letters* **2018**, *9*, 31–35.

[102] J. A. Steele, P. Puech, M. Keshavarz, R. Yang, S. Banerjee, E. Debroye, C. W. Kim, H. Yuan, N. H. Heo, J. Vanacken, et al., *ACS nano* **2018**, *12*, 8081–8090.

[103] R. Kentsch, M. Scholz, J. Horn, D. Schlettwein, K. Oum, T. Lenzer, *The Journal of Physical Chemistry C* **2018**, *122*, 25940–25947.

[104] M. T. Sirtl, F. Ebadi, B. T. Gorkom, P. Ganswindt, R. A. J. Janssen, T. Bein, W. Tress, *Advanced Optical Materials* **2021**, *9*, 2100202.

[105] F. Ji, J. Klarbring, F. Wang, W. Ning, L. Wang, C. Yin, J. S. M. Figueroa, C. K. Christensen, M. Etter, T. Ederth, et al., *Angewandte Chemie* **2020**, *132*, 15303–15306.

[106] Z. Li, S. R. Kavanagh, M. Napari, R. G. Palgrave, M. Abdi-Jalebi, Z. Andaji-Garmaroudi, D. W. Davies, M. Laitinen, J. Julin, M. A. Isaacs, et al., *Journal of Materials Chemistry A* **2020**, *8*, 21780–21788.

[107] N. Glück, T. Bein, *Energy & Environmental Science* **2020**, *13*, 4691–4716.

[108] K. M. McCall, C. C. Stoumpos, S. S. Kostina, M. G. Kanatzidis, B. W. Wessels, *Chemistry of Materials* **2017**, *29*, 4129–4145.

[109] A. Singh, S. Najman, A. Mohapatra, Y.-J. Lu, C. Hanmandlu, C.-W. Pao, Y.-F. Chen, C. S. Lai, C.-W. Chu, *ACS applied materials & interfaces* **2020**, *12*, 32649–32657.

[110] K. M. McCall, C. C. Stoumpos, O. Y. Kontsevoi, G. C. Alexander, B. W. Wessels, M. G. Kanatzidis, *Chemistry of Materials* **2019**, *31*, 2644–2650.

[111] A. Chakraborty, N. Pai, J. Zhao, B. R. Tuttle, A. N. Simonov, V. Pecunia, *Advanced Functional Materials* **2022**, *32*, 2203300.

[112] R. L. Hoye, L. C. Lee, R. C. Kurchin, T. N. Huq, K. H. Zhang, M. Sponseller, L. Nienhaus, R. E. Brandt, J. Jean, J. A. Polizzotti, et al., *Advanced Materials* **2017**, *29*, 1702176.

[113] I. Turkevych, S. Kazaoui, E. Ito, T. Urano, K. Yamada, H. Tomiyasu, H. Yamagishi, M. Kondo, S. Aramaki, *ChemSusChem* **2017**, *10*, 3754–3759.

[114] Z. Xiao, W. Meng, D. B. Mitzi, Y. Yan, *The journal of physical chemistry letters* **2016**, *7*, 3903–3907.

[115] B. Al-Anesi, G. K. Grandhi, A. Pecoraro, V. Sugathan, N. Viswanath, H. Ali-Löytty, M. Liu, T.-P. Ruoko, K. Lahtonen, D. Manna, et al., **2023**.

[116] S. Hosseini, M. Adelifard, *physica status solidi (a)* **2021**, *218*, 2000774.

[117] A. A. Ramachandran, B. Krishnan, D. A. Avellaneda, M. I. M. Palma, J. A. A. Martinez, S. Shaji, *Applied Surface Science* **2021**, *564*, 150438.

[118] H. C. Sansom, G. Longo, A. D. Wright, L. R. Buizza, S. Mahesh, B. Wenger, M. Zanella, M. Abdi-Jalebi, M. J. Pitcher, M. S. Dyer, et al., *Journal of the American Chemical Society* **2021**.

[119] N. Pai, J. Lu, T. R. Gengenbach, A. Seeber, A. S. Chesman, L. Jiang, D. C. Senevirathna, P. C. Andrews, U. Bach, Y.-B. Cheng, et al., *Advanced Energy Materials* **2019**, *9*, 1803396.

[120] Y.-T. Huang, S. R. Kavanagh, D. O. Scanlon, A. Walsh, R. L. Hoye, *Nanotechnology* **2021**, *32*, 132004.

[121] M. Leng, Y. Yang, K. Zeng, Z. Chen, Z. Tan, S. Li, J. Li, B. Xu, D. Li, M. P. Hautzinger, et al., *Advanced Functional Materials* **2018**, *28*, 1704446.

[122] Z. Tan, J. Li, C. Zhang, Z. Li, Q. Hu, Z. Xiao, T. Kamiya, H. Hosono, G. Niu, E. Lifshitz, et al., *Advanced Functional Materials* **2018**, *28*, 1801131.

[123] Z. Zhang, Y. Liang, H. Huang, X. Liu, Q. Li, L. Chen, D. Xu, *Angewandte Chemie International Edition* **2019**, *58*, 7263–7267.

[124] Y. Guo, G. Liu, Z. Li, Y. Lou, J. Chen, Y. Zhao, *ACS Sustainable Chemistry & Engineering* **2019**, *7*, 15080–15085.

[125] W. Pan, H. Wu, J. Luo, Z. Deng, C. Ge, C. Chen, X. Jiang, W.-J. Yin, G. Niu, L. Zhu, et al., *Nature photonics* **2017**, *11*, 726–732.

[126] S. Paramanik, A. Maiti, S. Chatterjee, A. J. Pal, *Advanced Electronic Materials* **2022**, *8*, 2100237.

[127] G. K. Grandhi, B. Al-Anesi, H. Pasanen, H. Ali-Löytty, K. Lahtonen, S. Granroth, N. Christian, A. Matuhina, M. Liu, A. Berdin, et al., *Small* **2022**, *18*, 2203768.

[128] G. K. Grandhi, S. Toikkonen, B. Al-Anesi, V. Pecunia, P. Vivo, *Sustainable Energy & Fuels* **2023**, *7*, 66–73.

Characterization methods 2

2.1 X-RAY DIFFRACTION

X-ray diffraction (XRD) is a powerful technique to study the structure of crystalline materials, yielding useful information about the phase, crystallite sizes and orientation among others. Because of the similar wavelength of X-ray radiation to the atomic interdistances in the crystal lattice, monochromatic electromagnetic radiation can be elastically scattered and undergo constructive and destructive interference, as described by Bragg's law (equation 2.1), with n defined as positive integer, λ as wavelength, d as interplanar distance and θ as scattering angle (schematically shown in figure 2.1).[1]

$$n\lambda = 2d\sin(\theta) \tag{2.1}$$

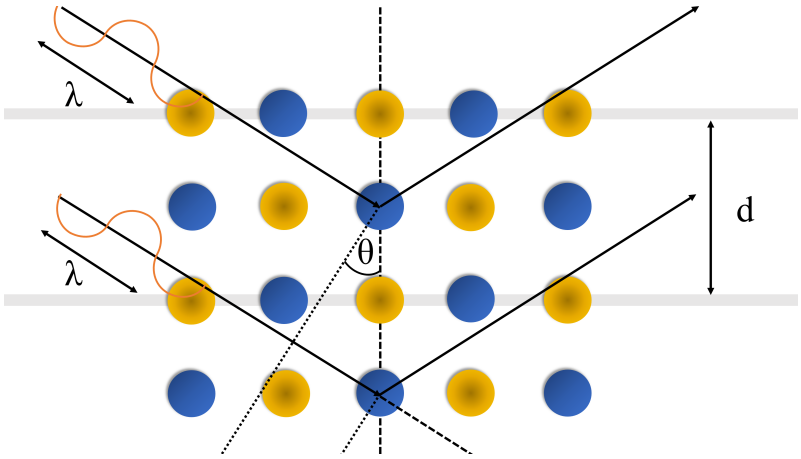

Figure 2.1: Constructive interference of X-rays in a crystalline material. λ is the wavelength, d the distance between crystal planes and θ the Bragg angle.

The incoming X-ray is commonly generated in a cathode ray tube by heating a filament, releasing electrons which are accelerated towards an anode material (usually Cu, Fe, Mo or Cr) and filtered to achieve monochromatic radiation.[2]

This electromagnetic radiation then interacts with the electrons around the atoms in sample to produce a diffraction signal when the Bragg condition seen in equation 2.1 is fulfilled. By varying the incident angle of the X-ray and/or angle of a detector, different peaks can be produced corresponding to individual Bravais lattices in the observed system.

2.1.1 Rietveld Refinement

When looking at diffraction from the geometric basis of the atoms, the periodicity of an atomic system results in a periodic electronic density, which enables the system to be analyzed via Fourier series.[3] When applying this to the observed crystal system, a construct is obtained which is widely used over all solid state physics: the reciprocal lattice. Here, the periodicity of the reference system still holds, but essential properties about the structure can be extracted from the Fourier components.[2] Moreover, the general diffraction condition can be written as follows:

$$\Delta k = G \tag{2.2}$$

Here, Δk refers to the scattering vector and G to a point in the reciprocal lattice.
Obviously, different electronic configurations lead to different scattering intensities around the atom center, with the amplitude being defined by the structure factor S_G as seen in the following equation:

$$S_G = \sum_j f_j exp(-iG \cdot r_j) \tag{2.3}$$

Here, j is an index for every atom in the cell, r_j the vector to the corresponding atom center, G a reciprocal lattice vector and f_j the atomic form factor being directly correlated to the electronic density around the atom and a parameter extracted from the Fourier series approach.
Therefore, minuscule atomic changes such as position and nature of atom can have a significant influence on the shape of the individual XRD patterns. This can be very useful when simulating a proposed crystal structure and comparing it to experimental results.
A very prominent technique to accomplish this is the Rietveld refinement method, where an experimental pattern is matched to a simulated profile and refined via a least-squares method to minimize the difference by varying parameters like atomic occupation, unit cell symmetry and dimension, which yields information about the crystallographic constants and general molecular constitution.[4]

2.1.2 Grazing Incidence Wide Angle X-Ray scattering

Grazing incidence wide angle X-ray scattering (GIWAXS) is a powerful XRD technique used to study surface and thin film nanostructures. While in a conventional locked-couple scan configuration plenty of signal from the substrate is recorded, in this technique low incidence angles can lead to a much increased signal as only the film surface is probed. Additionally, precise information about the orientation of the film is retrieved.[5,6] The basic working principle is illustrated in Figure 2.2.

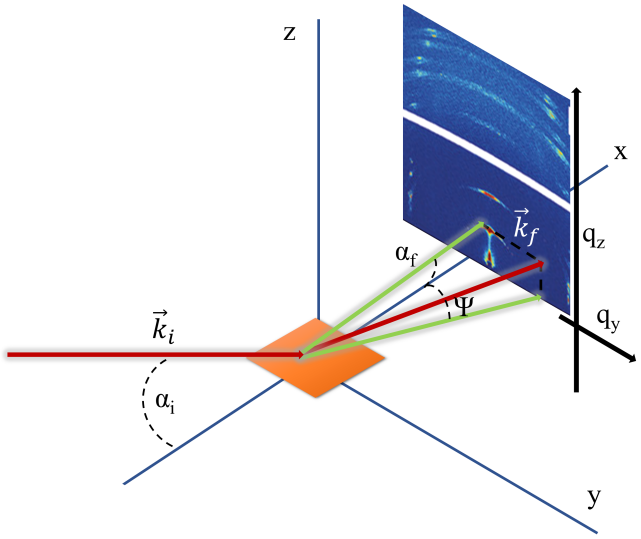

Figure 2.2: Illustration of wide-angle grazing-incidence scattering with vectors and significant scattering angles.

Here, an X-ray beam with the wavevector $\vec{k}_i$ is used to probe the sample under an incident angle α_i which is usually in the range of $< 1°$. This is typically chosen around the critical angle, i.e. where Total External Reflection of the wave occurs. After scattering on the sample surface or in the bulk, a two-dimensional detector is used to collect the intensity as values of α_f and Ψ that are then expressed as vertical (q_z) or lateral (q_y) wavevectors. Through this 2D imaging, special patterns depending on the orientation can be obtained, with partial rings, or dots in the case of single crystals or perfectly oriented thin films. Random orientation forms Debye-Scherrer rings with homogeneous intensity on the area detector.[7]

2.2 SCANNING ELECTRON MICROSCOPY

To investigate the morphology of materials on the nano- and micrometer scale, methods beyond optical microscopy have to be employed because of the Abbe limit in resolution as seen in equation 2.4.[8]

$$d = \frac{\lambda}{2NA} \tag{2.4}$$

Here, NA refers to the numerical aperture and λ to the wavelength of light, resulting in a limit of approximately $200\,\mathrm{nm}$ resolution. Circumventing this is accomplished for example by measuring the interaction of sample atoms with an incoming electron beam, as performed in scanning electron microscopy (SEM). Here, the much smaller De Broglie wavelength of electrons in comparison with photons enables imaging at a scale of only few nanometers.

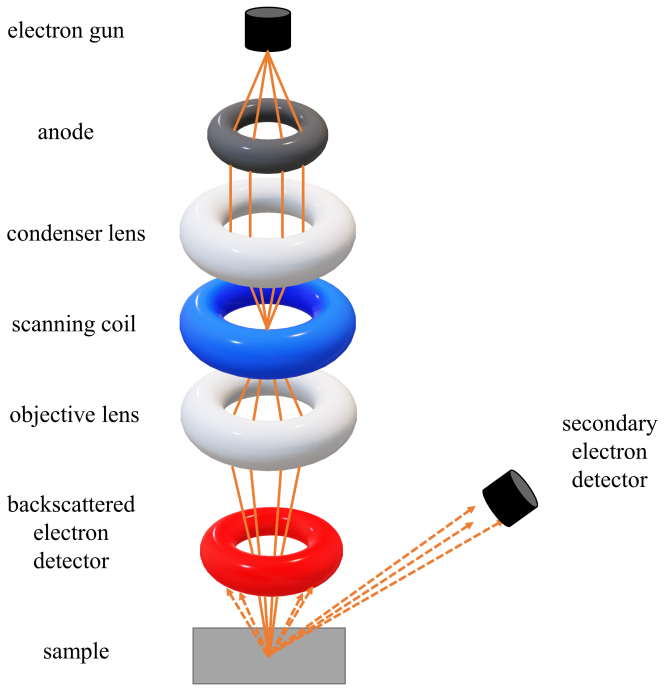

Figure 2.3: Schematic representation of the scanning electron microscope.

In a typical SEM setup as illustrated in Figure 2.3, an electron gun emits a divergent electron beam at acceleration voltages of $1\,\mathrm{kV}$ to $30\,\mathrm{kV}$ in high vacuum produced by a tungsten filament cathode or a field emission gun. After this, the beam is shaped and focused by a condenser and an objective lens. The image is generated by scanning over a sample and measuring the resulting interactions, mainly yielding secondary electrons with information about the morphology and higher energy backscattered electrons which provide information about the elemental composition.

2.3 PHOTOELECTRON SPECTROSCOPY

Photoemission or photoelectron spectroscopy (PES) is a powerful tool to study the energy distribution of electrons in a compound, revealing information about elemental composition, nature of chemical bonds, electronic states and VB energy levels among others. Generally, a sample is ionized by either ultraviolet (UV) or X-ray radiation and the kinetic energy of emitted electrons is measured. In general, the ionization process can be described as follows:

$$A + h\nu \rightarrow A^+ + e^- \tag{2.5}$$

As energy has to be conserved in the system and the electron's energy is only kinetic (KE), equation 2.5 can be rearranged and results in Einsteins photoelectric equation:[9]

$$KE = h\nu - (E(A^+) - E(A)) = h\nu - BE \tag{2.6}$$

The difference $(E(A^+) - E(A))$ is described as electron binding energy (BE). A schematic representation of a conventional spectrometer can be seen in Figure 2.4.

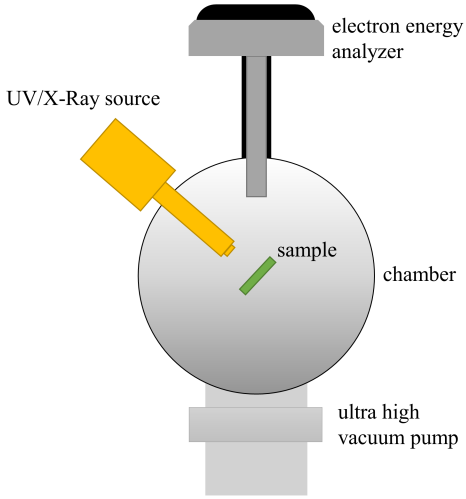

Figure 2.4: Schematic representation of a photoelectron spectrometer.

Importantly, the radiation source determines the information retrieved by the measurement and is divided into X-ray photoelectron spectroscopy (XPS) and ultraviolet photoelectron spectroscopy (UPS). In XPS, soft X-rays with an energy of $0.2\,\mathrm{keV}$ to $2\,\mathrm{keV}$ are generated by a vacuum tube with an anode material (most commonly Mg or Al) to study the energy levels of core electrons.[10] In UPS, gas discharge lamps (mostly He, Ne or

Ar) are used to ionize the sample with a photon energy of $10\,\mathrm{eV}$ to $45\,\mathrm{eV}$, which reveals characteristics of valence levels.[11]

2.4 UV-VIS SPECTROSCOPY

Ultraviolet–visible spectroscopy (UV-Vis) is a common and effective technique to examine light absorption and reflection of liquid or solid samples. Here, light in the wavelength range of approximately $200\,\mathrm{nm}$ to $1200\,\mathrm{nm}$ is used to irradiate a sample of interest, exciting electrons in the sample from the ground state into higher lying electronic states. In general, macroscopic absorption is described by the Lambert-Beer law as seen in equation 2.7.[12]

$$A(\lambda) = -\log_{10}\left(\frac{I(\lambda)}{I_0(\lambda)}\right) = -\log_{10}(T(\lambda)) = \alpha_{10}(\lambda)l \tag{2.7}$$

$A(\lambda)$ defines the absorbance, $I(\lambda)$ the transmitted intensity of light, $I_0(\lambda)$ the light intensity on the sample and $\alpha_{10}(\lambda)$ describes the absorption coefficient with l being the thickness of the sample the light has to travel through. The quotient $I(\lambda)/I_0(\lambda)$ is also referred to as transmittance $T(\lambda)$. Absorbance is measured using a white light source and scanning λ with a monochromator whilst detecting $I(\lambda)$. As a fundamental parameter of semiconducting materials, the bandgap can be approximated by a method named after the Czech physicist Jan Tauc.[13] This method was originally developed for amorphous semiconductors but can be very useful to get rough estimates of this value. It is based on the following assumption that the absorption coefficient can be expressed as a function of energy:

$$(\alpha h\nu)^{1/\lambda} = B(h\nu - E_g)\begin{cases}\lambda = 0.5 & \text{direct allowed}\\ \lambda = 1.5 & \text{direct forbidden}\\ \lambda = 2.0 & \text{indirect allowed}\\ \lambda = 3.0 & \text{indirect forbidden}\end{cases} \tag{2.8}$$

α is the absorption coefficient, $h\nu$ the photon energy, B is a constant and λ is a value that accounts for the specific type of transition. Nonetheless, this can only be used reliably if no sub-band absorption is present in the material, which is not the case for defect-containing or non-single crystalline samples.[14] These sub-band gap states are accounted for by an Urbach tail, an exponential increase of absorption depending on the energy, described in equation 2.9.[15]

$$\alpha(E) = \alpha_0 \exp\left(\frac{E - E_1}{E_u}\right) \tag{2.9}$$

α_0 and E_1 are free parameters and E_u is the Urbach energy, which accounts for the energetic disorder.

2.4.1 Exitonic Absorption in Semiconductors & Elliott Model

As the absorption processes in semiconducting materials arise from fundamental properties of interest, a better model to describe these transitions can be an extraordinarily powerful way to characterize new materials based on a quick and non-destructive technique like UV-Vis spectroscopy. It was shown that in hybrid organic-inorganic perovskites, the assumption of a completely delocalized electron wavefunction and therefore negligible electron-electron interaction does not necessarily hold as they show pronounced excitonic behavior, forming a hydrogen-like quasiparticle.[16] In order to account for this, Elliott derived a formula based on the electron-hole susceptibility starting from the semiconductor Bloch equations and shown in equation 2.10.[17]

$$\alpha(\nu) = \alpha_0^{3D}\left[\sum_{n=1}^{\infty}\frac{4\pi E_b^{3/2}}{n^3}\delta\left(h\nu - E_g - \frac{E_b}{n^2}\right) + \frac{2\pi\sqrt{E_b}}{1-e^{-2\pi\sqrt{\frac{E_b}{h\nu-E_g}}}}H(h\nu - E_g)\right] \tag{2.10}$$

Here, α_0^{3D} is a parameter scaling relative to the density of states, n is a positive integer defining line transitions, E_g is the bandgap and E_b is the exciton binding energy, defining the energy required to ionize an exciton into free carriers. δ is the Dirac delta function, accounting for continuum absorption in the first term and H is the Heaviside step function for the excitonic absorption in the second term. D'Innocenzo et al. furthermore reported a modified equation for the case of $\mathrm{MAPbI_3}$, which includes a term for inhomogeneous thermal broadening Γ and a parameter b for non-parabolicity of the density of states, and can be seen in equation 2.11.[18]

$$\alpha(\nu) = \alpha_0^{3D}\left[\sum_{n=1}^{\infty}\frac{4\pi E_b^{3/2}}{n^3}sech\left(\frac{h\nu - E_g - \frac{E_b}{n^2}}{\Gamma}\right) + \int_{E_g}^{\infty}sech\left(\frac{h\nu-\epsilon}{\Gamma}\right)\frac{2\pi\sqrt{E_b}}{1-e^{-2\pi\sqrt{\frac{E_b}{h\nu-E_g}}}}\frac{1}{1-b(\epsilon-E_g)}d\epsilon\right] \tag{2.11}$$

Additionally, the Dirac and Heaviside functions were approximated by the hyperbolic secant function $sech(x)$. To illustrate the profound influence of the parameters on the shape and position of the absorption curve, the Elliott Formula was simulated in Figure

2.5, varying one parameter at a time starting from common values shown in the legend.

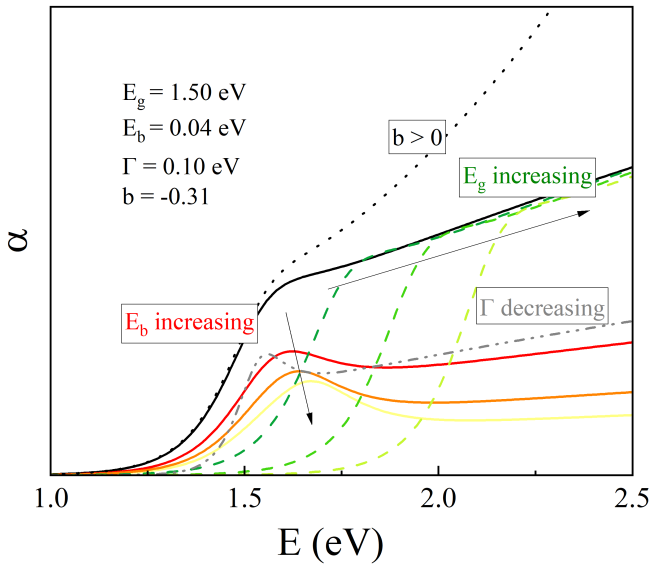

Figure 2.5: Simulation of a UV-Vis spectrum with the Elliott Formula with the varying parameters band gap E_g, exciton binding energy E_b, inhomogeneous broadening Γ and non-parabolicity factor b, starting from common values in perovskite materials. The band gap was increased (green curves) incrementally by $0.2\,\mathrm{eV}$, the exciton binding energy (red curves) by $0.04\,\mathrm{eV}$. Γ was doubled in the light grey spectrum and the non-parabolicity factor was set as $+0.31$ in the dotted black line without changing the other parameters.

2.5 PHOTOLUMINESCENCE SPECTROSCOPY

While absorption spectroscopy is used for studying light that is lost, photoluminescence (PL) spectroscopy measures light emission generated by radiative recombination from an excited state to the ground state in a semiconductor material. Experimentally, a sample is excited by a laser with wavelengths in the range of $350\,\mathrm{nm}$ to $900\,\mathrm{nm}$ and the resulting emission is measured. Mechanistically, this can happen directly from and to the frontier bands or can also be mediated by a trap state in the bandgap. Nonetheless, not every semiconductor - especially a material with an indirect bandgap - emits radiation when recombining. Here, the extra energy is released via generation of a phonon (Shockley-Read-Hall) or given to another electron in form of kinetic energy (Auger).[19,20] The different processes are illustrated in Figure 2.6. By measuring steady-state PL spectra, information about the recombination nature, charge transfer efficiency and bandgap can be obtained. Furthermore, this technique can be expanded by measuring over time, where the recombination kinetics can be investigated. The lifetime of charge carriers can

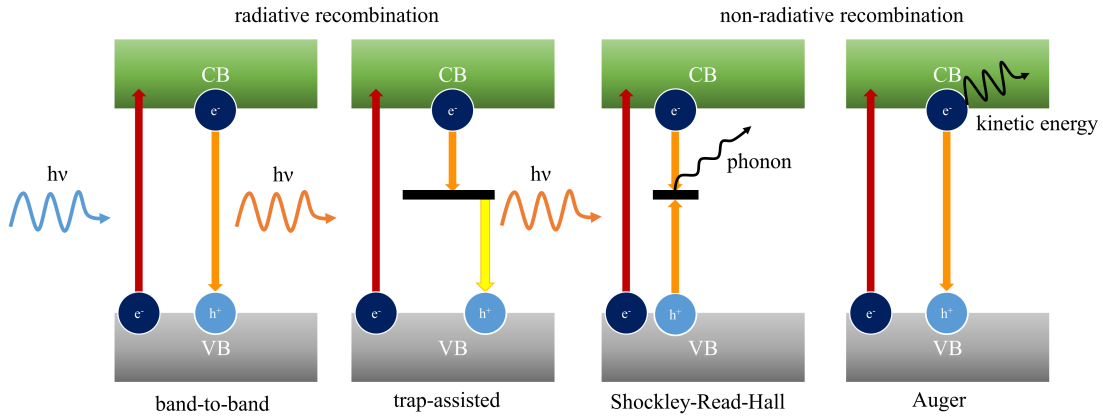

Figure 2.6: Illustration of typical recombination pathways in semiconductors.

also be studied, which is an important material property especially for optoelectronic applications. Obviously, the recombination mechanisms presented in Figure 2.6 will differ in their respective kinetics, with the individual rate equations shown in the following:[21]

$$U_{band} = B(np - n_i^2) \tag{2.12}$$

$$U_{Auger} = (C_{p0}p + C_{n0})(np - n_i^2) \tag{2.13}$$

$$U_{SHR} = \frac{np - n_i^2}{\tau_p(n + n_t) + \tau_n(p + p_t)} \tag{2.14}$$

The quantities n and p are the electron and hole densities, respectively, and B, C_{p0}, C_{n0} are coefficients for the band-to-band and Auger recombination processes. Defect-mediated recombination is illustrated by the Shockley-Read-Hall formula, where τ_p and τ_n are average lifetime parameters which are dependent on the defect concentration and the trap energy level. n_t and p_t are electron and hole densities when the quasi Fermi level (QFL) is identical to the energy of the trap state.

2.6 DENSITY FUNCTIONAL THEORY

Density functional theory (DFT) is a quantum mechanical method to calculate properties and the electronic structure of many-electron systems from first principles. The main advantage of this method is a high cost-effectiveness, which is a bottleneck for many ab-initio quantum mechanical simulations when complex system are observed or high accuracy is needed. The core principle revolves around expressing the energy of a system as a functional of the electron density as opposed to the wave function as in regular quantum-mechanical theories.[22] Therefore, the Schrödinger equation with fixed nuclei

(Born-Oppenheimer approximation) can be written as follows:[23]

$$\hat{H}\Psi = E\Psi = \left[\sum_{i=1}^{N}\left(-\frac{\hbar^2}{2m_i}\nabla_i^2\right) + \sum_{i=1}^{N} V(r_i) + \sum_{i<j}^{N} U(r_i, r_j)\right]\Psi \tag{2.15}$$

$\hat{H}$ is the main Hamilton operator, which can also be described as $(T + V + U)$ with the kinetic energy, potential energy and electron-electron interaction operator, respectively. Ψ is the wave function, m_i the mass of a particle of interest and r_i,r_j are the vectors describing the position of such. As the wave function is difficult to interpret and is dependent on all coordinates of all electrons in a system, a description of equation 2.15 with a physical observable would be very advantageous. This was the starting point for the theorems of Hohenberg and Kohn, where they postulated that all the information of a system is described by the electronic density, a simple function with only 3 coordinates.[24] In classical wave function theory, the Schrödinger equation is solved by minimizing it by varying a trial wave function:

$$E = \min_{\Psi}\langle\Psi|E|\Psi\rangle \tag{2.16}$$

In DFT on the other hand, the energy can be expressed as seen in following equation, as the second Hohenberg-Kohn theorem proves that a ground state density exists which minimizes the overall energy of the system:

$$E = \min_{n}\int V(\vec{r})n(\vec{r})d^3\vec{r} + F[(n(\vec{r}))] \tag{2.17}$$

Where n defines the electronic density and F is a functional containing the kinetic energy T and the electron self-interaction term U. V is a system-specific measure for the external potential of the nuclei. Nonetheless, the key problem with this theory is that the exact form of $F[(n(\vec{r}))]$ is unknown. The general formula can be seen in equation 2.18.

$$F[n] = T[n] + U[n] = T[n] + J[n] + E_{xc}[n] \tag{2.18}$$

J is the electrostatic repulsion of the electrons, which is easily derived from classical theory. The calculation of T is avoided by employing Kohn-Sham functions, which introduce fictional one-electron wave functions that result in the same electronic density as the system of interest.[25] E_{xc} defines the exchange-correlation functional, the key unknown in modern DFT. Many methods were presented to circumvent these issues, all of these varying in computational cost and accuracy, depending on the needs of the system under study. Some examples are definitions of E_{xc} based only on the electronic density (local) or the gradients thereof, e.g. generalized gradient approximations (GGA) like the Perdew-Burke-Ernzerhof (PBE) functional.[24] Another class are the frequently used hybrid func-

tionals, which mix DFT energies with contributions of wave function-based methods like Hartree-Fock, e.g. the Heyd-Scuseria-Ernzerhof (HSE) functional, often used in calculating hybrid organic-inorganic perovskites.[26]

2.7 CURRENT-VOLTAGE MEASUREMENTS

To characterize as-fabricated solar cells, current-voltage (*JV*) measurements are the most straightforward method to study their performance and extract key parameters like the power conversion efficiency (PCE), short circuit current density (J_{sc}), open circuit voltage (V_{oc}) and fill factor (FF). For this, an external bias voltage is applied and scanned in a range of $-0.1\,\mathrm{V}$ to $1.5\,\mathrm{V}$ while illuminating the solar cell using a standard air mass 1.5 global (AM1.5G) spectrum with an incident power of $100\,\mathrm{mW\,cm^{-2}}$.[27] The resulting output current is measured and divided by the area of the solar cell to extract the current density. A typical *JV* curve is illustrated in Figure 2.7.

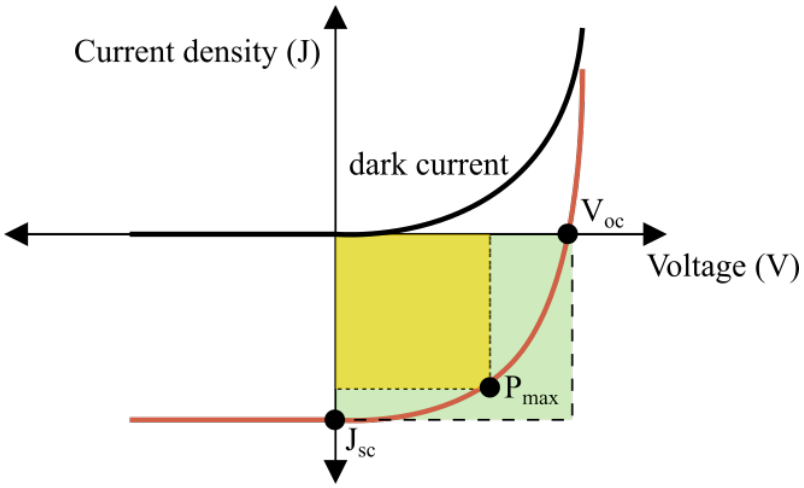

Figure 2.7: Illustration of a typical JV curve with photovoltaic parameters, these are explained in detail in the text.

In a typical pn-junction, this shape is described by the Shockley diode equation in the dark:[28]

$$J = J_s \left[exp\left(\frac{eV}{kT}\right) - 1 \right] \tag{2.19}$$

J_s is the voltage-independent reverse saturation current density, eV the electron charge times the voltage, kT is the Boltzmann constant times temperature. When light is applied to the junction, the curve gets shifted up by J_{sc} and starts generating power.

$$J = J_s \left[exp\left(\frac{eV}{kT}\right) - 1 \right] + J_{sc} \tag{2.20}$$

The V_{oc} describes the voltage where the net current that flows in the solar cell equals zero. This value is linked to characteristic material properties like the band gap, which is the theoretical limit for the V_{oc} when maximum QFL splitting is assumed. However, non-radiative recombination processes and short charge carrier lifetimes can influence and thus reduce this value.
The J_{sc}, on the other hand, defines the maximum current flow in the cell at zero bias voltage. This value is determined by charge carrier collection efficiency and generation rate and thus by optical factors like incident light intensity/absorption.
The maximum power point (MPP) specifies a certain point P_{max} in the JV curve where the maximum output power from the solar cell is obtained (yellow rectangle in Figure 2.7). This is connected to the V_{oc} and J_{sc} through a parameter defined as fill factor and can be seen in equation 2.21.

$$FF = \frac{P_{MPP}}{V_{oc}J_{sc}} = \frac{V_{MPP}J_{MPP}}{V_{oc}J_{sc}} \tag{2.21}$$

This value is often linked to the general solar cell quality and is strongly influenced by resistances like shunt (R_{sh}) and series (R_s) resistance. These are illustrated in the solar cell circuit model in Figure 2.8.

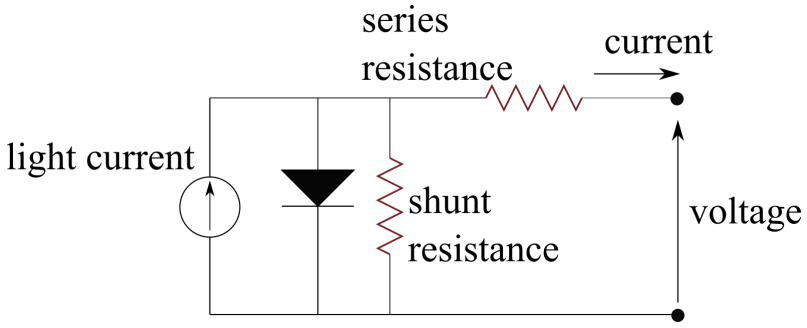

Figure 2.8: Equivalent circuit for an illuminated solar cell with internal shunt and series resistances.

With these resistances, the *JV* equation can be written as follows:

$$J = J_{sc} - J_s \left[exp\left(\frac{e(V + JR_s)V}{kT}\right) - 1 \right] - \frac{V + JR_s}{R_{sh}} \tag{2.22}$$

Generally, a high series resistance and low shunt resistance leads to a increasingly linear curve shape and therefore smaller FFs and efficiency, with the limit being 0.25 for a completely linear trend.

2.8 EXTERNAL QUANTUM EFFICIENCY

The quantum efficiency (QE) is defined as percentage of photons that is converted into charge carriers. Here, we distinguish external quantum efficiency (EQE) and internal quantum efficiency (IQE) with the first describing the incident photon to charge carrier conversion efficiency and the latter the same efficiency with respect to *absorbed* photons. In the first place, the spectral response function SR has to be determined. This is accomplished by measuring the current density of a sample solar cell J_{sa} at short circuit conditions and scanning over different wavelengths. This is then compared to a reference diode current density J_{ref}.[27]

$$SR(\lambda \pm \Delta\lambda) = \frac{J_{sa}(\lambda \pm \Delta\lambda)}{J_{ref}(\lambda \pm \Delta\lambda)} \tag{2.23}$$

The EQE is then calculated as seen in equation 2.24.

$$EQE(\lambda) = SR(\lambda)\frac{hc}{e\lambda} \tag{2.24}$$

The IQE can then be derived with the reflectance R, when no other loss mechanisms such as scattering are considered:

$$IQE(\lambda) = \frac{EQE(\lambda)}{1 - R(\lambda)} \tag{2.25}$$

Furthermore, by integrating over the EQE, the integrated photocurrent can be retrieved, which is used as a confirmation for J_{sc} values from *JV* measurements as they should be approximately equal.

$$J_{sc,eqe} = e\int_0^\infty \Phi(\lambda)EQE(\lambda)d\lambda \tag{2.26}$$

$\Phi(\lambda)$ defines the photon flux of one sun.

2.9 TIME-RESOLVED MICROWAVE CONDUCTIVITY

Time-resolved microwave conductivity (TRMC) is a spectroscopic method to study the carrier mobility in semiconductors. Herein, a sample of interest is excited by a laser pulse at the nano to femtosecond time scale. The carriers created this way, both electrons and holes, change the microwave conductivity, i.e. the ability of a material to conduct current at microwave frequencies ($300\,\mathrm{MHz}$ to $300\,\mathrm{GHz}$).[29] This is accomplished via a resonance cavity. A circulator is employed to reduce back reflections when the microwaves are

directed. An illustration of a typical measurement device is shown in Figure 2.9.

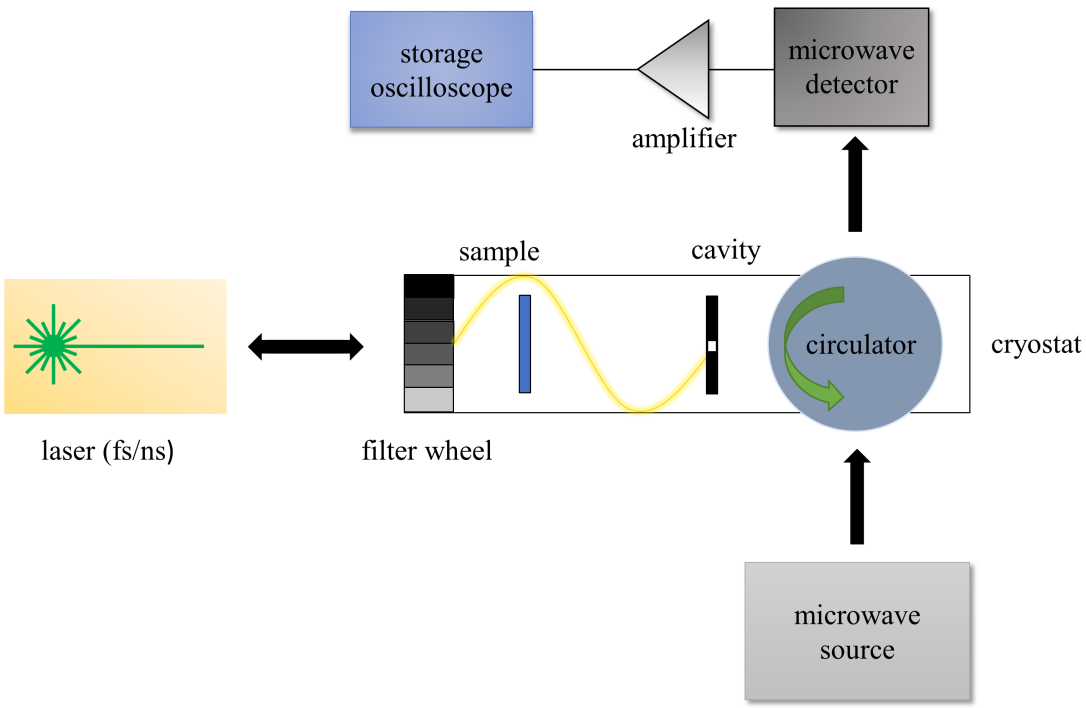

Figure 2.9: Schematic illustration of a typical TRMC setup.

Here, the changes in conductance G are defined as proportional to changes in the incident power of the microwaves ΔP as derived from Maxwell's equations.

$$\Delta G = -\frac{1}{K}\frac{\Delta P}{P} \tag{2.27}$$

P is the background microwave power and K is a sensitivity factor.
To obtain information about the mobility of charge carriers, the conductance can be written as follows.

$$\Delta G = \Delta\sigma\beta l \tag{2.28}$$

$\Delta\sigma$ is defined as the change in conductivity, while β defines the dimensions of the measurement cavity and l the length of the sample. In general, σ can be related to the mobility by equation 2.29.

$$\Delta\sigma = ne\sum_i \mu_i \tag{2.29}$$

n defines the charge carrier density, e the elemental charge and μ_i finally describes the charge carrier mobilities.
Furthermore, the yield of charge carriers Φ correlates the carrier density with the laser

intensity I_0.

$$\Phi = \frac{nl}{I_0 F_A} \tag{2.30}$$

l is the sample length as discussed before, F_A the absorbed quantity of light.
Finally, the product of quantum yield for charge carrier generation and mobility can be calculated via equation 2.31.

$$\Phi \sum_i \mu_i = \frac{\Delta G}{\beta e I_0 F_A} \tag{2.31}$$

2.10 REFERENCES

[1] W. H. Bragg, W. L. Bragg, *Proceedings of the Royal Society of London. Series A Containing Papers of a Mathematical and Physical Character* **1913**, *88*, 428–438.

[2] C. Kittel, *Introduction to solid state physics*, *Vol. 8*, John Wiley & Sons, Inc., **2021**.

[3] C. Kittel, P. McEuen, *Introduction to solid state physics*, John Wiley & Sons, **2018**.

[4] H. M. Rietveld, *Physica Scripta* **2014**, *89*, 098002.

[5] H. Dosch, B. Batterman, D. Wack, *Physical Review Letters* **1986**, *56*, 1144.

[6] P. Dubček, *Vacuum* **2005**, *80*, 92–97.

[7] A. L. Patterson, *Physical Review* **1939**, *56*, PR, 978–982.

[8] K. D. Vernon-Parry, *III-Vs Review* **2000**, *13*, 40–44.

[9] A. Pais, *Reviews of modern physics* **1979**, *51*, 863.

[10] J. D. Andrade, *Surface and Interfacial Aspects of Biomedical Polymers: Volume 1 Surface Chemistry and Physics* **1985**, 105–195.

[11] J. H. D. Eland, *Photoelectron spectroscopy: an introduction to ultraviolet photoelectron spectroscopy in the gas phase*, Elsevier, **2013**.

[12] H. Rose, *Nature* **1952**, *169*, 287–288.

[13] J. Tauc, *Materials Research Bulletin* **1968**, *3*, 37–46.

[14] P. Makuła, M. Pacia, W. Macyk, *The Journal of Physical Chemistry Letters* **2018**, *9*, 6814–6817.

[15] F. Urbach, *Physical Review* **1953**, *92*, 1324.

[16] G. Grancini, A. R. Srimath Kandada, J. M. Frost, A. J. Barker, M. De Bastiani, M. Gandini, S. Marras, G. Lanzani, A. Walsh, A. Petrozza, *Nature photonics* **2015**, *9*, 695–701.

[17] R. Elliott, R. Loudon, *Journal of Physics and Chemistry of Solids* **1959**, *8*, 382–388.

[18] V. D'Innocenzo, Doctoral Thesis, Politecnico di Milano, **2016**.

[19] A. Richter, S. W. Glunz, F. Werner, J. Schmidt, A. Cuevas, *Physical Review B* **2012**, *86*, 165202.

[20] W. Shockley, W. T. Read, *Physical Review* **1952**, *87*, PR, 835–842.

[21] B. V. Zeghbroeck, Principles of Semiconductor Devices, Web Page, **2020**.

[22] C. Fiolhais, F. Nogueira, M. A. Marques, *A primer in density functional theory*, *Vol. 620*, Springer Science and Business Media, **2003**.

[23] E. Schrödinger, *Physical Review* **1926**, *28*, PR, 1049–1070.

[24] P. Hohenberg, W. Kohn, *Physical Review* **1964**, *136*, B864.

[25] W. Kohn, L. J. Sham, *Physical Review* **1965**, *140*, A1133.

[26] J. Heyd, G. E. Scuseria, *The Journal of chemical physics* **2004**, *121*, 1187–1192.

[27] P. Würfel, *Physics of Solar Cells: From Principles to new concepts*, Wiley-VCH Verlag, **2005**.

[28] C.-T. Sah, R. N. Noyce, W. Shockley, *Proceedings of the IRE* **1957**, *45*, 1228–1243.

[29] C. Colbeau-Justin, M. Valenzuela, *Revista mexicana de fisica* **2013**, *59*, 191–200.

Formation of Stable 2D Methylammonium Antimony Iodide Phase for Lead-free Perovskite-like Solar Cells 3

This chapter is based on following publication:

N. Giesbrecht*, A. Weis*, T. Bein, Journal of Physics: Energy **2020**, 2, 024007.
*These authors contributed equally to this work

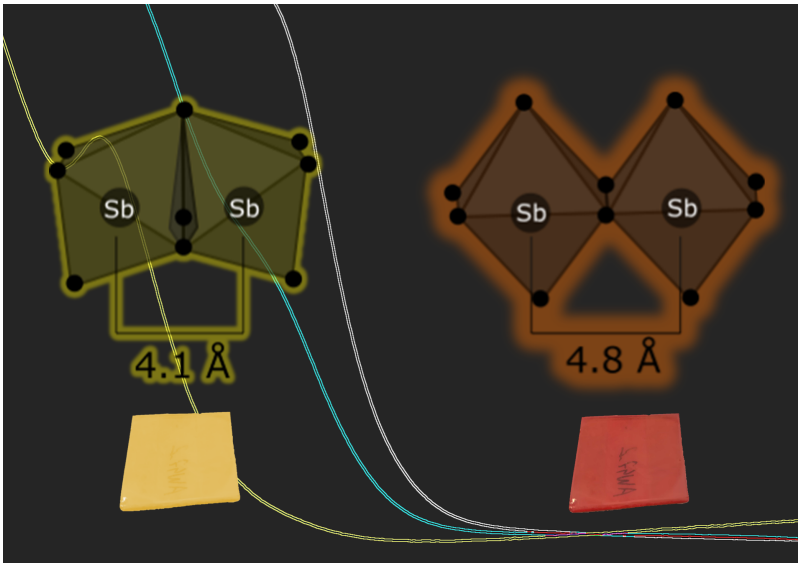

3.1 ABSTRACT

The presence of lead in novel hybrid perovskite-based solar cells remains a significant issue regarding commercial applications. Therefore, antimony-based perovskite-like $A_3M_2X_9$ structures are promising new candidates for low toxicity photovoltaic applications. So far, $MA_3Sb_2I_9$ was reported to only crystallize in the "zero-dimensional" (0D) dimer structure with wide indirect bandgap properties. However, the formation of the 2D layered polymorph is more suitable for solar cell applications due to its expected direct and narrow bandgap. Here, we demonstrate the first synthesis of phase pure 2D layered $MA_3Sb_2I_9$, based on antimony acetate dissolved in alcoholic solvents. Using in situ methylammonium antimony iodide (MASI) methods, we confirm the stability of the layered phase towards high temperature, but the exposure to 75% relative humidity for several hours leads to a rearrangement of the phase with partial formation of the 0D structure. We investigated the electronic band structure and confirmed experimentally the presence of a semi-direct bandgap at around $2.1\,\mathrm{eV}$. Our work shows that careful control of nucleation via processing conditions can provide access to promising perovskite-like phases for photovoltaic applications.

3.2 INTRODUCTION

The hybrid lead halide perovskite material methylammonium lead iodide ($MAPbI_3$) emerged with an initial photovoltaic performance of 3.8% in 2009.[1] Today, the solar cell efficiencies using $MAPbI_3$-based absorbers already exceed 25% due to the material's intrinsic outstanding optoelectronic properties.[2] In particular, lead-based perovskites exhibit high optical absorption coefficients, balanced electron and hole mobilities, long photogenerated carrier lifetimes, long diffusion lengths, low trap densities and small exciton binding energies.[3–8] These exceptional material properties originate from a combination of high crystal symmetry, the chemistry of the $\mathrm{Pb}\ 6s^2$ lone-pair states and the ionic nature of the structure with large atomic sizes.[9] However, the toxicity of lead together with the instability of this and related perovskite compounds towards moisture and high temperature limit the commercialization of lead-based perovskite solar cells.[10–14]

To find alternatives replacing lead, researchers have focused on other isovalent ions, like Sn^{2+} or Ge^{2+}. Here, both $MASnI_3$ and $MAGeI_3$ are suitable candidates

for photovoltaic applications due to a possible crystallization in a black perovskite crystalline phase.[15–23] Unfortunately, the divalent ions in tin- and germanium-based perovskites are prone to oxidize to Sn^{4+} or Ge^{4+}, respectively. Therefore, these absorbers are especially unstable in air and moisture, limiting their photovoltaic applications.[20,24,25]

Maintaining the chemistry of the lone-pair ns^2 state, the trivalent antimony and bismuth ions represent another possible alternative to replace lead. However, the higher oxidation state of antimony or bismuth compared to lead in $MAPbI_3$ makes similar perovskite phase formation impossible. Instead, $MA_3Sb_2I_9$ or $MA_3Bi_2I_9$ form. The methylammonium-based compounds crystallize predominantly in a non-perovskite, zero-dimensional (0D) phase, consisting of face-sharing bioctahedral clusters of $(Sb_2I_9)^{3-}$ or $(Bi_2I_9)^{3-}$. The antimony-based absorber layers crystallize in high quality with extended HI treatment.[26] If applied in solar cells, those layers enable power conversion efficiencies PCE of 2% and can be further improved to 2.8% efficiency with a hydrophobic scaffold at the bottom interlayer.[27,28] The already promising photovoltaic performance indicates the suitability of $MA_3Sb_2I_9$ as an absorber layer, even though the 0D structure exhibits neither a direct bandgap nor interconnected octahedral layers for charge transport in any dimension.

In DFT calculations, MASI features more favorable materials properties when crystallized in a layered 2D structure. The projected improved materials properties include a direct bandgap, higher electron and hole mobilities and better tolerance to defects caused by higher dielectric constants.[26,28–30] However, the crystallization of the layered phase preferably occurs with smaller cations than MA^+, such as Rb^+ or NH^{4+}.[31–33] Absorber layers based on $Rb_3Sb_2I_9$ and $(NH_4)_3Sb_2I_9$ exhibit a direct bandgap and reach PCEs of 0.7% and 0.5%, respectively.[32,33] Introduction of bulkier Cs^+ cations in the layered 2D structure requires more extended processing conditions, such as recrystallization of the dimer phase in SbI_3 vapor.[30] Exhibiting a direct bandgap, $Cs_3Sb_2I_9$ enables a PCE of 1.5%.[30] With MA^+ as a cation, so far, layered $MA_3Sb_2I_{9-x}Cl_x$ could only be achieved via partial anion substitution using the smaller anion Cl^-.[34] In devices, high quality 2D thin films achieved a PCE of 2.2%, but the slightly wider bandgap of $2.1\,eV$ suggests that even higher efficiencies could arise from a material with a narrower bandgap.[34]

In this work, we present a novel synthesis approach based on antimony acetate precursor to crystallize a pure $MA_3Sb_2I_9$ 2D perovskite-like phase. We perform solvent-engineering to induce the crystallization of the layered structure, confirmed with MASI and UV-Vis analysis. Further investigations using in situ MASI proved the stability of the material toward phase transition and degradation upon exposure to heat and substantially

to moisture. In first-principles calculations, we predict a semi-direct bandgap of the 2D compound and confirm these results with optical absorbance spectroscopy, showing a direct bandgap of $2.1\,\mathrm{eV}$. Even though we fabricated rather low-quality thin film morphologies of MASI, devices reach already PCEs around 0.6%, indicating the materials' aptness for photovoltaic applications.

3.3 RESULTS AND DISCUSSION

The two known phases of MASI differ significantly, considering the crystal structure. The dimer phase, as explained above, consists of face-sharing $(\mathrm{Sb_2I_9})^{3-}$ bioctahedral clusters with $\mathrm{MA^+}$ and iodide, forming a quasi-hexagonal close packing.[35] In this structure, the closest $\mathrm{Sb-Sb}$ interatomic distance is $4.1\,\text{Å}$. Increasing the range of antimony-iodide octahedra such that the antimony atoms are separated by $4.8\,\text{Å}$, MASI forms in the layered structure with corner-sharing octahedral. The $\mathrm{MA^+}$ and $\mathrm{I^-}$ ions form a quasi-cubic close packing. This 2D phase can be understood as a defective $\mathrm{MAPbI_3}$-like perovskite structure with the formula $\mathrm{MA(Sb_{2/3}\square_{1/3})I_3}$. However, the 2D structure predominantly forms with smaller cations than $\mathrm{MA^+}$. Regarding literature results, only $\mathrm{SbI_3}$ was utilized as an antimony precursor in the different syntheses, with $4.4\,\text{Å}$ separating the antimony atoms surrounded octahedrally by iodide. Therefore, only small cations like $\mathrm{Rb^+}$ and $\mathrm{NH_4^+}$ seem to easily squeeze between the octahedra in $\mathrm{SbI_3}$ to form the layered phase and larger cations instead push the octahedra closer towards the dimer phase, as illustrated in Figure 3.1. Thus, we considered the antimony acetate precursor. In $\mathrm{Sb(OAc)_3}$, antimony is coordinated with seven oxygen atoms, leading to a separation of $4.9\,\text{Å}$ between the closest antimony atoms. We suggest that with the introduction of MA- and I-ions to $\mathrm{Sb(OAc)_3}$, antimony iodide octahedra form with $\mathrm{MA^+}$ fitted in between, resulting in the 2D-MASI phase (see Figure 3.1).

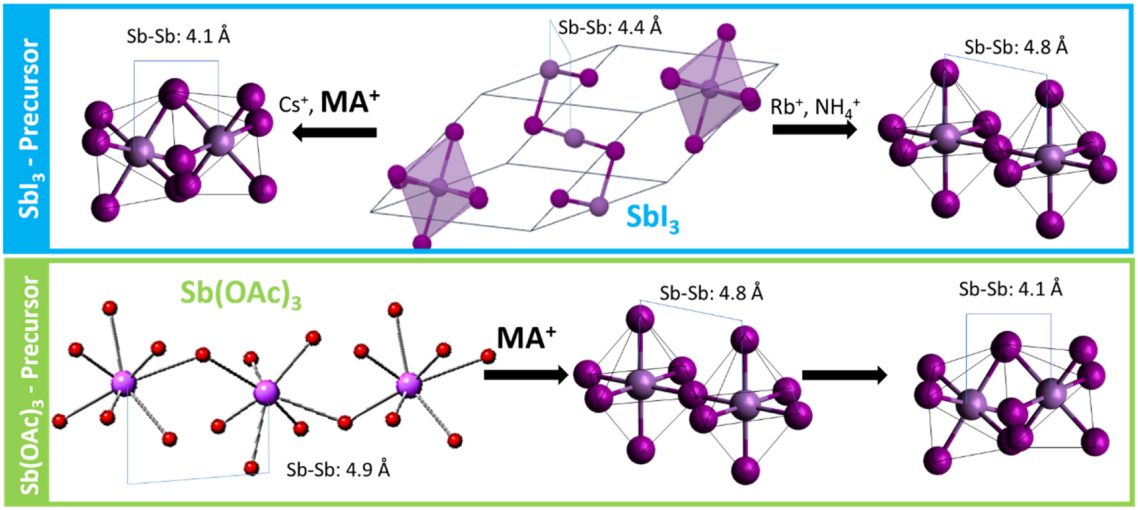

Figure 3.1: Schematic illustration of polyhedra arrangement in different antimony precursors and 0D-, 2D-MASI phase.

With powder XRD analysis, we confirm the successful synthesis of thin films of 2D-MASI. The resulting crystal structure strongly agrees with the simulated pattern of the material. Only small amounts of an additional dimer phase are visible. or the formation of the 2D-MASI phase from antimony acetate precursor, the nature of the solvent is decisive. Using dimethylformamide (DMF), the dimer phase forms predominantly with traces of the layered phase, see Supporting Information (SI). Solvents containing sulfur leading to a strong interaction with antimony, like dimethyl sulfoxide (DMSO) or tetrahydrothiophene 1-oxide (THTO), induce phase pure dimer phase crystallization (see SI).[36] However, solvents based on alcohols are highly suitable for MASI formation in the 2D phase, with best results observed when using methanol (MeOH), see SI for more details on exact thin film synthesis details. During MASI thin-film crystallization from MeOH, the annealing temperature is decisive for the phase formation. With annealing temperatures below $100\,^{\circ}\mathrm{C}$, the crystallization process slows down, which correlates with added dimer formation (see SI). Therefore, we suggest a fast crystallization process to form MASI in the layered phase and not in the more thermodynamically preferred dimer phase.

Other alcohols such as ethanol (EtOH) also induce 2D phase formation of MASI from antimony acetate precursor (see SI). However, the solubility decreases dramatically to a concentration of $0.125\,\mathrm{mmol}\ \mathrm{Sb(OAc)_3}$ in $1\,\mathrm{mL}\ \mathrm{EtOH}$. Therefore, alcohols with longer organic chains like isopropanol (IPA) are not suitable for the synthesis. If not otherwise stated, in the following, we always refer to the 2D-MASI compound prepared from MeOH.

Other than structural differences, the dimer and the layered MASI phases are clearly distinguished by their optoelectronic properties. The most significant divergence lies in

the nature and width of the semiconductor's bandgap. To predict the electronic band structure of the 0D and 2D-MASI phases, we performed first-principles calculations using plane-wave pseudopotential methods within DFT as implemented in the Quantum Espresso Package.[37] For the sake of computational efficiency, all calculations were carried out with the Cs cation since the organic cation shows no influence regarding the frontier electronic band structure.[38,39] Neglecting the well-known deficiency of the gradient corrected method PBE functional to estimate the magnitude of the bandgap, the indirect nature of the bandgap is more strongly pronounced for the dimer phase compared to the layered phase, see Figure 3.7.[40] The more pronounced indirect bandgap characteristics most probably arise from the lower crystal lattice symmetry of the 0D polymorph in comparison with the 2D phase.[34] Additionally, the very flat band determined by the valence band maximum of the 2D phase indicates a quasi-direct-indirect transition, seen in the X $\rightarrow$ Y path in the Brillouin zone (see Figure 3.7).

To verify our theoretical calculations, we characterized our MASI films via UV-Vis absorbance spectroscopy. Based on the absorbance spectra in Figure 3.2a, we observed the onset at longer wavelengths with the layered phase indicating a narrower bandgap compared to the dimer phase.

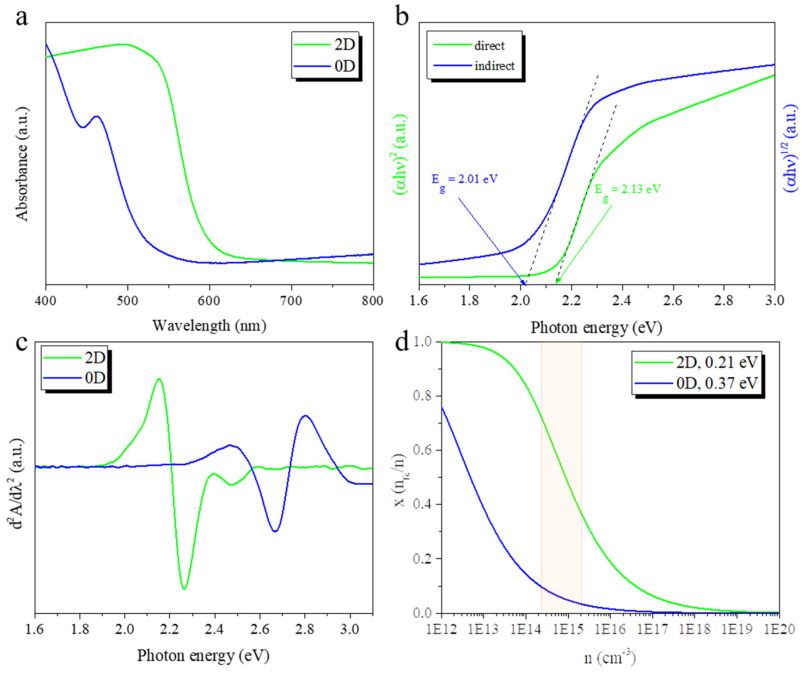

Figure 3.2: UV–Vis spectroscopy data of dimer and layered MASI phase. (a) Absorbance spectrum; (b) direct and indirect bandgap Tauc plot of layered MASI; (c) second derivative plot of the absorbance; (d) simulation of the free charge fraction over the total excitation density at thermal equilibrium, typical excitation densities in solar cells highlighted in orange.

Furthermore, calculated Tauc plots from the data of the layered material show a direct

transition at $2.1\,\mathrm{eV}$ and an indirect transition at $2.0\,\mathrm{eV}$, supporting the theoretical expectations and verifying the phase purity of 2D-MASI (see Figure 3.2b). In principle, materials benefiting from both direct and indirect bandgap behavior are favorable candidates for photovoltaic applications. Usually, strong absorption is coupled with a direct bandgap and long carrier lifetime with an indirect band-to-band transition, similar to what was observed in $\mathrm{MAPbI_3}$.[41] We note, that films synthesized from EtOH instead of MeOH indicate two onsets in the absorbance spectrum in SI Figure 3.5, implying a 2D and 0D phase mixture. Additional to the nature of the bandgap, the exciton binding energy E_b in a material determines the suitability of the compound for photovoltaic applications. Here, the minima in the second derivative of the absorbance can be used to estimate E_b.[42] Our results, displayed in Table 3.1, show that compared to $\mathrm{MAPbI_3}$, the exciton binding energy values in MASI thin films are one order of magnitude higher.[42] However, our 2D-MASI films show significantly weaker exciton binding compared

	First minimum (eV)	Second minimum (eV)	E_b (eV)
2D-MASI	2.26	2.47	0.21
0D-MASI	2.66	3.03	0.37

Table 3.1: Exciton binding energies estimated from the second derivative of the absorbance.

to the reported and our experimentally obtained values for the 0D-MASI films.[43] To understand the influence of the exciton binding energy on carrier dynamics, we employed a numerical method based on the Saha equation, described in detail in SI.[42] Figure 3.2d shows the results from the extracted data with a range of typical values reported for solar cell absorbers for total excitation density marked in an orange box.[42] With the dimer MASI phase the excitonic contribution is dominant in contrast to what we observed with our 2D-MASI thin films. Regarding the layered phase, the more desirable balanced contribution of free charge carriers and excitons is evident. Therefore, the layered MASI phase appears to be more suitable for photovoltaic applications compared to its 0D polymorph.

In addition to the optoelectronic properties of the materials, the stability of the compounds is crucial to consider their suitability for photovoltaic applications. Solar cells operate at temperatures of up to $85\,^{\circ}\mathrm{C}$ and degradation of the absorber material can, therefore, be a concern. In Figure 3.3a, we show an in situ XRD analysis conducted at $80\,^{\circ}\mathrm{C}$ for one hour and afterward at $130\,^{\circ}\mathrm{C}$ for one hour. We analyzed the powder obtained from the thin-film synthesis of the 2D-MASI phase to emphasize the substantially higher stability of the compound. The analysis of the powder in contrast to thin films additionally avoids the extinction of reflexes due to preferred crystal alignment and therefore highlights

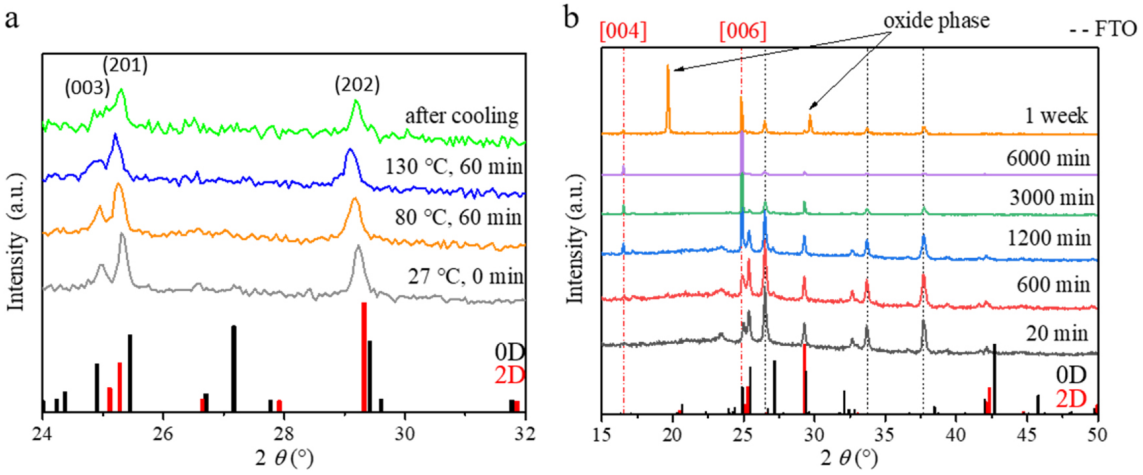

Figure 3.3: In situ XRD analysis of 2D-MASI. (a) Analysis of powder at high temperatures with marked prominent reflection indexes; (b) analysis of thin films at 75% relative humidity at temperatures between 27 °C and 31 °C.

here the presence of pure 2D-MASI phase, differing from the 0D-MASI phase with an additional peak at around 27° 2θ. Neither a phase transition to the dimer phase nor decomposition is evident in our study. The only apparent change in the high temperature investigations is the shift of the reflections to lower 2θ angles indicating an increase of the unit cell dimensions in the layered structure similar to the observations for $MAPbI_3$.[44] The increase of the unit cell dimensions is reversible, as demonstrated by the shift of the reflections to their original positions at higher 2θ angles after cooling.

Another essential factor concerning the stability of the material is its sensitivity towards moisture. Therefore, we performed an in situ XRD analysis at temperatures between 27 °C and 31 °C under 75% relative humidity conditions (see Figure 3.3b). Under these harsh conditions, our pristine layered MASI films partly recrystallized to the zero-dimensional phase after 10 h. In the course of further tracing the phase transition, we found a complete transformation to the dimer phase after 50 h. Further continuous moisture exposure for one week results in an oxidized antimony-containing phase as confirmed via energy dispersive X-ray spectroscopy (EDX) spectroscopy, shown in the SI. The observed instability towards moisture of the MASI compound is much less pronounced than that of $MAPbI_3$.[13] Studies with much thinner 2D-MASI films obtained from EtOH show that the sensitivity towards moisture becomes more evident, indicating a strong influence of morphology on stability (see SI).

Finally, we applied our novel 2D-MASI absorber layer in photovoltaic devices, using metal oxide as electron transport layer (ETL) and spiro-OMeTAD as a hole transport layer (HTL). As visible in the schematic in Figure 3.4a, the energy alignment of the ETL

with our absorber layer is not optimal for efficient electron transport and other device architectures are required.

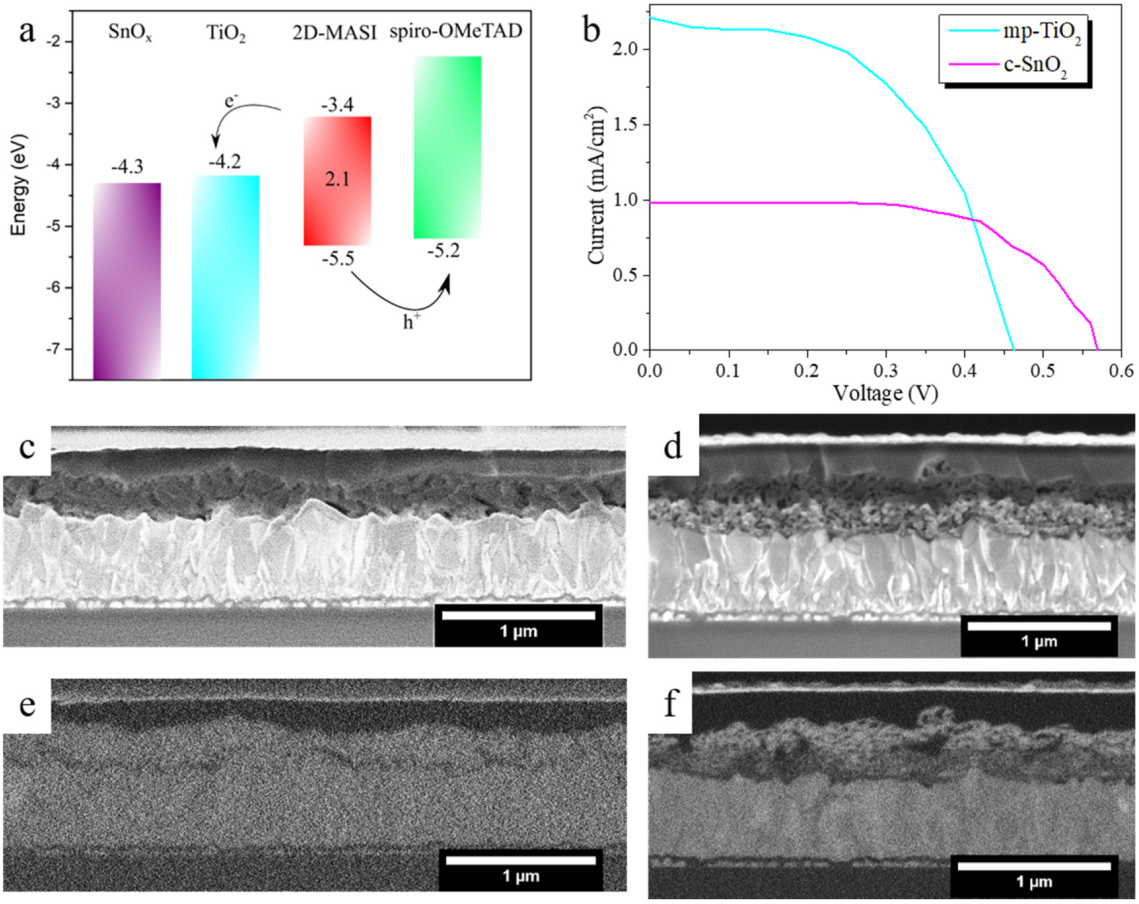

Figure 3.4: Photovoltaic devices with 2D-MASI absorber layer sandwiched between FTO/metal-oxide electron transport layer and the hole-transporter 2,2',7,7'-tetrakis[N,N-di(4-methoxyphenyl)amino]-9,9'-spirobifluorene (spiro-OMeTAD)/Au. (a) Schematic illustration of energy levels of SnO_2, TiO_2, 2D-MASI and spiro-OMeTAD; (b) *JV*-curves of devices with mesoporous titanium dioxide (mp-TiO_2) or compact tin oxide (c-SnO_2) as ETL; (c) + (e) SEM cross-section of devices with c-SnO_2 ETL with (top) topography sensitive secondary electrons detector and (bottom) mass sensitive detector; (d) + (f) SEM cross-section of devices with mp-TiO_2 ETL with (top): topography sensitive detector and (bottom) mass sensitive backscattered-electron detector.

The thin film morphologies of the MASI layer, shown in the SEM top-views in SI and SEM cross-sections of devices in Figure 3.4, are also not yet optimized with their low crystallinity and voids highly pronounced at ETL and absorber interface. However, even under these limiting conditions, devices reach already PCEs of around 0.6%. Devices with mp-TiO_2 as ETL perform best (see Table 3.2), highlighting the strong correlation of absorber layer morphology with photovoltaic performance. In general, the phase pure 2D-MASI films obtained from $MeOH$ solvent reach higher efficiencies compared to the

ETL	Current density ($\mathrm{mA\,cm^{-2}}$)	PCE (%)	Voltage (V)	Fill Factor (%)
mp-$\mathrm{TiO_2}$	2.21	0.54	0.46	52
c-$\mathrm{SnO_2}$	0.98	0.36	0.57	64

Table 3.2: Photovoltaic parameters of the fabricated solar cells from Figure 3.4

less stable and less phase pure films from EtOH solvent synthesized under similar conditions (see SI Figure 3.9). Similar to their hybrid lead halide relatives, MASI-based devices show high hysteresis in JV-scans.[45] Only with c-SnO_2 as ETL, we observed no pronounced hysteresis between forward and reverse scans (see SI Figure 3.9(a)) and improved values for fill factor and voltage but significantly low current density values (see Table 3.2 and SI). Additionally, the photovoltaic device performance using compact c-SnO_2 as ETL is more reproducible than that of the higher-performing mp-TiO_2 devices, see SI Figure 3.10. In particular, the lower current density limits the device performance distinctly, using planar device architectures. Thus, we suggest that high defect densities in the material due to the not densely-packed nanocrystalline MASI thin film morphologies are responsible for the low photovoltaic efficiencies. Assuming internal quantum efficiencies near unity as observed in $\mathrm{MAPbI_3}$-based solar cells, possible current densities based on our thin-film absorption are around $9\,\mathrm{mA\,cm^{-2}}$ (see SI Figure 3.5(d)).[46] In combination with a voltage of $1\,\mathrm{V}$, which is defined by the energy level alignment of the HTL and ETLs used in this work, device efficiencies of around 6% are probable. With more optimized device architectures, the photovoltaic performance might even exceed 10% if higher voltages with the wide bandgap material can be obtained.

3.4 CONCLUSION

In summary, we report the first synthesis of pure $\mathrm{MA_3Sb_2I_9}$ crystallized in a layered perovskite-like phase. Here, the use of the antimony acetate precursor is crucial for a fast 2D-MASI formation with the sustainable solvents EtOH or MeOH. Our theoretical calculations and experimental investigations agree regarding a semi-direct nature of the bandgap in the 2D material, in contrast to the strongly indirect bandgap of the 0D compound. Additionally, we find considerably weaker excitonic binding energies in 2D-MASI compared to the 0D polymorph, which is desirable for photovoltaic applications. At high temperatures, the 2D-MASI phase remains stable. However, at this point, the inhomogeneous thin film morphology limits the stability of 2D-MASI at high humidity levels and probably is responsible for the limited photovoltaic device performance. Therefore, we

expect that with further optimized thin film morphologies, 2D-MASI is a promising new candidate for lead-free photovoltaic applications.

3.5 SUPPORTING INFORMATION

3.5.1 Experimental Details

$MA_3Sb_2I_9$ Synthesis

All thin films were deposited via spin-coating in a nitrogen-filled glovebox. $80\,\mu L$ of the precursor solutions were dynamically spin-coated on top of $9\,cm^2$ large substrates at $5000\,rpm$ for $3\,min$. Afterwards, the substrates were annealed at $100\,°C$ for $30\,min$. All precursor solutions were prepared with antimony acetate, ($Sb(OAc)_3$, Sigma Aldrich) and methylammonium iodide (MAI, Dyesol) at a molar ratio of 2:9. We varied the solvents for optimization of 2D MASI phase formation. With pure MeOH and EtOH, we achieved the 2D MASI phase formation. The use of DMSO or THTO led to 0D MASI phase formation and DMF solvent resulted in a mixture of both. In SI Table 3.3, the variation of $Sb(OAc)_3$ concentrations corresponding to the particular solvents are listed.

Solvents	Concentration of $Sb(OAc)_3$ in $1\,mL$ solvent
MeOH	$0.25\,mmol$
EtOH	$0.125\,mmol$
DMF	$2\,mmol$
DMSO	$2\,mmol$
THTO	$2\,mmol$

Table 3.3: Summary of $Sb(OAc)_3$ concentration used in different solvents.

Device Fabrication

Fluorine-doped tin oxide (FTO, Pilkington, $7\,\Omega\,\mathrm{cm}^{-2}$) substrates were etched with 2 M HCl and zinc powder and cleaned in 2% Hallmanex detergent, acetone, ethanol and were plasma- cleaned in nitrogen plasma before deposition of charge transport layers.

A sol-gel approach was used to deposit the $\mathrm{TiO_2}$ layer with a solution containing $0.23\,\mathrm{M}$ titanium isopropoxide (Sigma-Aldrich, 99.999%) and $0.013\,\mathrm{M}$ HCl in isopropanol (IPA). The solution ($250\,\mu\mathrm{L}$ per $6\,\mathrm{cm} \times 6\,\mathrm{cm}$ substrate size) was spin-coated dynamically on top of the substrate at $2000\,\mathrm{rpm}$ for $45\,\mathrm{sec}$, dried at $150\,^{\circ}\mathrm{C}$ for $10\,\mathrm{min}$ and annealed at $500\,^{\circ}\mathrm{C}$ for $45\,\mathrm{min}$.

In devices with mp-$\mathrm{TiO_2}$ layer, an approx. $150\,\mathrm{nm}$ thick, mesoporous mp-$\mathrm{TiO_2}$ layer was applied by spin-coating $100\,\mu\mathrm{L}$ of a $\mathrm{TiO_2}$ nanoparticle paste (Dyesol DSL 18NR-T) diluted in absolute ethanol (1:6 weight ratio) onto the compact $\mathrm{TiO_2}$ layer at $2500\,\mathrm{rpm}$ for $30\,\mathrm{sec}$, followed by subsequent annealing at $500\,^{\circ}\mathrm{C}$ for $45\,\mathrm{min}$ under ambient conditions.

Devices employing a $\mathrm{C_{60}}$ monolayer were treated with $0.5\,\mathrm{mg\,mL}^{-1}$ 4-(1',5'-dihydro-1'methyl-2'H- [5,6]fullereno-C60-Ih-[1,9-c]pyrrol-2'-yl)benzoic acid solution in chlorobenzene (CLB) (Sigma Aldrich). The solution was spin-coated with $2000\,\mathrm{rpm}$ for $30\,\mathrm{sec}$ on top and dried at $100\,^{\circ}\mathrm{C}$ for $5\,\mathrm{min}$.

$\mathrm{SnO_x}$ ETL were prepared by atomic layer deposition as described in[47] on FTO coated glass substrates. Tetrakis(dimethylamino)tin(IV) (TDMASn, Strem, 99.99%) was used as a tin precursor while the oxygen precursor was provided by generated Ozone (INUSA AC2025). The tin precursor was held in a glass vessel at $75\,^{\circ}\mathrm{C}$ and the deposition was conducted at $118\,^{\circ}\mathrm{C}$ with a base pressure of $5\,\mathrm{hPa}$ in a Picosun R-200 Advanced ALD reactor. Nitrogen (99.999%, Air Liquide) was used as the carrier gas and purge gas with a flow rate of $50\,\mathrm{sccm}$. Afterward, the substrates were annealed at $180\,^{\circ}\mathrm{C}$ for $1\,\mathrm{h}$ in ambient conditions and transferred into the glovebox.

MASI thin films were deposited on top of the ETLs and a spiro-OMeTAD (99.6% purity, Borun New Materials Technology Ltd.) layer afterward. We used a $75\,\mathrm{mg\,mL}^{-1}$ spiro-OMeTAD solution in CB with 3 vol% of $170\,\mathrm{mg\,mL}^{-1}$ bis(trifluoromethane)sulfonimide lithium salt (LiTFSI) (Sigma-Aldrich) in acetonitrile (Sigma-Aldrich, anhydrous, 99.8%) and 1 vol% *tert*-butylpyridine (TBP) (Sigma-Aldrich, 96 %). The solution ($80\,\mu\mathrm{L}$ per $3\,\mathrm{cm} \times 3\,\mathrm{cm}$ substrate size) was spin-coated at $2000\,\mathrm{rpm}$ for $45\,\mathrm{sec}$. The devices were stored for one day in a desiccator to oxidize the Li-TFSI additive in spiro-OMeTAD. To

finalize the devices, a $40\,\mathrm{nm}$ thick Au counter electrode was thermally evaporated under high vacuum conditions ($\leq 10^{-7}\,\mathrm{mbar}$) through a metal aperture leading to devices with active areas in the range of $0.10\,\mathrm{cm}^2$. The active area was determined with a $0.0831\,\mathrm{cm}^2$ metal aperture.

3.5.2 Characterization

X-Ray Diffraction

Every XRD analysis was performed with a Cu-K_α X-ray source. Films were deposited on $\mathrm{TiO_2}$-coated FTO-coated glass and θ-θ scans were obtained using a Bruker D8 Discover X-ray diffractometer with a position-sensitive detector (LynxEye). Powder X-ray diffraction (PXRD) data (2θ scans) in transmission were obtained with an STOE Stadi MP diffractometer equipped with a DECTRIS MYTHEN 1 K solid-state trip detector. The X-rays were generated in both sources with a voltage of $40\,\mathrm{kV}$ and $40\,\mathrm{mA}$.

In-situ X-Ray Diffraction

In-situ XRD measurements were all conducted employing a Bruker D8 Discover X-ray diffractometer operating at $40\,\mathrm{kV}$ and $30\,\mathrm{mA}$, equipped with a Ni-filtered Cu-K_α radiation source (λ = 1.5406) and a position-sensitive LynxEye detector.
The heat treatment analysis was achieved under ambient conditions.
The investigations under controlled humidity were performed using a custom-made hydration chamber with a volume of around $250\,\mathrm{mL}$ made of X-ray transparent polymers as already reported.[48] The air humidity within the hydration chamber was held at about 75% relative humidity (RH) employing vials filled with deionized water and quantified using a hygrometer. All experiments were conducted without illumination at temperatures between $26\,^\circ\mathrm{C}$ to $29\,^\circ\mathrm{C}$.

UV-Vis Spectroscopy

Steady-state absorption spectra were acquired with a Lambda 1050 UV-vis spectrophotometer (Perkin Elmer) using an integrating sphere. MASI films were prepared on glass for characterization

First-Principles Calculations

All calculations were carried out using plane-wave pseudopotential methods within DFT as implemented in the Quantum Espresso Package.[37] The electron-ion interactions were

described using the Standard Solid State Pseudopotentials (SSSP) library optimized for efficiency.[49,50] A kinetic energy cut off of $400\,\mathrm{Ry}$ was used and Monkhorst-Pack k-meshes in the size of $4 \times 4 \times 4$ for tetragonal unit cells and $5 \times 5 \times 2$ for hexagonal unit cells were employed for Brillouin zone integrations.[51] The structure parameters were optimized through energy minimization with the forces on the atoms converging below 1×10^{-3} a.u. The generalized gradient approximation formulated by Perdew, Burke and Ernzerhof was used as the exchange-correlation functional.[40]

Saha Equation[52]

$$\frac{x^2}{1-x} = \frac{1}{n}\left(\frac{2\pi k_B T}{h^2}\right)^{2/3} e^{\left(\frac{E_b}{k_B}T\right)} \tag{3.1}$$

In the equation, x defines the ratio of free carriers n_{fc} to the total excitation density n, which is given by the sum of free carriers n_{fc} and the exciton density n_{exc}. The reduced mass μ is approximated as $\mu = 0.5m_e$ for 0D-MASI and $0.25m_e$ for 2D-MASI.

Scanning Electron Microscopy

A scanning electron microscope (FEI Helios NanoLab G3 UC) was used to acquire SEM images of perovskite layers prepared on $\mathrm{TiO_2}$-coated FTO glass.

Device Characterization

Photovoltaic device performance was measured with a Keithley 2400 source meter in air at $25\,^{\circ}\mathrm{C}$ under illumination by a Newport Oriel Sol2A solar simulator, which was calibrated to $100\,\mathrm{mW\,cm^{-2}}$ with a Fraunhofer ISE certified silicon cell with a mismatch factor of 1.01. The active area of the solar cell was defined with a square metal aperture mask of $0.0831\,\mathrm{cm^2}$.

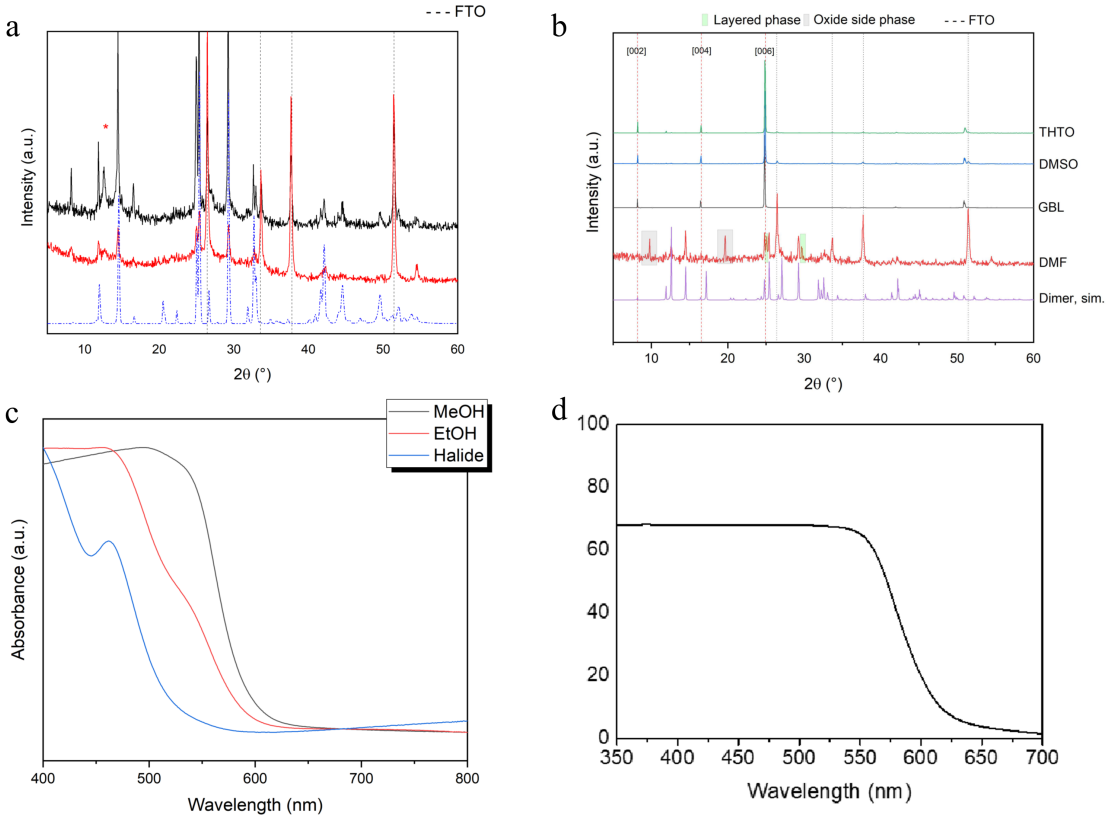

Figure 3.5: Thin-film XRD and EDX analysis: a) XRD results of 2D MASI films synthesized from MeOH or EtOH solvent with simulated pattern as reference; b) XRD results of 0D MASI films synthesized from DMSO or THTO and mixed phases from reactions based on DMF solvent; c) UV-vis spectra of 2D MASI films synthesized from MeOH or EtOH solvent and pure 0D MASI films obtained from halide-based precursor mixture; d) absorptance spectrum from 2D MASI films from MeOH.

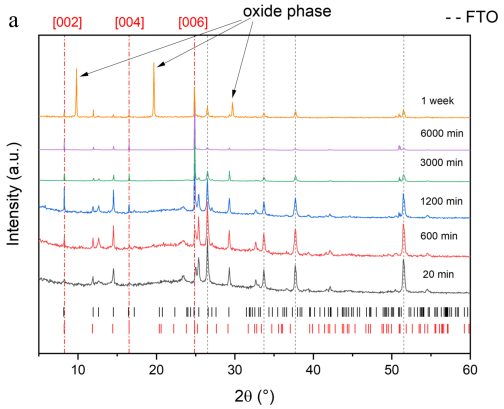

b

Element	Atomic percent (%)	Expected atomic percent in 2D-MASI
Sb	11.74	7.00
I	5.94	64.29
O	29.47	0.00

Figure 3.6: a) In situ XRD analysis at 75% relative humidity with 2D MASI films synthesized from EtOH; b) EDX Analysis of the film from a) after oxidation.

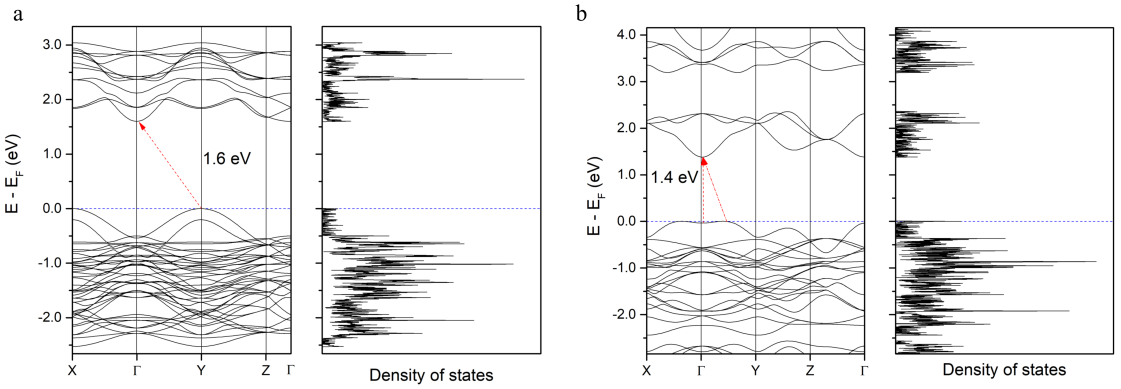

Figure 3.7: Band structure and DOS, a) for the dimer MASI phase; b) for the layered MASI phase.

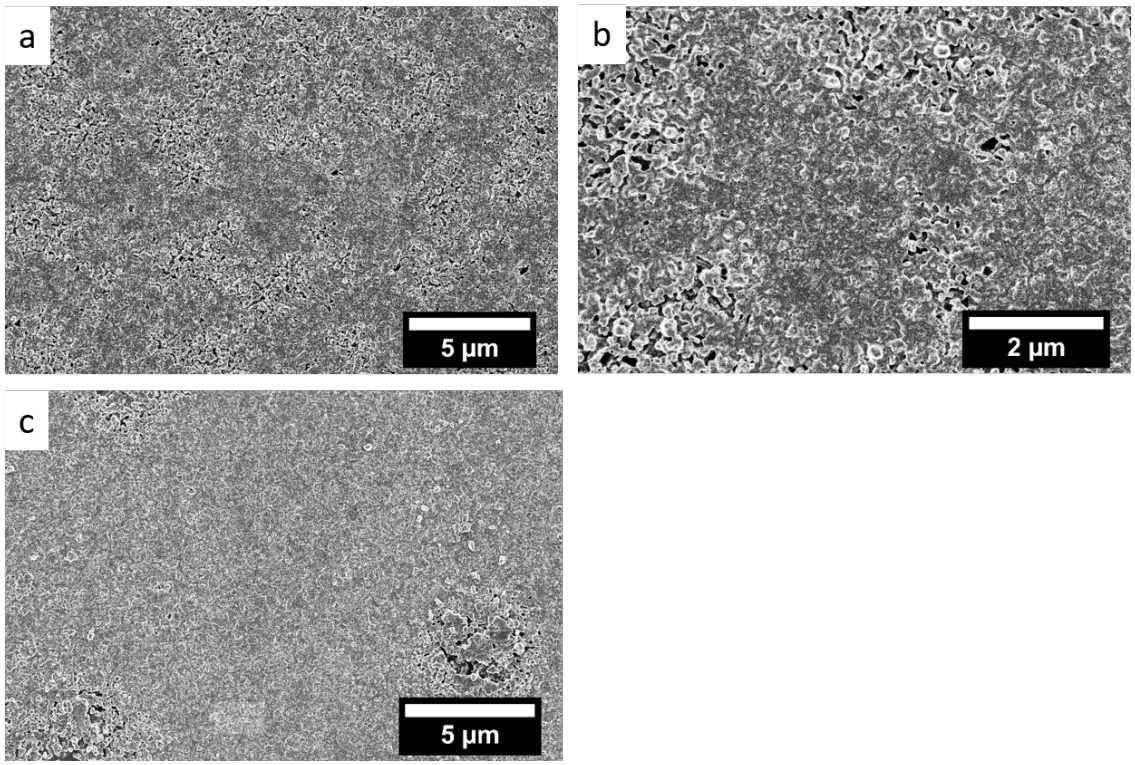

Figure 3.8: Top view SEM images of films prepared with: a+b) MeOH solvent; c) EtOH solvent.

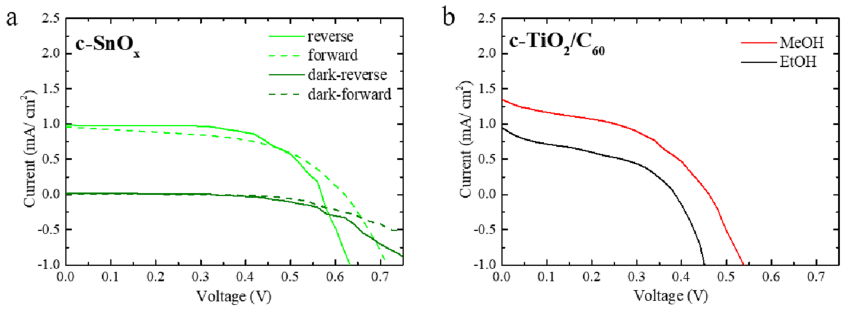

c

ETL	Current Density (mA/cm^2)	PCE (%)	Voltage (V)	Fill Factor (%)
c-SnO_2 (reverse)	0.98	0.36	0.57	64
c-SnO_2 (forward)	0.97	0.32	0.62	53
c-TiO_2/ C_{60} (MeOH)	1.35	0.27	0.46	43
c-TiO_2/ C_{60} (EtOH)	0.95	0.13	0.37	37

Figure 3.9: Photovoltaic devices with compact SnO_2 or with additional C_{60}-SAM interlayer on top of compact TiO_2: a) *JV*- curves with forward and reverse scans in light and dark conditions of devices with SnO_2 as ETL; b) JV-curves of devices with absorber layer prepared from MeOH or EtOH and C_{60}-covered c-TiO_2 as ETL; c) table with photovoltaic parameters.

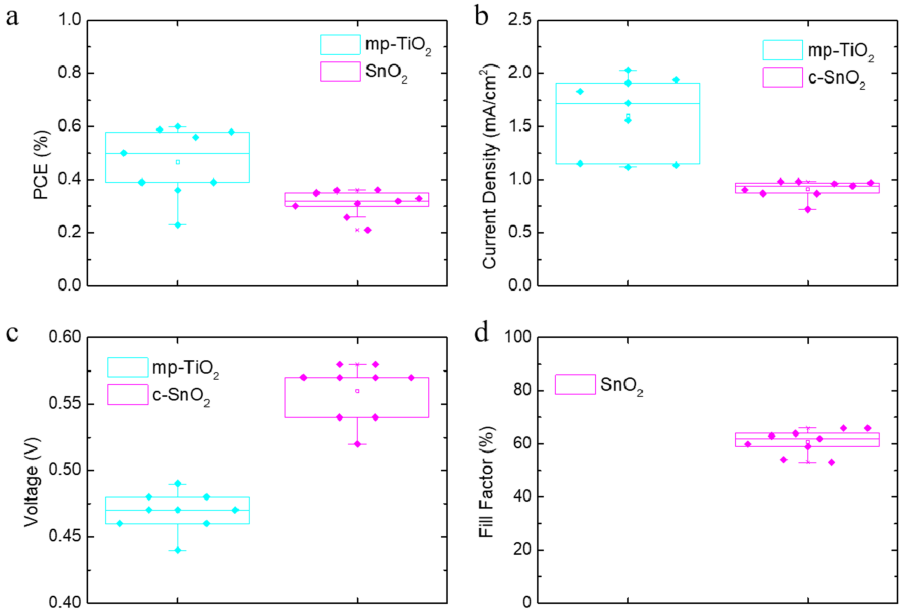

Figure 3.10: Photovoltaic performance statistics for devices with 2D-MASI absorber layer sandwiched between FTO/metal- oxide electron transport layer and the hole-transporter spiro-OMeTAD/Au. In our experiments, devices with mp-TiO_2 layers tend to show higher current densities closer to open-circuit than short-circuit, resulting in false fill factor values. Therefore, we present in b) maximum values for the current densities on mp-TiO_2 and exclude the deviations of fill factor of mp-TiO_2-based devices.

3.6 REFERENCES

[1] A. Kojima, K. Teshima, Y. Shirai, T. Miyasaka, *Journal of the american chemical society* **2009**, *131*, 6050–6051.

[2] N. NREL, Research cell record efficiency chart,(2020).

[3] G. Xing, N. Mathews, S. Sun, S. S. Lim, Y. M. Lam, M. Grätzel, S. Mhaisalkar, T. C. Sum, *Science* **2013**, *342*, 344–347.

[4] G. E. Eperon, S. D. Stranks, C. Menelaou, M. B. Johnston, L. M. Herz, H. J. Snaith, *Energy & Environmental Science* **2014**, *7*, 982–988.

[5] C. Wehrenfennig, G. E. Eperon, M. B. Johnston, H. J. Snaith, L. M. Herz, *Advanced materials* **2014**, *26*, 1584–1589.

[6] E. Edri, S. Kirmayer, A. Henning, S. Mukhopadhyay, K. Gartsman, Y. Rosenwaks, G. Hodes, D. Cahen, *Nano letters* **2014**, *14*, 1000–1004.

[7] J. T.-W. Wang, Z. Wang, S. Pathak, W. Zhang, D. W. deQuilettes, F. Wisnivesky-Rocca-Rivarola, J. Huang, P. K. Nayak, J. B. Patel, H. A. Mohd Yusof, Y. Vaynzof, R. Zhu, I. Ramirez, J. Zhang, C. Ducati, C. Grovenor, M. B. Johnston, D. S. Ginger, R. J. Nicholas, H. J. Snaith, *Energy Environ. Sci.* **2016**, *9*, 2892–2901.

[8] W.-J. Yin, T. Shi, Y. Yan, *Advanced materials* **2014**, *26*, 4653–4658.

[9] W.-J. Yin, T. Shi, Y. Yan, *The Journal of Physical Chemistry C* **2015**, *119*, 5253–5264.

[10] G. Flora, D. Gupta, A. Tiwari, *Interdisciplinary toxicology* **2012**, *5*, 47–58.

[11] G. Nordberg, B. Fowler, M. Nordberg, Handbook on the Toxicology of Metals, 4th Edit, **2015**.

[12] H. Needleman, *Annu. Rev. Med.* **2004**, *55*, 209–222.

[13] M. L. Petrus, Y. Hu, D. Moia, P. Calado, A. M. Leguy, P. R. Barnes, P. Docampo, *ChemSusChem* **2016**, *9*, 2699–2707.

[14] B. Conings, J. Drijkoningen, N. Gauquelin, A. Babayigit, J. D'Haen, L. D'Olieslaeger, A. Ethirajan, J. Verbeeck, J. Manca, E. Mosconi, et al., *Advanced Energy Materials* **2015**, *5*, 1500477.

[15] Y. Zhou, H. F. Garces, B. S. Senturk, A. L. Ortiz, N. P. Padture, *Materials Letters* **2013**, *110*, 127–129.

[16] I. Chung, B. Lee, J. He, R. P. Chang, M. G. Kanatzidis, *Nature* **2012**, *485*, 486–489.

[17] I. Chung, J.-H. Song, J. Im, J. Androulakis, C. D. Malliakas, H. Li, A. J. Freeman, J. T. Kenney, M. G. Kanatzidis, *Journal of the american chemical society* **2012**, *134*, 8579–8587.

[18] K. P. Marshall, R. I. Walton, R. A. Hatton, *Journal of materials chemistry A* **2015**, *3*, 11631–11640.

[19] C. C. Stoumpos, C. D. Malliakas, M. G. Kanatzidis, *Inorganic chemistry* **2013**, *52*, 9019–9038.

[20] T. Krishnamoorthy, H. Ding, C. Yan, W. L. Leong, T. Baikie, Z. Zhang, M. Sherburne, S. Li, M. Asta, N. Mathews, S. G. Mhaisalkar, *J. Mater. Chem. A* **2015**, *3*, 23829–23832.

[21] X. Liu, K. Yan, D. Tan, X. Liang, H. Zhang, W. Huang, *ACS Energy Letters* **2018**, *3*, 2701–2707.

[22] W. Liao, D. Zhao, Y. Yu, C. R. Grice, C. Wang, A. J. Cimaroli, P. Schulz, W. Meng, K. Zhu, R.-G. Xiong, et al., *Advanced Materials* **2016**, *28*, 9333–9340.

[23] W. Wang, D. Zhao, F. Zhang, L. Li, M. Du, C. Wang, Y. Yu, Q. Huang, M. Zhang, L. Li, et al., *Advanced Functional Materials* **2017**, *27*, 1703953.

[24] T. Leijtens, R. Prasanna, A. Gold-Parker, M. F. Toney, M. D. McGehee, *ACS Energy Letters* **2017**, *2*, 2159–2165.

[25] C. C. Stoumpos, L. Frazer, D. J. Clark, Y. S. Kim, S. H. Rhim, A. J. Freeman, J. B. Ketterson, J. I. Jang, M. G. Kanatzidis, *Journal of the American Chemical Society* **2015**, *137*, 6804–6819.

[26] K. M. Boopathi, P. Karuppuswamy, A. Singh, C. Hanmandlu, L. Lin, S. A. Abbas, C. C. Chang, P. C. Wang, G. Li, C. W. Chu, *Journal of Materials Chemistry A* **2017**, *5*, 20843–20850.

[27] P. Karuppuswamy, K. M. Boopathi, A. Mohapatra, H.-C. Chen, K.-T. Wong, P.-C. Wang, C.-W. Chu, *Nano Energy* **2018**, *45*, 330–336.

[28] B.-W. Park, B. Philippe, X. Zhang, H. Rensmo, G. Boschloo, E. M. Johansson, *Advanced materials* **2015**, *27*, 6806–6813.

[29] J.-C. Hebig, I. Kuhn, J. Flohre, T. Kirchartz, *ACS Energy Letters* **2016**, *1*, 309–314.

[30] B. Saparov, F. Hong, J.-P. Sun, H.-S. Duan, W. Meng, S. Cameron, I. G. Hill, Y. Yan, D. B. Mitzi, *Chemistry of Materials* **2015**, *27*, 5622–5632.

[31] P. C. Harikesh, H. K. Mulmudi, B. Ghosh, T. W. Goh, Y. T. Teng, K. Thirumal, M. Lockrey, K. Weber, T. M. Koh, S. Li, et al., *Chemistry of Materials* **2016**, *28*, 7496–7504.

[32] J.-P. Correa-Baena, L. Nienhaus, R. C. Kurchin, S. S. Shin, S. Wieghold, N. T. Putri Hartono, M. Layurova, N. D. Klein, J. R. Poindexter, A. Polizzotti, et al., *Chemistry of Materials* **2018**, *30*, 3734–3742.

[33] C. Zuo, L. Ding, *Angewandte Chemie* **2017**, *129*, 6628–6632.

[34] F. Jiang, D. Yang, Y. Jiang, T. Liu, X. Zhao, Y. Ming, B. Luo, F. Qin, J. Fan, H. Han, et al., *Journal of the American Chemical Society* **2018**, *140*, 1019–1027.

[35] D. Ju, X. Jiang, H. Xiao, X. Chen, X. Hu, X. Tao, *Journal of Materials Chemistry A* **2018**, *6*, 20753–20759.

[36] J. Olivier-Fourcade, A. Ibanez, J. Jumas, M. Maurin, I. Lefebvre, P. Lippens, M. Lannoo, G. Allan, *Journal of Solid State Chemistry* **1990**, *87*, 366–377.

[37] P. Giannozzi, S. Baroni, N. Bonini, M. Calandra, R. Car, C. Cavazzoni, D. Ceresoli, G. L. Chiarotti, M. Cococcioni, I. Dabo, et al., *Journal of physics: Condensed matter* **2009**, *21*, 395502.

[38] F. Brivio, A. B. Walker, A. Walsh, *Apl Materials* **2013**, *1*, 042111.

[39] I. Borriello, G. Cantele, D. Ninno, *Physical Review B* **2008**, *77*, 235214.

[40] J. P. Perdew, K. Burke, M. Ernzerhof, *Physical review letters* **1996**, *77*, 3865.

[41] E. M. Hutter, M. C. Gélvez-Rueda, A. Osherov, V. Bulović, F. C. Grozema, S. D. Stranks, T. J. Savenije, *Nature materials* **2017**, *16*, 115–120.

[42] V. D'innocenzo, G. Grancini, M. J. Alcocer, A. R. S. Kandada, S. D. Stranks, M. M. Lee, G. Lanzani, H. J. Snaith, A. Petrozza, *Nature communications* **2014**, *5*, 3586.

[43] M. Scholz, M. Morgenroth, K. Oum, T. Lenzer, *The Journal of Physical Chemistry C* **2018**, *122*, 5854–5863.

[44] F. Ruf, M. F. Aygüler, N. Giesbrecht, B. Rendenbach, A. Magin, P. Docampo, H. Kalt, M. Hetterich, *Apl Materials* **2019**, *7*, 031113.

[45] H. J. Snaith, A. Abate, J. M. Ball, G. E. Eperon, T. Leijtens, N. K. Noel, S. D. Stranks, J. T.-W. Wang, K. Wojciechowski, W. Zhang, *The journal of physical chemistry letters* **2014**, *5*, 1511–1515.

[46] N. Giesbrecht, J. Schlipf, I. Grill, P. Rieder, V. Dyakonov, T. Bein, A. Hartschuh, P. Müller-Buschbaum, P. Docampo, *Journal of Materials Chemistry A* **2018**, *6*, 4822–4828.

[47] M. F. Aygüler, A. G. Hufnagel, P. Rieder, M. Wussler, W. Jaegermann, T. Bein, V. Dyakonov, M. L. Petrus, A. Baumann, P. Docampo, *ACS applied materials & interfaces* **2018**, *10*, 11414–11419.

[48] J. Schlipf, Y. Hu, S. Pratap, L. Bießmann, N. Hohn, L. Porcar, T. Bein, P. Docampo, P. Müller-Buschbaum, *ACS Applied Energy Materials* **2019**, *2*, 1011–1018.

[49] G. Prandini, A. Marrazzo, I. E. Castelli, N. Mounet, N. Marzari, *npj Computational Materials* **2018**, *4*, 72.

[50] K. Lejaeghere, G. Bihlmayer, T. Björkman, P. Blaha, S. Blügel, V. Blum, D. Caliste, I. E. Castelli, S. J. Clark, A. Dal Corso, et al., *Science* **2016**, *351*, aad3000.

[51] H. J. Monkhorst, J. D. Pack, *Physical review B* **1976**, *13*, 5188.

[52] C.-C. Chueh, C.-Z. Li, A. K.-Y. Jen, *Energy & Environmental Science* **2015**, *8*, 1160–1189.

Heterovalent Tin Alloying in Layered $MA_3Sb_2I_9$ Thin Films: Assessing the Origin of Enhanced Absorption and Self-Stabilizing Charge States

4

This chapter is based on following publication:
A. Weis, P. Ganswindt, W. Kaiser, H. Illner, C. Maheu, N. Glück, P. Dörflinger, M. Armer, V. Dyakonov, J. P. Hofmann, The Journal of Physical Chemistry C **2022**, 126, 21040-21049.

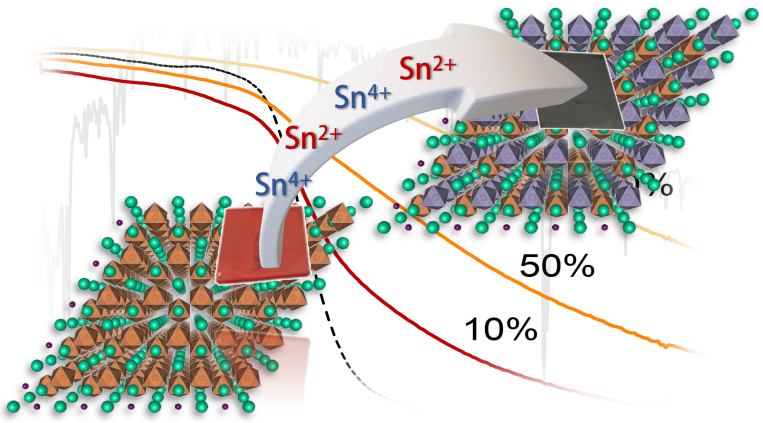

4.1 ABSTRACT

Heteroatom alloying of lead-free perovskite derivatives is a highly promising route to tailor their optoelectronic properties and stability for multiple applications. Here, we demonstrate the facile solution-based synthesis of Sn-alloyed layered $\mathrm{MA_3Sb_2I_9}$ thin films by precursor engineering, combining acetate and halide salts. An increasing concentration of tin halides in different oxidation states leads to a strong boost in absorption over the whole visible spectrum. We demonstrate phase-pure synthesis and elucidate the heterovalent incorporation of Sn into the $\mathrm{MA_3Sb_2I_9}$ lattice, proving the formation of additional electronic states in the bandgap by theoretical calculations. On this basis, we dissect the strong absorption increase into three components that we attribute to intervalence and heteroatom-induced interband absorption. Finally, we show the charge-stabilizing effect of the system through robustness towards precursors in mixed oxidation states and trace the improved ambient stability of this material back to this feature.

4.2 INTRODUCTION

Metal halide perovskite materials have been the focus of optoelectronic research as active layers in photovoltaic (PV) devices since their discovery in 2009 by Kojima et al., based on their unique optoelectronic properties, low-cost solution processing and rapid rise in PV efficiencies, exceeding 25% PCE.[1–3] Unfortunately, the central lead atom in commonly used perovskites in PV also introduces significant challenges for commercial application because of an inherent low stability against moisture, light and temperature as well as its high toxicity for humans and the environment of the resulting Pb(II)-based compounds.[4,5] Therefore, the search for materials with similar properties, decreased material cost, facile processability and lower toxicity has been an active field of research in the last years, mainly employing cations with the same ns^2 electronic configuration of Pb ($[Xe]6s^24f^{14}5d^{10}6p^2$).[6] Many strategies to replace lead in the regular $\mathrm{ABX_3}$ stoichiometry made use of group IV cations like Sn and Ge, which unfortunately suffer from stability issues because of rapid oxidation from state +II to +IV.[7–9] An alternative approach to achieve isostructural materials is to combine heterovalent metal cations like monovalent Ag and trivalent Bi, giving rise to double perovskite structures such as $\mathrm{Cs_2AgBiBr_6}$.[10] However, this class of materials features large, indirect bandgaps and prominent non-radiative recombination causing low PCEs not exceeding 4%.[11] Because of these limitations, Savory et al. suggested that moving beyond the cubic perovskite

lattice could enhance cation interactions and circumvent these problems.[12] Hence, another strategy to access perovskite-like structures was based on implementing trivalent group IV cations like Sb^{3+} and Bi^{3+} into the ternary perovskite structure, resulting in to so-called "vacancy-ordered perovskites" of stoichiometry $A_3B_2X_9$, which crystallize predominantly in two non-perovskite polymorphs: a 0D dimer structure (space group $P6_3/mmc$, no. 194) with fused bioctahedra and a 2D layered structure (P-$3m1$, no. 164) with corner-sharing octahedra as shown in Figure 4.1.

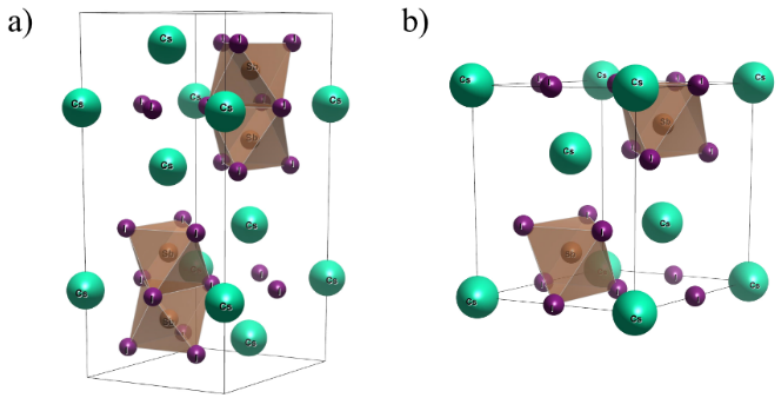

Figure 4.1: Crystal structure of 0D (a.) & 2D (b.) $Cs_3Sb_2I_9$, visualized with Vesta.[13]

The 0D phase of $MA_3Sb_2I_9$ was shown to achieve up to 2.8% PCE with adequate device engineering,[14] but still exhibits high exciton binding energies and an indirect bandgap of over 2 eV, similar to $Cs_2AgBiBr_6$. On the other hand, DFT calculations suggest that the 2D phase of $MA_3Sb_2I_9$ is more favorable as an active material in solar cells because of a lower band-gap and lower exciton binding energies, although still featuring an indirect transition of around $2\,eV$. Notably, the formation of this phase is thermodynamically unfavorable, which however can be circumvented by precursor engineering, e.g. using acetate salts as main antimony source or by introducing chloride into the system, leading to efficiencies exceeding 3%.[15] However, the bandgap issue still persists, hampering the potential of this material for single-junction photovoltaic devices. One approach to reduce the bandgap is to introduce heteroatoms like Sn into the structure, which was recently shown to boost the efficiency from 0.57% to 2.70% in $Sn(IV)$-substituted 0D-$MA_3Sb_2I_9$.[16–19] Furthermore, *Krajewska* et al. recently showed that mixed-valence $Sn(II)/Sn(IV)$ doping in $2D - Cs_3Sb_2I_9$ powders resulting from alloying with $Sn(II)$-based precursors drastically enhances the visible light absorption with unexpectedly high stability, which is rather uncommon for Sn-containing perovskites.[18] Nonetheless, a route to produce thin films of this compound has not been reported yet. Here, we establish the first solution-processing route to access homogeneous thin films of 2D-$MA_3Sb_2I_9$ alloyed with tin, employing tin chloride and tin iodide precursors with divalent and tetravalent oxida-

tion states. We showcase the successful incorporation of tin into the vacancy-ordered perovskite structure by X-ray photoelectron spectroscopy (XPS) and X-ray diffraction (XRD). Furthermore, we demonstrate a mixed valence synthesis approach for the first time, highlighting charge-stabilizing effects in the system. DFT calculations underline the successful incorporation of $\mathrm{Sn(II)}$ and $\mathrm{Sn(IV)}$, which introduce additional states in the bandgap and explain the dramatically enhanced absorption over the entire visible spectrum. Furthermore, we assign the striking spectral changes of the absorption to intervalence and interband state transitions.[18] Lastly, we show the extraordinary stability of this system in comparison to common Sn-based perovskite systems. Based on these results, we illustrate the properties and challenges of this alloyed perovskite-like compound as optoelectronic material and contribute to the understanding of heterovalent doping into vacancy-ordered perovskite materials and their facile synthesis.

4.3 RESULTS AND DISCUSSION

For the synthesis of Sn-alloyed $\mathrm{MA_3Sb_2I_9}$, an acetate-based route was employed to access the 2D polymorph because of its promising optoelectronic properties. As it was shown that addition of chloride anions can also facilitate the formation of this 2D phase,[20] thin films were fabricated with $\mathrm{SnI_2}$ and $\mathrm{SnCl_2}$ as tin precursors to investigate the influence of different halides on the structural and morphological properties. Additionally, a mixed valence precursor of 1:1 $\mathrm{SnI_2}$/$\mathrm{SnI_4}$ was introduced, as previous research efforts indicate that the incorporation of the tin cations in the large bandgap defect-ordered perovskite $\mathrm{Cs_3Sb_2I_9}$ occurs by replacing two trivalent $\mathrm{Bi^{3+}}$ cations (Wyckoff site $2d$) in a mixed valence cluster of $\mathrm{Sn^{2+}}$/$\mathrm{Sn^{4+}}$.[18] Contrary to the common halide synthesis approach, we show that a color shift from red to black in thin films can also be achieved by partially employing $\mathrm{Sn^{4+}}$ based precursors. The corresponding thin film XRD patterns can be seen in Figure 4.3 for films containing Sn/Sb precursor ratios of 0.5 and 1.0 versus the pristine (undoped) reference.

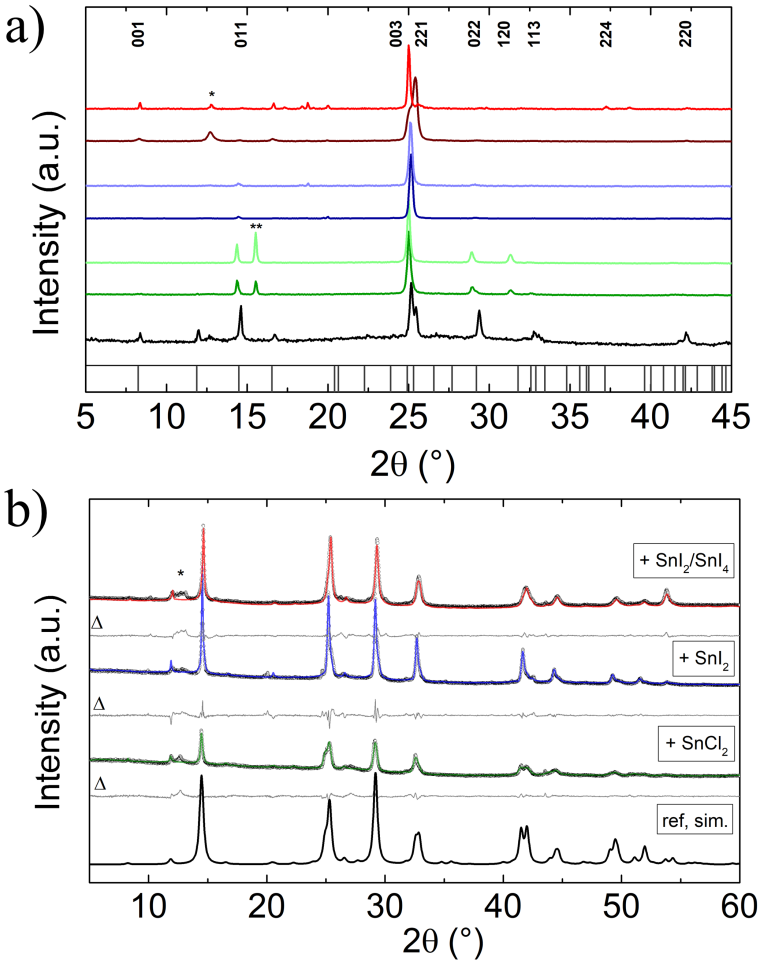

Figure 4.2: (a) Thin film XRD of $Sn : MA_3Sb_2I_9$ with Sn/Sb = 0.5 & 1 and theoretical patterns for 2D-$MA_3Sb_2I_9$ (red = mixed valence iodide precursor, blue = iodide precursor, green = chloride precursor). The asterisks indicate the side phases (*) 0D-$MA_3Sb_2I_9$ and $MASnCl_3$ (**). The darker colored patterns refer to a Sn/Sb ratio of 0.5 and the lighter ones to a ratio of 1. (b) Rietveld-fitted XRD data of $Sn : MA_3Sb_2I_9$ powders with Sn/Sb = 0.8 (red = mixed valence iodide precursor, blue = iodide precursor, green = chloride precursor, black dots = experimental data, colored traces = Rietveld fits) compared to the simulated pattern of 2D-$MA_3Sb_2I_9$ (black), which was broadened by a Gaussian function with a width of $0.4°$ 2θ. The difference plots of the fits are shown in light grey below the corresponding curves. The asterisk indicates the side phase (*) 0D-$MA_3Sb_2I_9$.

We note that a high Sn/Sb precursor ratio of at least 0.4 in comparison to the antimony source is needed to guarantee phase purity and homogeneous coverage (Figure 4.1). The XRD patterns of the thin films exhibit excellent agreement with the theoretical patterns, high crystallinity and a pronounced orientation in the [003] direction, as also seen for the undoped material.[15] To verify the phase formation independent of orientation effects, we also performed X-ray diffraction on powders obtained from multiple thin films, and fitted them via the Rietveld method (Figure 4.3b).[21,22] The recorded patterns nicely match with the simulated reference pattern of 2D-$MA_3Sb_2I_9$ with an added Gaussian broadening

of $0.4°$ 2θ to capture experimental conditions. The Rietveld fits also show only minor discrepancies in the difference function (Δ in Figure 4.3b). In general, the different tin halide precursors lead to slightly different peak positions and minor side phases like the 0D polymorph of $MA_3Sb_2I_9$ (* in Figure 4.3a-b) and $MASnCl_3$ (** in Figure 4.3a). A slight shift towards smaller 2θ angles in the prominent (003) reflection can be observed in general for the alloyed samples, indicating a stretch of the c axis of the unit cell due to the integration of thin heteroatoms in the structure, likely caused by the larger ionic radius of Sn^{2+} $(118\,pm)$/ Sn^{4+} $(83\,pm)$ in comparison to Sn^{2+} $(76\,pm)$.[23] The exact values for the unit cell axes were calculated via Bragg's Law and are compared to the results obtained from the Rietveld refinement in Tables 4.2 and 4.10. The corresponding thin film morphologies as observed by optical photography (a) and scanning electron microscopy (b) in Figure 4.4, show a strong change with different tin precursor concentrations.

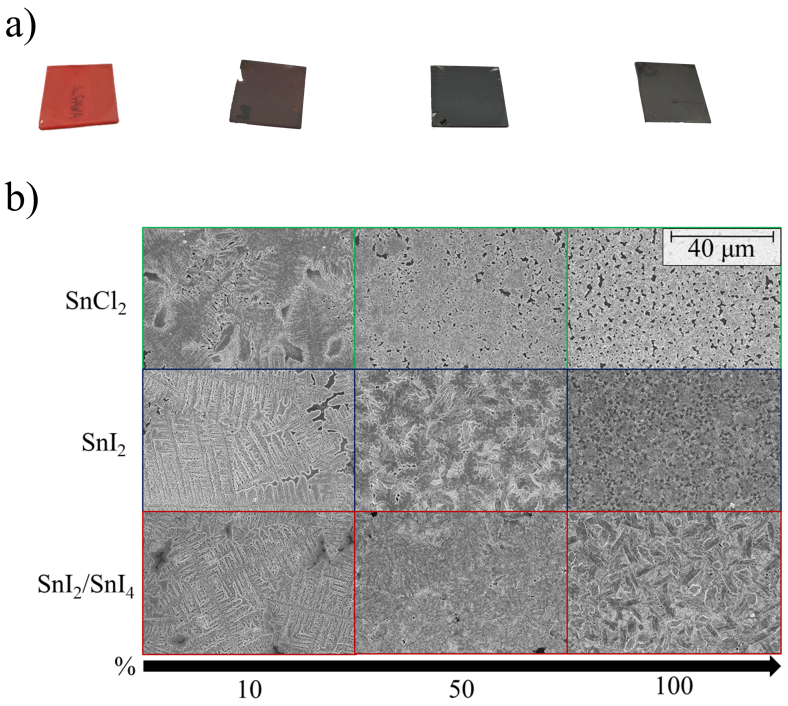

Figure 4.3: Optical photography (a) and scanning electron microscopy (b) images of $Sn : MA_3Sb_2I_9$ with different Sn percentage added in synthesis.

Low tin content in the precursor solution (10% in relation to the antimony acetate precursor) results in mostly dendritic growth for all samples where the small dendrites partially grow together to form larger domains. An increased tin content of 50% seems to significantly aid the crystallization behavior of tin-doped $MA_3Sb_2I_9$ films, resulting in more homogeneous coverage and overall less pinholes, in accordance with the improved phase purity established in the thin film XRD measurements. Nonetheless, Cl-containing samples prepared with 50% tin precursor concentration still exhibit some pinholes, which be-

come even more pronounced within film morphologies prepared with a 1:1 ratio of Sb to Sn precursor. Interestingly, this is not the case when exclusively employing iodide-based precursors both in a divalent and mixed valence state, exhibiting an improved coverage, which we tentatively attribute to the larger iodide anion stabilizing the alloyed crystal structure. The influence of tin incorporation on the optical absorption is striking when looking at optical photographs of the pristine reference versus Sn-alloyed samples, which show a change from bright red to jet-black (Figure 4.4a). The corresponding absorption measurements over the visible spectrum are depicted in Figures 4.6b-d, with the fitted absorbance spectrum of the undoped reference shown in Figure 4.6a.

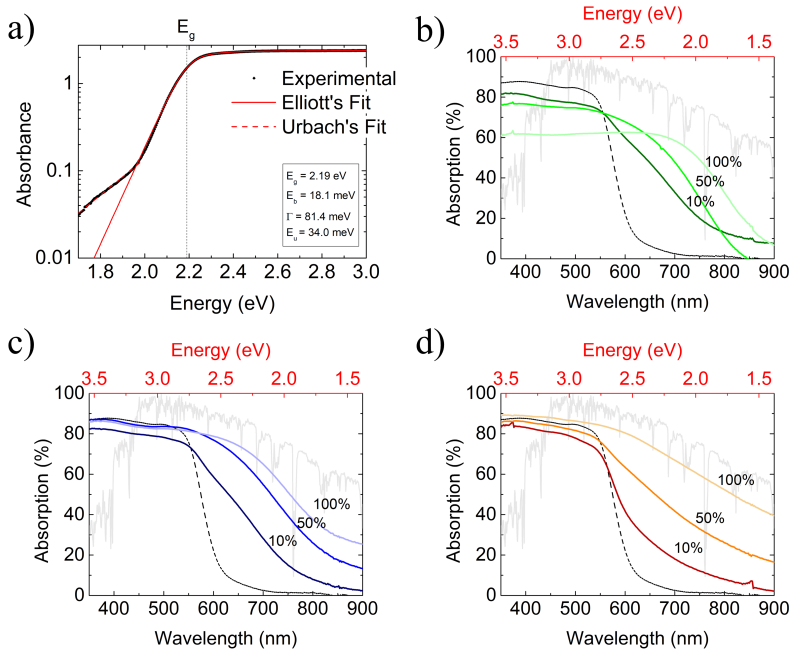

Figure 4.4: (a) Absorbance spectra of undoped 2D-$MA_3Sb_2I_9$, fitted with Elliott's method close to the band edge (yielding the bandgap E_g the exciton binding energy E_b and the inhomogeneous broadening parameter Γ) and with *Urbach*'s method in the bandgap (yielding the Urbach energy E_u). (b-d) Absorption spectra of $Sn : MA_3Sb_2I_9$ with Sn/Sb = 0.1, 0.5 & 1 in the precursor solution. (Black, dashed: 2D-$MA_3Sb_2I_9$, green = chloride precursor, blue = iodide precursor, red = mixed valence iodide precursor, light gray: normalized AM1.5 solar spectrum).

The absorbance spectrum of pristine 2D-$MA_3Sb_2I_9$ can be fitted by Elliott's method in proximity of the band edge[24,25] and Urbach's method in the bandgap,[26,27] pointing to an overall excitonic absorption behavior with a bandgap (E_g) of 2.19 eV, an Urbach energy of 34.0 meV in the range of other reported Sn perovskites[28] and a small exciton binding energy of 18.1 meV, which is probably overshadowed by the large inhomogeneous broadening component Γ of 81.4 meV. This broadening component is significantly higher than in regular lead-based perovskites ($\approx$ 20 meV).[29] The substantial broadening

further hints at pronounced exciton-phonon coupling as already seen in other materials based on the octahedral antimony-halide motif.[30] However, fitting of the data with an excitonic absorption model was not possible with the absorbance curves of the tin-alloyed material (4.12), where the exact origin will be discussed in the last section of this work. Nonetheless, a remarkable surge in light absorption over the whole spectrum is apparent for the samples alloyed with any ratio of tin, which can be controlled by increasing the tin content. The absorption in the short wavelength regions decreases for chloride-containing samples, whereas it remains mostly constant for thin films prepared with only $\mathrm{SnI_2}$ and mixed $\mathrm{SnI_2}$/$\mathrm{SnI_4}$ precursors. This finding could be attributed to the more inhomogeneous morphology and increasing side phases when employing $\mathrm{SnCl_2}$ as tin precursor. Interestingly, the strongest absorption increase can be observed for the films prepared with mixed valence tin iodide precursors in 1:1 ratio to antimony acetate. Moreover, the absorption increases more strongly in the low energy region than the absorption of compounds prepared with only Sn(II) as tin source, suggesting relevant contributions of Sn(IV) in the final morphology. Overall, these optical results further confirm successful tin alloying in $\mathrm{MA_3Sb_2I_9}$ and establish the facile tunability of the light absorption by increasing Sn concentration, coupled with homogeneous thin film coverage and orientation in the $[003]$ direction (Figure 4.3a).

DFT calculations were performed to rationalize the origin of enhanced absorption upon Sn incorporation. For sake of simplicity, the equivalent $\mathrm{Cs_3Sb_2I_9}$ perovskite was used due to the expectedly small impact of the A-site cation on the electronic structure[31] and optical properties.[32] The rotational dynamics of MA in classical $\mathrm{MAPbI_3}$ can affect the octahedral tilting and with this the impact of spin-orbit coupling (SOC),[31] which however is of less relevance in the given case of Sb and Sn as B-site elements (see also SI Figure 4.15), justifying the use of Cs. Ionic positions of the pristine and the Sn-doped structures were obtained by PBE0+D3 geometry optimization, with refined electronic structure calculations using the hybrid HSE06 functional including SOC and van der Waals corrections to obtain accurate defect properties,[33] see Supporting Information for computational details. Our calculations on the pristine $\mathrm{Cs_3Sb_2I_9}$ predict a band gap of $2.10\,\mathrm{eV}$, see Figure 4.5a, in good agreement with the experimental results.

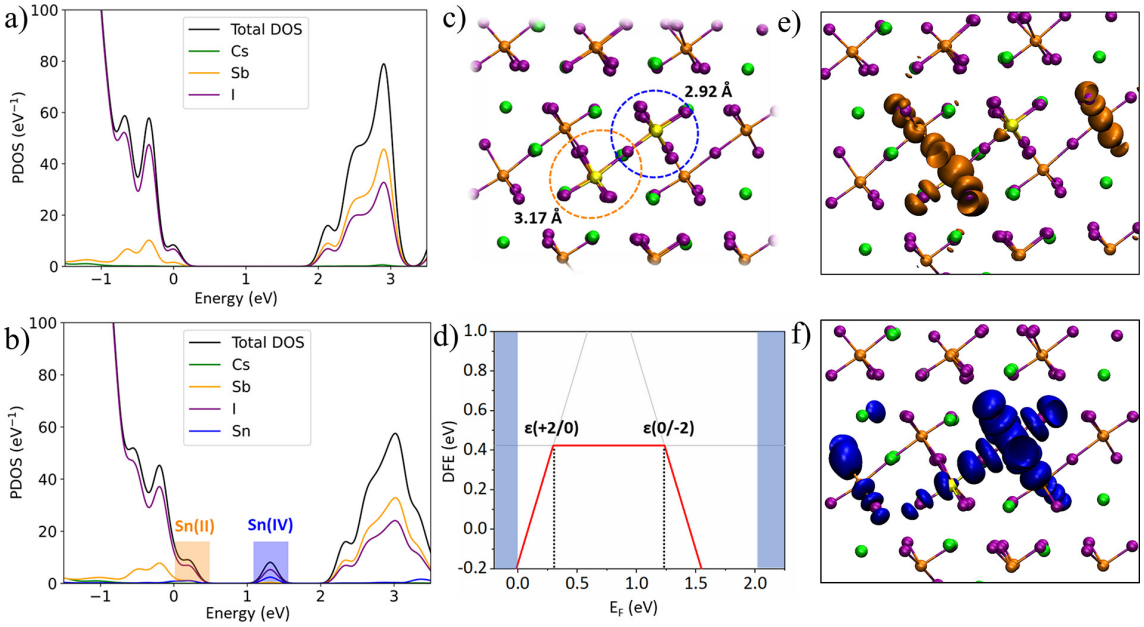

Figure 4.5: Projected density of states of (a) pristine $Cs_3Sb_2I_9$ and of (b) heterovalent $Sn(II)/Sn(IV)$ doped $Cs_3Sb_{1.75}Sn_{0.25}I_9$ with Cs = green, Sb = orange, I = purple, Sn = blue. $Sn(II)$ occupied and $Sn(IV)$ unoccupied orbitals are highlighted in orange and blue color, respectively, in panel b. (c) Local structure of $Cs_3Sb_{1.75}Sn_{0.25}I_9$ and average $Sn^{\smile}I$ bond lengths, highlighting the $Sn(II)$ ion in orange circle and the $Sn(IV)$ ion in blue circle. (d) Calculated defect formation energy for the paired $Sn_{Sb} - Sn_{Sb}$ as function of the Fermi level E_F. Thermodynamic ionization levels are indicated within the graph. Panels (e) and (f) visualize the occupied $Sn(II)$ and unoccupied $Sn(IV)$ orbitals, respectively.

Sn-doping is modeled by replacing Sb^{3+} ions in a 2×2×2 supercell at different Sn:Sb ratios. To understand the impact of heterovalent Sn(II)/Sn(IV) doping, we replace two neighboring Sb^{3+} by Sn ions, the most stable configuration in 0 charge state (see SI Figure 4.16), at different charge states of the supercell $(+2/0/-2)$, in line with previous studies on the similar compound $Cs_3Bi_2Br_9$.[18] At charge state -2, representing two Sn(II) ions, Sn 5s orbitals introduce additional occupied states at around $0.29\,eV$ above the highest occupied Sb states as well as additional states at $3.3\,eV$, see SI Figure 4.16. The lowest unoccupied orbital delocalizes within the Sn-free layer, while the highest occupied Sb orbital is delocalized within the whole supercell. For the neutral supercell, we observe the appearance of additional unoccupied Sn 5s states at 1.3 eV above the Sb occupied states, see Figure 4.5b, while occupied Sn 5s states are shifted slightly towards the Sb occupied states ($0.22\,eV$). Considering the individual Sn ions, we observe substantially shortened $Sn^{\smile}I$ bonds of $2.92\,Å$ and a Bader charge of $+1.25$ for the Sn ion (highlighted in blue, Figure 4.5c) that attributes the additional gap states, being characteristic for Sn(IV) species.[33] The other Sn ion shows Sn–I bonds of $3.17\,Å$ and Bader charge of $+0.98$ (highlighted in orange, Figure 4.5c), representing a Sn(II) ion. The occupied Sn(II) and unoccupied Sn(IV) orbitals are localized on the respective Sn

ions, see Figure 4.5e and 4.5f, respectively. Changing the charge state of the supercell from 0 to $+2$, we observe both Sn ions in $4+$ oxidation state, represented by an additional undercoordinated Sn ion with Bader charge of $+1.23$, see SI Figure 4.18. Now, the occupied Sn $5s$ states disappear and additional unoccupied Sn $5s$ states appear, highlighting the presence of $\mathrm{Sn(IV)}$. To further investigate the stability of the different oxidation states, we calculated the defect formation energy (DFE) and thermodynamic ionization level (TIL) of the $\mathrm{Sn_Sb}$-$\mathrm{Sn_Sb}$ doped structure, see Figure 4.5d. We observe a DFE for the neutral $\mathrm{Sn_Sb}$-$\mathrm{Sn_Sb}$ defect of $0.42\,\mathrm{eV}$, and TILs at $0.29\,\mathrm{eV}$ for the $+2/0$ transition and at $1.24\,\mathrm{eV}$ for the $0/-2$ transition. While oxidation of $\mathrm{Sn(II)}$ to $\mathrm{Sn(IV)}$ is known to be unfavorable in bulk methylammonium tin iodide, $\mathrm{Sn(IV)}$ can be stabilized in combination with $\mathrm{Sn(II)}$, opening additional bands for sub-gap absorption in tin-alloyed $MA_3Sb_2I_9$ as observed in our experiments. As recently proposed by Ricciarelli et al.,[34] the key to observe $\mathrm{Sn(IV)}$ in perovskites is the presence of partially disconnected octahedra with shortened $\mathrm{Sn}^{\smile}\mathrm{I}$ bonds. Thus, alloying with heterovalent tin precursors, resulting in $\mathrm{Sn(II)/Sn(IV)}$ pairs, is a general feature of layered, vacancy-ordered perovskites and not limited to $MA_3Sb_2I_9$ or the previously studied $Cs_3Bi_2Br_9$.[18]

To examine the chemical environment and oxidation states of the atoms of interest in as-synthesized thin films, XPS measurements were conducted on films synthesized with only divalent and with mixed valent tin iodide precursors. Samples were measured with (Figure 4.6a-d) and without Argon (Figure 4.18) sputtering to remove possible surface contamination and compare surface and bulk results.

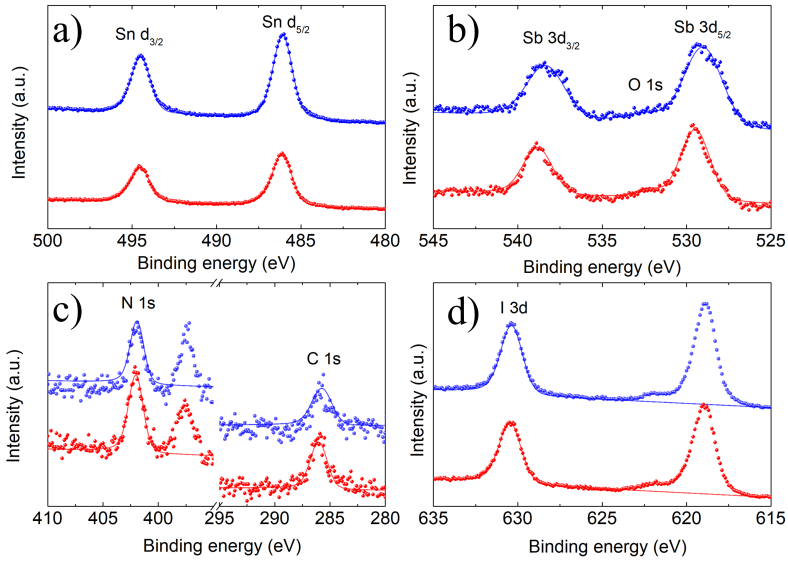

Figure 4.6: XPS spectra of Ar-sputtered Sn : $MA_3Sb_2I_9$ thin films with $\mathrm{(Sn/Sb)}$ = 1 thin films for blue = iodide precursor, red = mixed valence iodide precursor. a.) Sn-d states, b.) Sb-d and O-s states, c.) N-s and C-s states and d.) I-d states.

Intriguingly, both samples yield the same results except for a shift of $0.13\,\mathrm{eV}$ higher binding energies which is probably due to a Fermi level shift towards the CB for the mixed valence precursor. As seen in Figure 4.6a, the Sn-d orbitals show the same binding energies, independent of the precursor being only $\mathrm{SnI_2}$ or a mixture of $\mathrm{SnI_2}$/$\mathrm{SnI_4}$. The presence of a single signal suggests strongly interacting Sn centers, as isolated and different oxidation states would strongly shift the signals as seen with degraded samples (Figure 4.19). Strikingly, the ratio of Sn/Sb is also the same for both samples, indicating successful incorporation of both species (presented in Table 4.8 for all samples). This incorporation could be explained by a self-regulating charge mechanism as established for $\mathrm{CsSnI_3}$/$\mathrm{Cs_2SnI_6}$, which shows that holes are not localized on single atoms but rather distributed through the octahedral motif.[35,36] The Sn-$3d_{5/2}$ has a binding energy of $486.1\,\mathrm{eV}$ with a spin-orbit splitting of $8.4\,\mathrm{eV}$, in agreement with previous reports.[37] Furthermore, the remaining atoms in Sn:$\mathrm{MA_3Sb_2I_9}$ can be seen in Figure 4.6b-d and are in the expected ranges for conventional hybrid organic-inorganic perovskites, confirming the homogeneous formation of the target material in the bulk and on the surface.[37] If we assume delocalized valences in the strongly coupled $\mathrm{Sn-I-Sn}$ motif as for Sn:$\mathrm{Cs_3Bi_2Br_9}$,[18][36] we can attribute Sn:$\mathrm{MA_3Sb_2I_9}$ belonging to either Class II or III mixed-valence compounds as defined by Robin and Day in 1968.[38] Nonetheless, these two mixed-valence types can be very difficult to distinguish experimentally and theoretically.[39] Both these classes are known to exhibit strong and broad absorption bands in the visible or infrared region of the spectrum. This approach can be used to understand the origin of the enhanced absorption in Sn:$\mathrm{MA_3Sb_2I_9}$ by subtracting the normalized absorbance spectrum of the undoped compound from the spectra of the alloyed materials. The corresponding results are shown in Figure 4.7a-i.

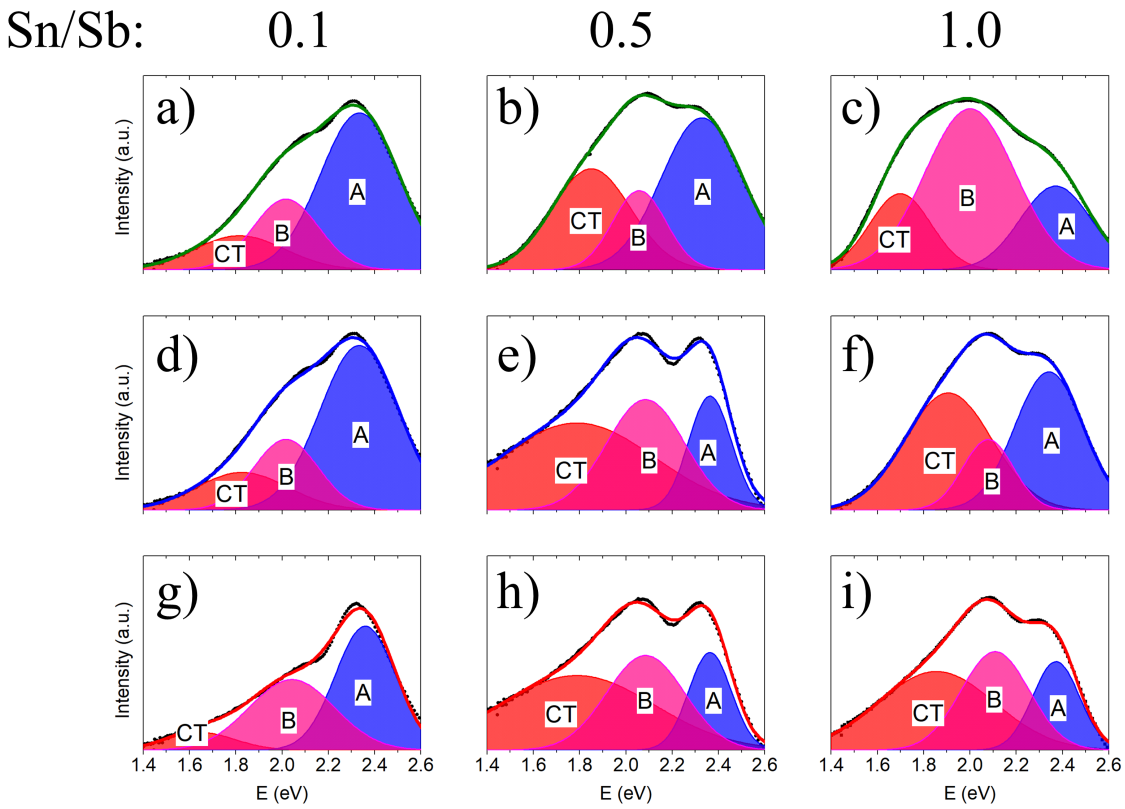

Figure 4.7: Absorbance difference spectra for tin-doped versus undoped $MA_3Sb_2I_9$. a-c: Thin films prepared with $SnCl_2$ as precursor with increasing concentration of Sn. d-f: Thin films prepared with SnI_2 as precursor with increasing concentration of Sn. g-i: Thin films prepared with a mixture of SnI_2/SnI_4 as precursors with increasing concentration of Sn. All the data were fitted via three gaussian functions labeled as A (VB to Sn_{disocc}), B (Sn_{occ} to CB) and CT (Sn_{occ} to Sn_{disocc}). The fitting curves are depicted as green (+$SnCl_2$), blue (SnI_2) and red (+SnI_2/SnI_2) line.

A striking trend can be seen when observing the curve maxima from left to right with increasing Sn concentration. The ratio of the two peaks at approximately 2.0 eV (B) and 2.3 eV (A) seems to grow while being approximately the same for samples with 50% Sn concentration (4.7b,e,h). In agreement to our DFT calculations, we assign the additional contributions to the absorption to two new transitions from Sn states to the frontier bands of $MA_3Sb_2I_9$. The high energy components A and B (Figure 4.7) may be assigned to transitions between occupied Sb-p/I-p to Sn-p/I-p (VB to Sn, A) and between occupied Sn-s to unoccupied Sb-p/I-p (Sn to CB, B), respectively, as seen in Figure 5d. We may expect a rise in the occupied Sn DOS with increasing Sn concentration, which consequently leads to a stronger contribution of transition B in comparison to A. Adding a third gaussian function (CT) to capture intervalence absorption between Sn(II) and Sn(IV) orbitals, as expected in a Robin Day class II/III compound results in an excellent fit of the absorbance differences (Figure 4.7, red: CT, pink: Sn to CB, B, blue: VB to Sn, A). The

corresponding schematic diagram is shown in Figure 4.8.

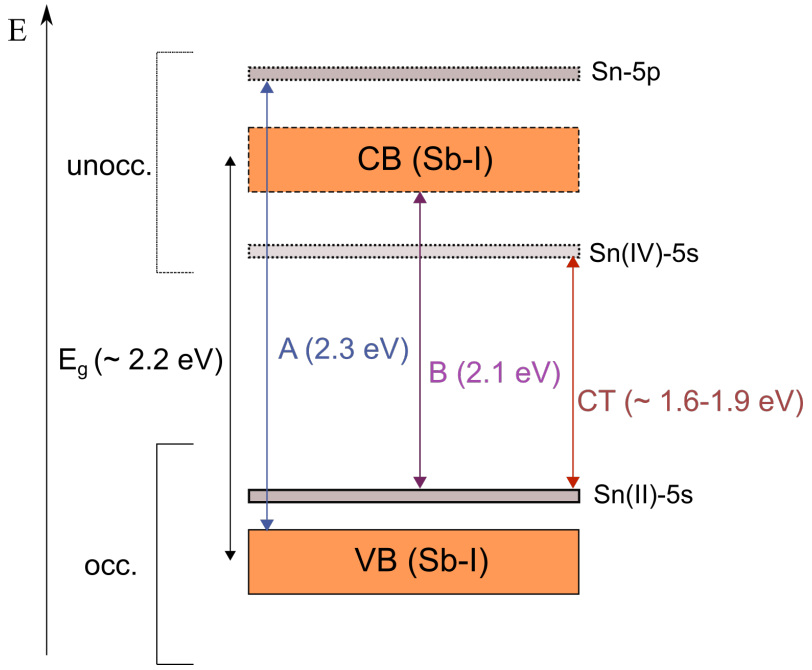

Figure 4.8: Schematic illustration of the additional absorption features in $\mathrm{Sn} : \mathrm{MA_3Sb_2I_9}$. The orange blocks indicate the frontier bands of the reference material.

Intriguingly, the energy differences add up extraordinarily well with the experimental bandgap determined via Elliott's method and the theoretically obtained energy levels arising from the formation of the unoccupied Sn band above the reference CB. Furthermore, they seem to be very consistent while iteratively least-squares fitting over all sample data, independent of concentration and precursor (Figure 4.13). Attempts to employ the tin alloyed thin films in usual solar cell architectures only led to below-par efficiencies (under 0.05%), which could be explained by the additional Sn states acting as deep traps for charge carriers. Furthermore, photoluminescence and time-resolved microwave conductivity measurements did not yield any measurable signal, which further reinforces this interpretation. This effect could also arise and be enhanced by the usual strong electron-phonon coupling found in this class of materials.[30] Additionally, valence band XPS measurements reveal a shift of the Fermi level closer to the CB with increasing Sn content (Figure 4.19). This leads to a strongly n-doped nature thus limiting conventional applications in optoelectronic devices with common architectures. An approach to address these issues could be improving the alignment of charge extraction layers or by employing novel concepts such as intermediate band solar cells.[40]

Finally, the stability of the thin films was examined, as rapid degradation and oxidation of Sn in conventional Sn-based perovskite solar cells is a significant problem

hampering potential applications. The corresponding UV-Vis spectroscopy and XRD measurements are shown in Figure 4.19 and 4.20. Strikingly, the thin films show a very high stability when stored in air over weeks and when exposed to high temperatures of up to $125\,^{\circ}\mathrm{C}$, which is highly unusual for materials containing Sn. We attribute this stabilization to the proposed (and favored) tin mixed valence incorporation having a beneficial effect and preventing complete oxidation. When degrading under ambient conditions at $25\,^{\circ}\mathrm{C}$ and 70% RH $SnCl_2$-alloyed films undergo a similar mechanism as regular 2D-$MA_3Sb_2I_9$, partially rearranging to the 0D polymorph first and then dissociating into MAI and diverse oxide phases such as Sb_2O_5, Sb_2O_4 and Sn_3O_4 as shown in Figure 4.21.

4.4 SUMMARY

In conclusion, a facile solution-based synthesis route for the otherwise elusive tin-alloyed layered $MA_3Sb_2I_9$ is presented for the first time. A significant increase in overall optical absorption can be observed, and first-principles calculations show the formation of heteroatom defect states above the valence band. Furthermore, a synthesis approach based on mixed Sn oxidation states in the precursors is described, which leads to the same electronic states compared to a synthesis using only divalent Sn halides. Starting from delocalized valences in the strong-coupling $\mathrm{Sn-I-Sn}$ motif, a model for the additional absorption is suggested based on mixed-valence and defect state absorption. This is used to describe the challenges such heteroatom-alloyed systems face for employment in common optoelectronic devices. Lastly, the thin films are found to show very good stability in ambient conditions which is attributed to self-balancing valences. Collectively, these results can help to achieve enhanced synthetic control and general understanding of the benefits and challenges of heterovalent alloying in lead-free perovskite materials.

4.5 SUPPORTING INFORMATION

4.5.1 Methods

Precursor Solution

To synthesize $\mathrm{Sn:MA_3Sb_2I_9}$, MAI (397.69 mg, 2.5 mmol, 5 eq., Sigma-Aldrich, $\geqslant 99\%$), $\mathrm{Sb(CH_3CO_2)_3}$ (150.00 mg, 0.5 mmol, 1 eq., Sigma-Aldrich, 99.99%) and varying amounts of Sn precursors ($\mathrm{SnI_2}$ (Sigma-Aldrich, $\geq 99\%$), $\mathrm{SnI_4}$ (Sigma-Aldrich, $\geq 99\%$), $\mathrm{SnCl_2}$ (TCI, $\geq$ 97.0%)) were weighed in a $\mathrm{N_2}$-filled glove box and dissolved in N,N-dimethylformamide (500 µL Sigma-Aldrich) to yield a 1 M solution. The percentage addition of Sn refers to the constant amount of $\mathrm{Sb(CH_3CO_2)_3}$ in the solution. (e.g. 10% = 0.05 mmol $\mathrm{SnX_{2/4}}$, 50 % = 0.25 mmol $\mathrm{SnX_{2/4}}$, 100 % = 0.5 mmol $\mathrm{SnX_{2/4}}$. For the mixed samples the amount of substance was divided by two, respectively (100 % = 0.25 mmol $\mathrm{SnX_2}$ + 0.25 mmol $\mathrm{SnX_4}$).

Thin film deposition

For deposition of $\mathrm{Sn:MA_3Sb_2I_9}$, varying substrate types were cleaned with oxygen plasma under vacuum. Glass and fluorine doped tin oxide (FTO) substrates were cleaned at 50% power for 5 min. Indium tin oxide (ITO) and silicon substrates were cleaned at 80 % power for 20 min. 75 µL of the solution was then spin-coated onto the substrates in a nitrogen-filled glove box at 4000 rpm for 3 min and the substrates were annealed at 100 °C for 30 min in nitrogen atmosphere.

X-Ray diffraction

X-ray diffractometry for thin films was recorded on a Bruker D8 Discover operating at 40 kV and 30 mA with Cu-K_α radiation ($\lambda = 1.5406$ Å) and a position-sensitive LynxEye detector. XRD patterns were measured in the range of 5 °2θ to 60 °2θ with a step size of 0.05°. Powders were measured on a STOE STADI P diffractometer with Cu-K_α radiation and a Ge(111) single crystal monochromator equipped with a DECTRIS solid state strip detector MYTHEN 1K, which was used for wide angle X-ray diffraction measurements in transmission mode. Powder patterns were measured in the same range and resolution and a step size between 0.5° and 4° with a counting time of 20 s to 90 s per step. To fit the experimental data, the least-squares method was used as implemented in the EXPO2014

software.[41] The background was modeled by a shifted-Chebyshev function and non-structural parameters were refined with the Le Bail method.[42]

Ultraviolet-Visible Spectroscopy

UV-VIS spectroscopy was conducted with a Perkin Elmer Lambda 1050 UV/VIS/NIR spectrometer equipped with a $150\,\mathrm{nm}$ integrating sphere. A tungsten-halogen and a deuterium lamp were used to create a visible and ultraviolet light spectrum, respectively. For adjustment of discrete wavelengths, a monochromator was employed. The measurement interval was chosen from $350\,\mathrm{nm}$ to $900\,\mathrm{nm}$ with a step size of $2\,\mathrm{nm}$.

Scanning Electron Microscopy

For analysis of the thin film morphology, thickness and composition, SEM was performed on a FEI Helios Nanolab G3 UC-DualBeam scanning electron microscope with an acceleration voltage between $2\,\mathrm{keV}$ to $5\,\mathrm{keV}$.

X-Ray Photoelectron Spectroscopy

Two set-ups were used for the XPS measurements, one in Munich and one in Darmstadt. The regular XPS measurements in the main text were performed with a TA10 X-ray source (Mg-K_α energy) and a VSW HA100 hemispherical analyzer and measured in Munich to assure a controlled sample environment. For sputtering the sample, argon gas with p = $3\,10^{-5}\mathrm{mbar}$ was introduced into the chamber at a voltage of $1\,\mathrm{kV}$ and kept for 20 minutes. The photoelectron peaks were fitted in Igor Pro 6.0.2.4 based on a convolution of a Doniach-Šunjić-function and a Gaussian function, the background was subtracted linearly. All measurements expect noted were carried out on this machine. The second setup is a ThermoFisher VG Escalab 250 spectrometer and was used to acquire valence band data. XPS was performed with a monochromatic Al-K_α source ($1486.6\,\mathrm{eV}$) set at $13\,\mathrm{mA}$ and $15\,\mathrm{kV}$. The pressure inside the analytical chamber was monitored below $10^{\breve{}9}\,\mathrm{mbar}$. The valence band region (12, -2 eV) was acquired with a pass energy of $10\,\mathrm{eV}$ and a step size of $0.05\,\mathrm{eV}$. In this configuration, the instrumental resolution was estimated to $0.35\,\mathrm{eV}$ based on the Fermi edge of a clean Ag foil. The latter was also used for the calibration of the spectra. For the experiment performed in Darmstadt, the samples were prepared, packed under nitrogen atmosphere and shipped from Munich.

Computational Details

DFT calculations have been performed using a $2\times2\times2$ supercell of the undoped $\mathrm{Cs_3Sb_2I_9}$ and the tin-doped $\mathrm{Cs_3Sb_{1.75}Sn_{0.25}I_9}$ perovskite. In all cases, lattice parameters are fixed

to $a = b = 8.661$ and $c = 10.625$, with $\alpha = \beta = 90°$ and $\gamma = 120°$.[43] We chose Cs as A-site cation instead of methylammonium (MA) due to the low impact of the A-site on the conduction and valence bands.

Hybrid functional PBE0 calculations have been performed for geometry optimization using the freely available CP2K software package,[44] keeping the Fock exchange α at 0.25 and including van der Waals interactions with the DFT-D3 scheme including Becke-Johnson damping.[45] Kohn-Sham orbitals are expanded in a double-zeta basis set (DZVP-MOLOPT)[46] in combination with the norm-conserving Goedecker-Teter-Hutter (GTH)[47] pseudopotentials, and a cutoff of $300\,\mathrm{Ry}$ for expansion of the electron density in plane waves. The auxiliary density matrix method with the cFIT auxiliary basis set was applied to accelerate the optimization of ionic positions within hybrid functional calculations.[48]

Electronic structure calculations on the optimized geometries were performed using the HSE06 functional[49] including spin-orbit coupling and DFT-D3 dispersion corrections[50] within the Quantum Espresso package.[51] We used full relativistic norm-conserving pseudopotentials (Sn, 22 electrons, $4s^2$, $4p^6$, $4d^10$, $5d^2$, $5p^2$; Sb, 15 electrons, $4d^{10}$, $5s^2$, $5p^3$; I, 7 electrons, $5s^2$, $5p^5$; Cs, 9 electrons, $5s^2$, $5p^6$, $6s^1$) with a cutoff on the wave functions of $40\,\mathrm{Ry}$ and $80\,\mathrm{Ry}$ on the Fock grid, an increased fraction of exact exchange in the HSE06 functional of $\alpha = 0.43$ and sampling the Brillouin zone at the gamma point. PDOS plots have been generated with a Gaussian smearing of $0.1\,\mathrm{eV}$. Bader charges in the Sn-doped structures were characterized using the code of Henkelman et al.[52] DFE and TIL were calculated as follows:[53]

$$DFE[X^q] = E[X^q] - E[prist] - \sum_i n_i\mu_i + q(E_{VBM} + E_F) \tag{4.1}$$

$$TIL[q/q^{'}] = \frac{DFE[X^q] - DFE[X^{q'}]}{q^{'} - q} \tag{4.2}$$

where $E[X^q]$ is the energy of the defective supercell with defect X in charge state q, $E[prist]$ is the energy of the pristine supercell, n_i and μ_i are the number and chemical potential of the added and subtracted species, respectively, E_{VBM} and E_F are the valence band energy and the Fermi energy, respectively, and E^q_{corr} are electrostatic potential corrections due to the finite size of the supercell. Electrostatic finite-size effects have been accounted for using the Freysoldt-Neugebauer-Van de Walle approach as implemented in the sxdefectalign code.[54]

4.5.2 Supplementary Data

Structural Properties & XRD

Figure 4.9a depicts thin films alloyed with only 10% Sn precursor and the asterisks show the pronounced MAI side phase in all the alloyed thin films, highlighting the need for a high concentration of Sn halides to obtain phase purity. In Figure 4.9b a zoom on the relevant 003/221 reflex is shown, which highlights the enlargement of all unit cell axes.

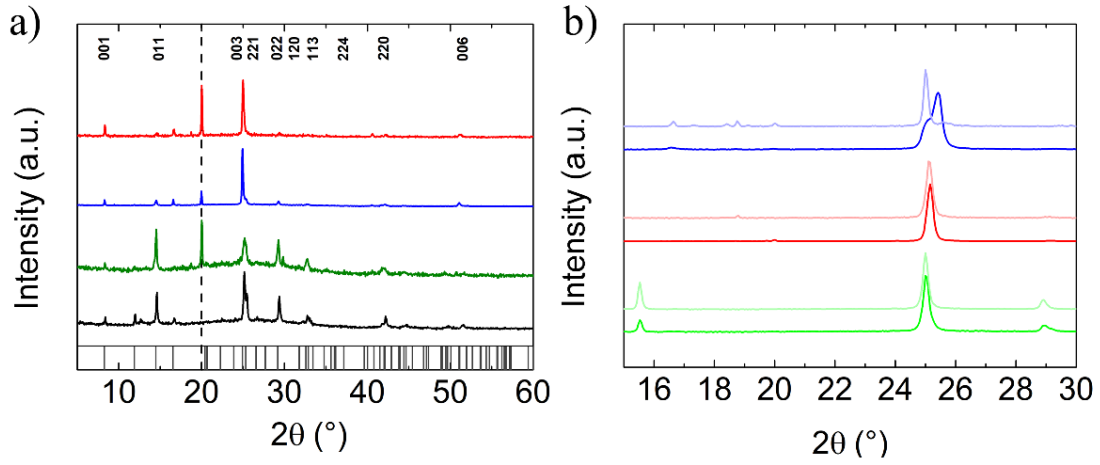

Figure 4.9: XRD patterns of (a) Sn : $MA_3Sb_2I_9$ films with 10% Sn precursors and (b) zoom on the relevant (003) reflection of 50% (light color) and 100% Sn-alloyed thin films for chloride (green), iodide (blue), mixed valence iodide (red) and the pure control (black).

The unit cell parameters in Table 4.1 were calculated via the following equation based on the hexagonal unit cell:

(003) 2θ (°)/c axis length [Å]	10%	50%	100%
+ $SnCl_2$	25.19/10.60	25.01/10.67	24.99/10.68
+ SnI_2	25.19/10.60	25.13/10.62	25.11/10.63
+ SnI_2/+ SnI_4	25.19/10.60	25.07/10.65	25.01/10.67
(011) 2θ (°)/a(b) axis length [Å]	10%	50%	100%
+ $SnCl_2$	14.60/8.53	14.38/8.70	14.36/8.71
+ SnI_2	14.60/8.53	14.46/8.65	14.45/8.65
+ SnI_2/SnI_4	14.60/8.53	14.52/8.58	14.42/8.66

Table 4.1: Unit cell parameters.

The parameters for the Rietveld refinement as shown in the main text are seen in Table 4.2.

	80% $SnCl_2$	80% SnI_2	80% SnI_2/SnI_4
R_p	4.06	5.13	4.69
R_{wp}	5.42	7.18	6.57
R_e	2.64	2.76	2.71
χ^2	4.21	6.76	5.86
a (=b) [Å]	8.60	8.67	8.63
c [Å]	10.72	10.65	10.69

Table 4.2: Rietveld refinement fit parameters.

Optical Properties

The absorbance was calculated starting from the measured thin film transmission via the following equation:

$$A = 2 - \log(\%T) \tag{4.3}$$

Absorbance data near the band edge for the reference material were fitted with a least-squares approach via Elliott's method with added thermal broadening as described by D'Innocenzo et al, shown in the following.[55]

$$\begin{aligned}\alpha(\nu) = \alpha_0^{3D}\Bigg[\sum_{n=1}^{\infty}\frac{4\pi E_b^{3/2}}{n^3}sech\left(\frac{h\nu - E_g - \frac{E_b}{n^2}}{\Gamma}\right) \\ + \int_{E_g}^{\infty} sech\left(\frac{h\nu-\epsilon}{\Gamma}\right)\frac{2\pi\sqrt{E_b}}{1-e^{-2\pi\sqrt{\frac{E_b}{h\nu-E_g}}}}\frac{1}{1-b(\epsilon-E_g)}d\epsilon\Bigg]\end{aligned} \tag{4.4}$$

To fit the absorbance in the bandgap, a simple Urbach fit as shown in equation 4.5 was employed (with α_0 and E_1 being fitting parameters and E_0 the Urbach energy).[26,27]

$$\alpha(E) = \alpha_0 \exp\frac{E - E_1}{E_0} \tag{4.5}$$

The absorbance data for the different samples and the corresponding transmission and reflection plots are shown in Figure 4.10.

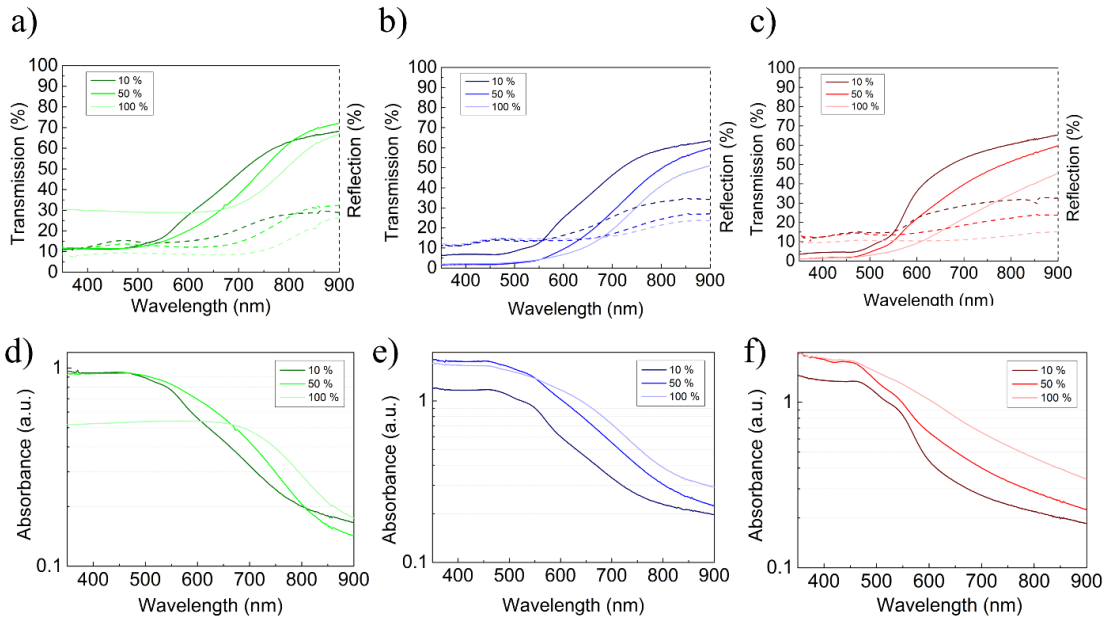

Figure 4.10: a-c) Transmission and reflection data for $MA_3Sb_2I_9$ thin films with different amounts of Sn precursor. (d-f) Corresponding absorbance data plotted logarithmically for chloride (green), iodide (blue), and mixed valence iodide precursors (red).

From the logarithmic plot of the absorbance data, the characteristic shape of the absorbance for Sn-doped $MA_3Sb_2I_9$ can be seen with the approximately three linear contributions, represented as gaussian functions in the main text. The absence of a PL signal is illustrated in Figure 4.12, measured with a $405\,nm$ excitation laser.

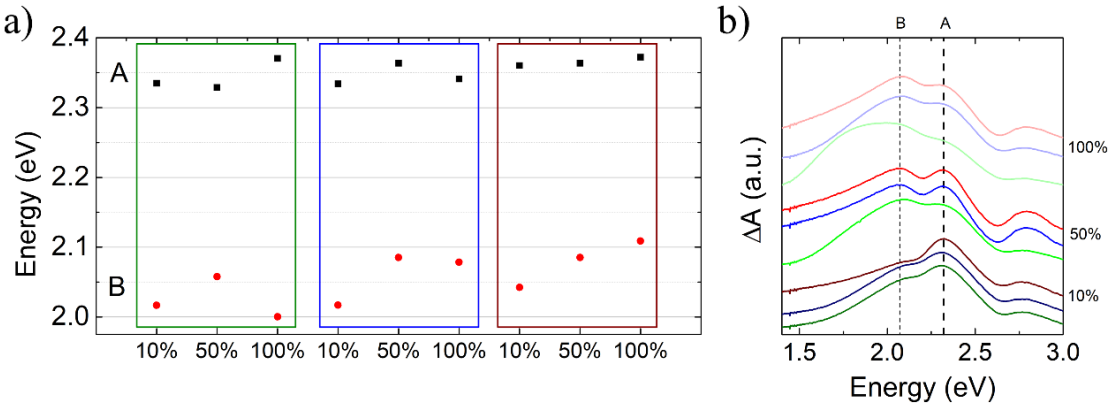

Figure 4.11: Fitting parameters for contribution A and B over all samples (a) and absorbance difference for all samples (b).

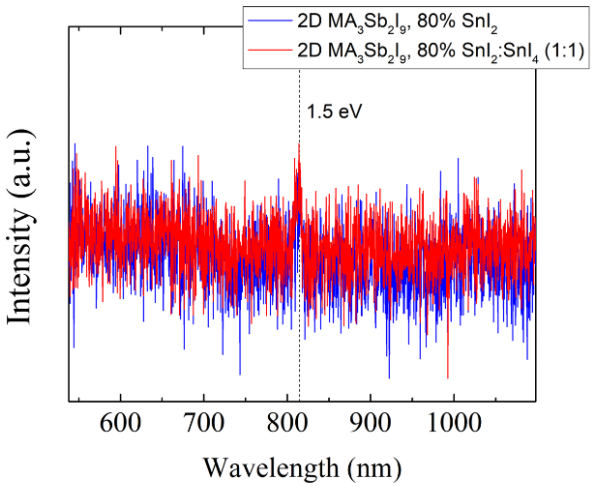

Figure 4.12: Room temperature PL spectra of $MA_3Sb_2I_9$ thin films with different Sn iodide precursors.

DFT Calculations

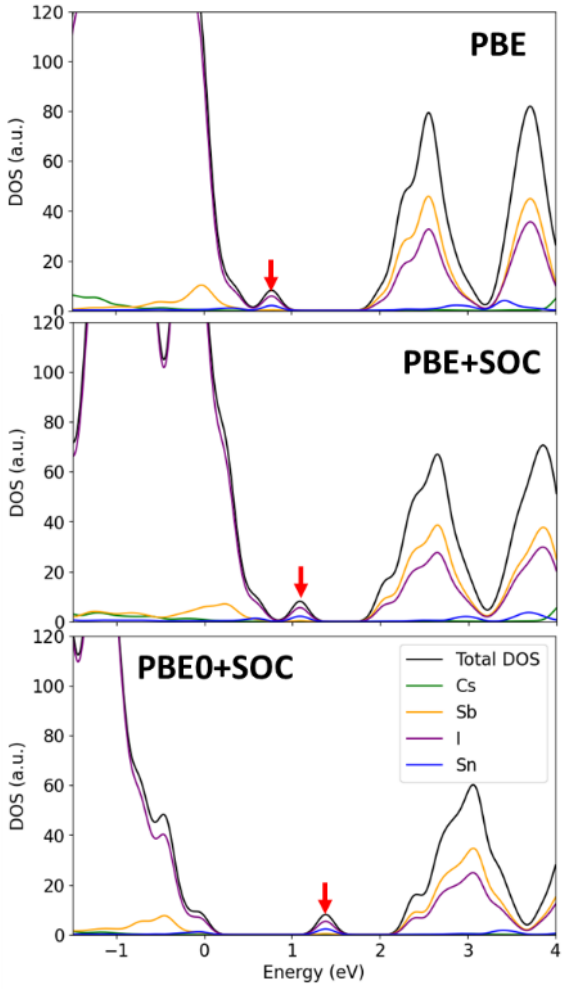

Figure 4.13: Density of states of the $Cs_3Sb_{1.75}Sn_{0.25}I_9$ $2\times2\times2$ supercell in 0 charge state, mimicking Sn(II)/Sn(IV) heterovalent doping, obtained from DFT calculations based on the (top) PBE functional without spin-orbit coupling and (mid) with spin-orbit coupling (SOC). The lower panel gives the density of states obtained from the PBE0 functional with original Fock exchange of 25% and SOC. The red arrow visualizes the position of the Sn(IV) $5s$ orbitals in each panel.

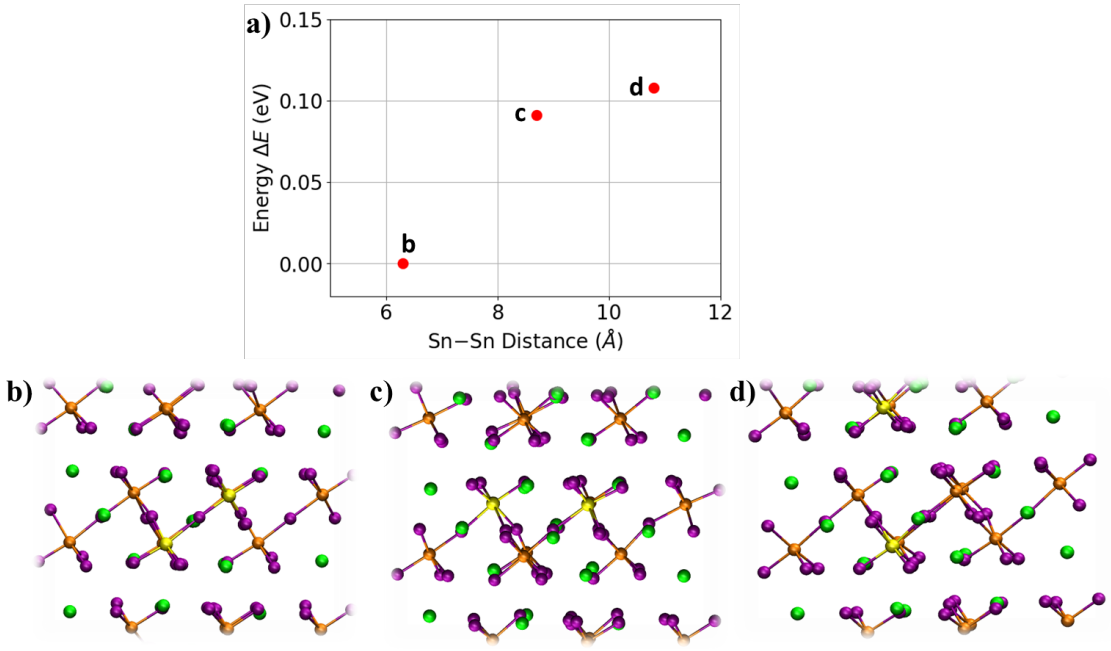

Figure 4.14: (a) Relative energy of the $Cs_3Sb_{1.75}Sn_{0.25}I_9$ $2 \times 2 \times 2$ supercell in 0 charge state, mimicking Sn(II)/Sn(IV) heterovalent doping, as function of the $Sn - Sn$ distance.; (b) to (d) visualize the optimized structures, with Sn represented by yellow balls.

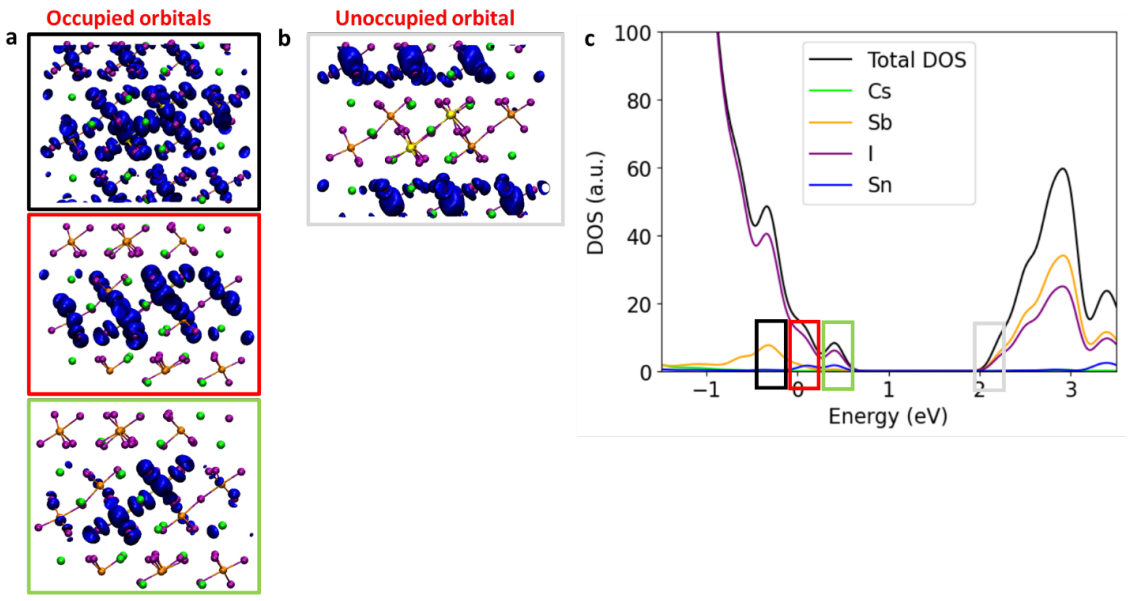

Figure 4.15: Electronic structure of the $Cs_3Sb_{1.75}Sn_{0.25}I_9$ $2 \times 2 \times 2$ supercell in -2 charge state; (a) and (b) visualize the occupied and unoccupied molecular orbitals. (c) Projected density of states of the $Cs_3Sb_{1.75}Sn_{0.25}I_9$ $2 \times 2 \times 2$ supercell in -2 charge state, with both tin ions being in II oxidation state. The colored rectangles indicate the respective region in the DOS used for the isodensity orbital plots in panels a and b. Bader charges of the Sn ions are $+0.99$ and $+1.00$.

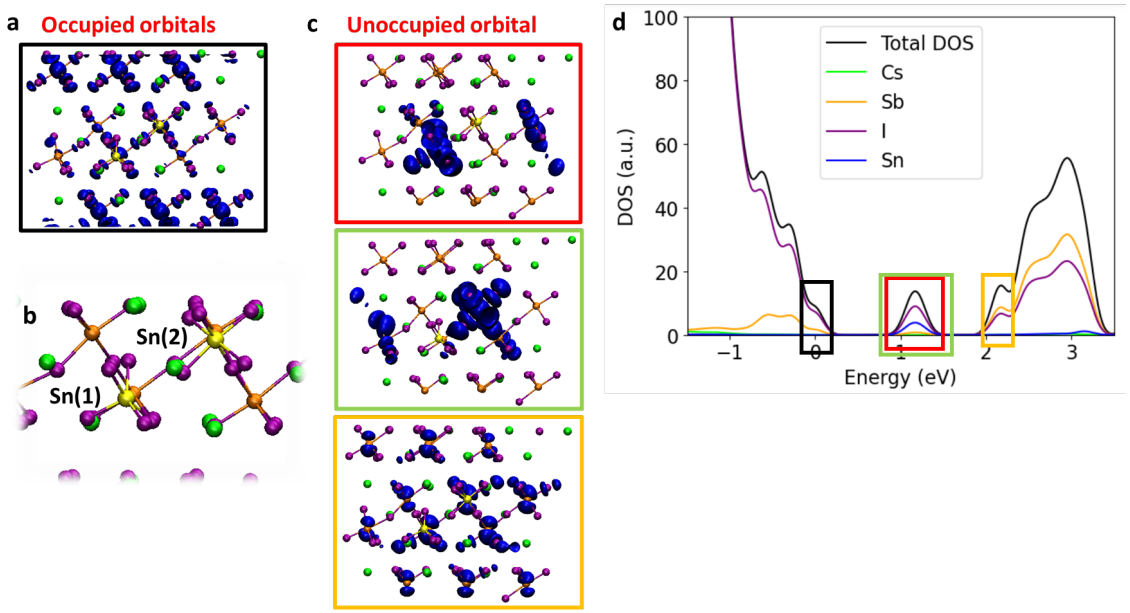

Figure 4.16: Electronic structure of the $Cs_3Sb_{1.75}Sn_{0.25}I_9$ $2 \times 2 \times 2$ supercell in $+2$ charge state; (a) and (c) visualize the occupied and unoccupied molecular orbitals. (b) Geometry representation of the $Sn_{Sb} - Sn_{Sb}$ pair. Bader charges of the Sn ions are $+1.23$ (Sn(1)) and +1.28 (Sn(2)), indicating that both Sn ions are in oxidation state +IV. (d) Projected density of states of the $Cs_3Sb_{1.75}Sn_{0.25}I_9$ $2 \times 2 \times 2$ supercell in $+2$ charge state, with both tin ions being in +IV oxidation state. The colored rectangles indicate the respective region in the DOS used for the isodensity orbital plots in panels a and c.

XPS & Electronic Structure

The overview spectra of the 100% alloyed iodide samples as seen in the main text can be seen in Figure 4.17a Furthermore, the Sb and Sn spectra of the unsputtered ones are shown in 4.17b and 4.17c, showcasing only minor change with respect to the data shown in the main text.

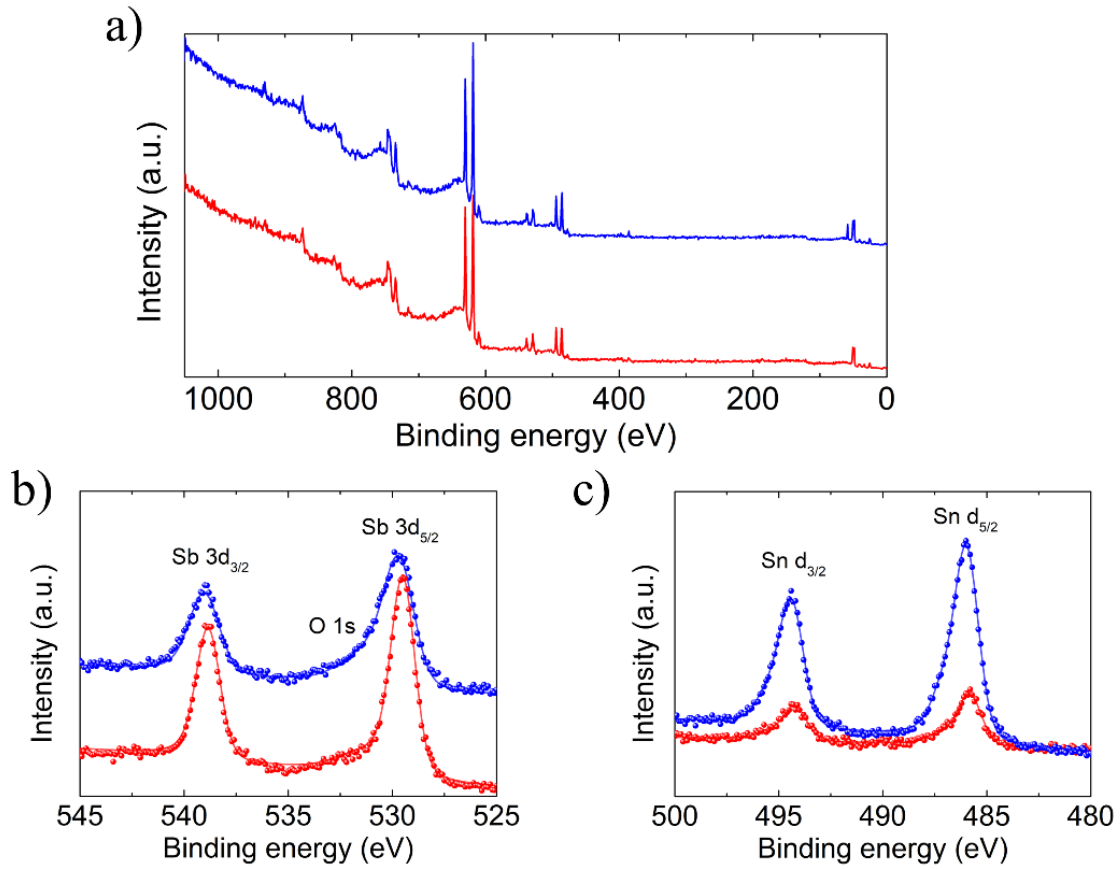

Figure 4.17: (a) Overview XPS spectra of Ar sputtered thin films prepared with 100% iodide and mixed valent iodide precursors (blue, red). Sb 3*d* (b) and Sn 3*d* (c) spectra with fits for unsputtered films.

XPS data of surface oxidized thin films can be seen in Figure 4.18 and showcases a distinct difference between Sn(II) and Sn(IV) species, strengthening the assumption that no defined mixed valent incorporation is taking place.

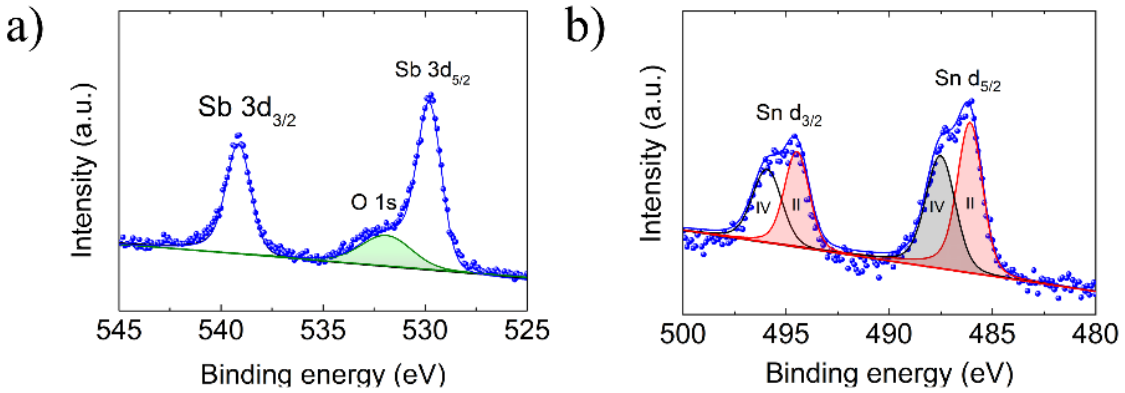

Figure 4.18: Sb 3*d* (a) and Sn *d* (b) spectra with fits for a surface oxidized film.

Tables 4.8 showcase the atomic ratios found in all XPS measurements discussed in the main text and of the degraded samples, highlighting the incorporation of tin.

Table 4.3: XPS elemental ratios of an $MA_3Sb_2I_9$ thin film prepared with 100% SnI_2 without Ar sputtering.

Sn tot	Sn +II	Sn +IV	Sb	I
	87%	13%		
53%			48%	
16%				84%
			15%	85%

Table 4.4: XPS elemental ratios of an $MA_3Sb_2I_9$ thin film prepared with 100% SnI_2 with Ar sputtering.

Sn tot	Sn +II	Sn +IV	Sb	I
	99%	1%		
63%			37%	
26%				74%
			17%	83%

Table 4.5: XPS elemental ratios of an $MA_3Sb_2I_9$ thin film prepared with 100% SnI_2/SnI_4 without Ar sputtering.

Sn tot	Sn +II	Sn +IV	Sb	I
	86%	14%		
18%			82%	
4%				96%
			15%	85%

Table 4.6: XPS elemental ratios of an $MA_3Sb_2I_9$ thin film prepared with 100% SnI_2/SnI_4 with Ar sputtering.

Sn tot	Sn +II	Sn +IV	Sb	I
	95%	5%		
61%			39%	
20%				80%
			14%	86%

Table 4.7: XPS elemental ratios of an $MA_3Sb_2I_9$ thin film prepared with 100% SnI_2 after oxidation in air over 2 days.

Sn tot	Sn +II	Sn +IV	Sb	I
	49%	51%		
34%			66%	
9%				91%
			17%	83%

Table 4.8: XPS elemental ratios of different $MA_3Sb_2I_9$ thin films.

Valence band XPS data (measured on the ThermoFisher VG Escalab 250 spectrometer) are shown in Figure 4.19 for thin films prepared with tin chloride precursor to quantify the incorporation of Sn in combination with chloride anions. Fitting of the VB states was performed following the methodology detailed in.[56] The trend in the contributions I and II can be explained with the DOS being mostly made up of Sb in I and Sn in II (4.19a,d). Figure 4.19c shows the increase in Fermi level when increasing the Sn content in the structure.

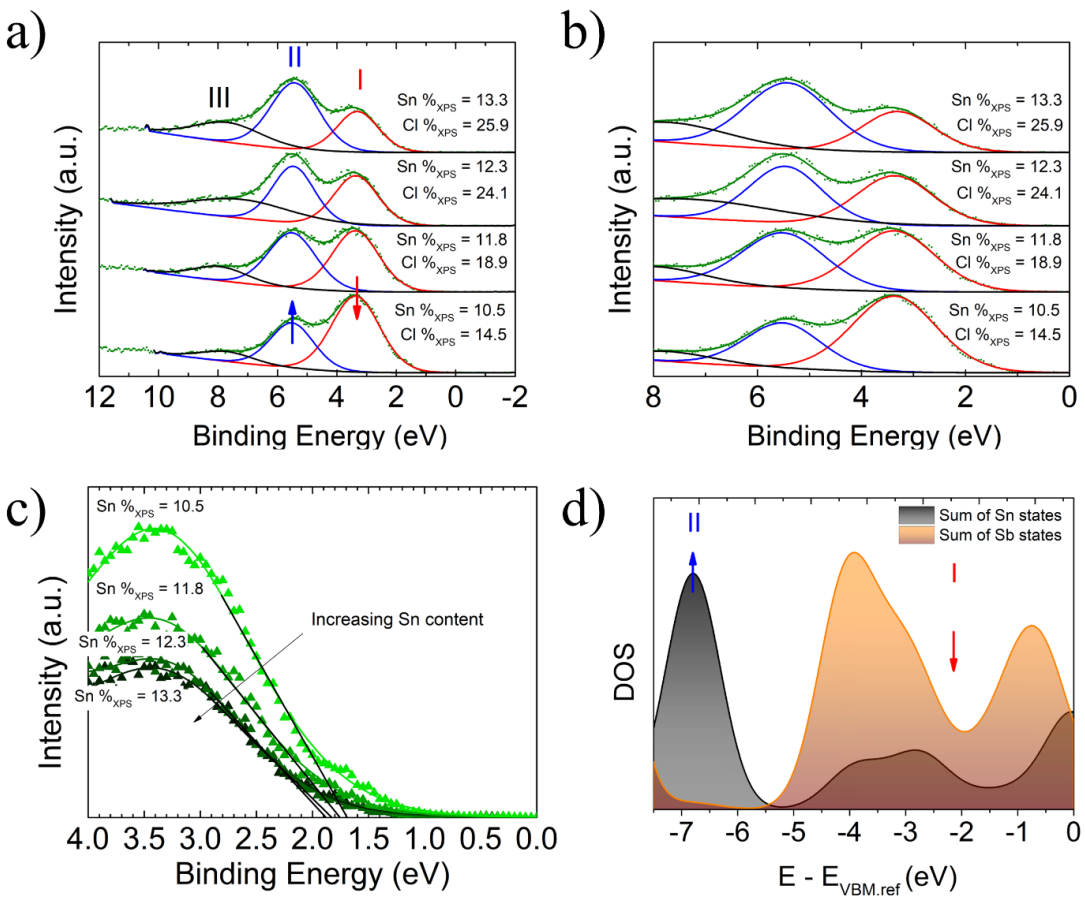

Figure 4.19: (a-c) Valence band XPS spectra for thin films doped with $SnCl_2$. (d) Highly broadened (σ = 0.1) density of states showing only antimony and tin contributions.

Stability

XRD and UV-Vis measurements for different conditions and for different precursors are shown in Figure 4.20 and 4.21. We note that the stability appears to be consistent throughout all samples, independent of precursors. For the temperature-dependent measurements, the thin films were kept at the specified temperature for 5 minutes and were then measured. If compared to Figure 4.21a, we can see the strong stabilizing effect of Sn in the system.

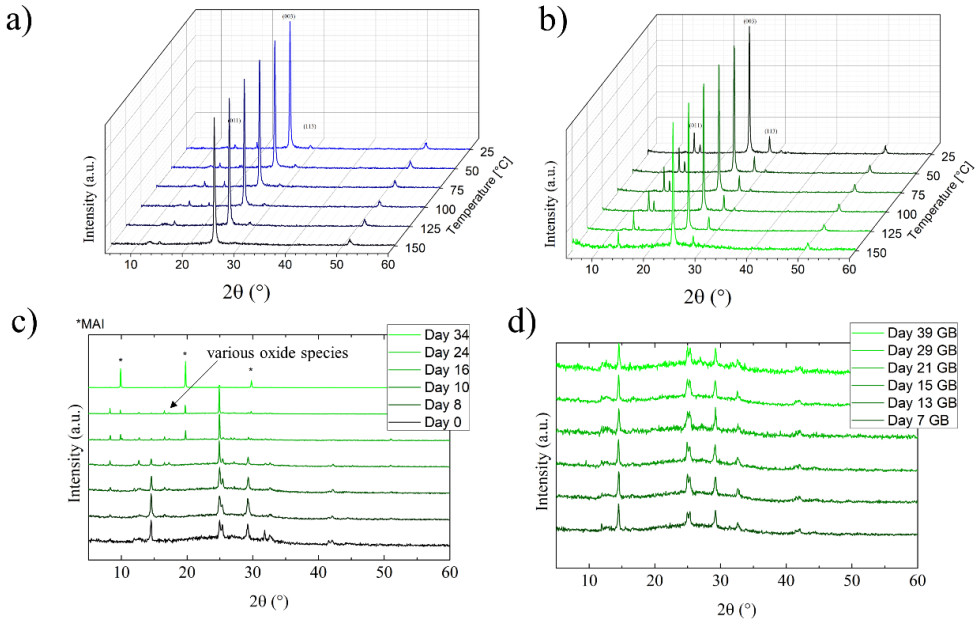

Figure 4.20: XRD measurements at varying temperature (a) for 100% SnI_2 precursors and (b) for 100% $SnCl_2$ precursor. (c) & (d) Thin film XRD measurements of 50% $SnCl_2$ alloyed thin films in ambient atmosphere and in the glove box (GB), respectively. The darkest green lines without legend refer to the reference film.

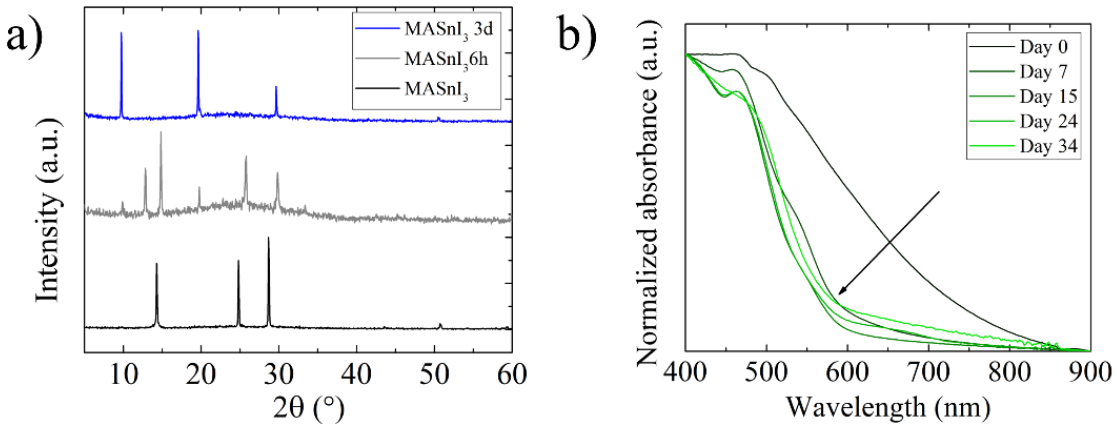

Figure 4.21: (a) Degradation of pure $MASnI_3$ thin films after 3d and (b) UV-Vis spectra of a 40% $SnCl_2$ prepared thin film over the course of one month.

4.6 REFERENCES

[1] L. Schmidt-Mende et al., *APL Materials* **2021**, *9*, doi: 10.1063/5.0047616, 109202.

[2] J. Jeong, M. Kim, J. Seo, H. Lu, P. Ahlawat, A. Mishra, Y. Yang, M. A. Hope, F. T. Eickemeyer, M. Kim, Y. J. Yoon, I. W. Choi, B. P. Darwich, S. J. Choi, Y. Jo, J. H. Lee, B. Walker, S. M. Zakeeruddin, L. Emsley, U. Rothlisberger, A. Hagfeldt, D. S. Kim, M. Grätzel, J. Y. Kim, *Nature* **2021**, *592*, 381–385.

[3] A. Kojima, K. Teshima, Y. Shirai, T. Miyasaka, *Journal of the American Chemical Society* **2009**, *131*, 6050–6051.

[4] A. M. Ganose, C. N. Savory, D. O. Scanlon, *Chemical Communications* **2017**, *53*, 20–44.

[5] A. Babayigit, A. Ethirajan, M. Muller, B. Conings, *Nature Materials* **2016**, *15*, 247.

[6] F. Igbari, Z.-K. Wang, L.-S. Liao, *Advanced Energy Materials* **2019**, 1803150.

[7] M.-G. Ju, J. Dai, L. Ma, X. C. Zeng, *Journal of the American Chemical Society* **2017**, *139*, 8038–8043.

[8] W. Kaiser, D. Ricciarelli, E. Mosconi, A. A. Alothman, F. Ambrosio, F. De Angelis, *The Journal of Physical Chemistry Letters* **2022**, *13*, doi: 10.1021/acs.jpclett.2c00273, 2321–2329.

[9] L. Lanzetta, T. Webb, N. Zibouche, X. Liang, D. Ding, G. Min, R. J. E. Westbrook, B. Gaggio, T. J. Macdonald, M. S. Islam, S. A. Haque, *Nature Communications* **2021**, *12*, 2853.

[10] W. Tress, M. T. Sirtl, *Solar RRL* **2022**, *6*, https://doi.org/10.1002/solr.202100770, 2100770.

[11] M. T. Sirtl, F. Ebadi, B. T. van Gorkom, P. Ganswindt, R. A. J. Janssen, T. Bein, W. Tress, *Advanced Optical Materials* **2021**, *9*, https://doi.org/10.1002/adom.202100202, 2100202.

[12] C. N. Savory, A. Walsh, D. O. Scanlon, *ACS Energy Letters* **2016**, *1*, 949–955.

[13] K. Momma, F. Izumi, *Journal of Applied Crystallography* **2011**, *44*, 1272–1276.

[14] P. Karuppuswamy, K. M. Boopathi, A. Mohapatra, H.-C. Chen, K.-T. Wong, P.-C. Wang, C.-W. Chu, *Nano Energy* **2018**, *45*, 330–336.

[15] N. Giesbrecht, A. Weis, T. Bein, *Journal of Physics: Energy* **2020**, *2*, 024007.

[16] S. Chatterjee, A. J. Pal, *ACS Applied Materials & Interfaces* **2018**, *10*, 35194–35205.

[17] D. Ju, X. Jiang, H. Xiao, X. Chen, X. Hu, X. Tao, *Journal of Materials Chemistry A* **2018**, *6*, 20753–20759.

[18] C. J. Krajewska, S. R. Kavanagh, L. Zhang, D. J. Kubicki, K. Dey, K. Gałkowski, C. P. Grey, S. D. Stranks, A. Walsh, D. O. Scanlon, R. G. Palgrave, *Chemical Science* **2021**, *12*, 14686–14699.

[19] K.-z. Du, W. Meng, X. Wang, Y. Yan, D. B. Mitzi, *Angewandte Chemie International Edition* **2017**, *56*, https://doi.org/10.1002/anie.201703970, 8158–8162.

[20] F. Jiang, D. Yang, Y. Jiang, T. Liu, X. Zhao, Y. Ming, B. Luo, F. Qin, J. Fan, H. Han, L. Zhang, Y. Zhou, *Journal of the American Chemical Society* **2018**, *140*, 1019–1027.

[21] H. M. Rietveld, *Journal of Applied Crystallography* **1969**, *2*, 65–68.

[22] K. Yamada, H. Sera, S. Sawada, H. Tada, T. Okuda, H. Tanaka, *Journal of Solid State Chemistry* **1997**, *134*, 319–325.

[23] R. Shannon, *Acta Crystallographica Section A* **1976**, *32*, 751–767.

[24] V. D'Innocenzo, G. Grancini, M. J. P. Alcocer, A. R. S. Kandada, S. D. Stranks, M. M. Lee, G. Lanzani, H. J. Snaith, A. Petrozza, *Nature Communications* **2014**, *5*, 3586.

[25] R. J. Elliott, *Physical Review* **1957**, *108*, PR, 1384–1389.

[26] F. Urbach, *Physical Review* **1953**, *92*, PR, 1324–1324.

[27] M. Ledinsky, T. Schönfeldová, J. Holovský, E. Aydin, Z. Hájková, L. Landová, N. Neyková, A. Fejfar, S. De Wolf, *The Journal of Physical Chemistry Letters* **2019**, *10*, 1368–1373.

[28] B. Subedi, C. Li, C. Chen, D. Liu, M. M. Junda, Z. Song, Y. Yan, N. J. Podraza, *ACS Applied Materials & Interfaces* **2022**, *14*, 7796–7804.

[29] B. J. Bohn, T. Simon, M. Gramlich, A. F. Richter, L. Polavarapu, A. S. Urban, J. Feldmann, *ACS Photonics* **2018**, *5*, doi: 10.1021/acsphotonics.7b01292, 648–654.

[30] K. M. McCall, C. C. Stoumpos, S. S. Kostina, M. G. Kanatzidis, B. W. Wessels, *Chemistry of Materials* **2017**, *29*, doi: 10.1021/acs.chemmater.7b01184, 4129–4145.

[31] A. Amat, E. Mosconi, E. Ronca, C. Quarti, P. Umari, M. K. Nazeeruddin, M. Grätzel, F. De Angelis, *Nano Letters* **2014**, *14*, doi: 10.1021/nl5012992, 3608–3616.

[32] M. A. Pérez-Osorio, R. L. Milot, M. R. Filip, J. B. Patel, L. M. Herz, M. B. Johnston, F. Giustino, *The Journal of Physical Chemistry C* **2015**, *119*, 25703–25718.

[33] D. Meggiolaro, D. Ricciarelli, A. A. Alasmari, F. A. Alasmary, F. De Angelis, *The Journal of Physical Chemistry Letters* **2020**, *11*, 3546–3556.

[34] D. Ricciarelli, D. Meggiolaro, F. Ambrosio, F. De Angelis, *ACS Energy Letters* **2020**, *5*, doi: 10.1021/acsenergylett.0c01174, 2787–2795.

[35] H. Raebiger, S. Lany, A. Zunger, *Nature* **2008**, *453*, 763–766.

[36] G. M. Dalpian, Q. Liu, C. C. Stoumpos, A. P. Douvalis, M. Balasubramanian, M. G. Kanatzidis, A. Zunger, *Physical Review Materials* **2017**, *1*, PRMATERIALS, 025401.

[37] T. Hellmann, M. Wussler, C. Das, R. Dachauer, I. El-Helaly, C. Mortan, T. Mayer, W. Jaegermann, *Journal of Materials Chemistry C* **2019**, *7*, 5324–5332.

[38] M. B. Robin, P. Day in *Advances in Inorganic Chemistry and Radiochemistry*, *Vol. 10*, (Eds.: H. J. Emeléus, A. G. Sharpe), Academic Press, **1968**, pp. 247–422.

[39] M. Parthey, M. Kaupp, *Chemical Society Reviews* **2014**, *43*, 5067–5088.

[40] Y. Okada, N. J. Ekins-Daukes, T. Kita, R. Tamaki, M. Yoshida, A. Pusch, O. Hess, C. C. Phillips, D. J. Farrell, K. Yoshida, N. Ahsan, Y. Shoji, T. Sogabe, J. F. Guillemoles, *Applied Physics Reviews* **2015**, *2*, 021302.

[41] A. Altomare, M. Camalli, C. Cuocci, C. Giacovazzo, A. Moliterni, R. Rizzi, *Journal of Applied Crystallography* **2009**, *42*, 1197–1202.

[42] A. Le Bail, *Powder Diffraction* **2005**, *20*, 316–326.

[43] B. Saparov, F. Hong, J.-P. Sun, H.-S. Duan, W. Meng, S. Cameron, I. G. Hill, Y. Yan, D. B. Mitzi, *Chemistry of Materials* **2015**, *27*, 5622–5632.

[44] J. VandeVondele, M. Krack, F. Mohamed, M. Parrinello, T. Chassaing, J. Hutter, *Computer Physics Communications* **2005**, *167*, 103–128.

[45] A. D. Becke, E. R. Johnson, *The Journal of Chemical Physics* **2005**, *122*, doi: 10.1063/1.1884601, 154104.

[46] J. VandeVondele, J. Hutter, *The Journal of Chemical Physics* **2007**, *127*, doi: 10.1063/1.2770708, 114105.

[47] S. Goedecker, M. Teter, J. Hutter, *Physical Review B* **1996**, *54*, PRB, 1703–1710.

[48] M. Guidon, J. Hutter, J. VandeVondele, *Journal of chemical theory and computation* **2010**, *6*, 2348–2364.

[49] J. Heyd, G. E. Scuseria, M. Ernzerhof, *The Journal of Chemical Physics* **2003**, *118*, doi: 10.1063/1.1564060, 8207–8215.

[50] S. Grimme, J. Antony, S. Ehrlich, H. Krieg, *The Journal of Chemical Physics* **2010**, *132*, doi: 10.1063/1.3382344, 154104.

[51] P. Giannozzi, S. Baroni, N. Bonini, M. Calandra, R. Car, C. Cavazzoni, D. Ceresoli, G. L. Chiarotti, M. Cococcioni, I. Dabo, et al., *Journal of physics: Condensed matter* **2009**, *21*, 395502.

[52] W. Tang, E. Sanville, G. Henkelman, *Journal of Physics: Condensed Matter* **2009**, *21*, 084204.

[53] D. Meggiolaro, F. De Angelis, *ACS Energy Letters* **2018**, *3*, doi: 10.1021/acsenergylett.8b01212, 2206–2222.

[54] C. Freysoldt, J. Neugebauer, C. G. Van de Walle, *Physical review letters* **2009**, *102*, 016402.

[55] V. D'innocenzo, G. Grancini, M. J. Alcocer, A. R. S. Kandada, S. D. Stranks, M. M. Lee, G. Lanzani, H. J. Snaith, A. Petrozza, *Nature communications* **2014**, *5*, 3586.

[56] C. Maheu, L. Cardenas, E. Puzenat, P. Afanasiev, C. Geantet, *Physical Chemistry Chemical Physics* **2018**, *20*, 25629–25637.

Stability and Performance of (Cu/Ag)-Sb-I Rudorffite Thin Films for Photovoltaic Applications 5

This chapter is based on following manuscript:
A. Weis, R. Hooijer, W. Kaiser, A. Biewald, P. Dörflinger, C. Maheu, O. Arsatiants, D. Helminger, V. Dyakonov, A. Hartschuh, E. Mosconi, F. De Angelis, T. Bein, *in submission* **2023**

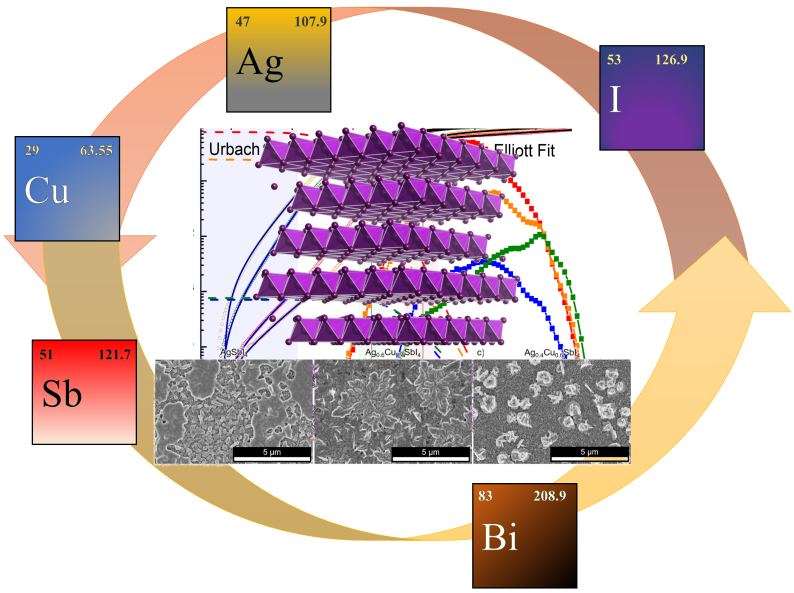

5.1 ABSTRACT

In the search for lead-free perovskites, silver pnictohalides recently gained attention as novel perovskite-inspired materials for photovoltaics due to their high stability, low toxicity and promising early efficiencies, especially for indoor applications. Recent research on such "rudorffites" mainly addresses silver bismuth iodides (Ag-Bi-I), while their antimony analogs are hardly investigated due to intrinsic challenges in the synthesis of Sb-based thin films. Here, we establish a synthetic route to prepare Ag-Sb-I thin films by employing thiourea as Lewis-base additive. Thin film morphologies were further optimized by alloying with Cu, resulting in improved power conversion efficiencies of 0.7% by reducing undesired side phases. Density functional theory calculations and optical characterization methods support the incorporation of Cu into a $Cu_{1-x}Ag_xSbI_4$ phase, keeping the stochiometry and band gap virtually unchanged upon alloying. Our results further reveal the detrimental role of Ag point defects representing trap states in the band gap, being responsible for low open-circuit voltages and sub gap absorption and emission features. Moreover, additional minor amounts of Bi are shown to boost efficiency and stabilize the performance over a wider compositional range. Despite the remaining challenges regarding device performances, we demonstrate a strong increase in external quantum efficiency when reducing the light intensity, highlighting the potential of Ag-Sb-I rudorffites for indoor photovoltaics.

5.2 INTRODUCTION

Lead-halide perovskites have drawn enormous interest for optoelectronics applications, particularly photovoltaics, from industry and research alike. Still, the practical applications of these materials remain limited by their notorious instability coupled with the high toxicity of the constituents and degradation products.[1–3] Nonetheless, through the recent upsurge of emerging semiconducting materials, the focus of photovoltaic research has greatly shifted from purely inorganic materials such as silicon or CIGS with high energy demands for production to novel compounds that combine favorable optoelectronic properties with remarkable defect tolerance, in combination with low-temperature solution syntheses.[4–8]

Starting from the prototypical methylammonium lead iodide, $MAPbI_3$, a classical strategy to circumvent the toxicity issues is homovalent or heterovalent substitution of the central lead atom while retaining the perovskite structure. This is commonly achieved

through elements with the same ns^2 electronic configuration, as this was repeatedly suggested to be the basis of the exceptional defect tolerance in lead-halide perovskites.[9–11] An obvious and intensely studied candidate for substitution is the group IV neighbor tin, which was shown to be both efficient and less problematic than lead in terms of environmental impact.[12,13] Nonetheless, $\mathrm{MASnI_3}$ and other $\mathrm{Sn(II)}$ based compounds are highly sensitive towards oxidation, requiring pure precursor chemicals and non-oxidizing solvents, which still hampers the successful implementation of these materials.[14–17] Alternative approaches combine adjacent elements of tin and lead in the periodic table, namely trivalent antimony(III) and bismuth(III), which still showcase the characteristic electronic ns^2 configuration, with monovalent cations like silver and copper, as prominently seen and studied in the archetype double-perovskite $\mathrm{Cs_2AgBiBr_6}$.[18,19] Although this compound exhibits several promising properties like long charge carrier lifetime and high environmental stability, the photovoltaic efficiency is bottlenecked by rapid non-radiative recombination and a large bandgap.[18–20]

If the monovalent metal ion is omitted entirely in the above systems, the original perovskite structure is sacrificed, leading to another class of perovskite-derived materials with the general structural formula $\mathrm{A_3B_2X_9}$, which also suffer from detrimental factors such as high exciton binding energies, strong exciton-phonon coupling and low dimensionality, among others. Herein, the A-site cations are mostly derived from the lead-based perovskite counterparts, namely methylammonium, formamidinium or cesium(I). Many reports have already shown the significant influence of this cation, not only on the electronic properties but also as structure templating agent.[21,22]

Most recently, a new class of $\mathrm{(Sb/Bi)}$-based materials has emerged, with the accompanying monovalent A cations being silver and/or copper, featuring the general structural formula $\mathrm{A_xB_yX_{x+3y}}$ and straying even further away from the original perovskite lattice. These compounds were coined "rudorffites"[23] in previous reports and are comprised of interconnected $\mathrm{[A/B]X_6}$ octahedra, where the A and B cations share equivalent lattice positions, thereby inducing a high degree of stoichiometric freedom. Notably, these pnictohalides show favorable bandgaps for single-junction solar cell devices and high absorption coefficients.[23,24] The hitherto published materials are mostly based on $\mathrm{Ag\text{-}Bi\text{-}I}$ and were shown to already surpass 5 % PCE within only a couple of years' time.[25] Moreover, rudorffites were also employed successfully in other types of devices like X-ray detectors,[26] memristors[27] or, as of latest, as highly efficient indoor light harvesters,[28,29] competing with commercial solar cells in this field. Alloying and substituting Ag with Cu was also shown to be an efficient way to tailor their structural and electronic properties.[28,29]

While research efforts to date have been mostly focused on Bi-based rudorffite structures,

only few reports concerning pure $(\mathrm{Ag/Cu})$-Sb-I materials can be found, some of which being inconclusive about important properties like color, bandgap and structure.[30,31] This may be due to synthetic difficulties when working with $\mathrm{SbI_3}$ as precursor,[32] which exhibits a high vapor pressure and is prone to evaporation when using film annealing temperatures above $100\,^{\circ}\mathrm{C}$. Furthermore, instability of the pristine $\mathrm{AgSbI_4}$ under ambient conditions was reported as well.[30]

Herein, we demonstrate the thin-film synthesis of $\mathrm{Cu_xAg_{1-x}SbI_4}$ (CASI) rudorffites using a Lewis-base assisted approach. We establish the formation of the crystalline target materials in thin films and furthermore we highlight the beneficial effect of an optimal ratio of 40% Cu to Ag on the morphology, reducing grain boundaries and improving the overall coverage. Notably, an additional incorporation of only 5% Bi lead to the aforementioned morphology improvement over a broader range until a Cu content of 90%, which can also be seen in the photovoltaic performance. Density functional theory (DFT) calculations shed light on the impact of the stoichiometry of various $\mathrm{Cu-Ag-Sb-I}$ phases, highlighting the incorporation of Cu into the layered $\mathrm{Cu_xAg_{1-x}SbI_4}$ composition. Ultraviolet photoelectron spectroscopy measurements demonstrate the disappearance upon Cu addition of other trivalent oxide antimony states like $\mathrm{SbI_3}$ and $\mathrm{SbO_x}$ as side phases likely created through degradation and surface oxidation. UV-Vis spectroscopy and photoluminescence measurements further reveal the presence of deep defect states and broad emission with large Stokes shift, confirmed by DFT calculations pointing to extraordinarily low defect Ag point defect formation energies of $0.16\,\mathrm{eV}$. Additionally, PL measurements reveal static emission and lifetime characteristics over the whole doping range, which we discuss in view of varying charge carrier mobilities and photovoltaic performance. Conceptually, we connect the luminescence behavior to the thin film morphology via hyperspectral optical measurements, explaining the improved performance in solar cells when using an optimal copper content. Lastly, EQE measurements reveal a much-improved photocurrent at low photon flux when no white light bias is employed, hinting at great promise of these materials for indoor photovoltaic applications.

5.3 RESULTS AND DISCUSSION

To synthesize thin films based on $\mathrm{Cu_xAg_{1-x}SbI_4}$ (CASI), a common spin-coating approach was employed by dissolving the corresponding halide precursors ($\mathrm{CuI/AgI/SbI_3}$) in a mixture of 1:1 DMF:DMSO to achieve a concentration of approximately 0.6 M, followed by deposition on different substrates (glass/FTO/ITO/mp-$\mathrm{TiO2}$). Furthermore, a small amount of the Lewis base thiourea (TU) was added to retard the crystallization of

the thin film, a crucial step in controlling the formation of the CASI material, which has been reported to exhibit significant stability issues.[30,31,33] This is a necessary step to obtain working devices and circumvent recurrent problems of the halide precursors, with AgI being only hardly soluble in organic solvents like DMF that are commonly used for spin-coating. The influence of the additive on the behavior of the precursor solution is presented in Figure S1 in the Supporting Information (SI). Similar effects have been shown for lead-based and lead-free perovskites.[34–37] Furthermore, SbI_3 is known to have a high equilibrium vapor pressure[32] which prohibits the use of elevated annealing temperatures, shown to be crucial for the formation of the Bi analogue.[24] In this work, we therefore employed a ramped thermal annealing approach from 50 °C for 1 h to 80 °C for a minute to anneal the films. An 'inverse' technique based on one short immediate heating step for 1 min at 120 °C leads to improved crystallinity but less complete coverage, as shown in the XRD graphs and SEM images in Figure 5.8.

The XRD patterns for $Cu_xAg_{1-x}SbI_3$ films on FTO/c-TiO_2/mp-TiO_2 are shown in Figure 1a for incremental replacement of Ag with Cu in 10% steps. The substrate material was chosen to reflect the crystallization conditions which will be later adopted in solar cell devices.

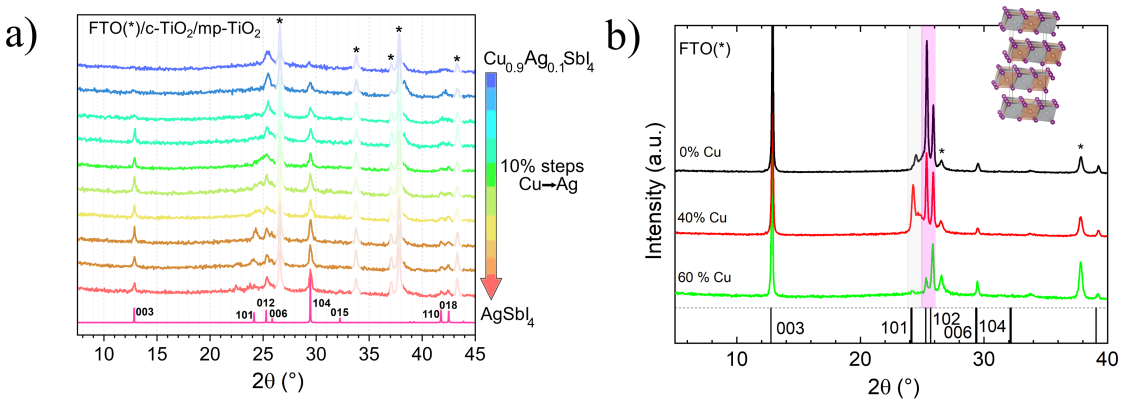

Figure 5.1: Thin film XRD data normalized to the highest intensity on FTO/c-TiO_2/mp-TiO_2 (a) and on FTO (b) of $Cu_xAg_{1-x}SbI_3$ thin films. a) Increasing Cu concentrations in steps of 10% from red to blue with theoretical patterns from Oldag et al.[38] The FTO reflections are removed for correct normalization and marked by an asterisk (*). b) $Cu_xAg_{1-x}SbI_3$ films on FTO with 0%, 40% and 60% Cu with [101] patterns highlighted in light gray and the [102]/[006] peak in light pink. Inset: Crystal structure used for simulation of $AgSbI_4$.

The patterns were normalized after removing the additional reflections arising from the substrate. As these match very well with the theoretical patterns extracted from the Bi analogue $AgBiI_4$,[39] we assume a similar space group ($R3m$) and a related crystal structure based on the CdCl2 prototype (Figure 5.1b), in line with Gray et al.[31] Materials

based on $A_xB_yX_{x+3y}$ stoichiometries with A being a monovalent transition metal cation (Ag^+/Cu^+), B a trivalent pnictogen cation (Bi^{3+}/Sb^{3+}) and X a monovalent halide anion, commonly I^-, are constructed of alternating occupied and unoccupied positions of edge-sharing octahedra $[AX_6]^{5-}$, $[BX_6]^{3-}$ and $[\Delta X_6]^{6-}$ (Δ = vacancy).[33] In our case, the halide ions occupy the octahedral corners (Wyckoff $6c$) and Ag/Cu/Sb occupy the Wyckoff positions $3a$ in the octahedral center.[40] Nonetheless, because of the aforementioned disorder, exact crystal structure analysis of such materials was shown to be a challenge.[33,39] This is caused by an important feature in rudorffites, namely A and B cations occupying the same Wyckoff sites, which enables a vast number of compositional permutations. In recent years, different elemental compositions for Ag-Bi-I systems were explored experimentally, ranging from $AgBi_2I_7$ to Ag_3BiI_6.[23,41–43] Furthermore, for silver- or copper-rich compositions, the monovalent A cations additionally may occupy the $3b$ positions in-between the octahedral slabs.[33,44] As shown later, we can carefully exclude compositions of other stoichiometries than the $AgSbI_4$ one on the basis of our theoretical calculations, which suggest that a a band gap collapse can be observed by having an excess of Ag in comparison to Sb or vice versa, in line with previous considerations on the Bi-based analogues.[45]

Interestingly, the peak positions in Figure 5.1a only show a very small shift upon incremental alloying with Cu, suggesting no significant change of the unit cell. The most pronounced change is the intensity decrease of the [104] and [003] reflections for increased Cu content. Furthermore, the intensity ratio of the neighboring [102]/[006] peaks reverses when more Cu is introduced, which can be seen in more detail in Figure 5.1b for films deposited on FTO despite a strong orientation along the [003] direction. This intensity change is linked to a decrease in sectional symmetry because of additional tetrahedral Cu polytypes centered at the $3a$ positions of Cu in the layers, as demonstrated by our DFT calculations which will be discussed later.

Previous reports suggested an intrinsic instability of the AgSbI4 phase, whereas the Bi-based analog with a larger ionic radius was shown to be highly stable under synthesis and in ambient conditions.[31] Moreover, Al-Anesi et al. showed local symmetry enhancement through Sb doping of Cu_2AgBiI_6, thereby improving photovoltaic efficiency through enhanced local structural symmetry and thus reduced defect density.[29] Consequently, we also prepared a system with only a small addition of 5 % Bi, resulting in a decrease in band gap (see below) and improved morphology. The corresponding XRD patterns show no significant change when comparing Bi-alloyed structures versus the pristine antimony thin films (see Figure 5.9).

In the following, we focus on samples with 0%, 40% and 60% Cu:Ag, as they are exemplary for the electronic and morphological changes in this system. The SEM images

for those samples, shown in Figure 5.2a-f, highlight the strong impact of the monovalent halide precursor on morphology and crystallization.

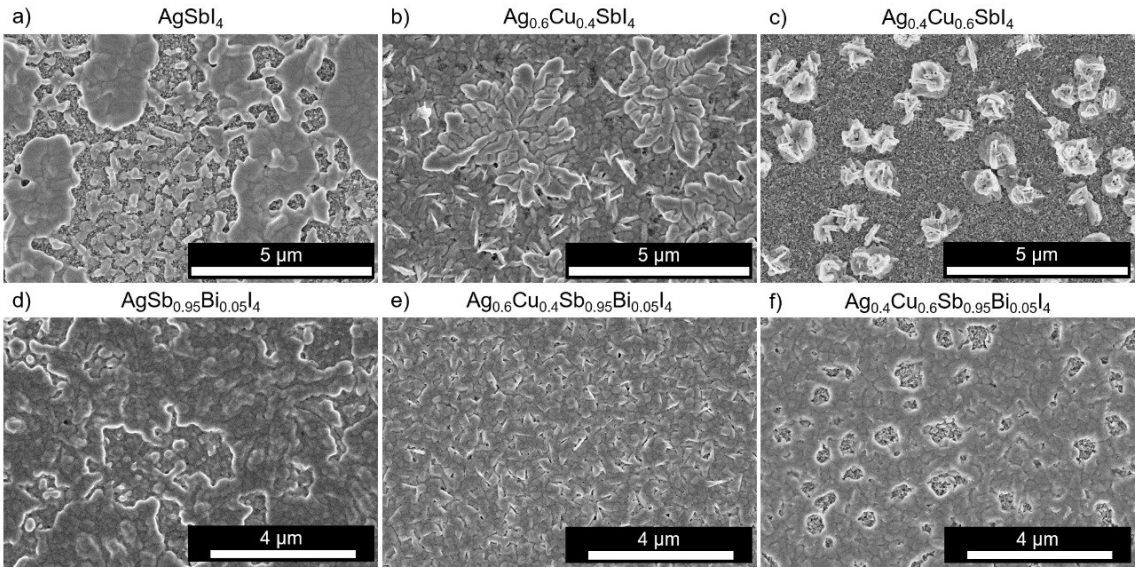

Figure 5.2: Scanning electron microscopy images of $Cu_xAg_{1-x}SbI_4$ thin films on FTO/c-TiO_2/mp-TiO_2. a)-c) Increasing amount of Cu (0%, 40%, 60%) and d)-f) increasing amount of Cu (0%, 40%, 60%) combined with 5% Bi/Sb substitution.

First of all, the addition of Bi seems to generally aid the crystallization, resulting in films with significantly better coverage and homogeneous morphologies. Enhanced lattice stability may further rationalize the increased coverage and high homogeneity at 40% Cu, resulting in overall homogeneously covered films. Beyond 50% Cu, the homogeneity decreases again.

XPS spectra confirm the incorporation of Cu and the presence of the expected elements, verifying the formation of the pure silver and copper-alloyed phases, see SI Figure S2a-c. Interestingly, the XPS spectra of the pure $AgSbI_4$, shown in SI Figure 5.7c, show additional states of either SbO_x, which could result from surface oxidation, or SbI_x side phases at approximately $585.5\,eV$. These side phases vanish when Cu is added to the system (see SI Figure 5.7).

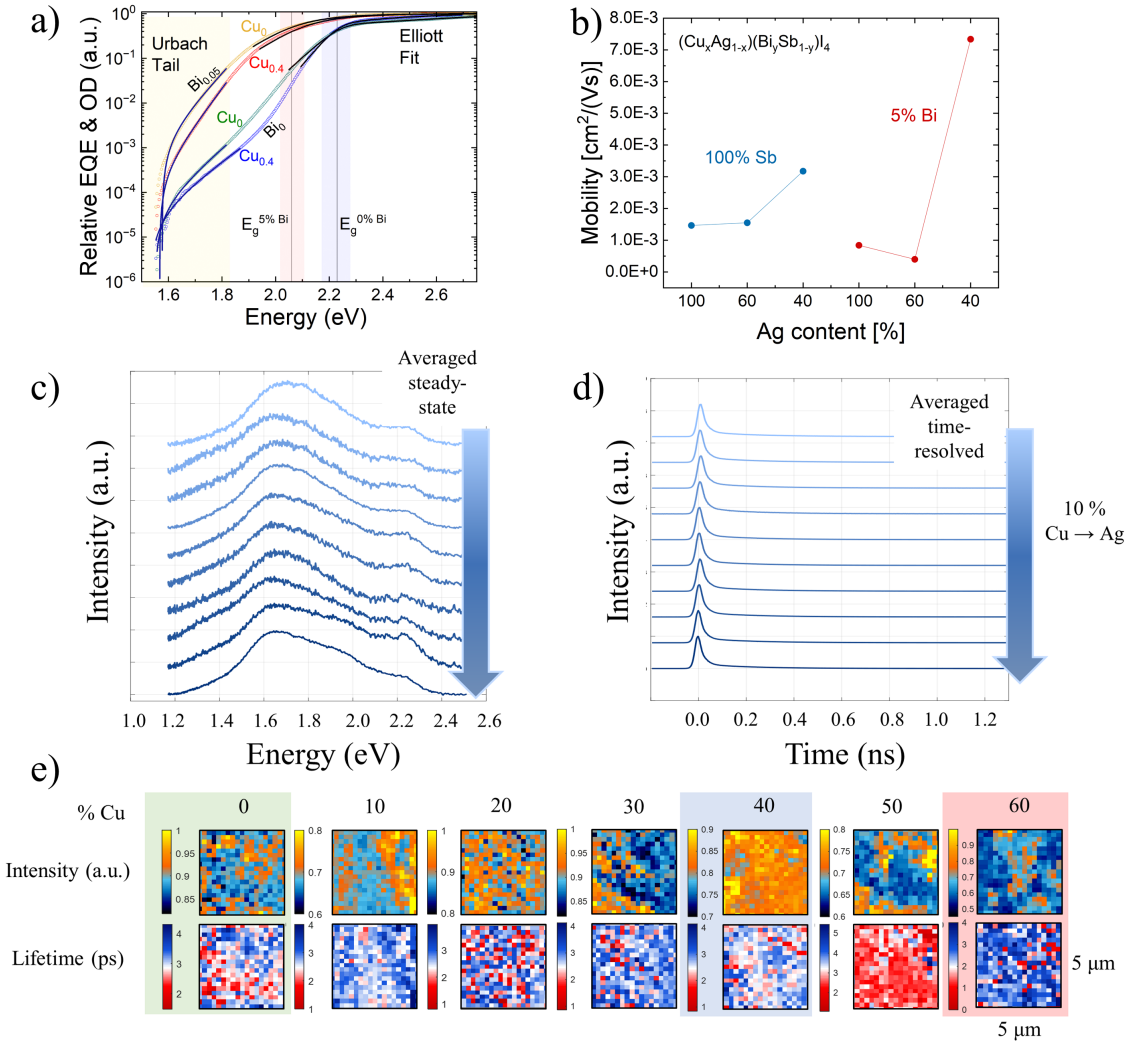

Figure 5.3: a) Fitted absorption coefficient of $AgSbI_4$ (green), $Cu_{0.4}Ag_{0.6}SbI_4$ (blue), $AgSb_{0.95}Bi_{0.05}I_4$ (yellow), $Cu_{0.4}Ag_{0.6}Sb_{0.95}Bi_{0.05}I_4$ (red). The red and blue boxes highlight the bandgap extracted from the Elliott fits. The straight lines around the band edge are fitted with Elliott's method and the black lines in the bandgap are exponential Urbach tails. b) Mobility values extracted from TRMC measurements for Ag concentrations of 100%, 60%, 40% without (blue) and with 5% Bi addition (red). c) Averaged spectra of photoluminescence measurements for incremental Cu percentage from 0% to 100% without Bi addition (dark to light blue: increasing Cu content). The yellow box highlights the self-trapped exciton emission and the light blue box the band-to-band emission. d) Averaged time-resolved photoluminescence measurements for incremental Cu percentage from 0% to 100% without Bi addition. (dark to light blue: increasing Cu content) e) Hyperspectral images of the photoluminescence intensity and time-resolved photoluminescence intensity distribution on a $5\,\mu m \times 5\,\mu m$ large area of a $Cu_xAg_{1-x}SbI_4$ thin film from 0% to 60% Cu/Ag ratio.

We now employ a combined fitting procedure following Elliott's method for the absorption coefficient close to the band edge and Urbach's tail to quantify the bandgap and sub-bandgap states.[46] The band gap of $AgSbI_4$ lies within the range of $2.0\,eV$ to $2.2\,eV$,

as in Figure 5.3a for $AgSbI_4$ (green), $Cu_{0.4}Ag_{0.6}SbI_4$ (blue), $AgSb_{0.95}Bi_{0.05}I_4$ (orange), $Cu_{0.4}Ag_{0.6}Sb_{0.95}Bi_{0.05}I_4$ (red). Changing the Cu:Ag ratio does not alter the band gap, while the addition of Bi reduces the bandgap by $0.2\,eV$. The decrease in band gap upon Bi/Sb alloying has previously been successfully assigned to the formation of aggregates rich of either Sb or Bi, being source of the reduction in the electronic band gap.[6,47] Furthermore, the Urbach tails all converge to the same energy of around $1.6\,eV$, pointing to the presence of trap states. This deep bandgap contribution is reduced through incorporation of 40% Cu, which is most likely tied to the improved crystallinity and morphology, suggesting that fewer defects are introduced in the synthesis compared to the reference systems as confirmed by absorbance log plots (SI Figure 5.11). These disorder-related deep levels are also confirmed by the photoluminescence emission as seen in Figure 5.3c, where the main emission maximum lies at around $1.6\,eV$ as well, with only a small contribution at the band edge ($2.3\,eV$), which agrees well with the band gap obtained from the Elliot fits. This low energy emission is probably caused by self-trapped excitons dominating the emission behavior, which was reported to be induced by exciton-phonon coupling and the resulting ultrafast carrier localization in multiple lead-free perovskite materials.[48–50] Furthermore, the lifetimes are also unaffected by additional Cu doping, and occur in the range of only ps (Figure 5.3d). The detailed spectral trends of photoluminescence and lifetime measurements for all samples are shown in Figure 5.13, with only negligible intensity and lifetime differences evident.

Mobility values for the thin films, extracted from TRMC, highlight an overall increase when reducing the silver contribution, shown in Figure 5.3b. This is in line with previous reports on the related $Cu_{4x}(AgBi)_{1-x}I_4$ compound, where small polaron formation was found to be responsible for ultrafast charge carrier localization that could be mitigated via the introduction of Cu.[48,50] The mobility values are mostly low when compared to other double perovskites like $Cs_2AgBiBr_6$.[51] Moreover, Bi addition does not increase the overall mobility in the pure $AgSbI_4$, but significantly boosts the mobility for systems with excess Cu of 60%.

To connect the optical properties with the morphology changes upon Cu doping, we performed fluorescence-lifetime imaging microscopy (FLIM) measurements; results are shown in Figure 5.3e. Here, the intensity of the PL emission and the lifetime are spatially resolved on a film area of the size $5\,\mu m \times 5\,\mu m$. These results confirm the trend of increased homogeneity of the surface of film samples alloyed with 40% Cu, showing the most consistent lifetimes overall and the best (homogeneous) distribution of luminescence intensity. The latter decreases sharply at 50% Cu and above, drastically decreasing the lifetime of the whole sample area. Keeping in mind the similar electronic characteristics over the whole substitution range, these measurements reveal the impor-

tant role the A cation plays in such structures, directing morphology, excitation behavior over a bigger sample size and, as shown in Figure 5.5, device performance and statistics. DFT calculations were then performed to shed light on the impact of composition of the $\mathrm{Ag-Sb-I}$ and $\mathrm{Cu/Ag-Sb-I}$ rudorffite phases. Ionic positions and cell parameters were optimized on the PBE level of theory including D3 dispersion corrections, with refined PBE0+SOC calculations for formation energies and electronic band gaps; see computational details in the SI. The cubic $\mathrm{ThZr_2H_7}$-type $\mathrm{AgSb_2I_7}$ stoichiometry,[45,52–54] see Figure 5.21, is unlikely to form as seen in the large formation energies of $4.86\,\mathrm{eV}$/f.u., see Table 5.1. Additionally, predicted band gaps of $0.39\,\mathrm{eV}$, far below the experimental values, rule out the existence of $\mathrm{AgSb_2I_7}$ stoichiometry, in line with studies on its Bi-based counterpart.[45] $\mathrm{AgSbI_4}$ and $\mathrm{Ag_3SbI_6}$ phases show disorder in their position of Sb and Ag ions, see Figures 5.15 and 5.16. Starting from the structure of the Bi-based counterparts,[38,52,55] a configurational screening was performed to obtain low energy configurations using DFT. Both compositions ($\mathrm{AgSbI_4}$ and $\mathrm{Ag_3SbI_6}$) show low energy structures with formation energies of $-0.01\,\mathrm{eV}$ and $0.03\,\mathrm{eV}$ with band gaps of $2.07\,\mathrm{eV}$ and $1.78\,\mathrm{eV}$ for $\mathrm{AgSbI_4}$ and $\mathrm{Ag_3SbI_6}$, respectively. Recalling the experimental bandgap values of $2.0\,\mathrm{eV}$ to $2.2\,\mathrm{eV}$, this supports the existence of layered $\mathrm{AgSbI_4}$ phases, see Figure 5.4a, while $\mathrm{Ag_3SbI_6}$-rich side phases may contribute to the sub-gap absorption and emission features. The DOS of the $\mathrm{AgSbI_4}$ phase shows the expected dominant role of iodide at the valence band edge, while the conduction band edge is dominated by Sb and I states from the $\mathrm{SbI_6}$ octahedra, with limited contribution from Ag, see Figure 5.4b. Note that entropic contributions, neglected in our study, likely contribute to the phase stabilization of such disordered phases.

System	E_F (eV/f.u.)	E_g (eV)	Lattice constants (Å)	Cell Angles (°)
$AgSb_2I_7$	4.86	0.39	a=b=c=14.637	α=β=γ=90
$AgSbI_4$	-0.01	2.07	a = 8.671	α=88.97
			b = 8.665	β=91.11
			c = 20.804	γ=120.58
Ag_3SbI_6	0.03	1.78	a = 9.178	α=86.57
			b = 8.751	β=92.47
			c = 20.763	γ=122.65
Cu_2AgSbI_6	0.42	1.90	a = 8.551	α=89.96
			b = 8.525	β=90.11
			c = 21.452	γ=119.52
$Cu_{0.5}Ag_{0.5}SbI_4$	0.14	2.13	a = 8.671	α=88.97
			b = 8.665	β=91.11
			c = 20.804	γ=120.58

Table 5.1: Optimized lattice parameters (PBE, D3) of the low energy configurations of the $Ag-Sb-I$ and the $Cu/Ag-Sb-I$ rudorffite phases. Formation energies (E_F) per formula unit and electronic band gaps (E_g) are given at the PBE0 level of theory with inclusion of SOC corrections on the PBE+D3 optimized geometries. Table 5.3 summarizes a configurational analysis for each composition

Moving to the $(Cu/Ag)-Sb-I$ compositions, especially the Cu_2AgSbI_6 phase has recently been proposed to form in the Bi-counterparts.[40] The structure of the given phase is highly disordered, with many cations occupying same lattice positions,, requiring a configurational screening, see Figure 5.17. The proposed low energy structure shows a formation energy of 0.42 eV/f.u., containing layers of $Ag/Cu-I$ without Sb incorporated, see configuration c11 in Figure 5.17, which is substantially lower than fully mixed structures, see Table 5.3. This may point to favorable phase segregation in such compounds. Electronic band gap values of $1.90\,eV$ are in fair agreement with experiments. Still, the successful incorporation of Cu ions over a wide range of Cu:Ag alloying in our experimental investigation raises concerns about the relevance of the Cu_2AgSbI_6 phase. Thus, we performed DFT calculations on the $Cu_{0.5}Ag_{0.5}SbI_4$ composition, keeping the overall A-B-X stoichiometry of 1-1-4 and replacing half of the Ag ions by Cu, as suggested by our XRD data in Figure 5.1. Interestingly, the formation energy of the $Cu_{0.5}Ag_{0.5}SbI_4$ phase, see Figure 5.4b, decreases to 0.14 eV/f.u. with a band gap of $2.13\,eV$, in excellent agreement to our experimental thin films. We further predict an upshift of the valence band edge by $0.24\,eV$ compared to the $AgSbI_4$ phase, see Figure 5.4c. Notably, valence

band (VB) XPS spectra (SI Figure 5.7d) show an increase in the VB energy upon Cu addition by $0.15\,\mathrm{eV}$ to $0.25\,\mathrm{eV}$, which confirms our DFT results and, most importantly, underlines the existence of the 1:1:4 stoichiometry in our synthesized thin films. Thus, we can expect that the 1:1:4 stoichiometry is accessible over a large range of Cu:Ag alloying.

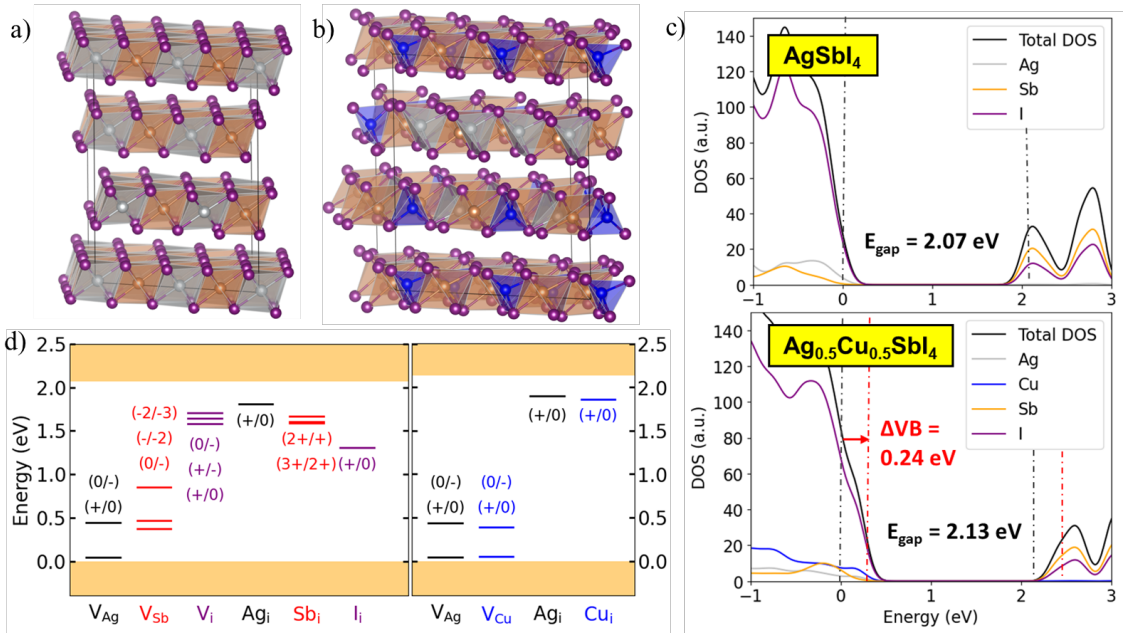

Figure 5.4: (a, b) Structural representation of AgSbI4 and $Cu_{0.5}Ag_{0.5}SbI_4$, respectively, with following color code: Ag = silver, Cu = green, Sb = orange, I = purple. (c) Density of states on the PBE0+SOC level of theory of (top) $AgSbI_4$ and (bottom) $Cu_{0.5}Ag_{0.5}SbI_4$. Electronic band gap values are given in each panel. The potential of the considered systems has been aligned with respect to the vacuum level to obtain the VB and CB shift between $AgSbI_4$ and $Cu_{0.5}Ag_{0.5}SbI_4$, as highlighted in red color. The DOS of the $AgSbI_4$ has been set to zero energy. (d) Thermodynamic ionization levels of point defects, vacancies V_X and interstitials X_i for each element X = (Ag, Cu, Sb, I), based on the hybrid PBE0+D3 DFT calculations with inclusion of SOC. The orange colored parts highlight the valence band (bottom) and conduction band (top). Computational details on the defect calculations are provided in the SI.

We further calculate the defect formation energies, see Figure 5.19 to 5.20, and thermodynamic ionization levels (TILs), see Figure 5.4, for the pure $AgSbI_4$ and the alloyed $Cu_{0.5}Ag_{0.5}SbI_4$ compounds, respectively. All geometries were optimized on the PBE+D3 level of theory, with refined calculations for DFE and TILs based on the PBE0 level of theory with inclusion of spin-orbit coupling corrections. We observe low DFEs of $0.16\,\mathrm{eV}$ for Ag vacancies (V_{Ag}^{-}) and interstitials (Ag_i^{+}), representing hole and electron trap states at $0.44\,\mathrm{eV}$ above the VBM and $0.25\,\mathrm{eV}$ below the CBM, see Figure 5.4d and Figure 5.19. This suggests that sub-gap emission features at $1.6\,\mathrm{eV}$ may likely be caused by recombination of electrons trapped at Ag vacancies. The low formation energies of Ag point

defects further are in line with features of $\mathrm{Ag-Bi-I}$ compounds that previously have been considered for ionic conduction due to their mobile Ag ions.[38] Notably, Sb and I point defects also act as trap states within the band gap, see Figure 5.4d, while showing moderate formation energies of $0.7\,\mathrm{eV}$ to $0.9\,\mathrm{eV}$, thus being of less relevance for the optoelectronic properties of $\mathrm{AgSbI_4}$.

Moving towards the alloyed $\mathrm{Cu_{0.5}Ag_{0.5}SbI_4}$, we observe negligible differences in the TILs and DFEs (Figure 5.20) for Ag and Cu vacancies and interstitials, in line with the low dependence of sub-gap emission on $\mathrm{Cu{:}Ag}$ alloying as shown in Figure 5.4c. This suggests further that the reduction of sub-gap absorption upon Cu addition is due to the growth of more homogeneous morphologies rather than a suppression of point defect formation. Consequently, Cu alloying is mainly relevant for reducing AgI rich side phases, while the concentration incremental Cu alloying shifts the type of detrimental defects between Ag and Cu.

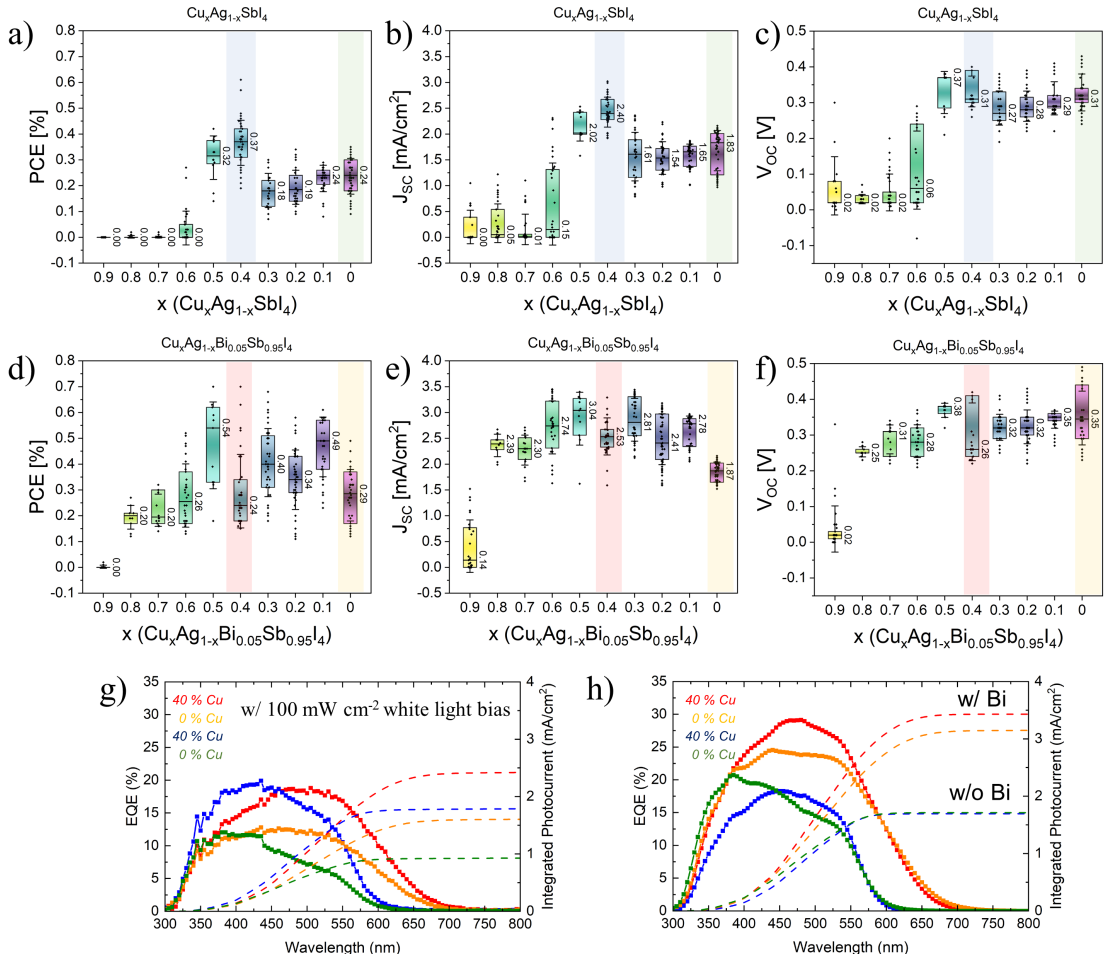

Figure 5.5: Characterization of photovoltaic devices. a-c) PCE, Jsc, Voc statistical box plots with median, interquartile range and statistical outliers for 10% changes of the Cu/Ag ratio from $Cu_{0.9}Ag_{0.1}SbI_4$ to $AgSbI_4$. The same color scheme for the colored boxes as for Figure 5.3a was used to highlight the reference and the most efficient alloying step. d-f) PCE, J_{sc}, V_{oc} statistical box plots for 10% changes of Cu/Ag ratio with fixed 5% Bi content from $Cu_{0.9}Ag_{0.1}Sb_{0.95}Bi_{0.05}I_4$ to $AgSb_{0.95}Bi_{0.05}I_4$. The same color scheme for the colored boxes as for Figure 5.3a was used to highlight the reference and the most efficient alloying step. g) and h), EQE spectra and integrated photocurrent density of the most efficient solar cells for $AgSbI_4$ (green), $Cu_{0.4}Ag_{0.6}SbI_4$ (blue), $AgBi_{0.05}Sb_{0.95}Bi_{0.05}I_4$ (orange) and $AgBi_{0.05}SbI_4$ (red). The data in g) are measured with a constant $100\,\mathrm{mW\,cm^{-2}}$ white light source in the background, while the data in h) are measured without white light bias.

After elaborating the structural and electronic properties of the CASI rudorffites, photovoltaic devices were fabricated in the n-i-p architecture with increasing amounts of Cu. Mesoporous titania was used as electron transporting layer and poly(triaryl amine) (PTAA) as hole transporting layer.[23,24,56] The statistical analysis of the device performance can be seen in Figure 5.5a-f. Firstly, the overall performance increases significantly when employing only a small substitution of 5% Bi, which is attributed to

the band gap decrease as seen in the absorbance curves shown in Figure 5.3a. Interestingly, this minor incorporation of Bi additionally stabilizes the performance over a wide range of $\mathrm{Cu/Ag}$ ratios. We attribute this impact of Bi to the improved homogeneity of morphology as seen in Figure 5.2f, hinting at a highly beneficial role of $\mathrm{BiI_3}$ in the precursor solution. In the Bi-free series, samples prepared with 40% Cu are generally the most efficient, showing the overall highest PCE, mostly due to the increased current density. Notably, the low open circuit voltage is the main bottleneck in these systems, as also suggested previously.[24,25] In our studies, only samples with added Bi surpass $0.4\,\mathrm{V}$ open circuit voltage in some cases, whereas Cu-alloyed samples show only small improvements. We attribute the low voltage to non-radiative recombination processes mediated by Ag point defects, representing trap states with low formation energies as shown by our DFT calculations, and ultrafast carrier localization.[46,48]

To further estimate the potential of Sb-based rudorffites for indoor photovoltaics, EQE measurements were carried out on well-performing solar cells with and without white light background illumination. As shown in Figure 5.5g, the EQE measured under white light illumination at $100\,\mathrm{mW\,cm^{-2}}$ is comparably small, with a maximum of 20% for Cu-alloyed films at $450\,\mathrm{nm}$ without Bi and at $550\,\mathrm{nm}$ with Bi. Interestingly, when using a chopped white light source without a white light bias, the overall EQE increases significantly by approximately 10% overall for all thin films except $\mathrm{Cu_{0.4}Ag_{0.6}SbI_4}$, which could be explained by a different recombination mechanism at high fluence intensities in this system as seen in the TRMC curves in Figure 5.12b. This is in line with the behavior of $\mathrm{Cu_2AgBiI_6}$ rudorffites, where the efficiency for indoor light illumination almost doubles up to 10% iPCE,[29] being attributed to reduced non-geminate recombination, which seems to be an intrinsic feature of $\mathrm{(Cu/Ag)-(Sb/Bi)-I}$ based materials.
Although the initial performance falls behind Bi-based "rudorffites", this class of materials suggests to offer a lot of potential for possible indoor applications while being easily tunable and also strongly influenced by the compositional freedom solution-processing offers.[23,38,53] This class of materials offers great potential for indoor applications while being easily tunable. Furthermore, our results demonstrate the compositional freedom of solution-processed rudorffites. We propose that through stoichiometry tweaking, precursor engineering - i.e. by employing acetates or other metal sources[14,57] - or further additive modification, the performance could be strongly improved to offer a viable alternative for low-cost indoor photovoltaics.

5.4 CONCLUSIONS

To summarize, we successfully synthesized "rudorffite"-type $\mathrm{Cu/Ag-Sb-I}$ thin films using the Lewis-base additive thiourea. We establish control of the thin film morphology by partial alloying of Ag with Cu atoms, resulting in homogeneous coverage, which was even improved upon partial substitution with Bi. DFT calculations and optical characterization point to the formation of a $\mathrm{AgSbI_4}$ phase in the pure Ag case and the incorporation of Cu ions, partially replacing Ag and forming $\mathrm{Cu_{1-x}Ag_xSbI_4}$. Other phases that have been previously discussed for the Bi-based counterparts could be ruled out to the large formation energies or low predicted band gaps. Our results further reveal the detrimental role of Ag point defects, which induce sub-bandgap electronic states that may act as recombination centers resulting in sub gap emission and absorption features. We further demonstrate that Cu alloying does not signifcantly alter the electronic band gap, which consequently represents a facile strategy for the optimization of Sb-based rudorffites. Solar cells based on the CASI rudorffites show low power conversion efficiencies of around 0.3%, mainly hampered by large losses in the open-circuit voltage. Interestingly, substituting a small amount of 5% bismuth raises the efficiencies to up to 0.7%, mainly through a reduction of the electronic band gap. We observe an apparent stabilization in current density and open-circuit voltage upon addition of Bi over a wide range of $\mathrm{Cu{:}Ag}$ alloys. Finally, white light bias-free EQE measurements suggest a much-improved performance of these materials for indoor photovoltaic applications, which we attribute to reduced geminate recombination at low light intensity. These observations offer opportunities for the control and design of novel Sb-based rudorffites as perovskite-inspired semiconductor for diverse optoelectronic applications such as indoor photovoltaics.

5.5 SUPPORTING INFORMATION

5.5.1 Methods

Precursor Solution

To synthesize (Cu/Ag)-(Bi/Sb)-I films, the corresponding iodides were dissolved in a 1:1 vol% mixture of DMF/DMSO in a 0.6 M precursor solution with a 1 wt% additive of TU. $1\,\mathrm{mL}$ precursor solutions for the $\mathrm{Cu_xAg_{1-x}SbI_4}$ system were weighed in as follows:
x is the molar ratio, the masses are given in weight/amount of substance [$\mathrm{mg/mmol}$].

x =	0	0.1	0.2	0.3	0.4	0.5
AgI (Sigma Aldrich)	140.8/0.6	126.8/ 0.54	112.7/ 0.48	98.6/ 0.42	84.5/ 0.36	70.4/ 0.3
CuI (Sigma Aldrich)	0/0	11.4 /0.06	22.9/ 0.12	34.3/ 0.18	45.7/ 0.24	57.1/ 0.3
SbI3 (Alfa Aesar)	301.4/ 0.6					
x =	0.5	0.6	0.7	0.8	0.9	1
AgI (Sigma Aldrich)	70.4/ 0.3	56.3/ 0.24	42.3/ 0.18	28.2/ 0.12	14.1/ 0.06	0/0
CuI (Sigma Aldrich)	57.1/ 0.3	68.6/ 0.36	80.0/ 0.42	91.4/ 0.48	102.8/ 0.54	114.27/ 0.6
SbI3 (Alfa Aesar)	301.4/ 0.6					

Table 5.2: Precursors and respective weights/substance amounts for the thin film synthesis of $\mathrm{Cu_xAg_{1-x}SbI_4}$ thin films.
To these mixtures, 1 wt% with respect to total precursor weight of thiourea (TU) was added (4.42 mg, 0.06 mmol, Sigma Aldrich) and dissolved in 0.5 mL DMF and 0.5 mL DMSO. Furthermore, for 5% Bi substitution, 17.69 mg (0.03 mmol) $\mathrm{BiI_3}$ was added and only 286.4 mg (0.57 mmol) SbI3 was used.

Thin Film Deposition

All solutions were heated at $70\,^{\circ}\mathrm{C}$ on a hotplane in $\mathrm{N_2}$ atmosphere for 30 min prior to spin-coating. For thin film deposition, $70\,\mu\mathrm{L}$ of the precursor solution was spin-coated on different substrates at 3000 rpm for 10 s followed by 6000 rpm for 50 s. Varying substrate types were cleaned with oxygen plasma under vacuum. Glass and fluorine-doped tin oxide (FTO) substrates were cleaned at 50% power for 5 min with a Diener Femto Plasma Etcher.

X-Ray Analysis

XRD data on thin films were recorded on a Bruker D8 Discover operating at $40\,\mathrm{kV}$ and $30\,\mathrm{mA}$ with Cu-K_α radiation ($\lambda = 1.5406\,\text{Å}$) and a position-sensitive LynxEye detector. XRD patterns were measured in the range of $5\,°2\theta$ to $60\,°2\theta$ with a step size of $0.05°$. Powders were measured on a STOE STADI P diffractometer with Cu-K_α radiation and a $\mathrm{Ge}(111)$ single crystal monochromator equipped with a DECTRIS solid state strip detector MYTHEN 1K, which was used for wide angle X-ray diffraction measurements in transmission mode.

Device Fabrication

A sol-gel approach was used to deposit the compact $\mathrm{TiO_2}$ layer from a solution containing 0.23 M titanium isopropoxide (Sigma-Aldrich, 99.999%) and 0.013 M HCl in isopropanol (IPA). The solution ($250\,\mu\mathrm{L}$ per $6 \times 6\ \mathrm{cm^2}$ substrate size) was spin-coated dynamically on top of the substrate at 2000 rpm for 45 s, dried at $150\,°\mathrm{C}$ for 10 min and annealed at $500\,°\mathrm{C}$ for 45 min.
In devices with mesoporous $\mathrm{TiO_2}$ layer, an approx. 150 nm thick, mesoporous (mp)-$\mathrm{TiO_2}$ layer was applied by spin-coating $100\,\mu\mathrm{L}$ of a $\mathrm{TiO_2}$ nanoparticle paste (Dyesol DSL 18NR-T) diluted in absolute ethanol (1 : 6 weight ratio) onto the above compact $\mathrm{TiO_2}$ layer at 2500 rpm for 30 s, followed by subsequent annealing at $500\,°\mathrm{C}$ for 45 min under ambient conditions.
PTAA (12 mg, average molecular weight Mn = 30000) was dissolved in 1 mL toluene and the resulting solution was filtered using a syringe filter (pore diameter $0.45\,\mu\mathrm{m}$). $70\,\mu\mathrm{L}$ of the filtered solution was spin-coated on top of the active layer in a single-step spin coating program at 3000 rpm for 35 s, and the obtained films were annealed at $100\,°\mathrm{C}$ for 5 min. The top electrode with a thickness of 40 nm was deposited by thermally evaporating gold under vacuum (at $\approx 10^{-7}$ mbar).

SEM Measurements

For analysis of the thin film morphology, thickness, and composition, scanning electron microscopy (SEM) was performed on an FEI Helios Nanolab G3 UC-DualBeam scanning electron microscope with an acceleration voltage between 2 and 5 keV.

X-Ray photoelectron spectroscopy

For XPS analysis, a ThermoFisher VG Escalab 250 spectrometer was used. XPS was performed with a monochromatic Al-K_α source (1486.6 eV) set at 13 mA and 15 kV. The pressure inside the analytical chamber was monitored to be below 1×10^{-9} mbar.

Photoluminescence Measurements

For photoluminescence (PL) measurements, hyperspectral images and time-resolved PL images, a home-built confocal laser scanning microscope was used. It is based on a microscope body (NIKON) which is combined with an xyz-piezo-scanning stage (PHYSIK INSTRUMENTE). The samples were measured upside down in epi-direction with an air objective (1.4 NA, Apo-Chromat, NIKON). A beamsplitter (MELLES GRIOT 03BTL005) and a spectral 490 nm long pass filter was used to separate the laser from the PL-light. A sub picosecond laser (ichrome TOPTICA) which is tunable from 476 nm to 645 nm was used for excitation. Here we measured only with the 476 nm laser light, which was additionally filtered by a band pass 473/10 nm (CHROMA) in the excitation arm. The detection side consists of two parts, which are separated by a flippable mirror. One has an avalanche photo diode (APD, type: MPD PDM, detector size 50 x 50 μm), which can be combined with a Time Correlated Single Photon Counting (TCSPC) electronics (BECKER UND HICKEL) measuring time resolved PL-transients. The second part consists of a spectrometer (ANDOR SHAMROCK SRi303) combined with an open electrode CCD camera (ANDOR NEWTON DU920) recording spectra. The data were recorded using a customized LABVIEW (NATIONAL INSTRUMENTS) program that combines the manufacturers' software with our desired measurements. Further processing and analysis were carried out using MATLAB (MATHWORKS) programs to obtain the PL spectra, TCSPC transients and the images.

TRMC Measurements

Thin films on sapphire substrates were placed in a microwave cavity. The TRMC technique was used to measure the change in reflected microwave (9 GHz) power after pulsed excitation (repetition rate 1 kHz) of the samples at 355 nm using the third harmonic of an Nd:YAG laser. The layers were illuminated from the back side.[51]

Solar Cell Characterization

Photovoltaic device performance was measured with a Keithley 2400 source meter in air at $25\,^{\circ}\mathrm{C}$ under illumination by a Newport Oriel Sol2A solar simulator, which was calibrated to $100\,\mathrm{mW\,cm^{-2}}$ with a Fraunhofer ISE certified silicon cell with a mismatch factor of 1.01. The active area of the solar cell was defined with a square metal aperture mask of 0.0831 $\mathrm{cm^2}$.

EQE Measurements

Measurements were performed on a home made system with a halogen lamp, a monochromator and a silicon reference diode. The light was chopped at 330 Hz and the signal was detected through a lock-in amplifier. The setup was calibrated with a silicon solar cell and no bias light was applied.

Computational Details

Density Functional Theory (DFT) calculations have been performed on $\mathrm{Ag\text{-}Sb\text{-}I}$ and the alloyed $\mathrm{Cu/Ag\text{-}Sb\text{-}I}$ rudorffites. Cell parameters were refined within the Quantum Espresso software package[58] (vc-relax) using the GGA-PBE exchange correlation functional.[59] Electron-ion interactions were described by scalar relativistic ultrasoft pseudopotentials (Ag, 11 electrons, $5s^2$, $4p^9$; Cu, 11 electrons, $4s^2$, $3d^9$; Sb, 5 electrons, $5s^2$, $5p^3$; I, 7 electrons, $5s^2$, $5p^5$). Plane-wave basis set cutoffs for the smooth part of the wave functions and the augmented density were 40 and 320 Ry, respectively. The Brillouin zone was sampled using a 4×4×1 Monkhorst-Pack grid.[60] Dispersion corrections were accounted for by the DFT-D3 scheme.[61] Accurate electronic band gaps were calculated using the PBE0 functional[62] including spin-orbit coupling within the Quantum Espresso package[58] Here, we used full relativistic norm-conserving pseudopotentials (Ag, 19 electrons, $4s^2$, $4p^6$, $4d^{10}$, $5s^2$, $4p^9$; Sb, 15 electrons, $4d^{10}$, $5s^2$, $5p^3$; I, 7 electrons, $5s^2$, $5p^5$) with a cutoff on the wave functions of 40 Ry and 80 Ry on the Fock grid and sampling the Brillouin zone using a 2×2×1 Monkhorst-Pack grid. PDOS plots have been generated with a Gaussian smearing of $0.1\,\mathrm{eV}$.

5.5.2

Supplementary Data

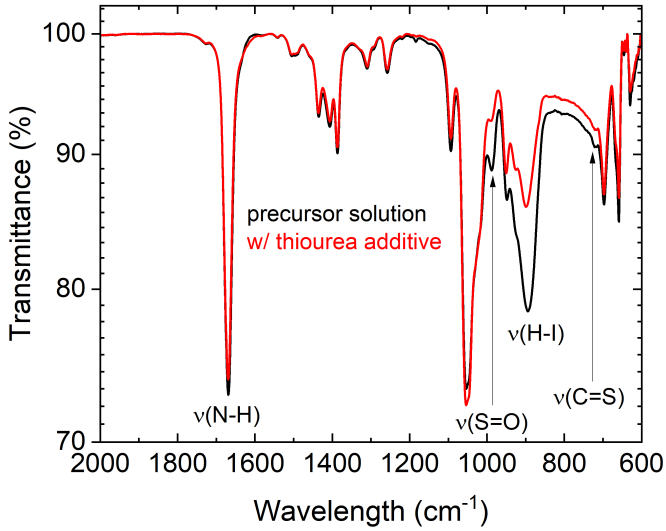

Figure 5.6: Infrared spectrum of two 1.0 M solutions of $AgSbI_4$ with (red) and without (black) 1 wt% (with respect to total precursor weight) thiourea additive. Characteristically changing vibrations are highlighted.

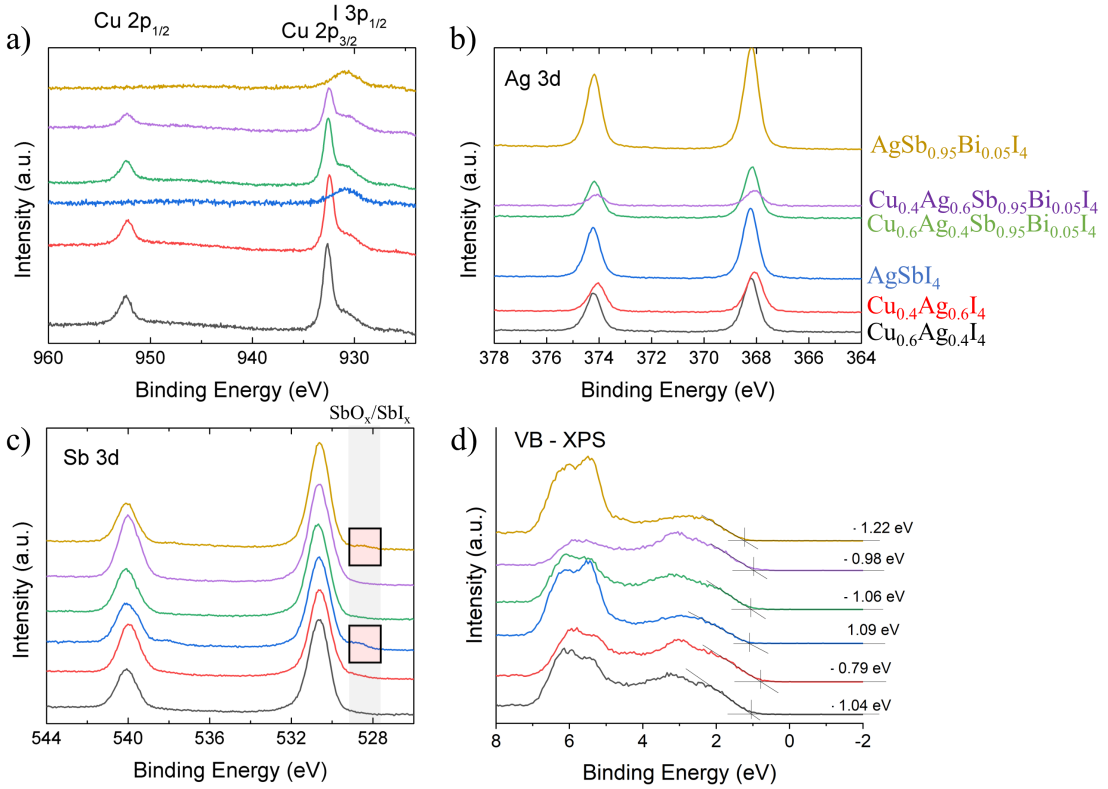

Figure 5.7: XPS spectra for $AgSbI_4$ thin films with and without Bi (5%) and Cu (40%, 60%) replacement. a) Cu $2p_{1/2}$ and I $3p_{1/2}$ regions. b) Ag $3d$ states. c) Sb $3d$ states with an inset of SbO_x/SbI_x states. d) Valence band XPS data with valence band edge for all samples.

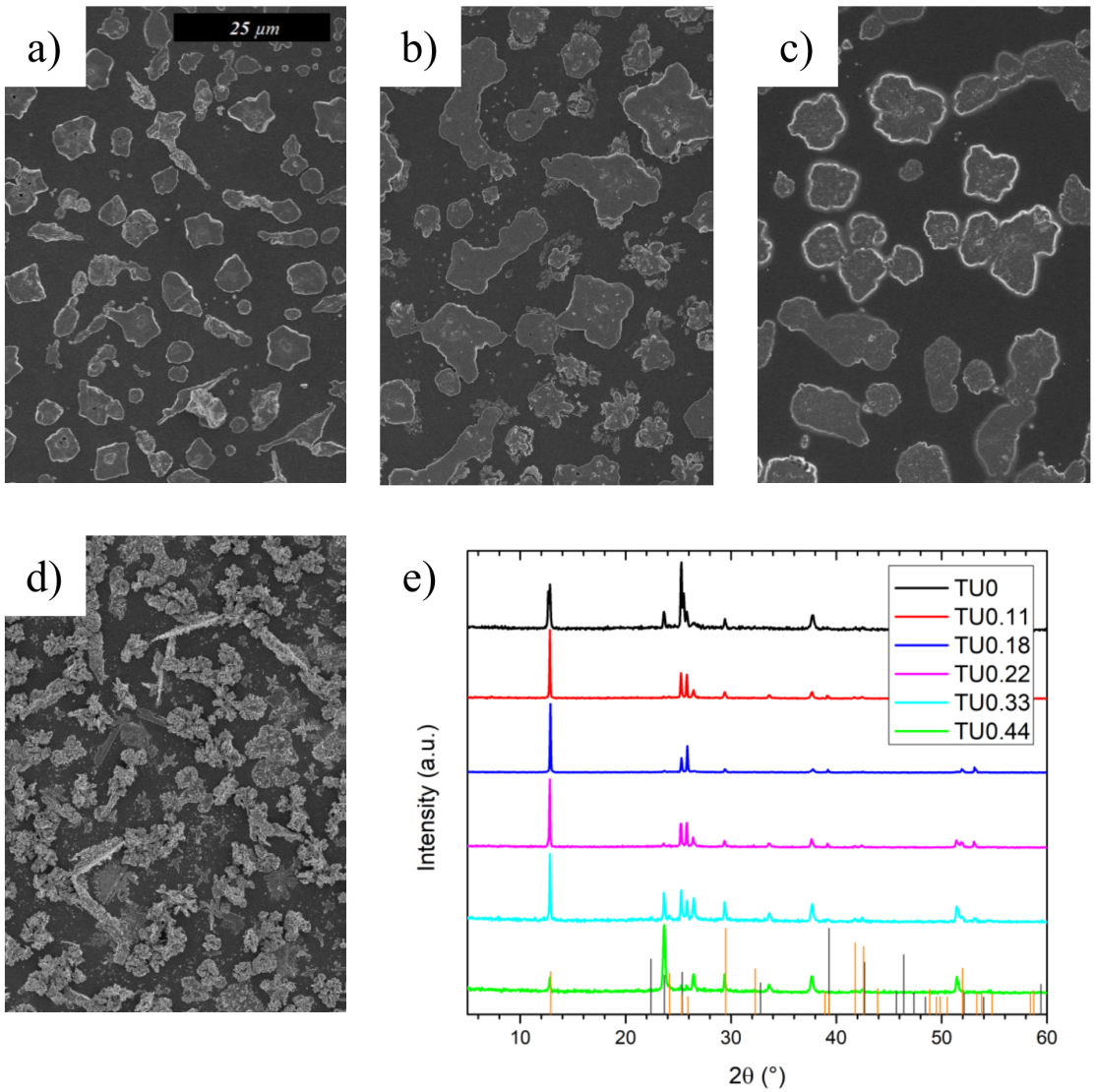

Figure 5.8: SEM images on compact TiO_2 and XRD data of $AgSbI_4$ thin films synthesized by annealing a 1 M precursor solution prepared as described in the methods section at 110 °C for 1 min and 70 °C for 1 h. a) Addition of 0 mol/L, b) 0.11 mol/L, c) 0.18 mol/L, and d) 0.33 mol/L thiourea. e) XRD patterns for different thiourea concentrations with theoretical patterns for $AgBiI_4$ (orange) and AgI (grey).

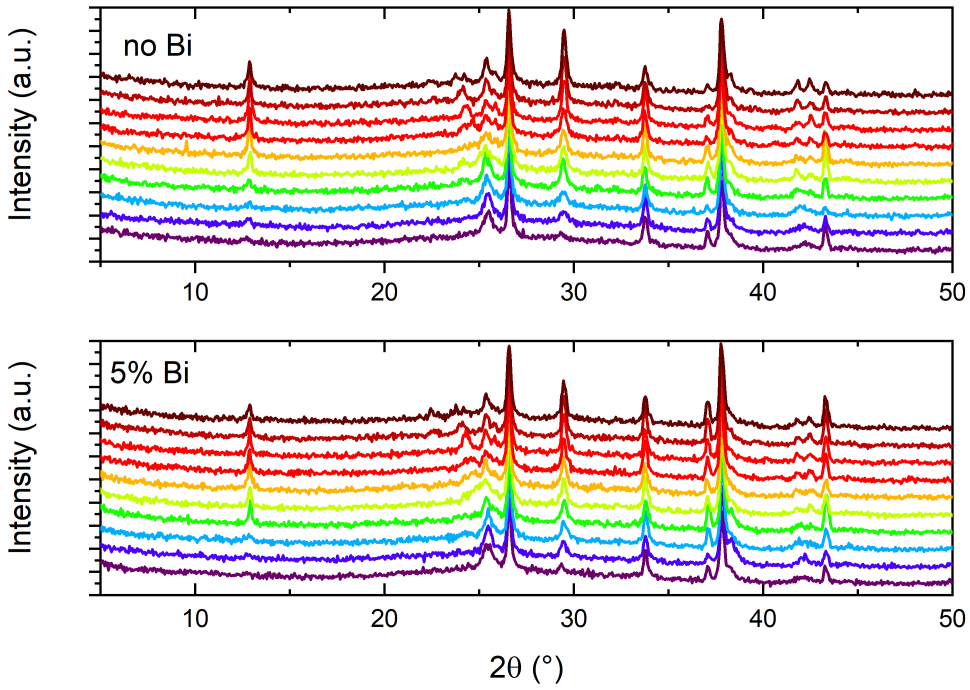

Figure 5.9: Thin film XRD data obtained on FTO/c-TiO_2/mp-TiO_2 for $Cu_xAg_{1-x}SbI_4$ thin films with increasing Cu concentrations (10% steps) from red (0%) to blue (100% Cu). (upper panel: films without added Bi, lower: 5% Bi additive)

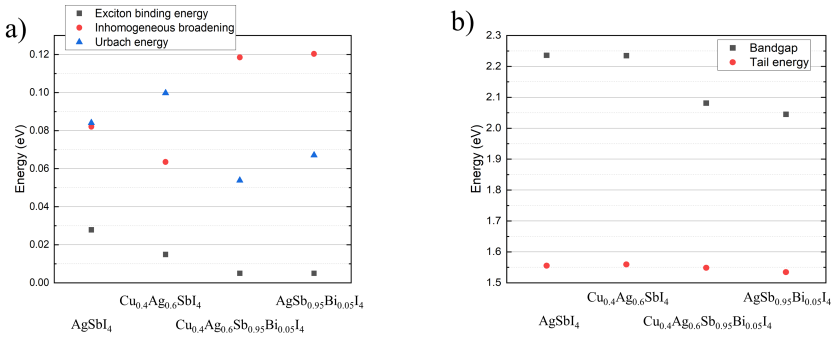

Figure 5.10: a) Fitting parameters for the Elliott fits in Figure 5.3a with exciton binding energy, inhomogeneous broadening and Urbach energy. b) Bandgap trend and tail energy of the exponential Urbach tails for the sample subset.

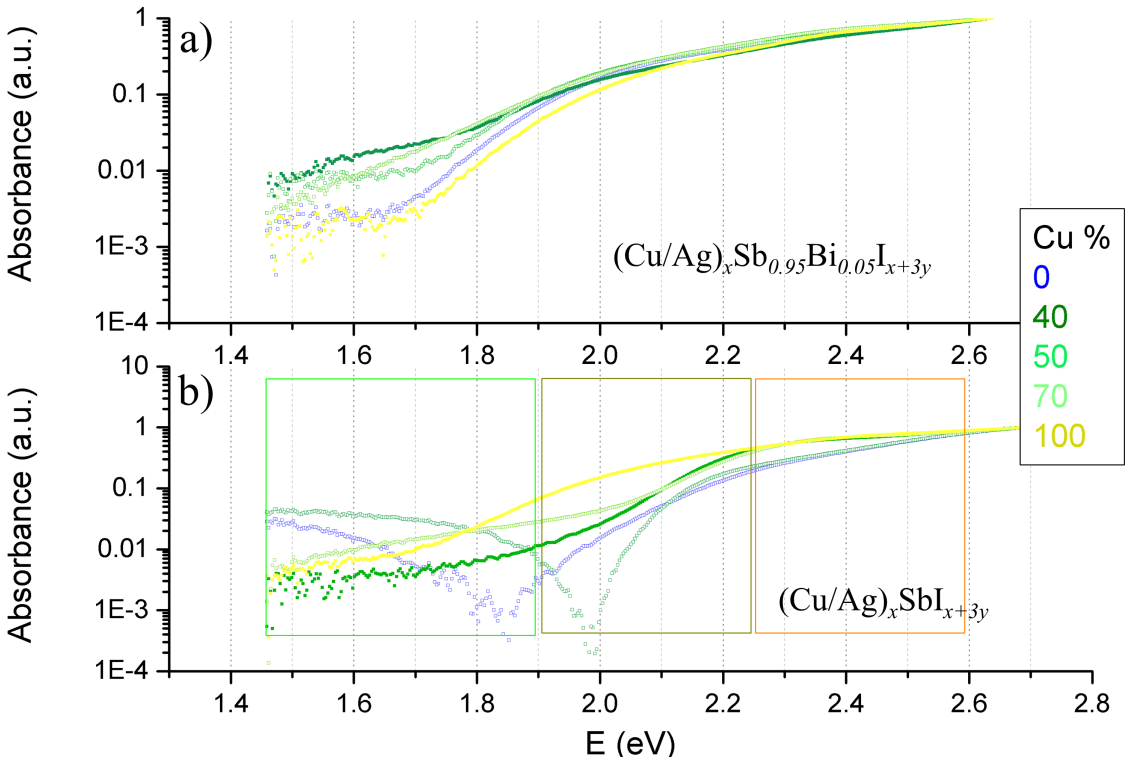

Figure 5.11: Logarithmic absorbance data for $Cu_xAg_{1-x}SbI_4$ thin films on glass with (a) and without (b) 5% Bi additive. In (b), the deep sub bandgap region beyond the Urbach tail is highlighted in green, the shallow sub bandgap region in dark yellow and the bandgap edge in orange.

Urbach and Elliott Fit

Absorbance data near the band edge for the reference material $AgSbI_4$ were fitted with a least-squares approach via Elliott's method with added thermal broadening as described by D'Innocenzo et al,[63] shown in equation 5.1 (with E_b being the exciton binding energy, n an integer describing the continuum transitions, $h\nu$ the photon energy, Γ the inhomogeneous broadening parameter, E_g the bandgap and $m_r b$ a factor determining the parabolicity of the fitting curve).

$$\alpha(\nu) = \alpha_0^{3D}\left[\sum_{n=1}^{\infty}\frac{4\pi E_b^{3/2}}{n^3}sech\left(\frac{h\nu - E_g - \frac{E_b}{n^2}}{\Gamma}\right) + \int_{E_g}^{\infty} sech\left(\frac{h\nu-\epsilon}{\Gamma}\right)\frac{2\pi\sqrt{E_b}}{1-e^{-2\pi\sqrt{\frac{E_b}{h\nu-E_g}}}}\frac{1}{1-b(\epsilon-E_g)}d\epsilon\right] \tag{5.1}$$

To fit the absorbance in the bandgap, a simple Urbach fit as shown in equation 5.2 was employed (with α_0 and E_1 being fitting parameters and E_0 the Urbach energy).[64,65]

$$\alpha(E) = \alpha_0 \exp \frac{E - E_1}{E_0} \tag{5.2}$$

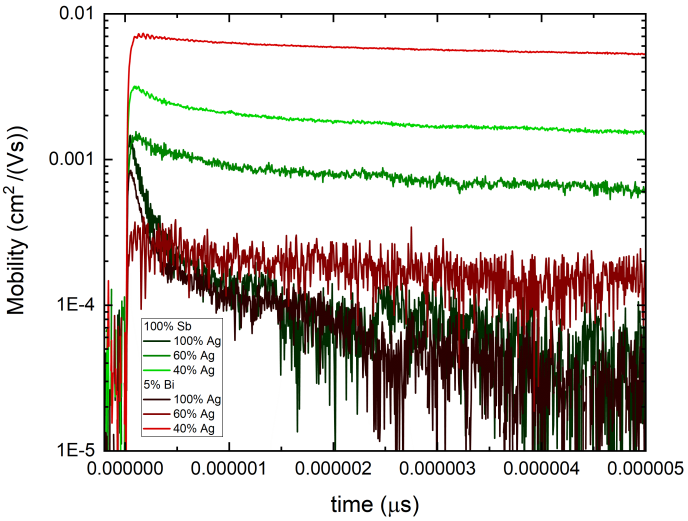

Figure 5.12: Traces of the TRMC measurements for thin films with and without Bi and 100%, 60% and 40% Cu/Ag ratio.

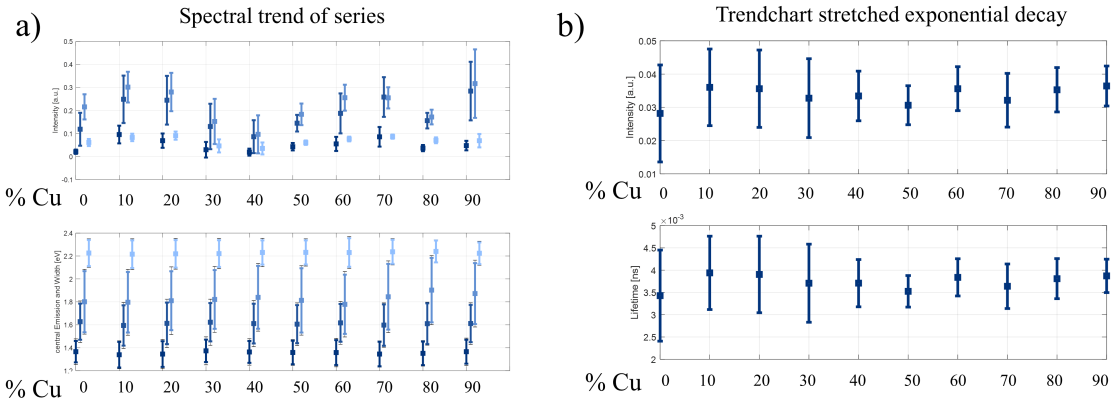

Figure 5.13: a) Spectral trend chart of photoluminescence measurements with intensity distribution and emission width. b) Spectral trend chart of the time-resolved photoluminescence traces fitted with an exponential decay function, with intensity and lifetime shown.

Compositional Analysis

Due to the presence of disorder in the lattice, we considered several permutations to obtain a low energy structure for further analysis. Formation energies are calculated with respect to the bulk phases of the precursors (CuI / AgI / SbI_3) matching the stoichiometry of the final composition.

First, we consider the cubic $ThZr_2H_7$-type crystal structure resulting in the $AgSb_2I_7$ stoichiometry,[45,52,53] Figure 5.14. Optimized lattice parameters of a=b=c=14.64 are obtained with a zero band gap at the PBE level of theory. Notably, large formation energies are observed, suggesting an intrinsic instability of this compound. This is in line with previous studies on the Bi-based analogue,[45] which allows us to rule out given geometry.

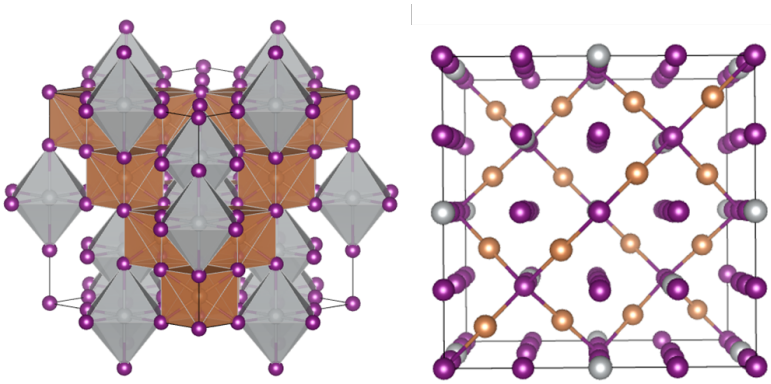

Figure 5.14: Optimized geometry (PBE, D3) of the $AgSb_2I_7$ composition resulting in a cubic structure with cell parameters a=b=c=14. At PBE level of theory, this composition shows metallic behavior with band gap of $0\,eV$. Colors are as follows: Sb, brown; Ag, silver; I, purple.

Next, we consider the $CdCl_2$-type crystal structures, in particular $AgSbI_4$ and Ag_3SbI_6, which have been frequently proposed for the Bi-based analogues.[38,54,55,66] Starting from the $AgSbI_4$, a $CdCl_2$-type crystal with $\frac{1}{2}$ Sb and $\frac{1}{2}$ Ag occupation of the octahedral centers, see Figure 5.15. We observe low differences in energies and cell parameters, see Table 5.3, with the c2 configuration that contains alternating Ag and Sb centers being most favorable.

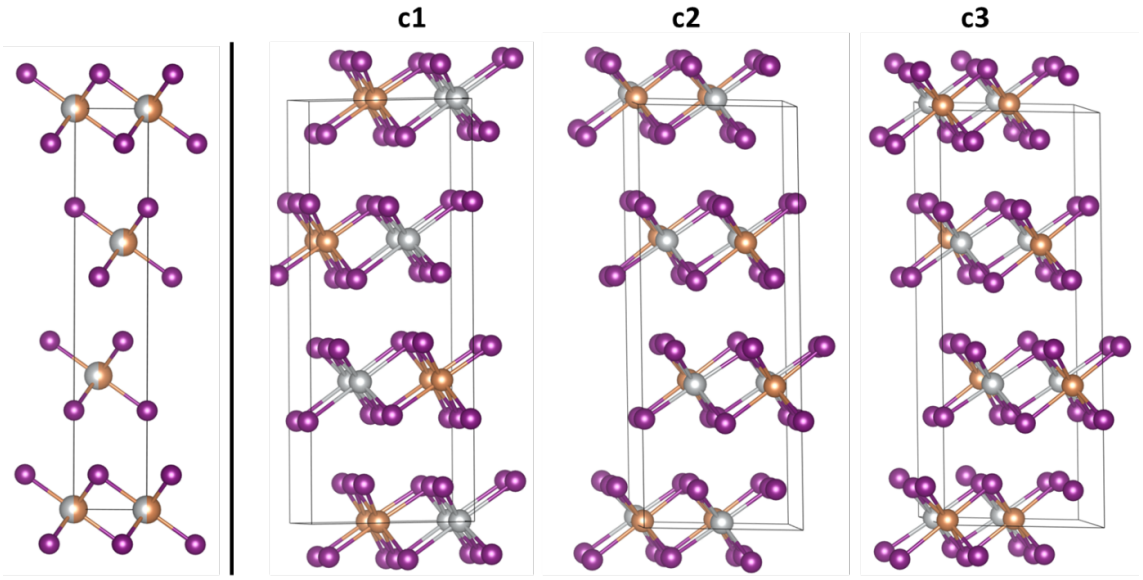

Figure 5.15: (left) $CdCl_2$-type structure with $AgSbI_4$ stoichiometry with metal centers occupied by $\frac{1}{2}$ Sb and $\frac{1}{2}$ Ag. (right) Permutations of the $AgSbI_4$ geometries, labeled with c1 to c3. Colors are as follows: Sb, brown; Ag, silver; I, purple.

Next, we focus on the crystal structure of Ag_3SbI_6. Starting from the structure proposed by Oldag et al.,[38] we consider various permutations and perform optimizations of the ionic positions and the cell parameters. Starting from the $AgSbI_4$, a $CdCl_2$-type crystal with $\frac{1}{2}$ Sb and $\frac{1}{2}$ occupation of the octahedral centers, see Figure 5.16. We observe low differences in energies and cell parameters, see Table 5.3, for final cell parameters, energies, and band gaps. Notably, the Ag_3SbI_6 structures show a reduction in electronic band gap compared to the $AgSbI_4$ ones and further feature larger formation energies, thus being less likely to appear.

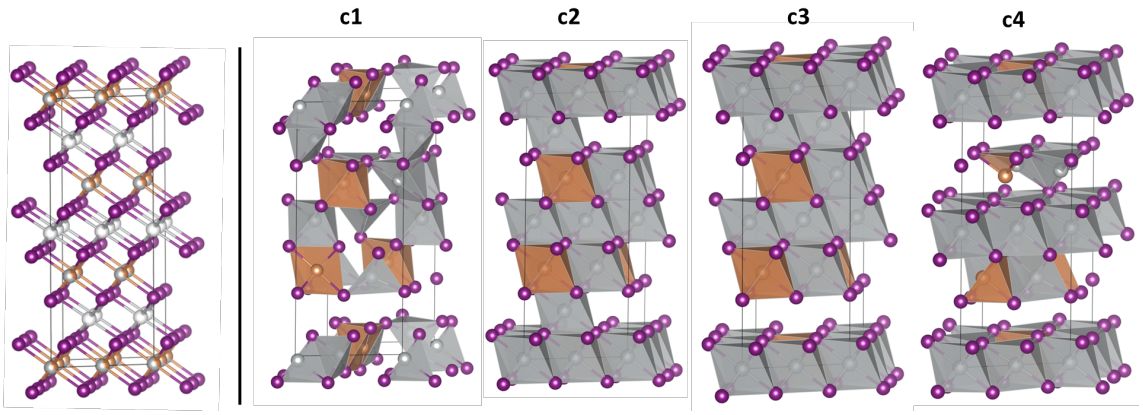

Figure 5.16: (left) $CdCl_2$-type structure with Ag_3SbI_6 stoichiometry following Oldag et al.[38] Metal centers in the mixed Sb/Ag layers are occupied by $\frac{1}{2}$ Sb and $\frac{1}{2}$ Ag. The sites in the interlayers are populated by 1/3 Ag to complete the stoichiometry. (right) Permutations of the Ag_3SbI_6 geometries, labeled with c1 to c4. Colors are as follows: Sb, brown; Ag, silver; I, purple.

Upon Cu addition, we consider the formation of a Cu_2AgSbI_6 phase as reported from recent studies on the Bi-based counterpart.[28] The fundamental crystal structure is modeled by replacing Bi of the Cu_2AgBiI_6[40] by Sb. As shown in Figure 5.17, there is disorder in the Ag/Sb sites and a plentitude of potential positions for Cu, highlighting the large disorder in this system. To derive low energy structures, we constructed a variety of several configurations, Figure 5.17, following some fundamental rules:

- Random distribution of Sb, Ag, and vacancies, with at least three Ag or Sb ions being in each layer.

- The charge of the Sb, Ag, and Cu ions in each layer should balance the charge of the 8 iodide ions. Thus, according to the amount of Sb and Ag placed in between the iodides, Cu ions are added randomly to bond undercoordinated I ions.

- We place maximal as many Cu ions in between the Sb/Ag layer as Ag or Sb are present. The remaining Cu ions are placed on the Ag/Sb sites.

Note that this certainly does not sample the full compositional space, but provides fundamental insight into the structural and electronic properties of the Cu_2AgSbI_6. We further note that the resulting structures show similar features as the low energy structures predicted by Sansom et al.[40] for the Bi-based system.

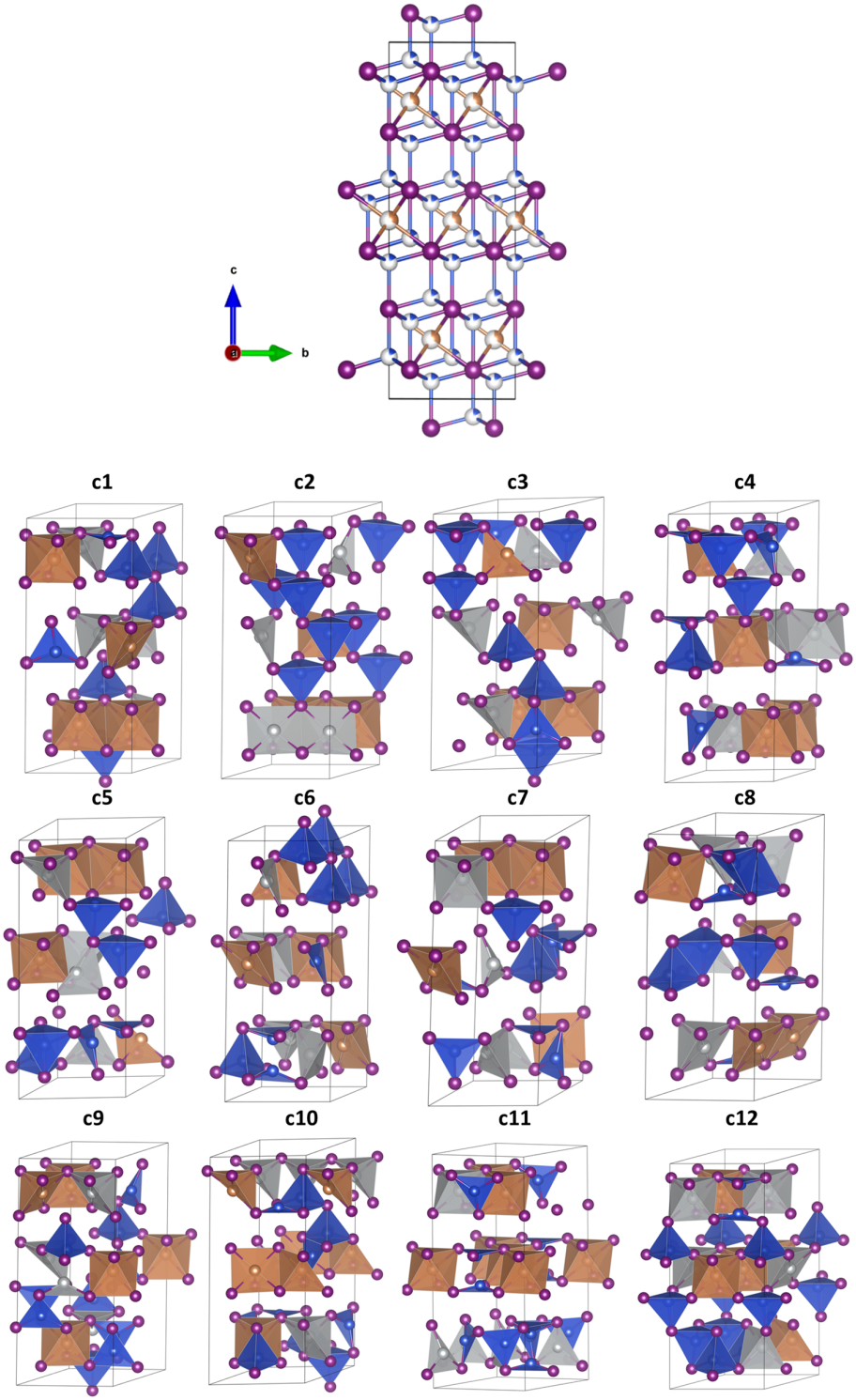

Figure 5.17: (Top) Visualization of the $CdCl_2$-type structure with Cu_2AgSbI_6 stoichiometry with partial occupations highlighted, following Sansom et al.[40] (Bottom) Exemplary structural configurations of the Cu_2AgSbI_6 stoichiometry. Colors are as follows: Sb, brown; Ag, silver; I, purple.

System	Config.	E_F (eV/f.u.)	E_g (eV)	Lattice constants (Å)	Cell Angles (°)
		PBE / PBE0	PBE / PBE0		
$AgSb_2I_7$	-	4.09 / 4.86	0 / 0.39	a=b=c=14.64	α=β=γ=90
$AgSbI_4$	c1	0.03 / 0.00	1.07 / 2.13	a = 8.684	α=89.99
				b = 8.579	β=89.26
				c = 20.828	γ=119.60
	c2	0.01 / -0.01	1.03 / 2.07	a = 8.671	α=88.97
				b = 8.665	β=91.11
				c = 20.804	γ=120.58
	c3	0.03 / -0.01	1.06 / 2.10	a = 8.696	α=89.22
				b = 8.692	β=90.79
				c = 20.870	γ=120.77
Ag_3SbI_6	c1	0.24 / 0.12	0.43 / 1.54	a = 8.569	α=90.03
				b = 8.983	β=91.81
				c = 20.829	γ=120.88
	c2	0.15 / 0.03	0.76 / 1.70	a = 9.123	α=87.35
				b = 8.659	β=91.76
				c = 20.852	γ=121.84
	c3	0.14 / 0.03	0.82 / 1.78	a = 9.178	α=86.57
				b = 8.751	β=92.47
				c = 20.763	γ=122.65
	c4	0.59 / 0.52	0.23 / 0.70	a = 8.685	α=89.66
				b = 8.684	β=90.31
				c = 20.383	γ=119.59
Cu_2AgSbI_6	c1	0.54 / 1.13	0.54 / 0.43	a = 8.640	α=90.11
				b = 8.588	β=89.89
				c = 20.720	γ=119.94
	c2	0.17 / 0.56	0.45 / 1.50	a = 8.567	α=89.81
				b = 8.539	β=90.45
				c = 20.991	γ=119.60
	c3	0.58 / 0.97	0.12 / 0.45	a = 8.786	α=87.17
				b = 8.572	β=89.96
				c = 20.953	γ=121.03
	c4	0.16 / 0.52	0.81 / 2.04	a = 8.574	α=89.43

				b = 8.635	β=90.85
				c = 21.161	γ=120.69
	c5	0.18 / 0.73	0.96 / 2.03	a = 8.593	α=90.70
				b = 8.611	β=90.32
				c = 21.051	γ=119.98
	c6	0.20 / 0.41	0.81 / 1.89	a = 8.571	α=90.69
				b = 8.598	β=90.75
				c = 21.242	γ=120.39
	c7	0.19 / 0.63	0.99 / 2.09	a = 8.674	α=90.02
				b = 8.548	β=90.58
				c = 21.196	γ=120.65
	c8	0.18 / 0.57	0.74 / 1.82	a = 8.593	α=88.20
				b = 8.539	β=89.88
				c = 21.323	γ=120.14
	c9	0.18 / 0.52	0.71 / 1.79	a = 8.728	α=89.57
				b = 8.654	β=90.41
				c = 20.792	γ=120.64
	c10	0.30 / 0.64	0.29 / 1.29	a = 8.688	α=88.49
				b = 8.618	β=91.12
				c = 20.906	γ=120.48
	c11	0.06 / 0.42	0.86 / 1.90	a = 8.551	α=89.96
				b = 8.525	β=90.11
				c = 21.452	γ=119.52
	c12	0.33 / 0.68	0.02 / 0.85	a = 8.574	α=88.96
				b = 8.618	β=90.51
				c = 20.884	γ=120.32
$Cu_{0.5}Ag_{0.5}SbI_4$	-	0.06 / 0.14	0.83 / 2.13	a = 8.671	α=88.97
				b = 8.665	β=91.11
				c = 20.804	γ=120.58

Table 5.3: Optimized lattice parameters (PBE, D3) of the Ag-Sb-I and the Cu/Ag-Sb-I rudorffites. Formation energies and electronic band gaps are given at the PBE level of theory; refined band gaps and formation energies are calculated on the PBE0 level of theory with inclusion of SOC corrections on the PBE+D3 optimized geometries.

System	ϵ_{elec}	ϵ_{ion}
$AgSbI_4$	ϵ_{xx} = 7.46	ϵ_{xx} = 32.88
	ϵ_{yy} = 7.99	ϵ_{yy} = 36.65
	ϵ_{zz} = 5.84	ϵ_{zz} = 1.50
	ϵ_0 = 15.39	

Table 5.4: Electronic (ϵ_{elec}) and ionic contributions and (ϵ_{ion}), respectively, to the static dielectric constant for $AgSbI_4$. The averaged static dielectric constant, ϵ_0, is used for all defect calculations.

Defect Calculations

Electronic structure and defect calculations of the optimized geometries were performed using 2×2×1 supercells. The PBE0 functional[62] including spin-orbit coupling and DFT-D3 dispersion corrections[61] were employed within the Quantum Espresso package.[58] Here, we used full relativistic norm-conserving pseudopotentials (Ag, 19 electrons, $4s^2$, $4p^6$, $4d^{10}$, $5s^2$, $4p^9$; Sb, 15 electrons, $4d^{10}$, $5s^2$, $5p^3$; I, 7 electrons, $5s^2$, $5p^5$) with a cutoff on the wave functions of 40 Ry and 80 Ry on the Fock grid, an increased fraction of exact exchange in the HSE06 functional of α = 0.43 and sampling the Brillouin zone at the gamma point. PDOS plots have been generated with a Gaussian smearing of 0.1 eV.
DFE and TIL were calculated as follows:[67–69]

$$DFE[X^q] = E[X^q] - E[prist] - \sum_i n_i\mu_i + q(E_{VBM} + E_F) \tag{5.3}$$

$$TIL[q/q^{'}] = \frac{DFE[X^q] - DFE[X^{q'}]}{q^{'} - q} \tag{5.4}$$

where $E[X_q]$ is the energy of the defective supercell with defect X in charge state q, E[prist] is the energy of the pristine supercell, n_i and μ_i are the number and chemical potential of the added and subtracted species, respectively, E_{VBM} and E_F are the valence band energy and the Fermi energy, respectively, and E^q_{corr} are electrostatic potential corrections due to the finite size of the supercell. Electrostatic finite-size effects have been accounted for using the Makov-Payne correction scheme.[70]

Static dielectric constants of $AgSbI_4$ were obtained using the density functional perturbation theory (DFPT)[71] in the Vienna ab initio simulation package (VASP),[72] with PBE exchange-correlation functional[59] and the projector-augmented wave (PAW) method[73] using a 400 eV plane-wave cutoff, 6×6×1 Monckhorst-Pack k-point sampling, and a tightly converged electronic wavefunction (within 10-8 eV).

Role of the functional during defect geometry optimization on TILs

In lead-halide perovskites, defect geometries and TILs were shown to depend also on the role of the used functional during geometry optimization. Hybrid PBE0 calculations have been performed for geometry optimization of the ionic positions using the freely available CP2K software package,[74] keeping the Fock exchange ϵ at 0.25 and including van der Waals interactions with the DFT-D3 scheme including Becke-Johnson damping.[75] Kohn-Sham orbitals are expanded in a double-zeta basis set (DZVP-MOLOPT)[76] in combination with the norm-conserving Goedecker-Teter-Hutter (GTH)[77] pseudopotentials, and a cutoff of 600 Ry for expansion of the electron density in plane waves. The auxiliary density matrix method with the cFIT auxiliary basis set was applied to accelerate the optimization of ionic positions within hybrid functional calculations.[78]
The TILs, shown in Figure 5.18, show low dependence on the utilized exchange correlation functional during geometry optimization for the PBE and PBE0 level of theory. The most relevant Ag point defects show limited changes with the functional. Geometry optimizations with the PBE0 level of theory impose further challenges, resulting in large changes in the layered structures, and require further investigation. Consequently, we report the defect properties with geometries from PBE optimization in the manuscript.

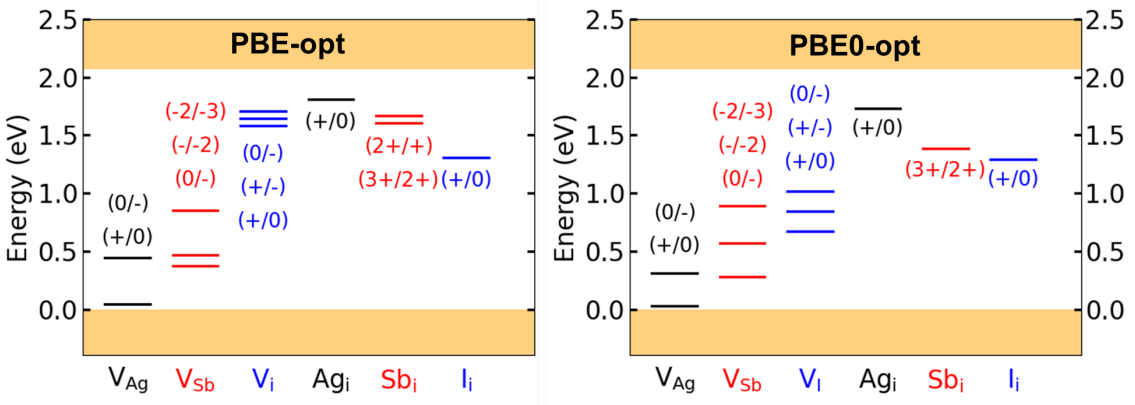

Figure 5.18: Role of exchange correlation functional during geometry optimization on the defect TILs.

Defect Formation Energies

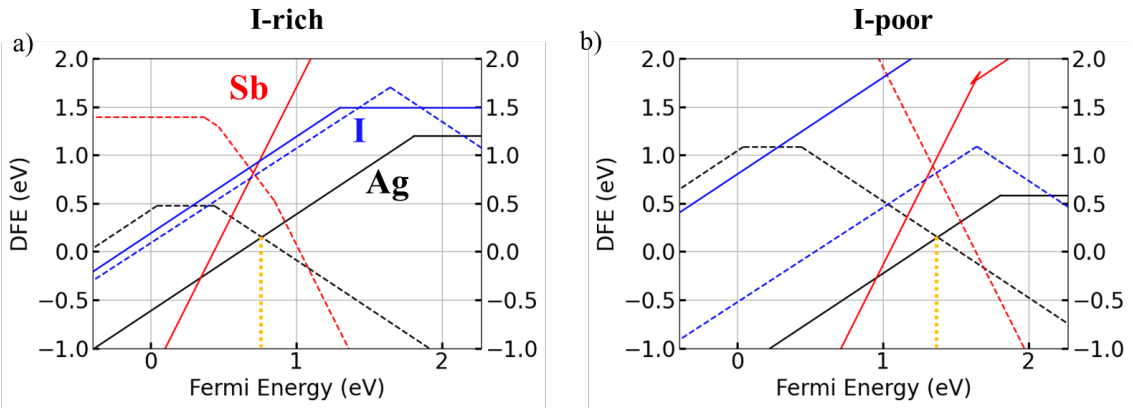

Figure 5.19: . Defect formation energies in $AgSbI_4$ under (a) I-rich and (b) I-poor conditions. Solid lines give the DFE for interstitials, dashed lines visualize DFEs for vacancies. The Fermi level of the system, dominated by the defect equilibrium between Ag vacancies and Ag interstitials, is highlighted by the dotted vertical line.

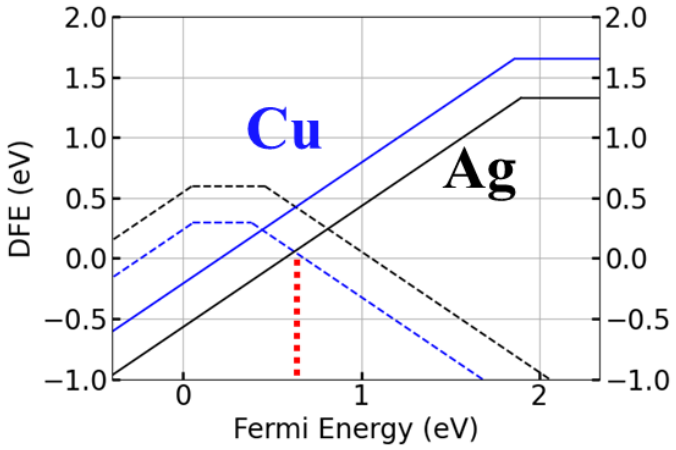

Figure 5.20: Defect formation energies of $Cu0.5Ag0.5SbI_4$ under I-rich conditions. Solid lines give the DFE for interstitials, dashed lines visualize DFEs for vacancies. The Fermi level of the system, dominated by the defect equilibrium between Ag vacancies and Cu interstitials, is highlighted by the dotted vertical line.

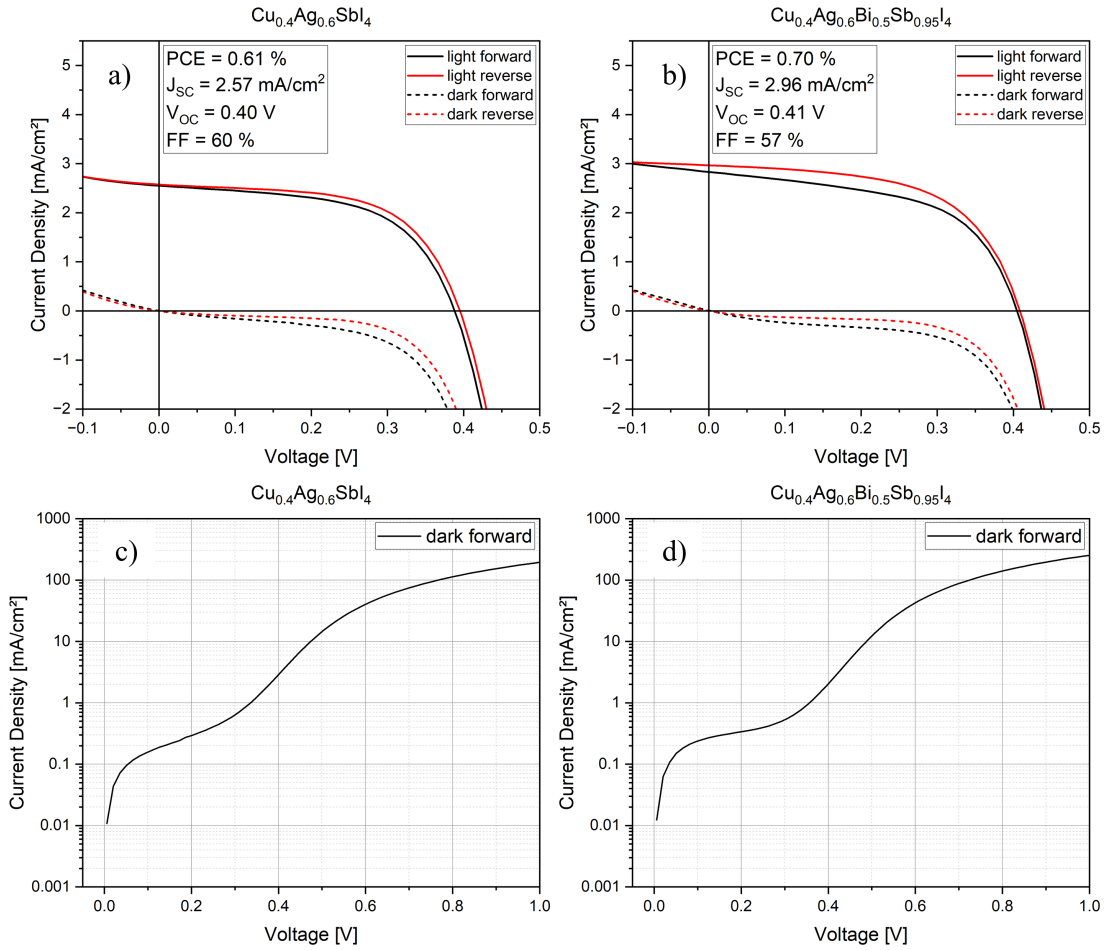

Figure 5.21: Light (a,b) and logarithmic dark (c,d) current-voltage curves for the record pixels (solar cells) discussed in the main text. (a,d) $Cu_{0.4}Ag_{0.6}SbI_4$ without Bi additive, and (b,c) with 5% Bi added.

5.6 REFERENCES

[1] G. Divitini, S. Cacovich, F. Matteocci, L. Cinà, A. Di Carlo, C. Ducati, *Nature Energy* **2016**, *1*, 1–6.

[2] C. C. Boyd, R. Cheacharoen, T. Leijtens, M. D. McGehee, *Chemical Reviews* **2019**, *119*, 3418–3451.

[3] S. P. Dunfield, L. Bliss, F. Zhang, J. M. Luther, K. Zhu, M. F. A. M. Hest, M. O. Reese, J. J. Berry, *Advanced Energy Materials* **2020**, *10*, 1904054.

[4] M. Grätzel, *Accounts of chemical research* **2017**, *50*, 487–491.

[5] F. C. Krebs, N. Espinosa, M. Hösel, R. R. Søndergaard, M. Jørgensen, *Advanced Materials* **2014**, *26*, 29–38.

[6] Z. Li, S. R. Kavanagh, M. Napari, R. G. Palgrave, M. Abdi-Jalebi, Z. Andaji-Garmaroudi, D. W. Davies, M. Laitinen, J. Julin, M. A. Isaacs, R. H. Friend, D. O. Scanlon, A. Walsh, R. L. Z. Hoye, *Journal of Materials Chemistry A* **2020**, *8*, 21780–21788.

[7] G.-.-W. Kim, A. Petrozza, *Advanced Energy Materials* **2020**, *10*, 2001959.

[8] K. X. Steirer, P. Schulz, G. Teeter, V. Stevanovic, M. Yang, K. Zhu, J. J. Berry, *ACS Energy Letters* **2016**, *1*, 360–366.

[9] A. M. Ganose, C. N. Savory, D. O. Scanlon, *Chemical communications (Cambridge England)* **2016**, *53*, 20–44.

[10] R. C. Kurchin, P. Gorai, T. Buonassisi, V. Stevanović, *Chemistry of Materials* **2018**, *30*, 5583–5592.

[11] R. E. Brandt, J. R. Poindexter, P. Gorai, R. C. Kurchin, R. L. Z. Hoye, L. Nienhaus, M. W. B. Wilson, J. A. Polizzotti, R. Sereika, R. Žaltauskas, L. C. Lee, J. L. MacManus-Driscoll, M. Bawendi, V. Stevanović, T. Buonassisi, *Chemistry of Materials* **2017**, *29*, 4667–4674.

[12] G. Nasti, A. Abate, *Advanced Energy Materials* **2020**, *10*, 1902467.

[13] L. Serrano-Lujan, N. Espinosa, T. T. Larsen-Olsen, J. Abad, A. Urbina, F. C. Krebs, *Advanced Energy Materials* **2015**, *5*, 1501119.

[14] A. Weis, P. Ganswindt, W. Kaiser, H. Illner, C. Maheu, N. Glück, P. Dörflinger, M. Armer, V. Dyakonov, J. P. Hofmann, *The Journal of Physical Chemistry C* **2022**, *126*, 21040–21049.

[15] T. Leijtens, R. Prasanna, A. Gold-Parker, M. F. Toney, M. D. McGehee, *ACS Energy Letters* **2017**, *2*, 2159–2165.

[16] D. Ricciarelli, D. Meggiolaro, F. Ambrosio, F. de Angelis, *ACS Energy Letters* **2020**, *5*, 2787–2795.

[17] M. Aldamasy, Z. Iqbal, G. Li, J. Pascual, F. Alharthi, A. Abate, M. Li, *Physical chemistry chemical physics : PCCP* **2021**, *23*, 23413–23427.

[18] W. Tress, M. T. Sirtl, *Solar Rrl* **2022**, *6*, 2100770.

[19] R. L. Z. Hoye, L. Eyre, F. Wei, F. Brivio, A. Sadhanala, S. Sun, W. Li, K. H. L. Zhang, J. L. MacManus-Driscoll, P. D. Bristowe, R. H. Friend, A. K. Cheetham, F. Deschler, *Advanced Materials Interfaces* **2018**, *5*, 1800464.

[20] M. T. Sirtl, F. Ebadi, B. T. Gorkom, P. Ganswindt, R. A. J. Janssen, T. Bein, W. Tress, *Advanced Optical Materials* **2021**, *9*, DOI 10.1002/adom.202100202.

[21] P. C. Harikesh, H. K. Mulmudi, B. Ghosh, T. W. Goh, Y. T. Teng, K. Thirumal, M. Lockrey, K. Weber, T. M. Koh, S. Li, S. Mhaisalkar, N. Mathews, *Chemistry of Materials* **2016**, *28*, 7496–7504.

[22] D. B. Mitzi, *Journal of the Chemical Society Dalton Transactions* **2001**, *0*, 1–12.

[23] I. Turkevych, S. Kazaoui, E. Ito, T. Urano, K. Yamada, H. Tomiyasu, H. Yamagishi, M. Kondo, S. Aramaki, *ChemSusChem* **2017**, *10*, 3754–3759.

[24] C. Lu, J. Zhang, H. Sun, D. Hou, X. Gan, M.-h. Shang, Y. Li, Z. Hu, Y. Zhu, L. Han, *ACS Applied Energy Materials* **2018**, *1*, 4485–4492.

[25] N. Pai, J. Lu, T. R. Gengenbach, A. Seeber, A. S. R. Chesman, L. Jiang, D. C. Senevirathna, P. C. Andrews, U. Bach, Y.-.-B. Cheng, A. N. Simonov, *Advanced Energy Materials* **2019**, *9*, 1803396.

[26] S. Tie, W. Zhao, W. Huang, D. Xin, M. Zhang, Z. Yang, J. Long, Q. Chen, X. Zheng, J. Zhu, W.-H. Zhang, *The journal of physical chemistry letters* **2020**, *11*, 7939–7945.

[27] H. Ye, B. Sun, Z. Wang, Z. Liu, X. Zhang, X. Tan, T. Shi, Z. Tang, G. Liao, *Journal of Materials Chemistry C* **2020**, *8*, 14155–14163.

[28] G. K. Grandhi, B. Al-Anesi, H. Pasanen, H. Ali-Löytty, K. Lahtonen, S. Granroth, N. Christian, A. Matuhina, M. Liu, A. Berdin, V. Pecunia, P. Vivo, *Small (Weinheim an der Bergstrasse Germany)* **2022**, *18*, e2203768.

[29] B. Al-Anesi, G. K. Grandhi, A. Pecoraro, V. Sugathan, N. Viswanath, H. Ali-Löytty, M. Liu, T.-P. Ruoko, K. Lahtonen, D. Manna, S. Toikkonen, A. B. Muñoz-García, M. Pavone, P. Vivo, *Antimony-bismuth alloying: the key to a major boost in the efficiency of lead-free perovskite-inspired indoor photovoltaics*, **2023**.

[30] R. Nishikubo, H. Kanda, I. Garcia-Benito, A. Molina-Ontoria, G. Pozzi, A. M. Asiri, M. K. Nazeeruddin, A. Saeki, *Chemistry of Materials* **2020**, *32*, 6416–6424.

[31] M. B. Gray, E. T. McClure, N. P. Holzapfel, F. P. Evaristo, W. Windl, P. M. Woodward, *Journal of Solid State Chemistry* **2021**, *297*, 121997.

[32] D. Ferro, B. Nappi, V. Piacente, *The Journal of Chemical Thermodynamics* **1979**, *11*, 193–201.

[33] A. Chakraborty, N. Pai, J. Zhao, B. R. Tuttle, A. N. Simonov, V. Pecunia, *Advanced Functional Materials* **2022**, *32*, 2203300.

[34] H. Luo, J. Wu, X. Liu, Y. Yang, Q. Liu, M. Zhang, P. Yuan, W. Sun, Z. Lan, J. Lin, *ACS Applied Energy Materials* **2018**, *1*, 6700–6706.

[35] J. V. Patil, S. S. Mali, C. K. Hong, *Nanoscale* **2019**, *11*, 21824–21833.

[36] S. Wang, Z. Ma, B. Liu, W. Wu, Y. Zhu, R. Ma, C. Wang, *Solar Rrl* **2018**, *2*, 1800034.

[37] Y. Yang, C. Liu, M. Cai, Y. Liao, Y. Ding, S. Ma, X. Liu, M. Guli, S. Dai, M. K. Nazeeruddin, *ACS applied materials & interfaces* **2020**, *12*, 17062–17069.

[38] T. Oldag, T. Aussieker, H.-L. Keller, C. Preitschaft, A. Pfitzner, *Zeitschrift fr anorganische und allgemeine Chemie* **2005**, *631*, 677–682.

[39] H. C. Sansom, G. F. S. Whitehead, M. S. Dyer, M. Zanella, T. D. Manning, M. J. Pitcher, T. J. Whittles, V. R. Dhanak, J. Alaria, J. B. Claridge, *Chemistry of Materials* **2017**, *29*, 1538–1549.

[40] H. C. Sansom, L. R. V. Buizza, M. Zanella, J. T. Gibbon, M. J. Pitcher, M. S. Dyer, T. D. Manning, V. R. Dhanak, L. M. Herz, H. J. Snaith, J. B. Claridge, M. J. Rosseinsky, *Inorganic Chemistry* **2021**, *60*, 18154–18167.

[41] L. F. Mashadieva, Z. S. Aliev, A. V. Shevelkov, M. B. Babanly, *Journal of Alloys and Compounds* **2013**, *551*, 512–520.

[42] A. Kulkarni, F. Ünlü, N. Pant, J. Kaur, C. Bohr, A. K. Jena, S. Öz, M. Yanagida, Y. Shirai, M. Ikegami, K. Miyano, Y. Tachibana, S. Chakraborty, S. Mathur, T. Miyasaka, *Solar Rrl* **2021**, *5*, 2100077.

[43] H. Ünlü, *Solid-State Electronics* **1992**, *35*, 1343–1352.

[44] A. Koedtruad, M. Goto, M. Amano Patino, Z. Tan, H. Guo, T. Nakamura, T. Handa, W.-T. Chen, Y.-C. Chuang, H.-S. Sheu, T. Saito, D. Kan, Y. Kanemitsu, A. Wakamiya, Y. Shimakawa, *Journal of Materials Chemistry A* **2019**, *7*, 5583–5588.

[45] Z. Xiao, W. Meng, D. B. Mitzi, Y. Yan, *The journal of physical chemistry letters* **2016**, *7*, 3903–3907.

[46] A. Merker, M. Morgenroth, M. Scholz, T. Lenzer, K. Oum, *The Journal of Physical Chemistry C* **2023**, *127*, 1487–1498.

[47] G. Giovilli, B. Albini, V. Grisci, S. Bonomi, M. Moroni, E. Mosconi, W. Kaiser, F. de Angelis, P. Galinetto, L. Malavasi, *Journal of Materials Chemistry C* **2023**, DOI 10.1039/D3TC01492D.

[48] L. R. V. Buizza, H. C. Sansom, A. D. Wright, A. M. Ulatowski, M. B. Johnston, H. J. Snaith, L. M. Herz, *Advanced Functional Materials* **2022**, *32*, 2108392.

[49] R. Hooijer, A. Weis, A. Biewald, M. T. Sirtl, J. Malburg, R. Holfeuer, S. Thamm, A. A. Y. Amin, M. Righetto, A. Hartschuh, L. M. Herz, T. Bein, *Advanced Optical Materials* **2022**, *10*, 2200354.

[50] A. D. Wright, L. R. V. Buizza, K. J. Savill, G. Longo, H. J. Snaith, M. B. Johnston, L. M. Herz, *The journal of physical chemistry letters* **2021**, *12*, 3352–3360.

[51] M. T. Sirtl, M. Armer, L. K. Reb, R. Hooijer, P. Dörflinger, M. A. Scheel, K. Tvingstedt, P. Rieder, N. Glück, P. Pandit, S. V. Roth, P. Müller-Buschbaum, V. Dyakonov, T. Bein, *ACS Applied Energy Materials* **2020**, *3*, 11597–11609.

[52] Y. Kim, Z. Yang, A. Jain, O. Voznyy, G.-H. Kim, M. Liu, L. N. Quan, F. P. García de Arquer, R. Comin, J. Z. Fan, E. H. Sargent, *Angewandte Chemie (International ed. in English)* **2016**, *55*, 9586–9590.

[53] H. Zhu, A. Erbing, H. Wu, G. J. Man, S. Mukherjee, C. Kamal, M. B. Johansson, H. Rensmo, M. Odelius, E. M. J. Johansson, *ACS Applied Energy Materials* **2020**, *3*, 7372–7382.

[54] K.-C. Hsiao, Y.-F. Yu, C.-M. Ho, M.-H. Jao, Y.-H. Chang, S.-H. Chen, Y.-H. Chang, W.-F. Su, K.-M. Lee, M.-C. Wu, *Chemical Engineering Journal* **2023**, *451*, 138807.

[55] A. Crovetto, A. Hajijafarassar, O. Hansen, B. Seger, I. Chorkendorff, P. C. K. Vesborg, *Chemistry of Materials* **2020**, *32*, 3385–3395.

[56] J. W. Park, Y. Lim, K.-Y. Doh, M. T. Jung, Y. in Jeon, I. S. Yang, H.-s. Choi, J. Kim, D. Lee, W. in Lee, *Sustainable Energy & Fuels* **2021**, *5*, 1439–1447.

[57] N. Giesbrecht, A. Weis, T. Bein, *Journal of Physics: Energy* **2020**, *2*, 024007.

[58] P. Giannozzi, S. Baroni, N. Bonini, M. Calandra, R. Car, C. Cavazzoni, D. Ceresoli, G. L. Chiarotti, M. Cococcioni, I. Dabo, A. Dal Corso, S. de Gironcoli, S. Fabris, G. Fratesi, R. Gebauer, U. Gerstmann, C. Gougoussis, A. Kokalj, M. Lazzeri, L. Martin-Samos, N. Marzari, F. Mauri, R. Mazzarello, S. Paolini, A. Pasquarello, L. Paulatto, C. Sbraccia, S. Scandolo, G. Sclauzero, A. P. Seitsonen, A. Smogunov, P. Umari, R. M. Wentzcovitch, *Journal of Physics: Condensed Matter* **2009**, *21*, 395502.

[59] J. P. Perdew, K. Burke, M. Ernzerhof, *Physical review letters* **1996**, *77*, 3865.

[60] H. J. Monkhorst, J. D. Pack, *Physical review B* **1976**, *13*, 5188.

[61] S. Grimme, J. Antony, S. Ehrlich, H. Krieg, *The Journal of Chemical Physics* **2010**, *132*, 154104.

[62] C. Adamo and V. Barone, *The Journal of Chemical Physics* **1999**, 6158–6170.

[63] V. D'innocenzo, G. Grancini, M. J. Alcocer, A. R. S. Kandada, S. D. Stranks, M. M. Lee, G. Lanzani, H. J. Snaith, A. Petrozza, *Nature communications* **2014**, *5*, 3586.

[64] F. Urbach, *Physical Review* **1953**, *92*, PR, 1324–1324.

[65] M. Ledinsky, T. Schönfeldová, J. Holovský, E. Aydin, Z. Hájková, L. Landová, N. Neyková, A. Fejfar, S. De Wolf, *The Journal of Physical Chemistry Letters* **2019**, *10*, 1368–1373.

[66] Z. Xiao, W. Meng, J. Wang, Y. Yan, *ChemSusChem* **2016**, *9*, 2628–2633.

[67] D. Meggiolaro, F. De Angelis, *ACS Energy Letters* **2018**, *3*, doi: 10.1021/acsenergylett.8b01212, 2206–2222.

[68] A. Alkauskas, P. Deák, J. Neugebauer, A. Pasquarello, C. G. de van Walle, *Advanced Calculations for Defects in Materials: Electronic Structure Methods*, 1. Auflage, Wiley-VCH, Weinheim, **2011**.

[69] D. Meggiolaro, F. de Angelis, *ACS Energy Letters* **2018**, *3*, 2206–2222.

[70] M. Leslie, N. J. Gillan, *Journal of Physics C: Solid State Physics* **1985**, *18*, 973–982.

[71] *De Gironcoli, AD Corso, S*, **2001**.

[72] A. S. Botana, M. R. Norman, *Physical Review Materials* **2019**, *3*, DOI 10.1103/physrevmaterials.3.044001.

[73] P. E. Blöchl, O. Jepsen, O. K. Andersen, *Physical review. B Condensed matter* **1994**, *49*, 16223–16233.

[74] T. D. Kühne, M. Iannuzzi, M. Del Ben, V. V. Rybkin, P. Seewald, F. Stein, T. Laino, R. Z. Khaliullin, O. Schütt, F. Schiffmann, D. Golze, J. Wilhelm, S. Chulkov, M. H. Bani-Hashemian, V. Weber, U. Borštnik, M. Taillefumier, A. S. Jakobovits, A. Lazzaro, H. Pabst, T. Müller, R. Schade, M. Guidon, S. Andermatt, N. Holmberg, G. K. Schenter, A. Hehn, A. Bussy, F. Belleflamme, G. Tabacchi, A. Glöß, M. Lass, I. Bethune, C. J. Mundy, C. Plessl, M. Watkins, J. VandeVondele, M. Krack, J. Hutter, *The Journal of Chemical Physics* **2020**, *152*, 194103.

[75] S. Ehrlich, J. Moellmann, W. Reckien, T. Bredow, S. Grimme, *ChemPhysChem* **2011**, *12*, 3414–3420.

[76] J. VandeVondele, J. Hutter, *The Journal of Chemical Physics* **2007**, *127*, 114105.

[77] S. Goedecker, M. Teter, J. Hutter, *Physical review. B Condensed matter* **1996**, *54*, 1703–1710.

[78] M. Guidon, J. Hutter, J. VandeVondele, *Journal of chemical theory and computation* **2010**, *6*, 2348–2364.

Low Temperature Optical Properties of Novel Lead-Free $Cs_2NaFeCl_6$ Perovskite Single Crystals

6

This chapter is based on following publication:
M. Armer*, P. Dörflinger*, A. Weis, C. Büchner, A. Gottscholl, J. Höcker, K. Frank, L. Nusser, M. T. Sirtl, B. Nickel, T. Bein, V. Dyakonov, Advanced Photonics Research **2023**, 2300017.

*These authors contributed equally to this work

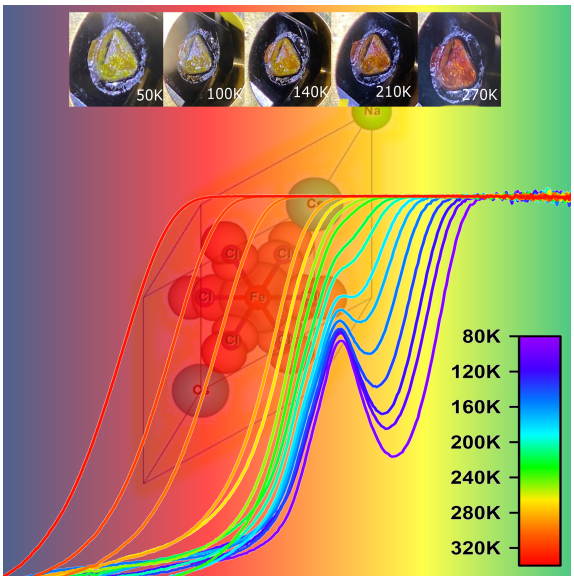

6.1 ABSTRACT

Lead-free double perovskites have attracted lots of attention as possible alternative to the lead halide based perovskite in photovoltaic applications. However, up to now, only few double perovskites have been successfully employed in optoelectronic technical device prototypes. Therefore, the search for other stable and lead-free materials is ongoing. Here, we present the successful growth of high-quality $\mathrm{Cs_2NaFeCl_6}$ single crystals and its temperature-dependent structural and optical properties. By combining electron paramagnetic resonance (EPR), crystal structure analysis and density functional theory (DFT) we could determine a cubic crystal structure with a spin of 5/2. Additionally, DFT revealed a spin polarized electronic character with an indirect semiconducting bandgap, which shows a direct transition located only $30\,\mathrm{meV}$ below the valence band maximum. Furthermore, connecting photoluminescence (PL) and absorption measurements we find a bandgap of approximately $2.1\,\mathrm{eV}$ at room temperature as well as the presence of excitonic states. Using Elliot's theory we are able to extract the temperature dependent behavior of the bandgap as well as an estimated exciton binding energy of only $20\,\mathrm{meV}$ at $80\,\mathrm{K}$.

6.2 INTRODUCTION

Lead-free double perovskites, are becoming more and more popular due to their promising properties, such as long photoluminescence lifetimes, high crystallinity and high stability to oxygen and humidity.[1–3] Nevertheless, the usage of lead-free double perovskites in electronic devices is an ongoing and challenging project although it is possible to manufacture prototypes of X-ray, photodetectors, and light emitting diodes.[4–9] Furthermore, it was recently shown that double perovskite solar cells are strongly limited by indirect band gaps, high trap densities, low charge carrier diffusion lengths, poor energy level alignment as well as poor contact selectivity in the device.[10,11] Therefore, the search for other lead-free double perovskite structures and the investigation of their characteristic physical properties and their limitations is still a hot topic in perovskite research in order to accelerate their industrial applications in the near future.

Recently, cesium sodium iron chloride ($\mathrm{Cs_2NaFeCl_6}$) single crystals were introduced as new promising lead-free double perovskite material for thermochromic applications.[12] It has been shown that the perovskite has a bandgap of $2.07\,\mathrm{eV}$ at room temperature (RT) and exhibits promising absorption in the visible region.[13] Furthermore, doping $\mathrm{Cs_2NaFeCl_6}$ with small amounts of the metal silver (Ag) resulted in significant changes in structural

and optoelectronic properties.[13] It was found that incorporating silver into the crystal structure leads to a decrease of the lattice constant.[13] As a result, it was also possible to significantly modify the bandgaps of crystals with a stoichiometry of $Cs_2Ag_xNa_{1-x}FeCl_6$ ($0 \leq x \leq 1$) from $2.07\,eV$ for the pure $Cs_2NaFeCl_6$ to $1.55\,eV$ for $Cs_2AgFeCl_6$.[13]
Although, silver-doped $Cs_2NaFeCl_6$ showed promising properties for the application in optoelectronic devices such as a tuneable bandgap and improved charge carrier mobilities,[13] only little is known about the fundamental physical properties of the pure $Cs_2NaFeCl_6$. Latest studies proposed a fundamental change of the optical properties from low to high temperatures, due to an order-disorder transition in the material.[12] The observed order-disorder transition is caused by the expansion of the lattice constant of $Cs_2NaFeCl_6$, which results in slight variations of bond lengths and bond angles with rising temperature. As a result, a reversible color change of the crystal was observed going from yellow at $80\,K$ to red at $300\,K$ and to black at $500\,K$. It was concluded that the color change of the crystal and the temperature dependent band gap variation makes $Cs_2NaFeCl_6$ a promising candidate for thermochromic applications.[12] Although, a significant temperature dependence of the band gap was reported by absorption measurements, nothing is yet reported about the emission properties of $Cs_2NaFeCl_6$ crystals. However, the material emission is another important key whether a material can be also used as absorber layer in optoelectronic devices.[14]
In this work, we first of all report the growth of high quality $Cs_2NaFeCl_6$ single crystals by the established controlled cooling growth method.[12,13,15–17] We then continued to perform detailed qualitative, quantitative and structural measurements by applying the techniques X-ray fluorescence (XRF), EDX, and X-ray diffraction (XRD) to confirm the growth of the single crystal with the specified stoichiometry. In addition, we analyzed the temperature dependence of the crystal structure through EPR, to investigate a possible structural phase transition of $Cs_2NaFeCl_6$ at low temperatures. Moreover, DFT calculations were conducted to elucidate the electronic structure and possible spin states as Fe(III) exhibits unpaired spins in the d orbital. In a last step, we intensively investigated the color change of the crystal by means of temperature-dependent photoluminescence (PL) and absorptance. The applied measurement techniques provided a deeper understanding of the fundamental properties of $Cs_2NaFeCl_6$.

6.3 RESULTS AND DISCUSSION

In order to improve the growth process and obtain reproducible, phase-pure and large-sized crystals, we prepared temperature dependent solubility diagrams. To achieve the correct stoichiometry, the precursor salts cesium chloride (CsCl, 2 eq), sodium chloride (NaCl, 1 eq) and iron(III) chloride ($\mathrm{FeCl_3}$, 1 eq) were dissolved in hydrochloric acid (HCl, 37 wt%). We found that the solubility of the perovskite is approximately 9 times higher at a temperature of 100°C compared to RT, as can be seen from the solubility curve in Figure 6.1a. Therefore, by slowly cooling down the solution at a rate of 1°C/h the solubility decreased. A reduced solubility with decreasing temperature has also been observed for the more common double perovskite $\mathrm{Cs_2AgBiBr_6}$ in the past, when acids were used as solvents.[18,19]

By slowly reducing the temperature, supersaturation of the perovskite solution was achieved at around 70°C, followed by the formation of small nuclei. By further cooling the solution the small crystal nuclei started to grow into larger red crystals. (Further details about the crystal growth setup, see Supporting Information (SI)). After successful growth, the crystals showed defined facets and a clear octahedral shape, typically observed for lead-free double perovskites.[7,9,10]

As a next step, we analyzed the grown crystals by means of XRF and EDX in order to confirm the incorporation of the elements caesium (Cs), sodium (Na), iron (Fe), and chloride (Cl) by their corresponding photon energies determining their stoichiometry. For XRF measurements the crystals were ground into a fine powder. Figure 6.1b clearly identifies the $L_{\alpha 1}$ and $L_{\beta 1}$ X-ray emission lines of Cs at $4.34\,\mathrm{keV}$ and $4.72\,\mathrm{keV}$ respectively. Moreover, we could assign, the $K_{\alpha 1}$ and $K_{\beta 1}$ lines of Fe and Cl at the photon energies $6.51\,\mathrm{keV}$, $7.10\,\mathrm{keV}$ and $2.79\,\mathrm{keV}$. We could not find any emission lines for Na, due to the very low photon energies of the Na shells.[20]

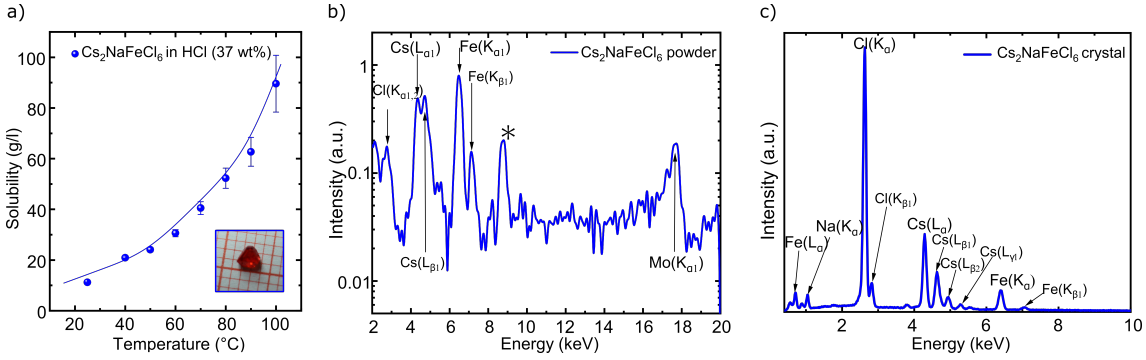

Figure 6.1: (a) Temperature-dependent solubility of $Cs_2NaFeCl_6$ precursor salts with a photograph of a millimeter sized crystal as inset. The solid line is a guide to the eye. (b) XRF spectrum of a ground $Cs_2NaFeCl_6$ crystal with the assigned energies for the elements Cs, Fe and Cl. The peak marked with an asterisk is due to the sample holder. (c) EDX spectrum of the crystal surface to verify the correct crystal composition and stoichiometry of $Cs_2NaFeCl_6$.

However, by measuring EDX, we were able to detect the elemental composition of the crystal surface. Figure 6.1c shows the obtained EDX spectrum, clearly showing the K shell emission line of Na at $1.04\,\mathrm{keV}$. Additionally, we found the emission lines for Cs ($L_{\alpha1} = 4.29\,\mathrm{keV}$, $L_{\beta1}$=4.63 keV, $L_{\beta2} = 4.95\,\mathrm{keV}$, $L_{\gamma1} = 5.30\,\mathrm{keV}$), Fe ($L_\alpha = 0.71\,\mathrm{keV}$, $K_{\alpha1} = 6.4\,\mathrm{keV}$, $K_{\beta1} = 7.05\,\mathrm{keV}$) and Cl ($K_\alpha = 2.62\,\mathrm{keV}$, $K_\beta = 2.82\,\mathrm{keV}$). Therefore, the obtained XRF and EDX results already hint towards a successful growth of $Cs_2NaFeCl_6$ crystals via the controlled cooling method. In order to determine the exact stoichiometry of the grown crystals, quantitative EDX measurements were additionally performed giving us information about the atom fractions of each element on the crystal surface. Table 6.1 shows a nearly perfect experimentally determined stoichiometry of $Cs_2NaFeCl_6$.

Element	**Theoretical atom fraction (%)**	**Experimental atom fraction (%) (Crystal Surface)**
Cs	20	18.76
Na	10	11.25
Fe	10	8.44
Cl	60	61.55

Table 6.1: Quantitative analysis of the $Cs_2NaFeCl_6$ crystal composition by EDX.

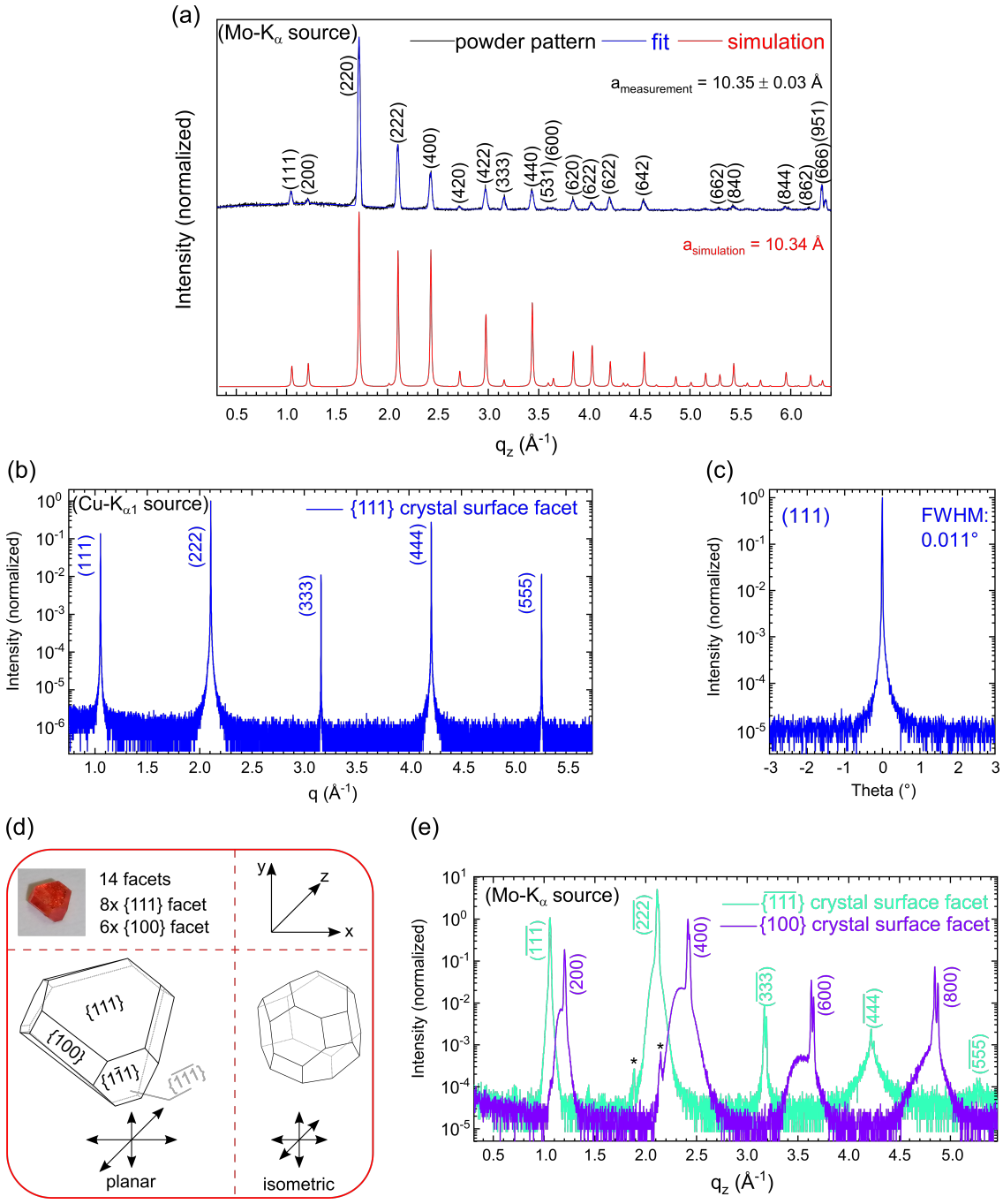

Figure 6.2: Crystal Powder, fitted and simulated XRD pattern for $Cs_2NaFeCl_6$. b) Out-of-plane XRD measurement on $\{111\}$ surface facet and c) corresponding rocking scan of a $Cs_2NaFeCl_6$ single crystal. d) 3D illustration of a $Cs_2NaFeCl_6$ truncated octahedron with determined crystal surface facets. e) XRD measurements on the $(\overline{1}\overline{1}\overline{1})$ surface and on [111] surface facet. The asterisks mark the peaks that can be assigned to the adhesive tape of the sample holder.

To further confirm the crystal structure, we performed XRD measurements of the crystal powder. The XRD pattern in Figure 6.2a suggests a phase-pure growth of $Cs_2NaFeCl_6$ when compared to the crystal structure analysis data from literature.[21] By fitting the

peaks of the obtained XRD pattern we were able to determine the Miller Indices and compared the identified reflexes with the simulated scan (Figure 6.2). We assigned a simple cubic (sc) crystal structure with a lattice constant of a = 10.35 $\pm$ 0.03 Å at RT, which is in perfect agreement with results published recently (for further information see also Figure 6.7).[13,21] In addition to the powder XRD, crystal structure analysis performed at RT verifies the single crystallinity of the grown crystals and the obtained lattice constant of 10.39 Å (Further details see crystal structure analysis in SI). In addition, we conducted out-of-plane XRD and rocking scans to gain more information about the quality of the grown crystals, which are shown in Figure 6.2b and 6.2c. From the out-of-plane XRD pattern, it is clear that the crystal only shows Bragg reflexes belonging to the $\{111\}$ peak series, proving that no other Bragg reflexes can be found on the crystal surface. Furthermore, the $\{111\}$ peak series shows narrow peaks observable up to the fifth order. Those results allow the conclusion of crystal growth along the [111] direction of the unit cell and indicate a single crystalline growth. To verify the quality of the crystal in more detail, we additionally performed rocking scans of the $\{111\}$ and $\{400\}$ reflexes, which are shown in Figure 6.2c and 6.8. The rocking scans revealed single, narrow and very sharp peaks with full width at half maximums (FWHM) below 0.04°. Therefore, we suggest a low mosaicity and conclude that the controlled cooling technique results in high quality and phase-pure $Cs_2NaFeCl_6$ crystals. To gain an understanding of the crystal morphology the next step was to draw a 3D model of a $Cs_2NaFeCl_6$ crystal. The model served as an orientation to assign in a further step the crystal surface facets, which were determined by reflectometry. A total of 4 different facets were measured which are shown in Figure 6.2d and Figure 6.9. The crystal facets of the contact surface in the growth vessel as well as the "free" surfaces grew along the [111] direction and showed the shape of hexagons of different size ratios. The measurement of another crystal surface showed the shape of a rectangle grown in the [100] direction. Using these measurement results and counting the total of 14 crystal surfaces, the eight hexagonal surfaces were assigned to the [111] direction and the 6 rectangular surfaces to the [100] direction. Concerning the crystal habit, the examined $Cs_2NaFeCl_6$ crystal agrees with that of a regular truncated octahedron (Figure 6.3d). Comparing both crystal models in terms of habit, one can assume an isometric one for the regular model since the growth velocity is constant in all three spatial directions x, y and z, symbolized by the arrows in Figure 6.3d. However, this is not the case for the $Cs_2NaFeCl_6$ crystal. Here, we assume a planar growth, since the growth in x and z seems to be preferred to the y-direction. This is an interesting aspect which seems to be independent of the perovskite crystal growth technique and has also been observed for lead-halide perovskite crystals such as methylammonium lead triiodide ($MAPbI_3$).[22]

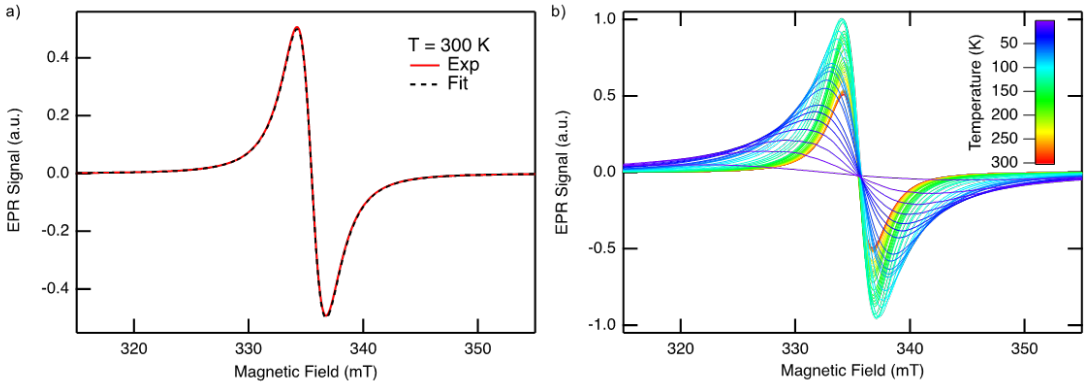

Figure 6.3: a) EPR spectrum of $Cs_2NaFeCl_6$ at RT consistent with a spin of S=1/2 or S=5/2 (with D=0). b) EPR spectra in the range 4-300K shows a cubic structure without any phase transitions (assuming S=5/2).

To further investigate temperature-dependent changes of the crystal structure caused by phase transitions in the material, we performed EPR measurements. EPR allows to directly address the paramagnetic ions , e.g., the Fe^{3+} ions, and predict their spin state and thus the environment.[23] An EPR spectrum of $Cs_2NaFeCl_6$ at RT is depicted in Figure 6.3. Note that the signal (red) shows no significant features and can thus be described by the derivative of a simple Lorentzian (dashed line). This is consistent with a spin S=1/2 or S=5/2 with a zero field splitting (ZFS) of D=0, which are both appropriate candidates for Fe^{3+}.[17] It was already demonstrated for $Cs_2AgBiBr_6$ that the environment (given by the lattice structure) has a direct influence on ZFS.[17] Thus, for a ZFS=0 a cubic and for a ZFS>0 a tetragonal crystal structure is present. Since the stoichiometry and the crystal structure of $Cs_2NaFeCl_6$ is identical to $Cs_2AgBiBr_6$, we use the same approach to investigate possible phase transitions of $Cs_2NaFeCl_6$ at low temperatures. Assuming a spin of S=5/2, as we will later confirm by DFT calculations, the RT measurement suggests the cubic crystal structure of the previously shown XRD data. In order to identify potential phase transitions, the sample was cooled down to $4\,K$ (see Figure 6.3b). In the entire temperature range, the EPR signal can always be fitted with the derivative of a simple Lorentzian, which consistently gives strong indications for a cubic structure of the crystal. In contrast to $Cs_2AgBiBr_6$, no phase transition can be identified $Cs_2NaFeCl_6$ when a spin S=5/2 is assumed.

DFT calculations within the localized spin-density approximation (LSDA) were conducted in order to verify the most stable spin configuration and to elucidate the electronic structure.[24] As the EPR results hint at indistinguishable total spin states of either 1/2 or 5/2, both phases were optimized and relaxed with respect to atomic positions and cell parameters. The relaxation calculations reveal a significantly better estimation of the $[FeCl_6]^{3-}$ octahedral geometry for the high spin state compared to the experimen-

tal single crystal data and a lower ground state energy (Table 6.3 in the SI), hinting at the fivefold unpaired electrons in the d-orbital of Fe (spin state = 5/2) being the more favourable configuration. Furthermore, Hubbard correction U was employed to correctly describe the localized d-subshell orbitals in Fe^{3+}, employing a factor of U = $4\,\mathrm{eV}$ (Table 6.3 in SI).[25] The PBE+U band structures for the spin up and down case for the suggested high-spin conformation are shown in Figure 6.4a and 6.4b, respectively. It can be seen that the electronic structure is completely spin-polarized around the Fermi level.

The spin-up band structure exhibits a direct and insulating band gap of $4.5\,\mathrm{eV}$ located at the Γ point in the center of the Brillouin zone. We note that the estimation of band gap magnitude by DFT-PBE is known to be flawed and therefore should only be treated as a rough estimate. The valence band maximum (VBM) is flat and degenerate, hinting at high effective masses for the holes, whereas the conduction band maximum (CBM) is more dispersed, suggesting smaller effective mass values for the electrons. The orbital contributions for the frontier bands are depicted in Figure 6.4c, showing that the character of the VBM is dominated by Fe-d and Cl-p orbitals. The CBM consists mostly of Na-s and Cl-p contributions. This transition is opposed to common $\mathrm{A_2B(I)B(III)X_6}$ double perovskites like $\mathrm{Cs_2AgBiBr_6}$, where the trivalent bismuth and halide atoms form the CB and the monovalent silver-halide bonds govern the CB character.[26] The band structures and DOS for both spin cases without Hubbard correction are further depicted in Figure 6.10 and Figure 6.11 in the ESI.

The spin-down band structure has semiconducting character with an indirect band gap of around $1.4\,\mathrm{eV}$, with the VBM at the Γ point and the CBM at the X point in the Brillouin zone which is indicated as blue arrow in Figure 6.4b. Additionally a direct transition is located only $30\,\mathrm{meV}$ under the VBM. For this case, the VB is mostly flat and highly degenerate, with the states above the Fermi level consisting of Fe-d and Cl-p contributions and the VB made up of Cl-p states, similar to previously reported double perovskite oxides.[27] Klarbring and co-workers recently demonstrated that the preferred magnetic state over $3\,\mathrm{K}$ for $\mathrm{Cs_2NaFeCl_6}$ is paramagnetic, which results in disordered spin directions at different sites.[28] To account for this, they employed disordered local moments (DLM) modeling to retrieve the effective band structure for the paramagnetic case, resulting in semiconducting character, as seen in the the spin down band structure presented in Figure 6.4b, which agrees well with our optical measurements.[28]

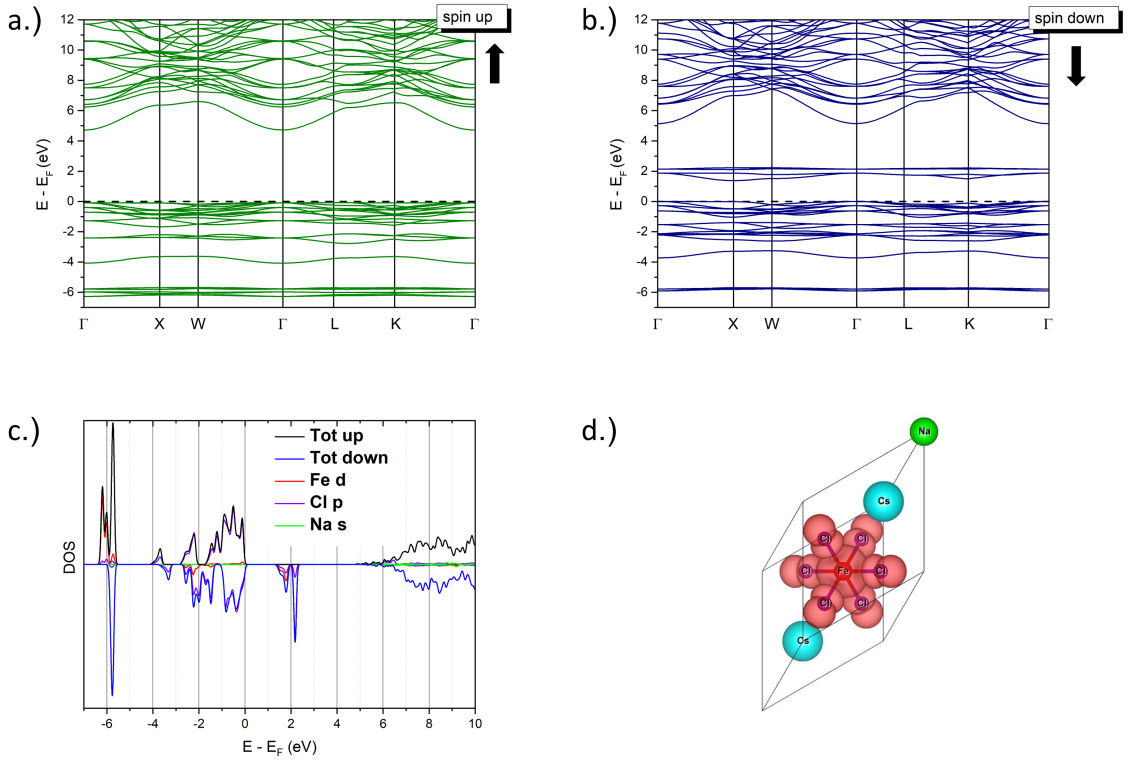

Figure 6.4: a) + b) Spin up (a., green) and down (b., blue) polarized band structures of $Cs_2NaFeCl_6$ (spin state = 5/2), with the Fermi energy set to zero, calculate with DFT-PBE + U (= 4 eV). c) Total and projected density of states for spin up (positive) and down (negative) with orbital contributions of Cl-p/Fe-d/Na-s. d.) Visualization of the spin density in the primitive unit cell (red: spin up, iso-value: 0.0011823).

As we were able to gain information about the structural properties and the band structure of $Cs_2NaFeCl_6$ we further studied the optical properties of the material in the following. We therefore performed temperature-dependent PL and optical transmission studies on the $Cs_2NaFeCl_6$ crystal. By lowering the temperature, we observed a continuous color change of the grown crystal from red at RT to yellow at $50\,\mathrm{K}$, as shown in Figure 6.5a. This effect is reversible and has been reported for $Cs_2NaFeCl_6$ crystals recently, where this thermochromic behavior was ascribed to an order-disorder transition in the material.[8]

We performed temperature-dependent PL measurements, as no PL has been reported for this material so far. One possible reason for this, as can be seen from Figure 6.5b, the sample hardly shows any luminescence under excitation above the band gap of $2.07\,\mathrm{eV}$ when measured at room temperature. However, upon cooling the crystal, we find increasing luminescence gradually shifting towards higher energy. Furthermore, the inset of Figure 6.5b shows a blue-shift and narrowing of the observed peak at around $2.1\,\mathrm{eV}$ when the temperature is reduced.

Surprisingly, at about $140\,\mathrm{K}$ it seems that either the PL peak splits into two individ-

ual peaks or a second peak appears at $2.4\,\mathrm{eV}$, which strongly increases its intensity by decreasing temperature. We further notice that the dip between these two PL peaks is around $2.32\,\mathrm{eV}$ and slightly blue shifting. The rise of additional PL peaks has also been reported for the lead halide perovskite $MAPbI_3$, and related to a phase transition from a tetragonal phase to the orthorhombic phase.[29] However, the previously presented EPR measurements showed no evidence of a structural phase transition for this material, and we therefore exclude a phase transition as the cause for the rise of the additional PL at $2.4\,\mathrm{eV}$.

In order to explain the blue-shift of the PL spectra as well as the rise of the second PL peak at higher energies, we performed temperature-dependent absorption measurements shown in Figure 6.5b. (Further information about the absorption measurement can be found in the SI). At room temperature, the absorption edge can be observed at around $2.05\,\mathrm{eV}$ which is consistent with bandgap values reported in the literature for $Cs_2NaFeCl_6$.[12,13] When the temperature is decreased, a strong blue-shift of the absorption onset was found, suggesting an increase of the bandgap at low temperatures. This effect has also been previously reported for temperatures ranging from $450\,\mathrm{K}$ to $260\,\mathrm{K}$.[12] Additionally Figure 6.5b shows a second pronounced absorption peak at $2.32\,\mathrm{eV}$ for temperatures lower than $140\,\mathrm{K}$. For further evaluation, we superimposed the two graphs for $80\,\mathrm{K}$, shown in Figure 6.5d, and found that the observed PL from the crystal seems to be partly reabsorbed by the state at $2.32\,\mathrm{eV}$ visible in the absorption spectra. Hence, we speculate that reabsorption is leading to the visible dip in the PL at $2.32\,\mathrm{eV}$ shown in Figure 6.5a and c and ultimately to an apparent second PL peak at higher energies. Additionally, it can be seen in Figure 6.5c that PL and absorptance overlap, which leads to a strong decrease in PL intensity at energies greater than $2.4\,\mathrm{eV}$.

The strong absorption at $3900\,\mathrm{K}$ in $Cs_2NaFeCl_6$ in combination with the weak PL indicate that non-radiative recombination processes dominate even in a high-quality and phase-pure crystal. Since the PL increases with decreasing temperature, we assume that recombination in the material is mainly first order (e.g., traps or defects) at elevated temperatures, with these being "frozen out" at lower temperatures. A similar effect was observed for lead halide perovskites namely that lowering the temperature causes a decrease of the monomolecular recombination rate while simultaneously the bimolecular recombination rate is increasing.[30,31] Hence, the measured PL signal is increasing.[30,31]

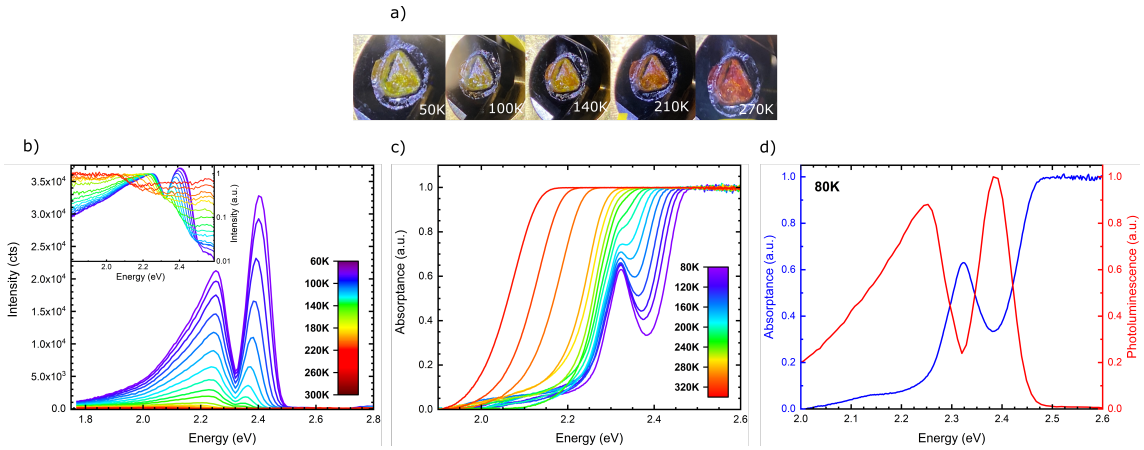

Figure 6.5: a) Photographs of the temperature-dependent color change from red (270K) to yellow (50K) of $Cs_2NaFeCl_6$ single crystals. b) Steady state PL of the $Cs_2NaFeCl_6$ single crystal, shows that PL of the crystals can only be observed at low temperatures. Inset shows the normalized PL on a logarithmic scale. c) Temperature-dependent absorptance shows an additional absorption peak for low temperatures d) Absorption and emission spectra of $Cs_2NaFeCl_6$ crystal at T=80K.

To further investigate the origin of the dip in PL as well as the additional absorption peak at $2.3\,\mathrm{eV}$ which arises at low temperatures, we investigated the excitonic properties of $Cs_2NaFeCl_6$ by means of Elliot's theory.[32] Therefore, we used fits according to the model of Elliot to analyze the measured absorption spectra and extract the band gap energy E_g, exciton binding energies as well as broadening parameters of the absorption peak at $2.3\,\mathrm{eV}$.[30] (For further details about the fitting procedure see section Elliot Fitting in SI). However, in order to account for the steep increase of the absorption after the excitonic contribution we added a parameter for the direct interband transition described by a second bandgap E_{g2}, which is very close to the indirect bandgap as seen in Figure 6.6b, in accordance with the difference of E_g and E_{g2} in the low temperature region.[33] Figure 6.6a shows the resulting Elliot fits together with the measured absorption data. Note that the fits for $190\,\mathrm{K}$ and $200\,\mathrm{K}$ are not included as they did not converge during the fitting routine. It is clear that the obtained fits match very well with the experimental results. Consequently, this allowed us to investigate the temperature dependence of the bandgap of $Cs_2NaFeCl_6$ crystals as shown in Figure 6.6b. We find that also within the Elliot model the bandgaps E_g and E_{g2} shift towards higher energies as soon as the temperature decreases. The variation of the energy values can be explained due to the influence of different carrier-phonon coupling at different points in the band structure, fluctuations in the automatic fitting procedure or divergent thermal broadening of discrete states due to the paramagnetic nature.[34] This behavior is expected for conventional semiconducting materials like Si, SiC, Ge, GaAs and InP and can be described by Varshni's empirical

expression.[35]

$$E_g\,(T) = E_g\,(0) - \frac{\alpha T^2}{T+\alpha} \approx E_g\,(0) + \frac{dEg}{dT}T \tag{6.1}$$

The obtained values for dE_g/dT can be found in Table 6.8 in the SI.

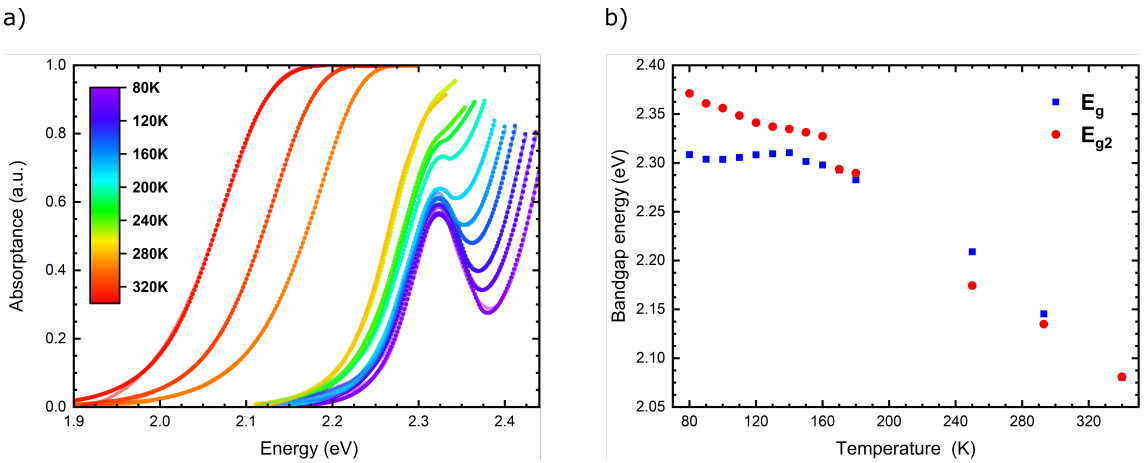

Figure 6.6: a) Measured absorptance (solid line) together with obtained Elliot fits (dotted lines) for temperatures between 80 K and 340 K . b) Extracted bandgap energies from the fits for the measured temperature range.

Additionally, we extracted the temperature dependence of the exciton binding energy for $Cs_2NaFeCl_6$ using the Elliot model. We found that the exciton binding energy at 80 K can be estimated to be approximately 20 meV, whereas hardly any excitons are present at RT as is shown in Figure 6.12a. The very low exciton binding energy of $Cs_2NaFeCl_6$ is a major advantage compared to the conventional $Cs_2AgBiBr_6$, which has exciton binding energies of approximately 268 meV at RT.[36] A slight increase of the exciton binding energy with decreasing temperature has also been observed in the past for other perovskites like $MAPbI_3$ and triple cation lead based perovskites.[37] Due to the very low exciton binding energy at RT of $<$10 meV, excitons dissociate into free carriers just by the thermal energy k_bT, and therefore presumably only free carriers are present. However, the fact that no PL has been observed at room temperature, strongly hints towards non-radiative recombination being the main recombination pathway of charge carriers.

We furthermore analyzed the broadening parameter Γ of the excitonic contribution in the absorption spectra, shown in Figure 6.12b. We observed that the broadening significantly increases when the temperature is increased from 80 K to 350 K. A linewidth broadening with increasing temperature is usually expected, and has been observed also previously for other perovskites such as $MAPbI_3$ and $Cs_2AgBiBr_6$.[29,38,39] The observed broadening is usually associated with electron-phonon coupling in the material.[29,40] We note that, it is not possible to differentiate between the coupling of longitudinal optical phonons and acoustic phonons in the shown temperature range. However, the temperature depen-

dence of the broadening parameter suggests that impurity scattering can be neglected in this material.[29] This is due to the fact that linewidth broadening caused by impurities should lead to a saturation of the linewidth at higher temperatures, which is not the case for $\mathrm{Cs_2NaFeCl_6}$.[29]

6.4 CONCLUSION

In conclusion, we present a method to grow high-quality crystals of the new double perovskite $\mathrm{Cs_2NaFeCl_6}$. XRF, EDX and ICP-OES proved a nearly perfect stoichiometry whereas the successful growth of $\mathrm{Cs_2NaFeCl_6}$ single crystals were verified by detailed X-ray studies. Furthermore, we were able to assess the spin properties of the material and correlate them with their crystal structure by connecting theoretical calculations with experimental data. We found that the spin 5/2 system $\mathrm{Cs_2NaFeCl_6}$ has a cubic crystal structure and although the crystal changes its color from red to yellow upon cooling, no structural phase transition was observed. Additionally, optical measurements suggest that non-radiative recombination is dominant at room temperature. However, upon cooling we find substantial emission, together with reabsorption of emission by an additional excitonic state with low binding energy of only $20\,\mathrm{meV}$ at $80\,\mathrm{K}$. We therefore conclude, that although the emission of $\mathrm{Cs_2NaFeCl_6}$ seems to be governed by non-radiative processes at high temperatures, its low exciton binding energy, substantial PL at low temperatures, and the reported high stability against thermal cycling,[12] still indicate a potential application for thermochromic windows,[12] or detectors and devices operating at low temperatures or in space.[41]

6.5 EXPERIMENTAL DETAILS

Materials And Solvents

$CsCl$ (2 mmol), $NaCl$ (1 mmol) and $FeCl_3$ (1 mmol) were weighed in stoichiometric amounts into a 3 mL glass vial in a nitrogen filled glovebox (Water and oxgen compound below 1 ppm). The solubility curve was achieved, by adding small amounts of HCl (200 µL) every hour under constant stirring of the solution until the precursor salts were completely dissolved. This was done for a temperature range from 25 °C to 100 °C, in order to obtain an exact solubility curve for $Cs_2NaFeCl_6$ in HCl.

$Cs_2NaFeCl_6$ crystal growth from controlled cooling

In order to obtain $Cs_2NaFeCl_6$ crystals from HCl the commonly known crystal growth protocol was followed.[15] A 0.3 molar solution of $CsCl$ (2 mmol, 252.54 mg), $NaCl$ (1 mmol, 43.83 mg) and $FeCl_3$ (1 mmol, 121.65 mg) was prepared with 10 mL of 37% wt HCl. The solution was placed on a hotplate, in an oil bath, and heated to 100 °C for 2 h in order to obtain a completely dissolved precursor solution. To promote crystal growth, the solution was cooled down at a rate of 1 °C h^{-1} to RT. The crystals were then washed and dried with dichloromethane (DCM) in order to avoid any precursor precipitates remaining on the surface.

EDX measurements

EDX characterization of the crystal surfaces were performed in high vacuum using a scanning electron microscope (SEM) Carl Zeiss Ultra 55+ and an INCAPentaFET-x3 Si(Li) detector to obtain the elemental distribution of Cs, Na, Fe, and Cl. At least 4 working areas on the crystals were measured. The obtained data was then normalized and averaged to obtain an average stoichiometry and elemental distribution over the whole crystal.

X-ray Diffraction and X-ray Fluorescence

Powder and single crystal XRD measurements as well as XRF measurements of the crystal powders were performed using a General Electric XRD 3003 TT with a monochromatic Cu- K_α radiation source (V = 40 kV, I = 40 mA) with wavelength λ of 1.5406 Å. Further XRF measurements were recorded with an XR-100T detector from Amptek and an X-ray unit from PHYWE. For the measurements, we applied an unfiltered Mo (Molybdenum)-K_α radiation source (V = 35 kV, I = 0.1 mA). All measurements were

performed at RT. The crystal surface facets were determined by reflectometry with a Mo-K_α radiation source (λ = 0.71073 Å, V = $50\,\mathrm{kV}$, I = $1\,\mathrm{mA}$). The crystals were placed on an adhesive tape to carry out the measurements. The recorded XRD patterns were plotted against the scattering vector $q_z = 4\pi/\lambda \cdot \sin(\theta)$, where θ is the scattering angle.[22]

Crystal structure analysis

An orange block-like specimen of $\mathrm{Cs_2NaFeCl_6}$, approximate dimensions $0.020\,\mathrm{mm}$ x $0.020\,\mathrm{mm}$ x $0.020\,\mathrm{mm}$ x $0.030\,\mathrm{mm}$, was used for the X-ray crystallographic analysis. The X-ray intensity data were measured on a Bruker D8 Quest system equipped with a multilayer mirror optics monochromator and a Mo K_α rotating-anode X-ray tube (λ = 0.71073 Å). The measurements were performed at $297\,\mathrm{K}$.

EPR measurements

The continuous wave EPR measurements were performed with a Magnettech MS 5000 X. In order to reach cryogenic temperatures, we extended the setup with an Oxford flow-type cryostat. The $\mathrm{Cs_2NaFeCl_6}$ crystal was placed on a quartz rod sample holder and positioned in the centre of the EPR resonator. We choose the lowest applicable microwave power (PMW=1 $\neq$ W) to exclude saturation effects and used a modulation amplitude of Bmod=$0.5\,\mathrm{mT}$ to gain a sufficiently high signal-to-noise ratio without broadening the line shape of the observed EPR signature.

Density functional theory calculations

DFT calculations were performed using the Quantum ESPRESSO package based on plane wave basis sets, employing the Perdew-Burke-Ernzerhof (PBE) parameterization of the generalized gradient approximation (GGA) for solids (PBEsol) to describe exchange correlation interactions.[24] The GBRV high-throughput ultrasoft pseudopotential library was utilized to describe the interactions between valence electrons and atomic cores.[42] Furthermore, the simplified Hubbard correction of Cococcioni and de Gironcoli was included.[43–45] A kinetic energy cutoff of $60\,\mathrm{Ry}$ for the wavefunctions and $500\,\mathrm{Ry}$ for the charge density was used. Self-consistent field (SCF) and geometry relax calculations were carried out on a fully converged 4x4x4 Monkhorst-Pack grid, while a larger mesh was utilized for the density of states calculations.

Photoluminescence measurements

Temperature dependent photoluminescence was measured using a FLS980. The sample was placed in vacuum in a cryostat and was cooled down using liquid nitrogen. PL was

measured in reflection geometry. As excitation a Xenon lamp with tunable wavelength was used. The excitation wavelength was chosen to be $336\,\mathrm{nm}$.

Transmission measurements

Temperature dependent transmission was measured in a cryostat under vacuum conditions. The sample was excited with a white light LED and transmission was detected using a Princeton Instruments Acton SpectraPro SP 2300 Spectrometer and a PyLoN Silicon CCD Detector. In order to calculate the absorptance from the obtained data, the reflection of the crystals was neglected and transmission calculated according to T=$\frac{I_{crystal}}{I_{lamp}}$. The resulting absorptance was then obtained by A=1-T.

6.6 SUPPORTING INFORMATION

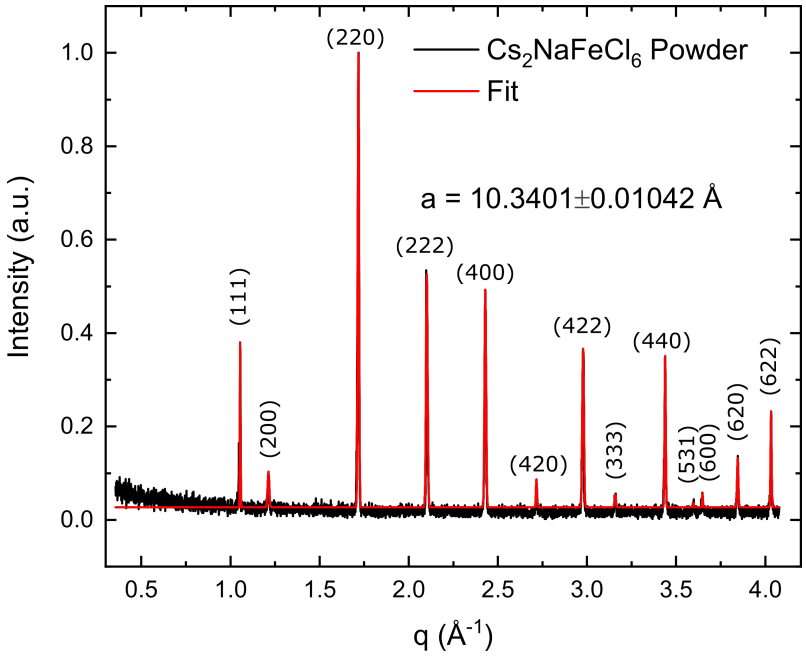

Figure 6.7: XRD pattern of $Cs_2NaFeCl_6$ powder, which were recorded with a monochromatic copper radiation source. The calculated XRD pattern (red) and the corresponding Miller indices for each peak are shown. From that we found a lattice constant of 10.341 Åand a cubic crystal structure.

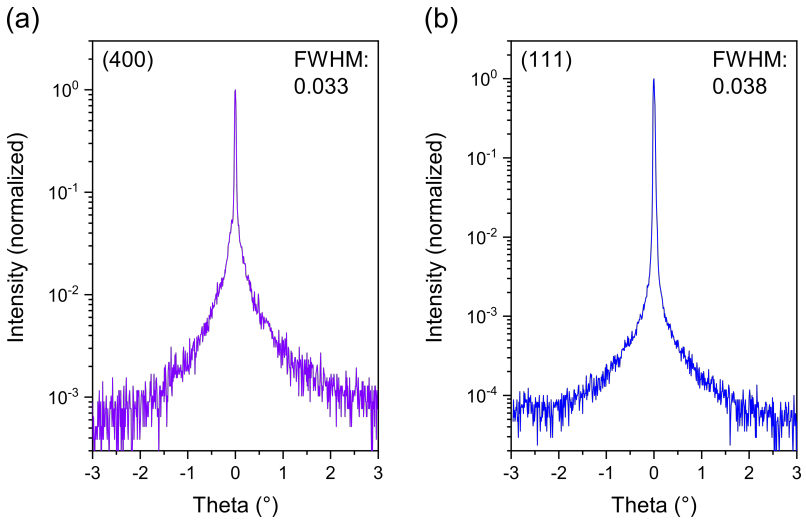

Figure 6.8: These exemplary rocking measurements were performed on the (400) peak and the (111) peak of a $Cs_2NaFeCl_6$ single crystal conducted with a Mo-K_α source. The low FWHMs of $< 0.04°$ indicate a low mosaicity hinting at a very high quality of the grown $Cs_2NaFeCl_6$ crystals.

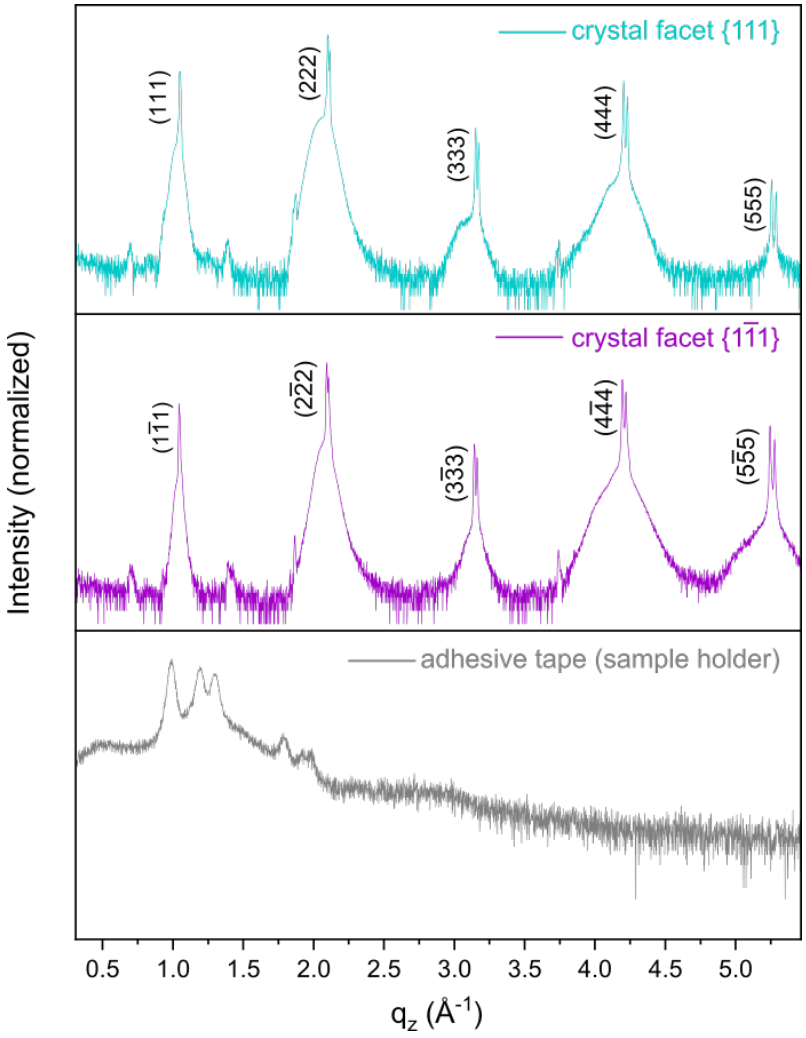

Figure 6.9: XRD measurements on (111) crystal surface facet (cyan-colored data set) and on the (1$\bar{1}$1) of powders, which were recorded with a molybdenum K_α radiation source. The XRD measurement of the tape shows reflections that are also seen in the crystal surface measurements.

Crystal Structure Analysis

Crystal data for $Cs_2NaFeCl_6$ single crystals obtained by crystal structure analysis, showing the lattice constant and angles for the cubic system.

Chemical formula	$Cs_2NaFeCl_6$
Formula weight	557.36 g/mol
Temperature	293 K
Wavelength	0.71073 Å
Crystal system	cubic
Space group	F m -3 m, Nr. 225
Unit cell dimensions	a = 10.3392(3) Å
Volume	1105.25(1) Å3
Z	4
Density (calculated)	3.350 g/cm3
Absorption coefficient	9.277 mm-1
F(000)	996

Diffractometer	Bruker D8 Quest (Microfocus)
Radiation Source	MoKα, Göbel-Mirror
Theta Range for Data collection	3.413° – 45.051°
Wavelength	0.71073 Å
Index ranges	-20 $\leq$ h, k, l $\leq$ 20
Reflections collected	26691
Independent reflections	282; 258 with I $\geq 2\sigma$(I)
Refinement method	Full Matrix Least-Squares on F2, SHELXL-2018/3
Structure solution technique	Direct Methods, SHELXS97
Function minimized	σw(Fo2-Fc2)2
Weighting scheme	w1 = 0.0161, w2 = 46.4725
Goodness-of-fit on F^2	1.095
Data/restraints/parameters	258/0/6
Final R indices	For I $\geq 2\sigma$(I): R1 = 0.0458, wR2 = 0.0895;
For all data: R1 = 0.0497, wR2 = 0.0916	
R.M.S. deviation from mean	0.298
Largest diff. peak and hole	2.911/-4.566
Refinement Program	SHELXL-2018/3

Atomic coordinates and equivalent isotropic atomic displacement parameters ($Å^2$):

	x/a	y/b	z/c	U(eq)
Na1	0	0	0	0.026(2)
Fe1	1/2	0	0	0.0145(3)
Cs1	1/4	1/4	1/4	0.0250(2)
Cl1	0.2687(2)	0	0	0.0249(3)

Bond lengths:

Atom 1	Atom 2	Length [Å]	Atom 1	Atom 2	Length [Å]
Fe1	Cl1	2.392	Cl1	Fe1	2.392
Fe1	Cl1	2.392	Cl1	Fe1	2.392
Fe1	Cl1	2.392	Fe1	Cl1	2.392
Fe1	Cl1	2.392	Fe1	Cl1	2.392
Na1	Cl1	2.778	Fe1	Cl1	2.392
Na1	Cl1	2.778	Fe1	Cl1	2.392
Na1	Cl1	2.778	Fe1	Cl1	2.392
Cl1	Fe1	2.392	Fe1	Cl1	2.392
Cl1	Fe1	2.392	Fe1	Cl1	2.392
Fe1	Cl1	2.392	Fe1	Cl1	2.392
Fe1	Cl1	2.392	Fe1	Cl1	2.392
Fe1	Cl1	2.392	Fe1	Cl1	2.392
Fe1	Cl1	2.392	Fe1	Cl1	2.392
Na1	Cl1	2.778	Fe1	Cl1	2.392
Na1	Cl1	2.778	Fe1	Cl1	2.392
Na1	Cl1	2.778	Fe1	Cl1	2.392
Cl1	Fe1	2.392	Fe1	Cl1	2.392
Cl1	Fe1	2.392	Fe1	Cl1	2.392
Fe1	Cl1	2.392	Fe1	Cl1	2.392
Fe1	Cl1	2.392	Fe1	Cl1	2.392
Fe1	Cl1	2.392	Fe1	Cl1	2.392
Fe1	Cl1	2.392	Fe1	Cl1	2.392
Fe1	Cl1	2.392	Fe1	Cl1	2.392
Na1	Cl1	2.778	Na1	Cl1	2.778
Na1	Cl1	2.778	Na1	Cl1	2.778
Na1	Cl1	2.778	Na1	Cl1	2.778
Cl1	Fe1	2.392	Na1	Cl1	2.778

Cl1	Fe1	2.392	Na1	Cl1	2.778
Fe1	Cl1	2.392	Na1	Cl1	2.778
Fe1	Cl1	2.392	Na1	Cl1	2.778
Fe1	Cl1	2.392	Na1	Cl1	2.778
Fe1	Cl1	2.392	Na1	Cl1	2.778
Na1	Cl1	2.778	Na1	Cl1	2.778
Na1	Cl1	2.778	Na1	Cl1	2.778
Na1	Cl1	2.778	Na1	Cl1	2.778
Cl1	Fe1	2.392	Na1	Cl1	2.778
Cl1	Fe1	2.392	Na1	Cl1	2.778
Na1	Cl1	2.778	Na1	Cl1	2.778
Na1	Cl1	2.778	Na1	Cl1	2.778
Na1	Cl1	2.778	Na1	Cl1	2.778
Cl1	Fe1	2.392	Na1	Cl1	2.778
Cl1	Fe1	2.392	Na1	Cl1	2.778
Na1	Cl1	2.778	Na1	Cl1	2.778
Na1	Cl1	2.778	Na1	Cl1	2.778
Na1	Cl1	2.778	Na1	Cl1	2.778
Cl1	Fe1	2.392	Na1	Cl1	2.778
Cl1	Fe1	2.392	Na1	Cl1	2.778
Na1	Cl1	2.778	Na1	Cl1	2.778
Na1	Cl1	2.778	Na1	Cl1	2.778
Na1	Cl1	2.778	Na1	Cl1	2.778
Cl1	Fe1	2.392	Na1	Cl1	2.778
Cl1	Fe1	2.392	Na1	Cl1	2.778
Na1	Cl1	2.778	Na1	Cl1	2.778
Na1	Cl1	2.778			
Na1	Cl1	2.778			

Bond angles:

Atom 1	Atom 2	Atom3	Angle [°]	Atom 1	Atom 2	Atom3	Angle [°]
Cl1	Fe1	Cl1	180.00	Cl1	Na1	Cl1	180.00
Cl1	Fe1	Cl1	90.00	Cl1	Na1	Cl1	90.00
Cl1	Fe1	Cl1	90.00	Cl1	Na1	Cl1	180.00
Cl1	Fe1	Cl1	90.00	Cl1	Na1	Cl1	90.00
Cl1	Fe1	Cl1	90.00	Cl1	Na1	Cl1	90.00
Cl1	Fe1	Cl1	90.00	Cl1	Na1	Cl1	90.00
Cl1	Fe1	Cl1	90.00	Cl1	Na1	Cl1	90.00
Cl1	Fe1	Cl1	90.00	Cl1	Na1	Cl1	180.00
Cl1	Fe1	Cl1	90.00	Cl1	Na1	Cl1	90.00
Cl1	Fe1	Cl1	180.00	Cl1	Na1	Cl1	90.00
Cl1	Fe1	Cl1	90.00	Cl1	Na1	Cl1	90.00
Cl1	Fe1	Cl1	90.00	Cl1	Na1	Cl1	90.00
Cl1	Fe1	Cl1	90.00	Fe1	Cl1	Na1	180.00
Cl1	Fe1	Cl1	90.00	Na1	Cl1	Fe1	180.00
Cl1	Fe1	Cl1	180.00	Na1	Cl1	Fe1	180.00
Cl1	Na1	Cl1	90.00	Na1	Cl1	Fe1	180.00
Cl1	Na1	Cl1	90.00	Na1	Cl1	Fe1	180.00
Cl1	Na1	Cl1	90.00	Na1	Cl1	Fe1	180.00
Cl1	Na1	Cl1	90.00				

DFT Calculations

	Exp. [RT]	Low Spin U = 0 eV	Low Spin U = 4 eV	High Spin U = 0 eV	High Spin U = 3 eV	High Spin U = 4 eV	High Spin U = 5 eV
Fe-Cl [Å]	2.392	2.311	2.321	2.422	2.430	2.439	2.445
Cs-Cl [Å]	3.661	3.637	3.670	3.773	3.732	3.736	3.736
Na-Cl [Å]	2.778	2.812	2.855	2.835	2.833	2.832	2.831
Unit cell length [Å]	7.311	7.321	7.321	7.434	7.443	7.454	7.462
E [Ry]		-749.26	-749.03	-749.33	-749.15	-749.21	-749.17

Table 6.3: Unit cell parameters and ground state energy of $Cs_2NaFeCl_6$ calculated by DFT-PBE (+U) depending on the spin state and U value.

The unit cell parameters and conformation energies were calculated in a relaxed unit cell to compare the influence of different spin configurations and Hubbard correction factors on the bond lengths and overall energy in the system. As can be seen in table S1, the low spin (S = 1/2) configuration with and without Hubbard correction drastically underestimates the Fe-Cl octahedral bond length, while the high spin calculations yield overall more accurate results (S = 5/2). Furthermore, starting from the optimized high spin structure, the Hubbard factor to accurately describe the localized Fe-3d unpaired electrons was estimated via a linear response method, resulting in U = 3.93 eV. This factor also leads to the lowest energy compared to U = 3 eV and U = 5 eV and was adopted throughout the calculations in the manuscript. As expected, the electronic structure is drastically influenced by the different spin configurations as seen in Figure 6.10 (low spin) and 6.11 (high spin). For the low-spin configuration, both spin up and down band structures exhibit semiconducting character, while the high-spin calculations yield the same results as with the PBE+U approach, showcasing insulating character for spin up and semiconducting for spin down. Interestingly, the VBM demonstrates partial Fe-d character for the band structures without Hubbard correction. Furthermore, the states for the high-spin spin-down case shift under the Fermi level when treated with the PBE approach, in contrast

to the Hubbard-corrected band structure. The unoccupied states over the Fermi level for PBE+U also demonstrate favoured electronic localization, which is expected because of the better treated on-site electron-electron interaction.

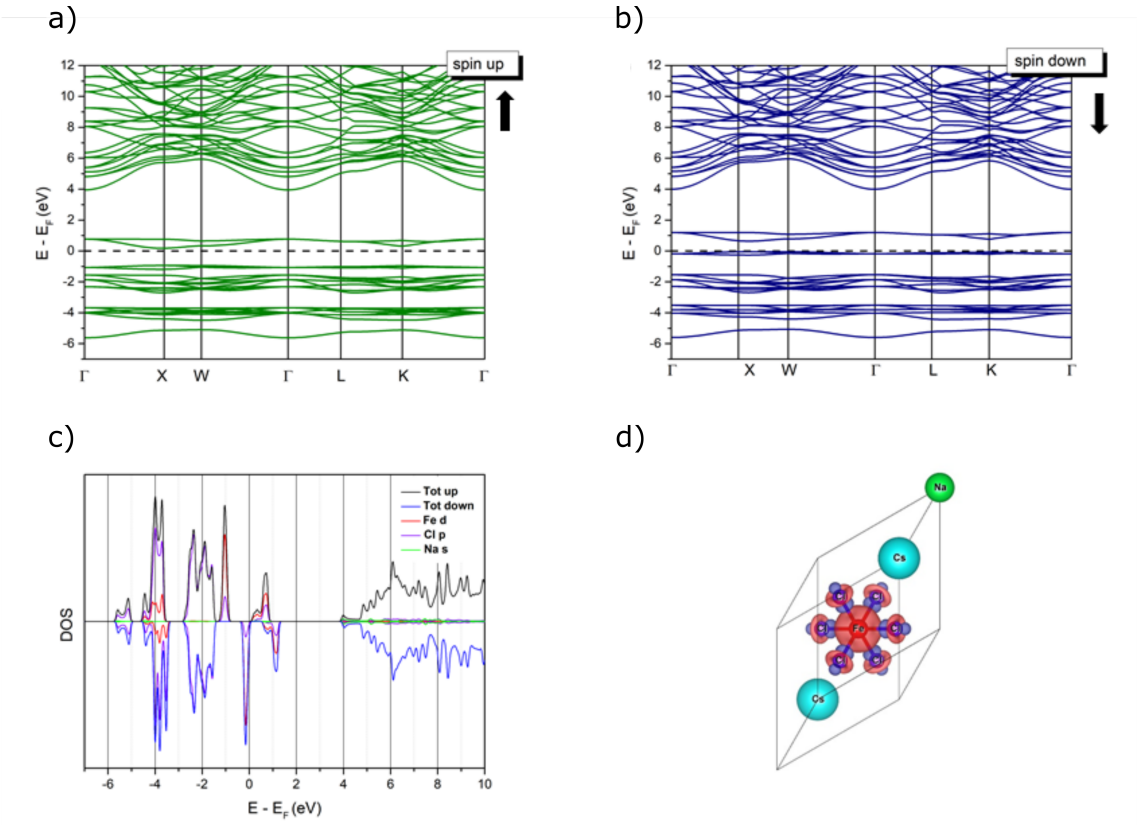

Figure 6.10: a) + b) Spin up (a., green) and down (b., blue) polarized band structures of $Cs_2NaFeCl_6$ (spin state = 1/2), with the Fermi energy set to zero, calculated with DFT-PBE. c) Total and projected density of states for spin up (positive) and down (negative) with orbital contributions of Cl p/Fe d/Na s. d.) Visualization of the spin density in the primitive unit cell (red: spin up, blue: spin down, iso-value: 0.0011823)

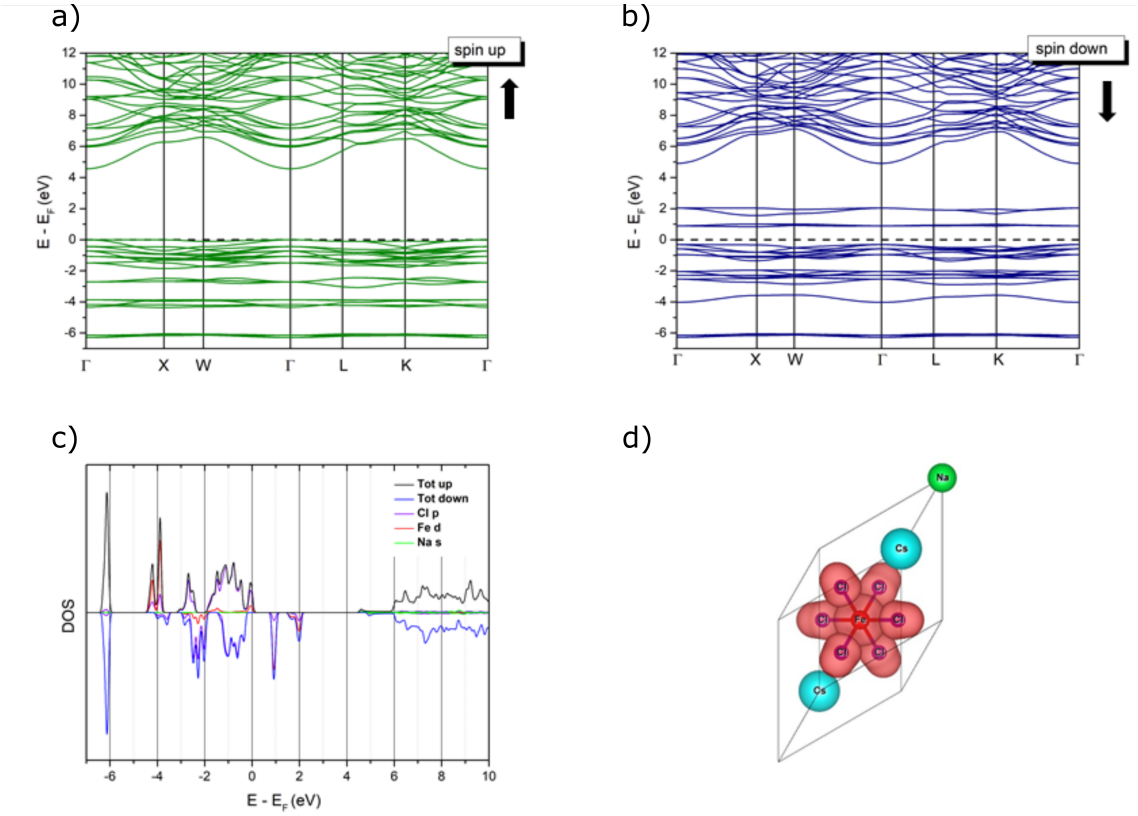

Figure 6.11: a) + b) Spin up (a., green) and down (b., blue) polarized band structures of $Cs_2NaFeCl_6$ (spin state = 5/2), with the Fermi energy set to zero, calculated with DFT-PBE. c) Total and projected density of states for spin up (positive) and down (negative) with orbital contributions of Cl-p/Fe-d/Na-s. d.) Visualization of the spin density in the primitive unit cell (red: spin up, iso-value: 0.0011823).

Elliott Fitting of The Absorption Data

To estimate the exciton binding energy, the inhomogeneous thermal broadening and the Varshni shift parameters, Elliott's model to fit the near-band gap absorption was used. Additionally, a parameter for the direct interband transition was added to account for the steep absorption increase after the excitonic contribution:

$$\alpha(\hbar\omega) = \alpha_0^{3D}\left[\sum_{n=1}^{\infty}\frac{4\pi E_b^{3/2}}{n^3}\cdot \mathrm{Sech}\left(\frac{\hbar\omega - E_G - \frac{E_b}{n^2}}{\Gamma}\right) + \int_{E_g}^{\infty}\mathrm{Sech}\left(\frac{\hbar\omega-\varepsilon}{\Gamma}\right)\cdot\frac{2\pi\sqrt{E_b}}{1-\exp 2\pi\sqrt{\frac{E_b}{\beta\nu - E_G}}}\cdot\frac{1}{1-\frac{8m_r b}{\hbar^3}(\varepsilon-\varepsilon_q)}d\varepsilon\right] + A_2\frac{\Gamma}{\pi}\int_0^{\infty}\frac{E'\theta\left(E-E_{2g}\right)\sqrt{E-E_{2g}}}{\left(E-E'\right)^2+\Gamma^2} \tag{6.2}$$

Temperature	dEg/dT [μeV/K]	dEg2/dT [μeV/K]
80 – 350 K	-0.87	-1.17
250 - 350 K	-1.43	-1.04
150 - 350 K	-1.18	-1.35

Table 6.4: Temperature dependent change of the bandgap energy dEg/dT calculated by Varshni's empirical expression, for different Temperature ranges.

Eb is the exciton binding energy, E_g and E_{2g} the first and second bandgap, Γ the inhomogeneous broadening parameter, A2 is a scaling constant for the additional absorption term and α_{03D} a prefactor for the joint density of states. The fits seen in figure 6a were solved iteratively for the whole dataset with a trust region reflective least-squares algorithm, providing the optimized parameters from the converged run to the higher temperature absorption curve and introducing a raw data cutoff of 0.025 eV towards higher energies to better reproduce the band edge.

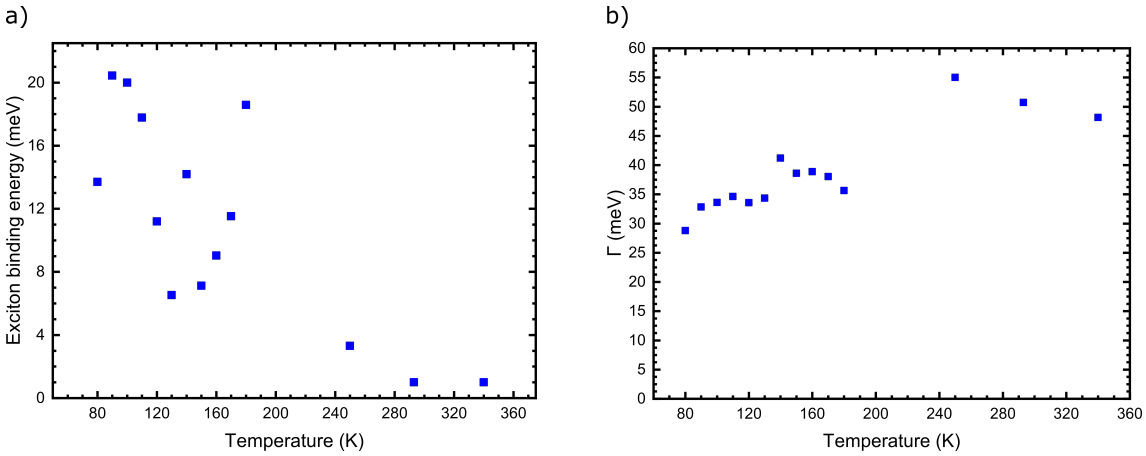

Figure 6.12: Evolution of a) exciton binding energy and b) broadening parameter gamma with temperature.

6.7 REFERENCES

[1] L. Chu, W. Ahmad, W. Liu, J. Yang, R. Zhang, Y. Sun, J. Yang, X. Li, *Nano-Micro Letters* **2019**, *11*, DOI 10.1007/s40820-019-0244-6.

[2] L. Liang, P. Gao, *Advanced Science* **2018**, *5*, 1700331.

[3] A. H. Slavney, R. W. Smaha, I. C. Smith, A. Jaffe, D. Umeyama, H. I. Karunadasa, *Inorganic Chemistry* **2017**, *56*, 46–55.

[4] E. Greul, M. L. Petrus, A. Binek, P. Docampo, T. Bein, *Journal of Materials Chemistry A* **2017**, *5*, 19972–19981.

[5] H. C. Sansom, L. R. V. Buizza, M. Zanella, J. T. Gibbon, M. J. Pitcher, M. S. Dyer, T. D. Manning, V. R. Dhanak, L. M. Herz, H. J. Snaith, J. B. Claridge, M. J. Rosseinsky, *Inorganic Chemistry* **2021**, *60*, 18154–18167.

[6] Z. Zhang, C.-C. Chung, Z. Huang, E. Vetter, D. Seyitliyev, D. Sun, K. Gundogdu, F. N. Castellano, E. O. Danilov, G. Yang, *Materials Letters* **2020**, *269*, 127667.

[7] W. Pan, H. Wu, J. Luo, Z. Deng, C. Ge, C. Chen, X. Jiang, W.-J. Yin, G. Niu, L. Zhu, L. Yin, Y. Zhou, Q. Xie, X. Ke, M. Sui, J. Tang, *Nature Photonics* **2017**, *11*, 726–732.

[8] Z. Li, S. R. Kavanagh, M. Napari, R. G. Palgrave, M. Abdi-Jalebi, Z. Andaji-Garmaroudi, D. W. Davies, M. Laitinen, J. Julin, M. A. Isaacs, R. H. Friend, D. O. Scanlon, A. Walsh, R. L. Z. Hoye, *Journal of Materials Chemistry A* **2020**, *8*, 21780–21788.

[9] H. Luo, J. Wu, X. Liu, Y. Yang, Q. Liu, M. Zhang, P. Yuan, W. Sun, Z. Lan, J. Lin, *ACS Applied Energy Materials* **2018**, *1*, 6700–6706.

[10] G. Longo, S. Mahesh, L. R. V. Buizza, A. D. Wright, A. J. Ramadan, M. Abdi-Jalebi, P. K. Nayak, L. M. Herz, H. J. Snaith, *ACS Energy Letters* **2020**, *5*, 2200–2207.

[11] M. T. Sirtl, F. Ebadi, B. T. Gorkom, P. Ganswindt, R. A. J. Janssen, T. Bein, W. Tress, *Advanced Optical Materials* **2021**, *9*, 2100202.

[12] W. Li, N. U. Rahman, Y. Xian, H. Yin, Y. Bao, Y. Long, S. Yuan, Y. Zhang, Y. Yuan, J. Fan, *Journal of Semiconductors* **2021**, *42*, 072202.

[13] Y. Xian, H. Yin, Y. Bao, Y. Xiao, S. Yuan, N. U. Rahman, Y. Yuan, Y. Zhang, X. Meng, S. Jin, W. Li, J. Fan, *The Journal of Physical Chemistry Letters* **2020**, *11*, 9535–9542.

[14] V. Sarritzu, N. Sestu, D. Marongiu, X. Chang, S. Masi, A. Rizzo, S. Colella, F. Quochi, M. Saba, A. Mura, G. Bongiovanni, *Scientific Reports* **2017**, *7*, DOI 10.1038/srep44629.

[15] A. H. Slavney, T. Hu, A. M. Lindenberg, H. I. Karunadasa, *Journal of the American Chemical Society* **2016**, *138*, 2138–2141.

[16] R. Babu, L. Giribabu, S. P. Singh, *Crystal Growth & Design* **2018**, *18*, 2645–2664.

[17] P. Han, C. Luo, W. Zhou, J. Hou, C. Li, D. Zheng, K. Han, *The Journal of Physical Chemistry C* **2021**, *125*, 11743–11749.

[18] M. Armer, J. Höcker, C. Büchner, S. Häfele, P. Dörflinger, M. T. Sirtl, K. Tvingstedt, T. Bein, V. Dyakonov, *CrystEngComm* **2021**, *23*, 6848–6854.

[19] L. Yin, H. Wu, W. Pan, B. Yang, P. Li, J. Luo, G. Niu, J. Tang, *Advanced Optical Materials* **2019**, *7*, 1900491.

[20] A. C. Thompson, D. Vaughan, et al., *X-ray data booklet*, *Vol. 8*, Lawrence Berkeley National Laboratory, University of California Berkeley, CA, **2001**.

[21] F. Wei, F. Brivio, Y. Wu, S. Sun, P. D. Bristowe, A. K. Cheetham, *Journal of Materials Chemistry C* **2018**, *6*, 3573–3577.

[22] J. Höcker, M. Ozcan, S. Hammer, M. Fischer, B. Bichler, M. Armer, P. Rieder, V. Drach, J. Pflaum, B. Nickel, V. Dyakonov, *Journal of Materials Chemistry C* **2020**, *8*, 8275–8283.

[23] Y. Puttisong, F. Moro, S. L. Chen, P. Höjer, W. Ning, F. Gao, I. A. Buyanova, W. M. Chen, *The Journal of Physical Chemistry Letters* **2020**, *11*, 4873–4878.

[24] P. Giannozzi, S. Baroni, N. Bonini, M. Calandra, R. Car, C. Cavazzoni, D. Ceresoli, G. L. Chiarotti, M. Cococcioni, I. Dabo, et al., *Journal of physics: Condensed matter* **2009**, *21*, 395502.

[25] J. Hubbard, *Physical Review B* **1979**, *19*, 2626–2636.

[26] F. Ji, J. Klarbring, F. Wang, W. Ning, L. Wang, C. Yin, J. S. M. Figueroa, C. K. Christensen, M. Etter, T. Ederth, L. Sun, S. I. Simak, I. A. Abrikosov, F. Gao, *Angewandte Chemie International Edition* **2020**, *59*, 15191–15194.

[27] M. M. Saad H.-E., A. Elhag, *Results in Physics* **2018**, *9*, 793–805.

[28] J. Klarbring, U. Singh, S. I. Simak, I. A. Abrikosov, Electronic structure of the magnetic halide double perovskites Cs2(Ag,Na)FeCl6 from first-principles, **2022**.

[29] A. D. Wright, C. Verdi, R. L. Milot, G. E. Eperon, M. A. Pérez-Osorio, H. J. Snaith, F. Giustino, M. B. Johnston, L. M. Herz, *Nature Communications* **2016**, *7*, DOI 10.1038/ncomms11755.

[30] C. L. Davies, M. R. Filip, J. B. Patel, T. W. Crothers, C. Verdi, A. D. Wright, R. L. Milot, F. Giustino, M. B. Johnston, L. M. Herz, *Nature Communications* **2018**, *9*, DOI 10.1038/s41467-017-02670-2.

[31] R. L. Milot, G. E. Eperon, H. J. Snaith, M. B. Johnston, L. M. Herz, *Advanced Functional Materials* **2015**, *25*, 6218–6227.

[32] N. Elliott, L. Pauling, *Journal of the American Chemical Society* **1938**, *60*, 1846–1851.

[33] M. Scholz, M. Morgenroth, K. Oum, T. Lenzer, *The Journal of Physical Chemistry C* **2018**, *122*, 5854–5863.

[34] H. Ünlü, *Solid-State Electronics* **1992**, *35*, 1343–1352.

[35] Y. P. Varshni, *Physica* **1967**, *34*, 149–154.

[36] R. Kentsch, M. Scholz, J. Horn, D. Schlettwein, K. Oum, T. Lenzer, *The Journal of Physical Chemistry C* **2018**, *122*, 25940–25947.

[37] F. Ruf, M. F. Aygüler, N. Giesbrecht, B. Rendenbach, A. Magin, P. Docampo, H. Kalt, M. Hetterich, *APL Materials* **2019**, *7*, 031113.

[38] J. A. Steele, P. Puech, M. Keshavarz, R. Yang, S. Banerjee, E. Debroye, C. W. Kim, H. Yuan, N. H. Heo, J. Vanacken, A. Walsh, J. Hofkens, M. B. J. Roeffaers, *ACS Nano* **2018**, *12*, 8081–8090.

[39] J. Leveillee, G. Volonakis, F. Giustino, *The Journal of Physical Chemistry Letters* **2021**, *12*, 4474–4482.

[40] B. J. Bohn, T. Simon, M. Gramlich, A. F. Richter, L. Polavarapu, A. S. Urban, J. Feldmann, *ACS Photonics* **2018**, *5*, 648–654.

[41] Y. Yang, C. Liu, M. Cai, Y. Liao, Y. Ding, S. Ma, X. Liu, M. Guli, S. Dai, M. K. Nazeeruddin, *ACS applied materials & interfaces* **2020**, *12*, 17062–17069.

[42] K. F. Garrity, J. W. Bennett, K. M. Rabe, D. Vanderbilt, *Computational Materials Science* **2014**, *81*, 446–452.

[43] M. Cococcioni, S. De Gironcoli, *Physical Review B* **2005**, *71*, 035105.

[44] J. Hubbard, *Physical Review B* **1979**, *19*, 2626.

[45] J. Hubbard, *Physical Review B* **1979**, *20*, 4584.

Silver-Bismuth Based 2D Double Perovskites $(4FPEA)_4AgBiX_8$ (X= Cl, Br, I): Highly Oriented Thin Films with Large Domain Sizes and Ultrafast Charge-Carrier Localization 7

This chapter is based on following publication:
R. Hooijer, A. Weis, A. Biewald, M. T. Sirtl, J. Malburg, R. Holfeuer, S. Thamm, A. A. Y. Amin, M. Righetto, A. Hartschuh, L. Herz, T. Bein, Advanced Optical Materials **2022**, 10, 2200354.

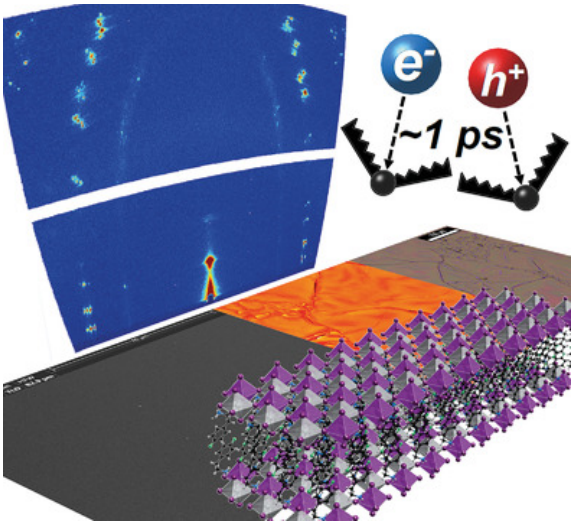

7.1 ABSTRACT

Two-dimensional (2D) hybrid double perovskites are a promising emerging class of materials featuring superior intrinsic and extrinsic stability over their 3D parent structures, while enabling additional structural diversity and tunability. Here, we expand the Ag–Bi-based double perovskite system, comparing structures obtained with the halides chloride, bromide, and iodide and the organic spacer cation 4-fluorophenethylammonium (4FPEA) to form the $n = 1$ Ruddlesden-Popper (RP) phases $(4FPEA)_4AgBiX_8$ (X= Cl, Br, I). We demonstrate access to the iodide RP-phase through a simple organic spacer, analyze the different properties as a result of halide substitution and incor-porate the materials into photodetectors. Highly oriented thin films with very large domain sizes are fabricated and investigated with grazing incidence wide angle X-ray scattering, revealing a strong dependence of morphology on substrate choice and synthesis parameters. First-principles calculations confirm a direct band gap and show type Ib and IIb band alignment between organic and inorganic quantum wells. Optical characterization, temperature-dependent photoluminescence, and optical-pump terahertz-probe spectroscopy give insights into the absorption and emissive behavior of the materials as well as their charge-carrier dynamics. Overall, we further elucidate the possible reasons for the electronic and emissive properties of these intriguing materials, dominated by phonon-coupled and defect-mediated polaronic states.

7.2 INTRODUCTION

The exploration of two-dimensional (2D) hybrid perovskites has gained increased attention, along with the success of their three-dimensional (3D) analogs as optoelectronic materials for solar cells, laser diodes, field-effect transistors, X-ray- and photodetectors or light-emitting diodes.[1–6] While a large number of 3D and 2D metal halide perovskites based on divalent metals such as Pb^{2+}, Sn^{2+},Cu^{2+}, Mn^{2+}, Cr^{2+} and Cd^{2+} have been reported, a larger variety of materials based on the double perovskite structure $A^{I}_2B^{I}B^{III}X_6$ with A- and B-site cations and halides X remain comparatively uninvestigated. If not only the compositional variety of 3D double perovskites is considered, but also the dimensional reduction to 2D phases of such, the structural and compositional possibilities become phenomenally vast. By introducing mono- or multivalent organic A-site spacer cations, the material properties can be tuned by the variation of the spacer cation and also the thickness of the octahedral layers of the perovskite that are separated by the spacer

cation.

Crystallographically speaking, a large number of double perovskites have been characterized or computed over the last 80 years, albeit the optoelectronic characterization and their potential for devices were only revisited recently.[7,8] Several halide double perovskites that are promising for optoelectronic application have been synthesized or computationally-predicted, such as $Cs_2AgBiCl_6$,[9] $Cs_2AgBiBr_6$,[5] $Cu_2AgBiBr_6$,[10] $(MA)_2TlBiBr_6$,[11] $Cs_2AgSbCl_6$,[12] $Cs_2AgInCl_6$,[13] $Cs_2AgTlBr_6$,[14] $ASbCuX_6$ (A = monovalent cation, X= Cl, Br, I)[15] and $(MA)_2KBiCl_6$.[16]

The currently most studied double perovskite is $Cs_2AgBiBr_6$, mostly owing to its promising charge-carrier properties and its stability, despite its relatively large band gap of $2.0\,eV$ to $2.3\,eV$.[17–22] Following this interest, more recently the effects of the dimensional reduction from 3D to 2D phases of $Cs_2AgBiBr_6$ have been reported by several groups by elaborating the theme in the form of $(BA)_4AgBiBr_8$, $(BA)_2CsAgBiBr_7$ (butylammonium (BA)),[23] $(PEA)_4AgBiBr_8$ (phenylethylammonium (PEA)),[20,24,25] $(iPA)_2CsAgBiBr_7$ (isopentylammonium (iPA)), $(iPA)_2CsAgBiBr_7$ (iPA),[26] $(PA)_4AgBiBr_8$(propylammonium (PA)), $(OCA)_4AgBiBr_8$ (octylammonium (OCA)), and $(BDA)_2AgBiBr_8$ (1,4-butyldiammonium (BDA)).[27]

As a way of modifying the band gap of halide perovskites, it is known that changing the halide anion decreases its size in the order of $Cl^- > Br^- > I^-$.[28] The desirable double perovskite Cs_2AgBiI_6 is unfortunately not easily synthesized because of its negative decomposition enthalpy resulting in $CsAg_2I_3$ and $Cs_3Bi_2I_9$.[29,30] Another beneficial effect of the dimensional reduction is that the 2D phases of this silver bismuth iodide system are thermodynamically stable and compounds of the Ruddlesden-Popper $n = 1$ structure $(OC^I_4AgBiI_8$ (OC^I = organic cation, monovalent; n = octahedral layer thickness) or the Dion-Jacobson $n = 1$ structure $(OC^{II}_4AgBiI_8$ (OC^{II} = organic cation, divalent) were successfully synthesized and reported, thus enabling access to iodide double perovskites. Besides the reduced band gap energies around $2\,eV$ caused by the heavier halide, a change in nature from indirect to direct band gap was reported several times to accompany the dimensional reduction from 3D to 2D systems.[23,31]

While bromide analogs have been reported with simple, alkylic and aromatic spacer cations such as butylammonium or phenethyl ammonium, the iodide analogues have only been reported recently with more strongly interacting organic spacer cations, as, for example, divalent molecules forming Dion-Jacobson phases or molecules with an increasing number of ring systems, thus increasing the strength of aromatic interactions. Organic spacer cations with atomic interactions through terminating atoms such as iodine, as demonstrated for $(3IPA)4AgBiI8$ (3IPA = 3-iodopropylammonium), or fluorine (our work) have also shown this ability to stabilize the lattice of thermodynamically un-

favoured iodide phases.[32] For these, a sufficient templating effect through either structural rigidity or stronger molecular interactions is required to discourage the formation of more stable 0D or 1D $\mathrm{Bi-I}$ lattices.[33] For the choice of the organic spacer cation, ammonium-terminated alkylic or aromatic molecules are most commonly used, optionally with chain/ring-incorporation of nitrogen or sulphur atoms or halogen substitution at various hydrogen positions.[34–37]

Here, we synthesized three new compounds of the $(\mathrm{OC})_4\mathrm{AgBiX}_8$ (X = Cl, Br, I) Ruddlesden-Popper $n = 1$ structure with 4-fluorophenethylammonium (4FPEA) serving as the organic cation. We present the first comparative halide study for 2D double perovskites. The compounds were structurally and optoelectronically characterized in powder and thin film form. We synthesized single crystals of $(4\mathrm{FPEA})_4\mathrm{AgBiBr}_8$ and $(4\mathrm{FPEA})_4\mathrm{AgBiI}_8$ while for $(4\mathrm{FPEA})_4\mathrm{AgBiCl}_8$ possible unit cell parameters were indexed. We use DFT to obtain insight into the electronic structure and atomic contributions to the frontier orbitals. Furthermore, we synthesized high-quality thin films and thoroughly characterized them employing GIWAXS. Finally, we provide initial insights into the charge-carrier dynamics and emissive properties, employing optical-pump terahertz-probe spectroscopy (OPTP) and PL measurements of these materials and incorporate them into photodetectors.

7.3 RESULTS AND DISCUSSION

7.3.1 Structural Characterization

The 3D halide perovskite structure is based on the general formula $\mathrm{ABX3}$ with corner-sharing BX_6 octahedra, divalent metal cations B^{2+} and halide anions X^-, where monovalent A^+ cations occupy the cuboctahedral cavities. For the 3D double perovskite, the general formula is expanded to $\mathrm{A}_2\mathrm{B}^{\mathrm{I}}\mathrm{B}^{\mathrm{III}}\mathrm{X}_6$, following the same occupational rules with the difference that the corner-sharing octahedra are now alternating between $\mathrm{B}^{\mathrm{I}}\mathrm{X}_6$ and $\mathrm{B}^{\mathrm{III}}\mathrm{X}_6$. Ruddlesden-Popper double perovskites with an octahedral layer thickness of $n = 1$ adopt the general formula $(\mathrm{OC})_4\mathrm{B}^{\mathrm{I}}\mathrm{B}^{\mathrm{III}}\mathrm{X}_8$, where the organic cation (OC) replaces the A^+ cation and is also monovalent. The organic cations separate the octahedral layers, with the positively-charged group (i.e. NH_3^+) terminating into the cuboctahedral cavities, while the uncharged part interacts via van der Waals (vdW) forces and dipole-dipole interactions, leaving a van der Waals gap between the organic layers.[38]

Investigating the structural properties of $(4\mathrm{FPEA})_4\mathrm{AgBiCl}_8$, $(4\mathrm{FPEA})_4\mathrm{AgBiBr}_8$ and

$(4FPEA)_4AgBiI_8$ (synthesized from a simple solution approach explained in detail in the experimental part) we find very small changes, where the $4FPEA$ cation seems to have the dominant influence on the structural direction, enabling synthesis of the chloride and bromide structure but also stabilizing the iodide structure. In contrast, the unsubstituted PEA cation can only yield the $(PEA)_4AgBiCl_8$ and $(4FPEA)_4AgBiBr_8$ compounds, but cannot stabilize the iodide structure (see XRD and EDX data in Figure 7.12 and Table 7.1).

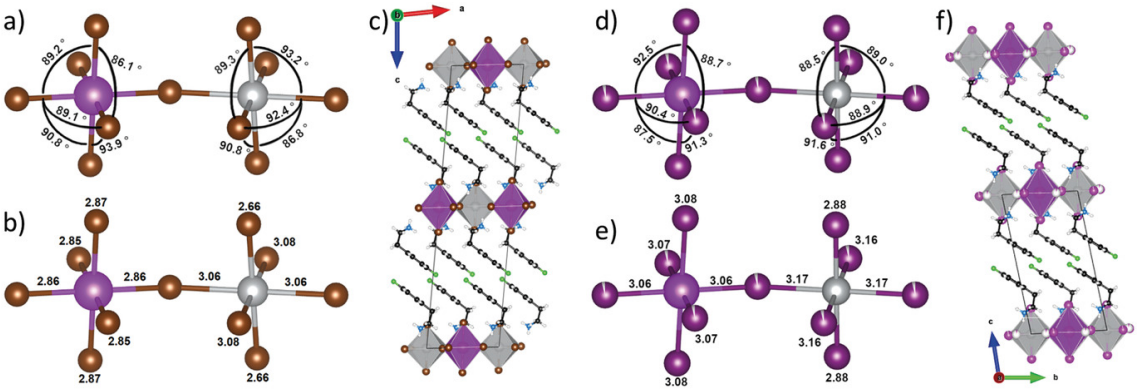

Figure 7.1: Single crystal structures of $(4FPEA)_4AgBiBr_8$ and $(4FPEA)_4AgBiI_8$ with octahedral angles in ° (a and d), bond lengths in Å (b and e) and comparative views of the unit cell of both structures (c and f). The bond angles shown are point symmetric with regard to their central metal atom and thus only shown once for clarity

.

The structures of $(4FPEA)_4AgBiBr_8$ and $(4FPEA)_4AgBiI_8$ were determined through single crystal X-ray diffraction, while for $(4FPEA)_4AgBiCl_8$ the lattice parameters were determined through indexing of powder XRD data. We note that the crystal structure of $(4FPEA)_4AgBiI_8$ was refined as a 2-component pseudomerohedral twin (pseudo-monoclinic cell) with a refined ratio of $0.75/0.25$ for the two domains. The two equatorial iodides are slightly disordered with ratios of site occupation factors refined to $0.97/0.03$ as seen in Figure 7.13. This disorder of equatorial iodines was also observed for other 2D iodide double perovskites such as $(AET)_2AgBiI_8$.[33] For the following comparative discussion, only the iodine sites with occupation of 97% will be considered. Furthermore, we limit the discussion to the comparison of the crystal structures to the bromide and iodide analogues as seen in Figure 7.1.

Unlike the octahedra in the cubic $Cs_2AgBiBr_6$ that exhibit equivalent bond lengths ($Bi-Br$ = 2.814 Å, $Ag-Br$ = 2.821 Å) and metal-halide-metal angles of 90 °, the octahedra in $(4FPEA)_4AgBiX_8$ are strongly distorted.[5] The angles in both structures in the Ag- and Bi-octahedra are equally distorted by up to 3.9 ° (Figure 7.1a and 7.1d). The bond lengths exhibit unequal distortion where the Ag-octahedra are strongly

tetragonally contorted, resembling a Jahn-Teller effect with short axial bonds ($Ag-Br$ = 2.66 Å, $Ag-I$ = 2.88 Å) and long equatorial bonds ($Ag-Br$ = 3.06/3.08 Å, $Ag-I$ = 3.17/3.16 Å), while the Bi-octahedra are mostly symmetrically and only marginally distorted ($Ag-Br$ = 2.85/2.86/2.87 Å, $Ag-I$ = 3.06/3.07/3.08 Å) (Figure 7.1b and e). This tendency of monovalent Ag is also observed in compounds such as $Ag^{I}Ag^{III}O_2$, compounds with other similar d^{10} transition metals, e.g. Au^+ or Cu^+ or other recently reported, Ag-containing 2D hybrid double perovskites and is attributed to a mixing of filled transition-metal nd orbitals with empty $(n+1)s$ orbitals, stabilizing a linear coordination geometry.[8,23,32,33,39,40]

One factor required to form 2D hybrid double perovskite iodides is the templating influence of the organic spacer cations, a term coined by Mitzi in 2000.[41] Both the RP and Dion-Jacobson (DJ) phases require an in-plane interaction of suitably sized organic spacers to stabilize the 2D lattice, for example, aromatic, vdW or dipole-dipole interactions. Contrarily, while the DJ phases have an intrinsically stronger interlayer connectivity by binding one organic layer to two adjacent inorganic layers through the divalent character, RP phases also require a strong interaction between organic spacer molecules along the out-of-plane direction. As of now, this synthetic difficulty has only yielded a small, but growing number of published structures, namely $(CHD)_2AgBiI_8{\cdot}H_2O$ (1,4-cyclohexandiamine (CHD)),[42] $(AE2T)_2AgBiI_8$ (AE2T),[33] $(3AMPY)_2AgBiI_8$ (3-(aminomethyl)pyridinium (3AMPY)),[36] $(4AMP)_2AgBiI_8$ (4-(aminomethyl)piperidinium (4AMP)),[43] $(3IPA)_4AgBiI_8$,[43] $(4IBA)_4AgBiI_8$ (4-iodobutylammonium (IBA)),[31] $(4AMP)_4AgBiI_8$,[44] $(APP)_4AgBiI_8$ (4-aminopiperidinium (APP)) and β-$(MPA)_4AgBiI_8$ (β-methylphenylethylammonium (β-MPA)).[45] In our work, we used the simple modification of the PEA^+ cation to the $4FPEA^+$ cation to achieve the stabilizing and templating effect. To emphasize this, the structural differences between $(PEA)_4AgBiBr_8$ and $(4FPEA)_4AgBiBr_8$ are shown in Figure 7.14 and Figure 7.15. We note that the structures of $(4FPEA)_4AgBiBr_8$ and $(4FPEA)_4AgBiI_8$ are sufficiently similar (as seen in Figure 7.1) to explain why $(PEA)_4AgBiI_8$ cannot be obtained without additional control of the interactions between layers. By simple comparison of the organic layers in the four shown directions (Figure 7.15) the increased order of the $4FPEA^+$ cations vs. the PEA^+ cations can be observed. When viewed along a the ring-to-ring stacking for both seems similar, but when viewed along b the twisting of the PEA^+ can be seen distinctly. In Figure 7.15 this is visualized by red lines connecting equal carbon atom positions in $4FPEA^+$ and PEA^+ and a yellow dot/lines displaying the channel formed by the arranged phenyl rings. The aromatic rings of $4FPEA^+$ are stacked in-plane of the organic layer along ab as well as out-of-plane along c, while PEA^+ is only stacked in-plane of the organic layer along ab and not also

out-of-plane along c which is a reason for the stabilizing binding effect between the organic layers. Furthermore, while in-plane stacking of $4FPEA^+$ cations is present in only one direction, as seen when viewed along b (Figure 7.15b)), PEA^+ cations in-plane stacking is present in two directions in an alternating fashion (Figure 7.15b) and d)). This increased out-of-plane stacking effect of the $4FPEA^+$ could be caused by the increased dipole moment of the molecule and/or the fluorine-fluorine attraction, leading to the observed point-symmetric anti stacking of the phenyl-rings (Figure 7.15b) and d)).[46,47] The calculated dipole moment for PEA^+ is 13.47 Debye, whereas for $4FPEA^+$ the value increased to 17.50 Debye, visualized in Figure 7.16. We further note that the substitution position of the fluorine atom seems crucial for the stabilizing effect for the 2D hybrid double perovskite iodide. While for lead- and tin-based 2D hybrid perovskites the ortho, meta and para position of the fluorine all yield the desired $n = 1$ 2D hybrid double perovskite phase, our attempts with $2FPEA$ and $3FPEA$ only yielded hybrid bismuth iodides (Figure 7.12), confirming that not only sufficient binding effects but also specific geometric requirements of the organic cation are needed to stabilize the silver bismuth iodide system.[48,49]

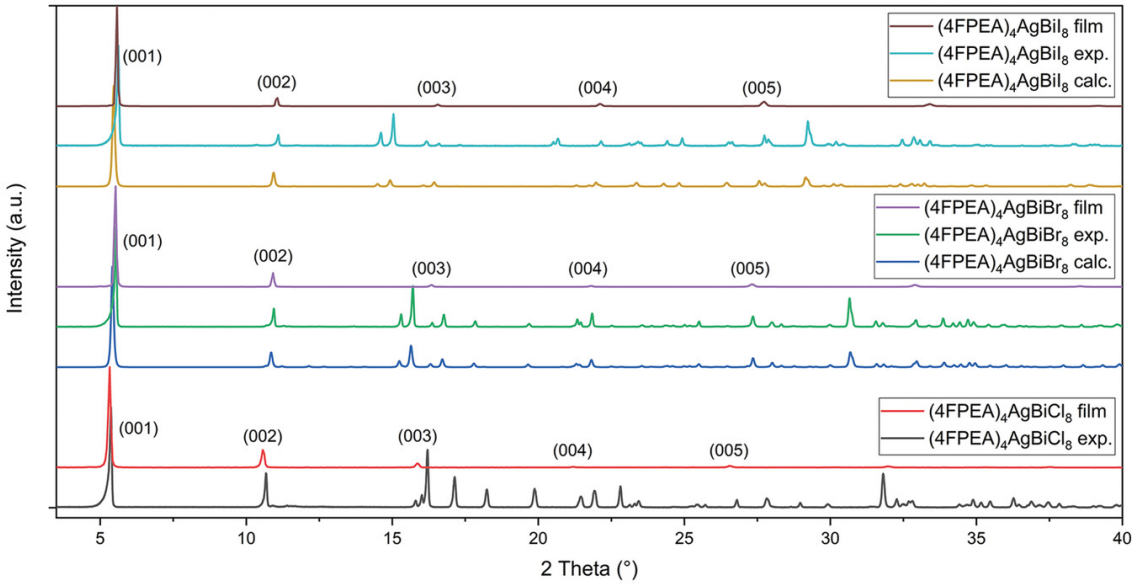

Figure 7.2: XRD patterns of thin films on ITO annealed at 140 °C and powdered crystals of $(4FPEA)_4AgBiX_8$ (X=Cl, Br, I) grown in solution along with calculated patterns for $(4FPEA)_4AgBiBr_8$ and $(4FPEA)_4AgBiI_8$ derived from single-crystal structures.

.

Figure 7.2 shows the XRD patterns of polycrystalline powders and thin films of $(4FPEA)_4AgBiX_8$ (X=Cl, Br, I) as well as theoretical patterns based on the single-crystal structures of $(4FPEA)_4AgBiBr_8$ and $(4FPEA)_4AgBiI_8$. For $(4FPEA)_4AgBiCl_8$ a single crystal has not been obtained, but the indexed lattice parameters agree well with the

powder XRD pattern and the lattice parameters of the bromide and iodide analog (Table 7.2). For the bromide and iodide compound, the experimental patterns also agree well with the simulated ones, without any detectable impurities, which we confirmed through a profile refinement (Figure 7.18). Consistently, energy dispersive X-ray spectroscopy confirms the stoichiometric ratio for both crystals and thin films for all three compounds (Table 7.3). A slight shift towards larger angles can be observed for both compounds from calculated to experimental diffractograms, indicating homogeneous lattice strain and thus a slightly compressed unit cell for experimental samples. From the thin film diffractograms, a strong orientation along the $(00l)$ planes can already be observed, which is characterized more thoroughly with GIWAXS measurements (see below). If the three halide compounds are compared from Cl to Br to I, a shift towards smaller angles for the $(hk0)$ planes can be observed, which is consistent with the increasing lengths of the unit cell in a and b directions, caused by the increase of ionic size of the halides and the increased equatorial metal-halide bond lengths (Table 7.2). In contrast, the $(00l)$ planes are shifted towards larger angles from Cl to Br to I, also in agreement with the decrease of the unit cell length in c direction. While the increase in bond distances and the ionic size is consistent for the axial octahedral bonds, the decrease in c direction can be attributed to slightly closer packing of the inorganic and organic layers.

7.3.2 Orientation and Thin Film Morphology

Thin films of $(4\mathrm{FPEA})_4\mathrm{AgBiCl}_8$, $(4\mathrm{FPEA})_4\mathrm{AgBiBr}_8$ and $(4\mathrm{FPEA})_4\mathrm{AgBiI}_8$ were fabricated by spin coating from N-Methyl-2-pyrrolidone (NMP) solutions onto different substrates with a subsequent annealing step. All three compounds in thin film form are strongly oriented along the $(00l)$ planes, corresponding to a parallel orientation of inorganic and organic layers to the substrate surface. This horizontal orientation is typical for single layered $n = 1$ 2D double perovskite phases and so far, no other orientations have been prepared.[45,47] Furthermore, while for Pb- and Sn-based 2D perovskites higher n phases and vertical orientations have been reported, for $\mathrm{Ag-Bi}$-based double perovskite systems $(\mathrm{BA})_2\mathrm{CsAgBiBr}_7$, $(\mathrm{iPA})_2\mathrm{CsAgBiBr}_7$ and $(\mathrm{PEA})_2\mathrm{CsAgBiBr}_7$ remain the only two known ones exhibiting the $n = 2$ thickness, though no thin films have been reported thus far.[23,25,26] While other studies have focused on initial thin film syntheses for $n = 1$ 2D double perovskites,[32,33,42,44] here we have optimized the morphology of the thin films on different substrates and were able to observe structural differences depending on the choice of substrate roughness, the different halides and annealing temperature.

To compare the influence of the substrate roughness we chose FTO-coated glass, indium-doped tin oxide (ITO)-coated glass and $\mathrm{Si\text{-}SiO}_2$ wafers as they are commonly used sub-

strates for optoelectronic applications such as photovoltaics, photodetectors, light emitting diodes or field effect transistors. The difference in surface roughness between these substrates is about one order of magnitude, with height differences (as RMS) of $\pm 60\,\mathrm{nm}$ for FTO, $\pm 5\,\mathrm{nm}$ for ITO and $\pm 1\,\mathrm{nm}$ for the polished SiO_2 wafer, see Figure 7.19 for line profile scans and AFM images.

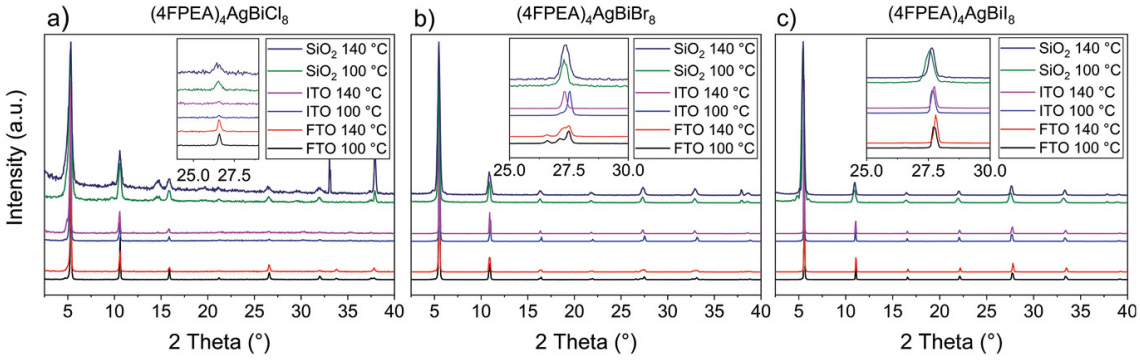

Figure 7.3: XRD patterns of thin films of a) $(4FPEA)_4AgBiCl_8$, b) $(4FPEA)_4AgBiBr_8$ and c) $(4FPEA)_4AgBiI_8$ on substrates FTO, ITO and SiO_2 from NMP solution with annealing at 100 °C or 140 °C. The different parameters are indicated in the legends, insets show a magnified view between 15-35° 2θ.

.

All thin film diffractograms show the same general orientation along $(00l)$ as shown in Figure 7.2 and 7.3. We observe the same trends in crystallinity and an increasing quality from Cl>Br>I (a more detailed discussion of the diffractograms is given in the supporting information under Figure 7.20). One key feature is the splitting and broadening of reflections for the Br films, which we attribute to increased lattice parameters for higher annealing temperatures of 140 °C vs. 100 °C, exerting tensile stress on the crystal lattice. To identify these different phases, a profile refinement revealed the slightly different lattice parameters for the concerned films, see Table 7.4. Interestingly, while the annealing temperatures for all three substrates were identical, there is an observable difference in the diffractograms. We attribute this to the varying thickness and heat conductivity of the substrates. While the silicon wafer already has a higher heat conductivity than ITO and FTO coated glass substrates, additionally the substrate thickness increases from $0.625\,\mathrm{mm}$ (Si-SiO_2 wafer) to $1\,\mathrm{mm}$ (ITO coated glass) and $3\,\mathrm{mm}$ (FTO coated glass), which leads to a faster heat transfer along FTO<ITO<SiO_2. This results in a decreasing rate of solvent evaporation and crystallization towards FTO substrates. We believe this to be a reason why for FTO samples a mixture of both phases is seen for both temperatures, while for ITO the two phases are formed much more distinctly and on SiO_2 the crystallization is basically too fast for a distinct phase to form, leading to a broad reflection profile indicating a very small crystallite size and a largely strained crystal lattice. Thin

films of $(4FPEA)_4AgBiI_8$ show no additional reflections and no reflection splitting, as observed in $(4FPEA)_4AgBiCl_8$ and $(4FPEA)_4AgBiBr_8$. Interestingly, the influence of the annealing temperature is inverse to that of $(4FPEA)_4AgBiBr_8$. With higher temperature the reflections shift towards higher angles compared to the diffractograms of 100 °C annealing. This leads to the conclusion that while films of $(4FPEA)_4AgBiBr_8$ at 140 °C display increased lattice parameters and tensile stress, films of $(4FPEA)_4AgBiI_8$ show decreased lattice parameters and thus compressive stress. This trend is seen for all three substrates and while again the SiO_2 films show broad reflections, they are also shifted towards higher angles.
To further analyze the influence of the substrate choice and annealing temperature, we performed GIWAXS measurements.

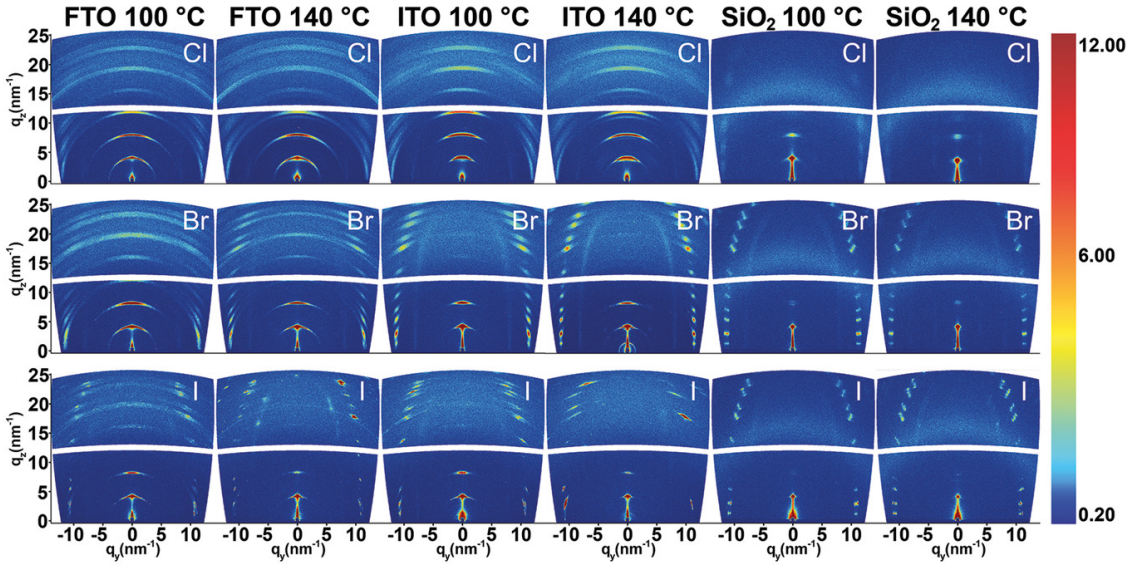

Figure 7.4: GIWAXS images of $(4FPEA)_4AgBiCl_8$,$(4FPEA)_4AgBiBr_8$ and $(4FPEA)_4AgBiI_8$ on FTO, ITO and SiO_2 annealed at 100 °C and 140 °C, measured with an incident angle α_i = 0.2°

.

The films prepared on FTO substrates, having the roughest surface of the three substrates, show the largest broadening of the reflections along the azimuthal angle χ compared to a smaller broadening for ITO substrates and sharp reflection dots for SiO_2 substrates (Figure 7.4). This orientational degree can be visualized quantitatively by plotting the intensity of the 001 reflection with χ as the abscissa and is discussed in more detail under **??**. The measurements shown in Figure **??** reveal that for all films the orientation is present and of the same degree throughout the complete film. Only for $(4FPEA)_4AgBiCl_8$ and $(4FPEA)_4AgBiBr_8$ films on FTO the orientations show slightly larger full width half maximum (FWHM) for the surface layers indicating a marginally smaller degree of hor-

izontal orientation. Furthermore, if annealing temperatures are compared, 140 °C compared to 100 °C results in sharper reflection dots and thus a higher degree of orientation. The main difference of these annealing temperatures is the increase of vapour pressure of the solvent NMP. With a boiling point of 202 °C, the vapor pressure increases almost tenfold from $3\,\mathrm{kPa}$ at 100 °C to $27\,\mathrm{kPa}$ at 140 °C, at ambient pressure.[50] This results in a much faster crystallization of the films, resulting in larger domains and a higher degree of orientation (Figure 7.24). Lastly, the crystallinity and degree of orientation increases for $\mathrm{Cl} < \mathrm{Br} < \mathrm{I}$ (7.25). This can be seen by the decreased azimuthal smearing of reflections for Cl, Br and I, respectively, as well as the increasing sharpness and intensity of reflections that originate from different $(11l)$ planes, located at scattering vectors q_y = $10\,\mathrm{nm}^{-1}$ and $-10\,\mathrm{nm}^{-1}$ (Figure 7.4). For the chloride perovskites these reflections are only visible as weak and very broad areas, while for the bromide perovskites they are more distinct with an increased sharpness from FTO < ITO < $\mathrm{SiO_2}$ and are distinctly shown as diffraction spots for the iodide. In the same way the reflections of the $00l$ planes are only visible on FTO, while on ITO for the bromide and iodide the relative intensity of the 001 and 002 reflection is too high for reflections of l>2 to be observable, demonstrating the high crystallinity of the $(4\mathrm{FPEA})_4\mathrm{AgBiBr_8}$ and $(4\mathrm{FPEA})_4\mathrm{AgBiI_8}$ thin films. This relative increase is seen again for films on the $\mathrm{SiO_2}$ substrates where only the 001 reflection is observable. To confirm the orientation and assignment of diffraction planes, indexed 2D GIWAXS images of thin films annealed at 100 °C are shown in Figure 7.25 for all three compounds confirming the crystal phase of the thin films. While the diffraction positions of $(00l)$ planes agree well with the calculated positions, the diffraction positions of planes including a and b lattice parameters exhibit a shift indicating a compressed unit cell in a and b. This almost single-crystalline, excellent orientation of the iodide thin films by a simple-solution based spin-coating process is remarkable. A similar high level of orientation and single-crystalline growth has been achieved very recently by Zhao et al. with (R/S-β-$\mathrm{MPA})_4\mathrm{AgBiI_8}$ utilizing a strongly crystallization-guiding capillary-bridge assembly technique.[45]

The surface morphology was probed with optical and scanning electron microscopy and both confirm the high quality of the films and their orientation. As examples, here we show films fabricated on ITO substrates with the same experimental conditions for all three halides in Figure 7.5. The films of $(4\mathrm{FPEA})_4\mathrm{AgBiI_8}$ are homogeneous and form large domains with dimensions of up to $100\,\mu\mathrm{m}$ as shown in Figure 7.5a and b. The smooth surface morphology is of very high quality as seen in the SEM image in Figure 7.5c, where the contrast is homogeneous over the complete surface and grain boundaries inside a single domain cannot be observed. $(4\mathrm{FPEA})_4\mathrm{AgBiBr_8}$ also forms homogeneous films throughout the complete film surface (Figure 7.5d and e), yet does not form the large

domains seen for the iodide perovskite. The domains seem bigger but rougher, which is also evident from the small holes in the SEM image in Figure 7.5f. Despite the small holes, the surface is still contrasted homogenously and grain boundaries cannot be observed. We note that for differently optimized parameters, an equally pristine surface can be obtained for $(4FPEA)_4AgBiBr_8$ films (Figure 7.26). For $(4FPEA)_4AgBiCl_8$, the film quality is not as pristine as for the iodide or bromide structure. The optical microscopy (OM) images (Figure 7.5g and h) show a grained surface morphology and this is more clearly observable in the SEM image (Figure 7.5i) where single grains with dimensions in the range of several microns can be observed. Furthermore, the layered structure of the material can be seen clearly, as the individual layers stacking in the grains are evident for slightly tilted grains and with uneven surfaces.

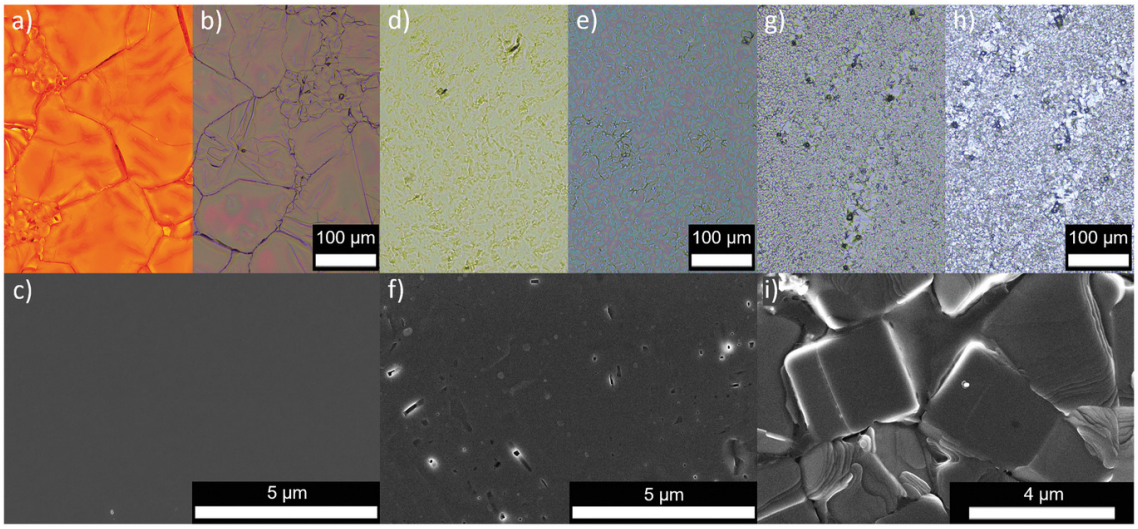

Figure 7.5: Optical microscopy images (top row) and SEM images (bottom row) for $(4FPEA)_4AgBiI_8$ (a-c), $(4FPEA)_4AgBiBr_8$ (d-f) and $(4FPEA)_4AgBiCl_8$ (g-i). OM images are shown in transmission lighting on the left and illumination lighting on the right (top) for the respective compound.

7.3.3 First Principle Calculations

To get insight into the electronic structure, DFT calculations were conducted. Figure 7.6a-c shows the PBE-SOC-TS band structures of $(4FPEA)_4AgBiX_8$ (X = Cl, Br, I). All calculations were carried out with the unit cells obtained from experimental single crystal data, although the band structure for $(4FPEA)_4AgBiCl_8$ was simulated starting from the iodide single crystal unit cell with the Rietveld refined unit cell parameters from the powder XRD measurements. The treatment of Bi-based 2D hybrid organic inorganic perovskites with SOC and dispersion correction is necessary to accurately describe the

electronic structure in these materials as shown extensively in previous works.[23] The inclusion of spin-orbit effects leads to a splitting of the CB, mostly consisting of Bi $6p_{1/2}$ orbitals (Figure 7.6d-f) in the CB. This was also shown prominently for the 3D compounds $Cs_2AgBiBr_6$ and $Cs_2AgBiCl_6$.[51] Furthermore, this conduction band separation leads to a change in the nature of the bandgap, centering the CB minimum at the Γ point as opposed to the X point as shown in Figure 7.28 for the non-SOC case, leading to a direct transition for all compounds. This was suggested to arise from band back-folding because of the structural distortion in 2D double perovskites as demonstrated by Connor et. al and is a common phenomenon described in multiple theoretical simulations.[23,33] Furthermore, the degeneracy from Γ to Z highlights the reduced electronic dimensionality. The bandgaps in all calculations are under $2\,\mathrm{eV}$, a significant and expected underestimation in comparison to the experimental results, mostly caused by the notorious ineffectiveness of DFT-PBE to quantitatively describe the experimental absorption edge values.[51]

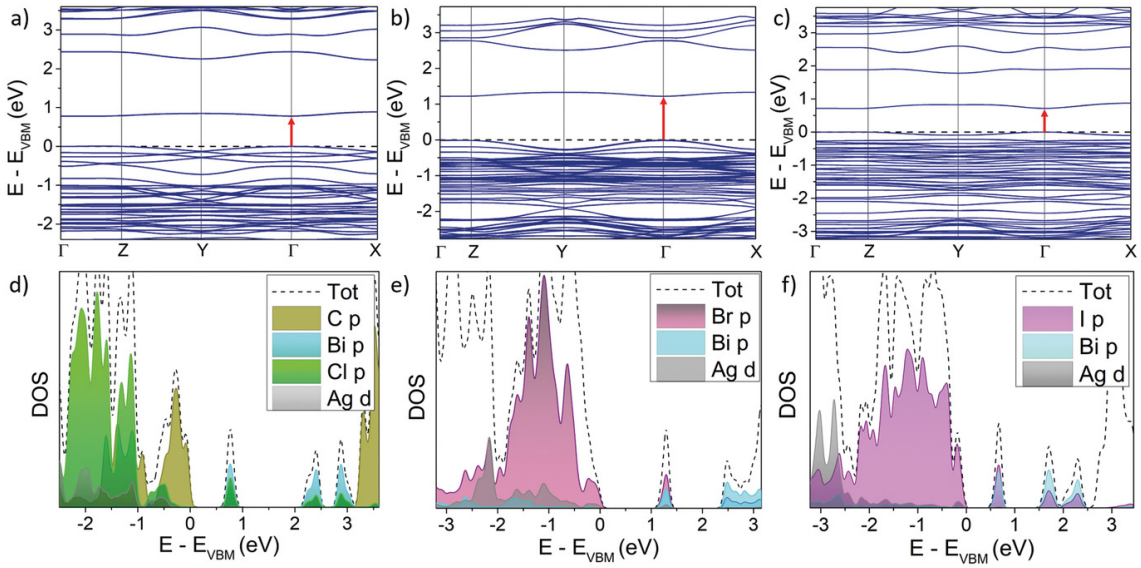

Figure 7.6: Band structures and projected density of states for a) and d) $(4FPEA)_4AgBiCl_8$, b) and e) $(4FPEA)_4AgBiBr_8$, and c) and f) $(4FPEA)_4AgBiI_8$.

To obtain insight into the atomic character of the frontier orbitals, the projected density of states (DOS) was evaluated for every compound. As expected, the character of the valence band maximum (VBM) and conduction band minimum (CBM) is similar for every halide, where the VB consists of mostly halide p and Ag-d orbitals and the CB is predominantly made up of Bi-p and a contribution of halide p orbitals (analogous to Pb-p and I-p for 2D Pb systems),[52] in agreement with previous publications.[23,33] However, the valence band character of $(4FPEA)_4AgBiCl_8$ seems to be of organic nature, with a dominant contribution of C-p states. Interestingly, the band dispersion appears to decrease from Cl to I, which we attribute to the growing degeneracy and separation of the organic highest

occupied molecular orbital (HOMO) and inorganic VB (Figure 7.29), where the organic frontier orbital is almost isoenergetic to the inorganic component for I, further apart for Br and well separated for Cl. The compounds therefore mostly form type Ib heterojunctions between inorganic and organic quantum wells, except the chloride phase, which manifests type IIb behavior, but considering the limits of DFT simulations the iodide phase could also represent a IIb heterojunction as shown for $[AE_2T]_2AgBiI_8$ by Jana et al.[33]

7.3.4 Optical Properties

We employed UV-Vis spectroscopy to determine the experimental values for the band gap energies for both powders and thin films. As the first principle calculations revealed the direct nature of the band gap, the Tauc plots for a direct allowed transition are shown as insets in Figure 7.7 for a, thin films and b, powders. For thin films, a corrected absorption was calculated by measurement of transmittance and reflectance spectra according to S21. The absorption and absorbance spectra show the typical blueshift for halide compounds with decreasing atomic number of the halide. The values for powders are $1.84\,eV$, $2.45\,eV$ and $2.99\,eV$ and for thin films $2.18\,eV$, $2.81\,eV$ and $3.33\,eV$ for $(4FPEA)_4AgBiI_8$, $(4FPEA)_4AgBiBr_8$ and $(4FPEA)_4AgBiCl_8$, respectively.

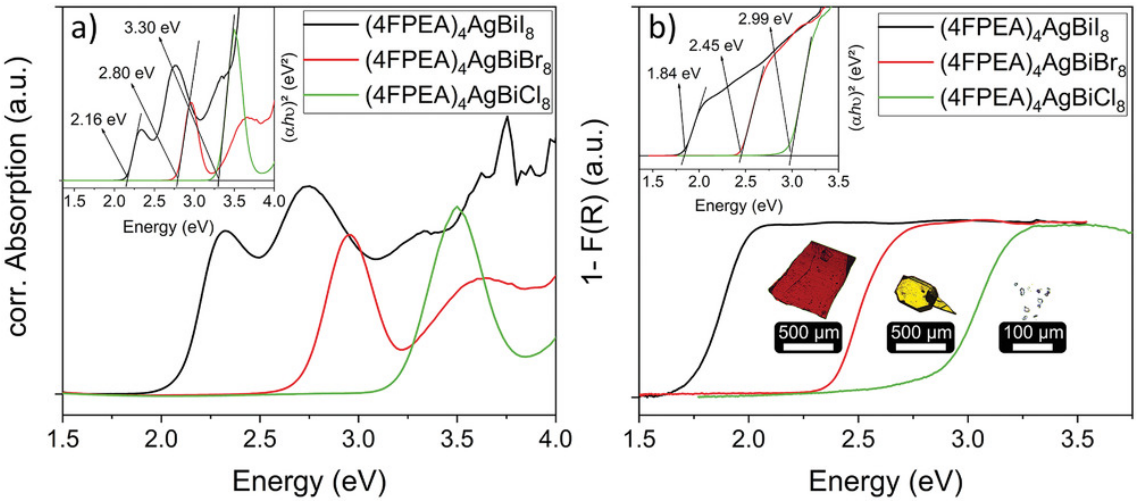

Figure 7.7: UV-Vis Absorption measurements with insets showing Tauc plots for a direct allowed transition for a) thin film and b) powder samples of $(4FPEA)_4AgBiCl_8$, $(4FPEA)_4AgBiBr_8$ and $(4FPEA)_4AgBiI_8$.

The lowest energy absorption in thin films is an isolated feature centered at $2.34\,eV$ (iodide), $2.98\,eV$ (bromide) and $3.53\,eV$ (chloride). This feature is in line with other findings, as a strong isolated absorption maximum is also found for thin films of the 3D analog $Cs_2AgBiBr_6$ or 2D analogs like $(BA)_4AgBiBr_8$ or $[AE_2T]_2AgBiI_8$.[23,48,53]The feature is

rather broad, in line with the aforementioned analogs and in contrast to the observed sharp excitonic feature in lead-based 2D perovskites.[54] The broad character, the absence of a strong temperature dependence and the large exciton binding energy attracted attention to the origin of this feature for $Cs_2AgBiBr_6$, and recently Wright et al. provided support for the theory that the absorption peak in the 3D compound arises from a direct exciton despite the mentioned anomalies.[51] A second isolated feature is visible at higher energies of $2.76\,eV$ (iodide) and $3.66\,eV$ (bromide) but overlapping with the UV absorption of the substrate and hence not measurable for the chloride. The second feature appears stronger for the iodide than for the bromide, being the absorption maximum at high energy blue light. This second feature is slightly less visible for the bromide and again not measurable for the chloride, due to the UV absorption overlap of glass. Furthermore, the simulated absorption from the dielectric response for the bromide reveals strikingly similar features, excluding excitonic effects (Figure 7.31). Here, the two first absorption maxima are attributed to the inorganic contribution in the VBM and CBM, probably caused by the aforementioned Bi $6p$ band splitting.[55] Moreover, a similar mechanism as described by Jana et al. is suggested, where the absorption is traced back to the equatorial halide ion rather than a direct Ag to Bi transition, as the contribution of Bi-p/Ag-d in the VBM/CBM are negligible.[33] The intense lowest-energy absorption peak has also been demonstrated theoretically for inorganic and hybrid double perovskites A_2SbCuX_6, with the iodide compounds showing the highest maxima compared to lighter halide compounds. This absorption thus seems intrinsic to the double perovskite halide family.[15]

The powder absorption data display a redshift for all three compounds and do not show the distinct absorption features of the thin films as clearly, but still visible upon scaling (Figure 7.32). The features, ordered from lower to higher energy, have their maxima for the iodide at $2.14\,eV$, $2.39\,eV$, $2.52\,eV$ and $2.96\,eV$, for the bromide at $3.07\,eV$ and for the chloride at $3.45\,eV$. The number of maxima match those of their respective thin film plots, although not as distinctly visible (for the iodide the feature at $2.14\,eV$ appears very small, whereas the maxima at $2.39\,eV$, $2.52\,eV$ and $2.96\,eV$ appear reminiscent of the observed pattern in the thin films, with the features at $2.39\,eV$ and $2.52\,eV$ either overlapping, which could be caused by the 2^{nd} and 3^{rd} CBM, or appearing due to low measurement resolution.) The shift of $0.34\,eV$ (iodide), $0.36\,eV$ (bromide) and $0.34\,eV$ (chloride) relative to thin film data might be caused by anisotropic absorption and thickness dependence where indirect transitions in bulk powder measurements are statistically more relevant than for thin films of a few hundred nanometers.

In the following, we discuss the charge-carrier dynamics and emissive behavior of thin films of $(4FPEA)_4AgBiBr_8$ and $(4FPEA)_4AgBiI_8$. While these processes and the excitonic character of 3D $Cs_2AgBiBr_6$ are well established in the literature, they are yet to

be fully explored for the 2D submembers of the double perovskite. Although substantial advances have been made recently by Schmitz et al. and Pantaler et al. elucidating the emissive features and charge-carrier dynamics of $Ag-Bi-Br$ based 2D double perovskites, a comprehensive view is still lacking.[25,46,53,55,56] Here, we observe similarities owing to the related $Ag-Bi$ double perovskite system, but also some differences between the perovskites with halides bromide and iodide.

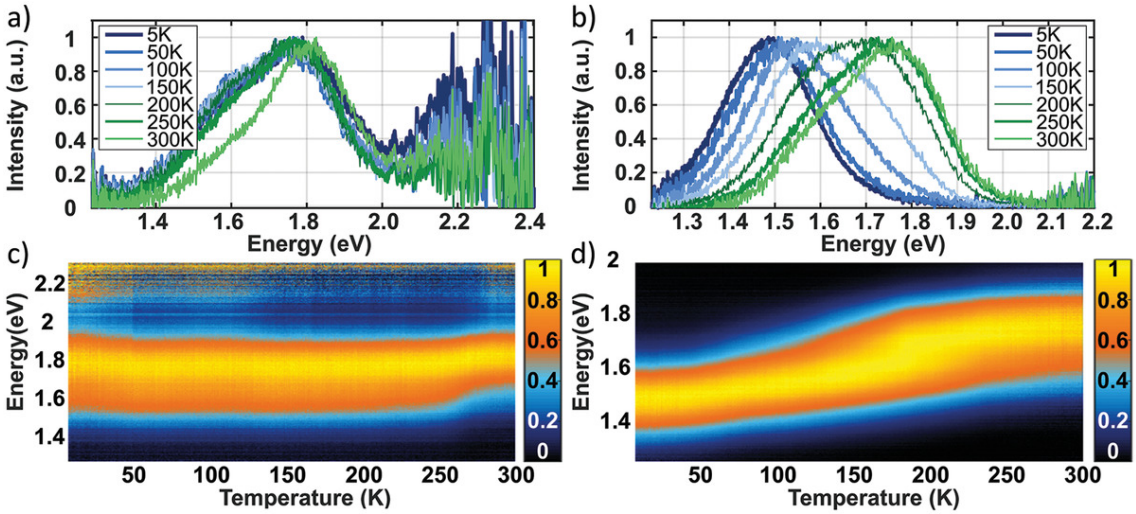

Figure 7.8: Temperature dependent PL spectra and color plots of the normalized PL spectra at temperatures between $5\,K$ to $300\,K$ for a) and c) ($(4FPEA)_4AgBiBr_8$, and b) and d) $(4FPEA)_4AgBiI_8$.

PL measurements on thin films show weak intensities and very broad emissions with a FWHM of $300\,meV$ for the iodide and $320\,meV$for the bromide at room temperature (Figure 7.8a and b). The characteristic broad emission for these systems is also observed in other 2D silver-bismuth-halide, 2D lead-halide and 3D silver-bismuth-halide systems.[23,43,46,51,53] In $Cs_2AgBiBr_6$, it is generally attributed to substantial electron-phonon coupling, leading to self-trapping or localization of the charge carriers or excitons. These self-trapped charge carriers subsequently diffuse to color centers and recombine, leading to the broad and strongly red-shifted PL.[25,53,57]

Intriguingly, for $(4FPEA)_4AgBiI_8$ a significant spectral shift of the emission with decreasing temperature is observed, with a redshift of the emission maximum from $1.7\,eV$ at $300\,K$ to $1.46\,eV$ at $5\,K$ (Figure 7.33). This is remarkable as this large shift is not observed in $Cs_2AgBiBr_6$ or other 2D silver-bismuth-halide double perovskites for which the temperature-dependent PL data have been examined.[33,53] While initially often argued that the broadness of the emission and thus the absence of a narrow emission at low temperatures is counterintuitive of a dominant excitonic contribution, we find a moderate reduction of the FWHM by $120\,meV$, from $320\,meV$ at $300\,K$ down to $200\,meV$

at $5\,\mathrm{K}$ (Figure 7.33). One reason for the persistent broadness of the PL is attributed to defect-mediated charge-carrier recombination and thus a considerable defect population. Since an intrinsic defect population has been reported for single crystals of $Cs_2AgBiBr_6$, demonstrating a tendency towards disorder and/or crystallographic imperfections arising from B-site metal disorder between Ag and Bi, we would assume this tendency of double perovskites to also be present in their 2D subsets.[17,57] Adding the fact that we measured thin film samples, with a rapid crystallization mechanism compared to a single crystal synthesis, we can assume an even higher number of defects, potentially explaining the large temperature-independent inhomogeneous broadening parameter $200\,\mathrm{meV}$ (ignoring scattering from ionized impurities).[57,58] Contrary to these two trends observed for the temperature-dependent emission of $(4FPEA)_4AgBiI_8$, the emission for $(4FPEA)_4AgBiBr_8$ peak shifts only slightly, from $1.78\,\mathrm{eV}$ at $300\,\mathrm{K}$ to $1.68\,\mathrm{eV}$ at $5\,\mathrm{K}$. On the other hand, the FWHM of the emission increases from $300\,\mathrm{meV}$ at $300\,\mathrm{K}$ up to $420\,\mathrm{meV}$ at $5\,\mathrm{K}$. However, by inspecting more closely the PL temperature-dependent lineshape, we notice that the emergence of a lower energy feature (peaked at $1.6\,\mathrm{eV}$) may conceal any spectral broadening and shifts of the peak observed at room temperature.

Interestingly, for $(PEA)_4AgBiBr_8$ a similar emission shape was observed for spectra recorded at $300\,\mathrm{K}$ and $80\,\mathrm{K}$, with a redshift or an emerging feature at lower energies for $80\,\mathrm{K}$.[25] We further notice a difference between the reported absorption with its maximum at $3.2\,\mathrm{eV}$ and our measurement with its absorption maximum at $3\,\mathrm{eV}$. Such prominent Stokes shifts are also commonly reported for $Cs_2AgBiBr_6$, where exact values can depend on the measurement technique, as well potentially on the morphology of the measured thin films (See Figure 7.27) showing the flat and homogeneous surface morphology observed for the samples, compared to the dendritic or needle-shaped morphology of $(PEA)_4AgBiBr_8$ thin films reported in[25]).

In the following, we compare the PL data collated as part of our study of $(4FPEA)_4AgBiBr_8$ and $(4FPEA)_4AgBiI_8$ with the available data reported in the literature for $(4FPEA)_4AgBiBr_8$,[25] $(BA)_4AgBiBr_8$[46] and $(iBA)_4AgBiBr_8$.[46] While the excitation energies and the reported PL ranges differ depending on the employed setup and the publication, they share similar overall features. Schmitz et al. proposed a sound explanation for the processes of the excited states,[46] which we confirmed and displayed schematically in Figure 7.9. Initially, at sufficient above band gap excitation free charge carriers are generated. Owing to the strong excitonic interactions in these materials, a fraction of the free carriers (depending on the exciton binding energy (EBE) usually in the hundreds of meV for these materials) will rapidly form a free exciton state. Furthermore, because of the strong carrier-phonon interactions prevalent in these systems, these free charge carriers or free excitons subsequently undergo an ultrafast localization process

or self-trapping forming a small polaron state. Moreover, these polarons will diffuse to color centers where recombination occurs.

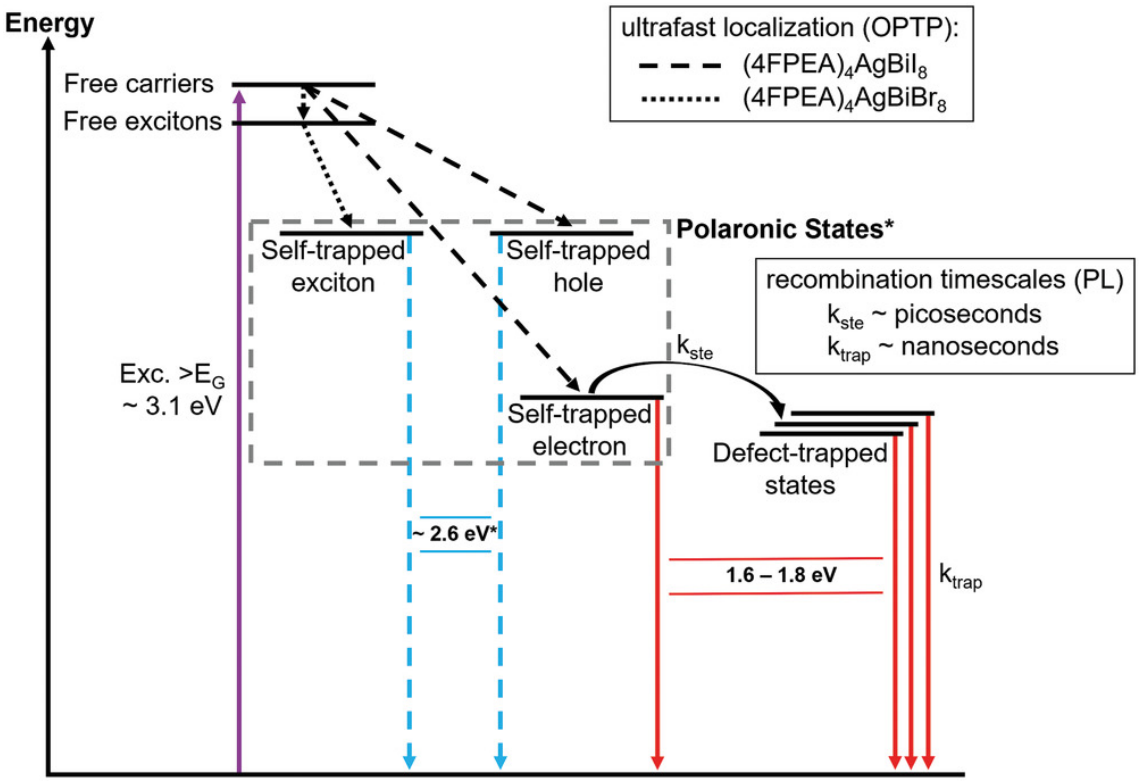

Figure 7.9: Schematic mechanism of the charge-carrier dynamics and emission for silver-bismuth based 2D double perovskites with exemplary energy ranges typical for the bromide compounds.

To further support the photophysical picture presented in Figure 7.9, we measured the early-time dynamics of photoexcited charge-carriers for $(4FPEA)_4AgBiI_8$ and $(4FPEA)_4AgBiBr_8$ thin films by using OPTP spectroscopy. This technique monitors the dynamics of free charge-carriers by measuring the change in transmitted THz electric-field amplitude (expressed here as $-\frac{\Delta T}{T}$) upon photoexcitation of the material using a $3.1\,eV$ femtosecond laser pulse.

OPTP measurements for $(4FPEA)_4AgBiI_8$ Figure 7.10a reveal an ultrafast and almost complete decay of the photoconductivity within $10\,ps$ after photoexcitation. Crucially, the observed photoconductivity signal is proportional to three factors: the photon-to-charge branching ratio ϕ (i.e. the fraction of free carrier density generated per absorbed photon density), the number of photogenerated charge carriers n and the electron-hole sum-mobility μ.[59] Therefore, in principle, the observed ultrafast decay can be caused by variations in each of these quantities, in processes such as exciton formation, charge-carrier localization and defect-mediated recombination. The reported EBEs for 2D and 3D silver-bismuth halide perovskite are in the hundreds of meV ($250\,meV$ for $(OC)_4AgBiBr_8$ and

$\sim 300\,\mathrm{meV}$ for $Cs_2AgBiBr_6$),[25,53] thus we expect strong excitonic interactions for thermally equilibrated charge carriers. However, we note that: (i) at the typical excitation densities of OPTP experiments ($\sim 10^{13}\,\mathrm{cm^{-2}}$), the Saha equation predicts a non-negligible fraction of free carriers for EBEs $> 200\,\mathrm{meV}$;[60] and (ii) the excess energy provided by $3.1\,\mathrm{eV}$ pump pulses implies the transient generation of free carriers rather than excitons. Recent studies on $Cs_2AgBiBr_6$ and Cu_2AgBiI_6 reported a similar ultrafast decay of the photoconductivity and attributed this to the strong carrier-phonon coupling and the formation of small polarons, i.e. to an ultrafast localization of the charge carriers caused by a significant distortion of the lattice.[53,61] To test this hypothesis, we fitted the fluence-dependent OPTP data with a two-level mobility model developed by Wright and co-workers (explained in details in the SI).[51] The excellent agreement between experimental data and fits supports the hypothesis of ultrafast carrier localization as a major cause in the ultrafast decay of photoconductivity. Furthermore, the fluence-independent nature of the OPTP signal (Figure 7.34) rules out exciton formation as a possible cause.

The average initial mobility value for $(4FPEA)_4AgBiI_8$ extracted across the range of fluences is $\phi\mu_{del} = 0.6 \pm 0.1\ \mathrm{cm^2\,V^{-1}\,s}$, almost five times lower than what was reported for $Cs_2AgBiBr_6$[53] and the observed localization rate is $k_{loc} = 0.7 \pm 0.1\ \mathrm{ps}$. Interestingly, the mobility after localization is below our detection limit and is set to zero in the fitting procedure. This observation supports the predictions of low electronic dimensionality for silver-bismuth halide elpasolites, which extended to bi-dimensional layers implies the complete electronic de-coupling of $[AgX_6]^{5-}$ and $[BiX_6]^{3-}$ octahedra (i.e., holes are localized on $[AgX_6]^{5-}$ octahedra, which are surrounded by $[BiX_6]^{3-}$ octahedra, thus hindering the charge-carrier hopping - and vice-versa for electrons).[62,63]

As shown in Figure 7.10b, the comparison between $(4FPEA)_4AgBiI_8$ and $(4FPEA)_4AgBiBr_8$ reveals a significantly reduced photoconductivity for the bromide counterpart. The estimated carrier mobility for $(4FPEA)_4AgBiBr_8$ is $\phi\mu = 0.6 \pm 0.06\ \mathrm{cm^2\,V^{-1}\,s}$ and the observed signal decay is almost limited by the time resolution of our setup ($\sim 290\,\mathrm{fs}$). Considering the higher EBE expected for bromides and the comparatively lower excess energy provided by the pump pulse (i.e. at $3.1\,\mathrm{eV}$, $(4FPEA)_4AgBiBr_8$ is excited almost directly on its absorption peak), we hypothesize that the lower OPTP signal and the observed ultrafast decay of the signal could imply ultrafast exciton formation rather than charge localization. These findings suggest that, while a significant fraction of free charge carriers contributes to the $(4FPEA)_4AgBiI_8$ excited state dynamics, the formation of excitons determines the charge-carrier dynamics for $(4FPEA)_4AgBiBr_8$ when excited at $3.1\,\mathrm{eV}$.

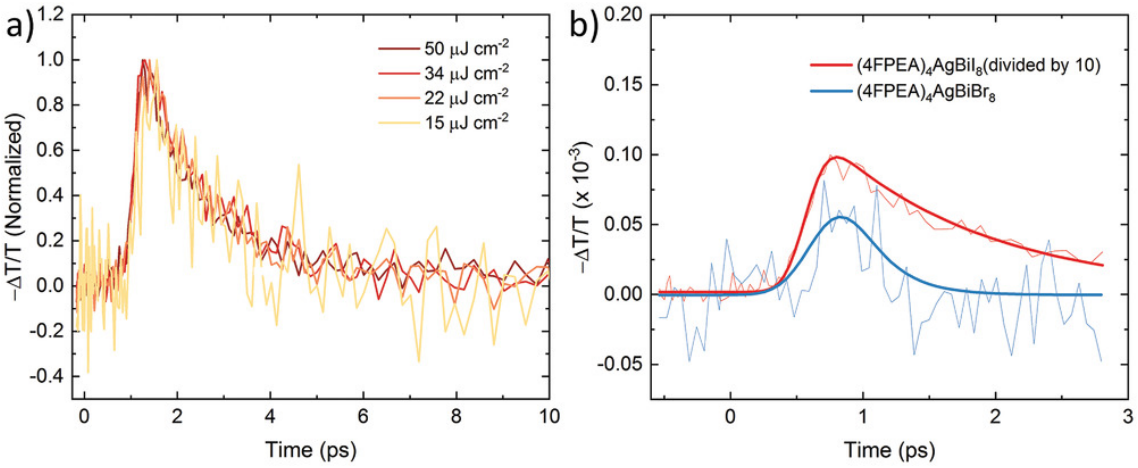

Figure 7.10: (a) Early time fluence-dependent optical pump terahertz probe (OPTP) signal measured for $(4FPEA)_4AgBiI_8$ after $3.1\,eV$ pulsed excitation and fitted with a two-level mobility model, with the fits shown as colored solid lines. The two-level mobility model is explained in detail in the Supporting Information section (see 7.35). (b) Comparison between early time OPTP signal measured for $(4FPEA)_4AgBiI_8$ and $(4FPEA)_4AgBiBr_8$ after $3.1\,eV$ pulsed excitation at a fluence of $50\,\mu J\,cm^{-2}$. The signal for $(4FPEA)_4AgBiI_8$ is divided by a factor of 10 to facilitate the comparison. Solid lines represent experimental data and dashed lines represent fits to the two-level mobility model, described in the Supporting Information section (see 7.35)

To further complement these interpretations, we draw attention to the DFT studies reported by Schmitz et al..[46] These first-principle calculations on $(PEA)_4AgBiBr_8$ suggest that the PL emission energies of the differently trapped excited states vary substantially, in good agreement with their experimental observations. Namely, for the $Ag-Bi-Br$ based materials, which feature the main absorption around $3\,eV$, they predicted the first, higher-energy emission at around $2.6\,eV$ to be caused by either band-to-band exciton recombination or self-trapped hole recombination. The second, lower-energy emission at around $1.8\,eV$ could be assigned to self-trapped electron or defect-mediated recombinations. Owing to our excitation energy of $3.06\,eV$ for the PL measurements, being barely resonant with the main band gap absorption of $(4FPEA)_4AgBiBr_8$ at room temperature, as well as our detection limit at $2.1\,eV$, such high-energy emission was not observable. Nonetheless, the observed low-energy emission at $1.8\,eV$ agrees well with the findings for the other $Ag-Bi-Br$ systems. To explain the small redshift and the possible appearance of a second emissive feature at $1.6\,eV$ with decreasing temperatures further research is still needed. Although the excitation energy of $3.06\,eV$ should be sufficiently above the band gap absorption for $(4FPEA)_4AgBiI_8$, we are still limited with a detection limit at $2.1\,eV$, but still the observed emission with its maximum at $1.7\,eV$ is in line with the expected energies for self-trapped electron or defect-mediated recombination. The origin of the seemingly single feature with its much larger redshift with decreasing temperature

compared to the bromide compound is also still an open question for further research.
We measured similar PL transients for both materials and fitted them with a biexponential decay function, which helped us identify two recombination processes occurring on different timescales. For $(4FPEA)_4AgBiI_8$ we report a first very short-lived component with lifetimes in the range of $20\,\mathrm{ps}$ at $300\,\mathrm{K}$ increasing to $100\,\mathrm{ps}$ at $5\,\mathrm{K}$. The second, longer-lived component showed lifetimes of $1\,\mathrm{ns}$ at $300\,\mathrm{K}$ increasing to $50\,\mathrm{ns}$ at $5\,\mathrm{K}$. The transients for both compounds are shown in Figure 7.36. In the given model, we would assign the first, short lifetime to a charge hopping process of the self-trapped electrons from a slightly higher energy level before they fall into defect trap states, which can be confirmed by time- and spectral-dependent measurements, as shown in Figure 7.37. For the energetically higher-lying spectral part above $1.7\,\mathrm{eV}$, we find a higher amplitude ratio for the short-lived component compared to the energetically lower lying spectra below $1.3\,\mathrm{eV}$. As the thermal barrier relatively increases at lower temperatures, this trap-mediation becomes less likely, self-trapped electrons live longer and thus the lifetime of the emission of self-trapped electrons increases. Additionally, we used an Arrhenius plot to extract an activation energy of $126\,\mathrm{meV}$ for $(4FPEA)_4AgBiBr_8$ and $20\,\mathrm{meV}$ for $(4FPEA)_4AgBiI_8$ as the energy barrier of said hopping process (Figure 7.38). The second, longer-lived lifetime component is assigned to defect-mediated recombination, which freezes out below temperatures of $100\,\mathrm{K}$. Overall, our findings agree with the current interpretation of the charge-carrier dynamics, displaying much more complicated, underlying photophysical processes compared to 3D lead perovskites, because charge carriers are almost exclusively present as excitonic pairs, subsequently forming polarons as a result of the inherent spatial localization on the $Ag-Bi$ based octahedra in the double perovskite structure, as well as structural reorganization following excitation which supports small-polaron formation.

7.3.5 Photodetectors

2D hybrid perovskites have been implemented successfully in various optoelectronic applications such as solar cells, field-effect transistors, X-ray- and photodetectors or light-emitting diodes.[24,31,35,64,65] Specifically, 2D Pb- and Sn-based perovskite photodetectors display excellent performance in terms of photoresponsivity and detectivity. However, their toxicity and environmental instability may limit their practical applications.[6] Recently, some of the emerging lead-free 2D double perovskites have been demonstrated as phototransistors and polarized-light detectors.[6,9,24,43,45] Recently a $Ag-Bi$-based 2D double perovskite crystal $(iPA)_2CsAgBiBr_7$ has been demonstrated as an electronic device with a polarized light sensitivity application.[43] Another recent work demonstrated

the high performance of a photodetector based on single-crystalline microwire arrays of (R/S-β-$\mathrm{MPA})_4\mathrm{AgBiI_8}$ after employing a capillary-bridge assembly technique. While photodetectors based on bulk single crystal (R/S-β-$\mathrm{MPA})_4\mathrm{AgBiI_8}$ achieved detectivities of 1.2×10^7 Jones, the incorporation into the microwire arrays achieved an increase up to a detectivity of $3.98x10^{11}$ Jones, demonstrating the importance of crystal quality, crystal orientation in regard to the electrode as well as the distance of the electrodes (single crystal channel area of $0.32\,\mathrm{mm^2}$ compared to microwire channel width of $2\,\mu\mathrm{m}$ x height of $0.225\,\mu\mathrm{m}$.[45,66]

Here, we demonstrate the first thin film, solution-processed $\mathrm{Ag-Bi}$ based 2D double perovskite photodetectors fabricated via a one-step processing method. The air-stable solutions of $(4FPEA)_4AgBiBr_8$ and $(4FPEA)_4AgBiI_8$ are compatible with deposition protocols such as spin coating, doctor-blading and drop casting, showing promise regarding scalable methods such as printing. The solutions for the devices can be prepared by directly dissolving the perovskite material, or dissolving the halide salts, as explained in the experimental section. The solutions were deposited on interdigitated gold electrodes (channel width of $10\,\mu\mathrm{m}$) either by doctor blading or drop casting and were annealed at 80 °C for $5\,\mathrm{min}$ directly afterwards. (Since the photoconductivity setup was operated with a halogen lamp operating from $400\,\mathrm{nm}$ which is not sufficient for the excitation of the large band gap perovskite $(4FPEA)_4AgBiCl_8$, only the responsivity and specific detectivity of $(4FPEA)_4AgBiBr_8$ and $(4FPEA)_4AgBiI_8$ were characterized (Figure 7.11). A current-voltage measurement applied between $0\,\mathrm{V}$ to $1\,\mathrm{V}$ provided a linear dependence for both materials, corresponding to an ohmic behavior with high resistance. At constant bias illumination with white light and an intensity of $100\,\mathrm{mW\,cm^{-2}}$ the current increased by a factor of three. The photodetectors based on $(4FPEA)_4AgBiI_8$ show responsivities of over $2\,\mathrm{mA\,W^{-1}}$ with a bias voltage of $1\,\mathrm{V}$ with a low noise level ($110\,\mathrm{pA\,Hz^{-1}}$), which results in a specific detectivity of up to 5×10^8 Jones (see 7.6). Photodetectors based on $(4FPEA)_4AgBiBr_8$ show higher responsivities of up to $10\,\mathrm{mA\,W^{-1}}$, with a similar noise level and a specific detectivity of up to 6×10^9 Jones. A comparison with state-of-the-art lead-free perovskite photodetectors is given in Table 7.6. Our devices based on $(4FPEA)_4AgBiI_8$ demonstrate a detectivity one order of magnitude higher than that based on bulk single crystal ((R/S-β-$\mathrm{MPA})_4\mathrm{AgBiI_8}$, but 3 orders of magnitude lower than those based on single crystalline microwire array (R/S-β-$\mathrm{MPA})_4\mathrm{AgBiI_8}$. We assume that the lower performance of the single-crystal-based device is caused by the top evaporated contacts, which should limit the out of plane charge transport and thus throughout the crystal, owing to the layered 2D structure and the insulating organic layers. This is partially overcome by using interdigitated contacts (i.e. microwire arrays). The crystallization method of a functionalized morphology to control the capillary spread employed in

the microwire arrays further increases the contact quality over the simple synthesis technique we employed here. Lastly, smaller channel widths or electrode distances seem to contribute to a better charge transport, because of the ultra-short lifetimes and large binding energies of the generated charge carriers in these materials. Although the 2D double perovskites show some intrinsic deficits compared to 3D Sn- and $\mathrm{Ag-Bi}$-based perovskites, their incipient performance is already comparable, demonstrating the potential of controlled crystallization and orientational freedom intrinsic to 2D structures. Lastly, both devices have shown stable performance for more than two weeks with measurements and storage under ambient conditions.

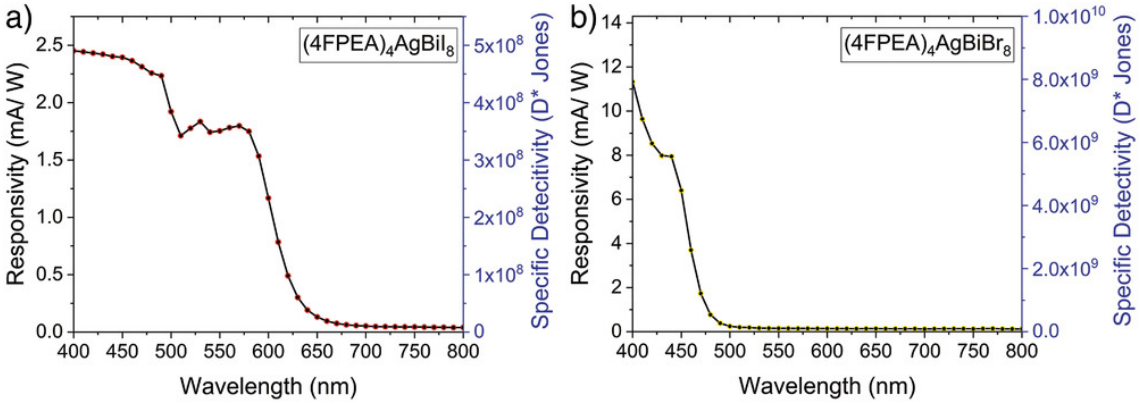

Figure 7.11: Responsivity and specific detectivity of photodetectors of a) $(4FPEA)_4AgBiI_8$ and b) $(4FPEA)_4AgBiBr_8$.

7.4 CONCLUSION

We demonstrate the synthesis of three new 2D hybrid silver-bismuth double perovskites $(4FPEA)_4AgBiX_8$ (X = Cl, Br, I) and demonstrate the ability of a simple, fluorinated organic spacer to stabilize the silver-bismuth-iodide double perovskite lattice. The simple solution-based synthesis yields highly crystalline materials in both bulk and thin-film form. The thin films crystallize as highly oriented structures in which organic and inorganic layers are oriented exclusively horizontally to the substrate surface. The crystalline thin-film quality can be tuned through choice of substrate and synthesis parameters to form domains of up to hundreds of microns with single-crystalline-grade morphology and orientation. DFT calculations reveal key properties such as the direct band gap caused by dimensional reduction. Moreover, we show how the band dispersion is influenced by the halides and attribute this to the growing degeneracy of the organic HOMO and inorganic VB from Cl to Br and I. Our temperature-dependent PL measurements show extremely broad emission and strongly Stokes shifted emission for all three materials.

OPTP measurements point towards photoexcitation being followed by an initial, ultrafast charge-carrier localization and the formation of small-polaron states. We are thus able to account for the observed charge-carrier dynamics and emissive behavior through a mechanism based on inherent exciton formation, small-polaron formation (or "self-trapping") and defect-mediated recombination. Finally, we demonstrate the incorporation of $(4\mathrm{FPEA})_4\mathrm{AgBiBr}_8$ and $(4\mathrm{FPEA})_4\mathrm{AgBiI}_8$ into photodetector devices showing promising performance, if the interplay of intrinsic 2D double perovskite properties and morphological control for device fabrication is considered. Our work provides detailed insights into the emerging structural class of lead-free 2D hybrid double perovskites and their distinct properties in comparison to 3D double perovskite structures.

7.5 SUPPORTING INFORMATION

7.5.1 Experimental Section & Methods

Bulk and single crystals

4-Fluorophenethylammonium salts ($4FPEAX$, X = Cl, Br, I) were synthesized by dissolving 1 eq. 4-fluorophenethylamine (Sigma-Aldrich 99%) in $150\,mL$ ethanol (Fischer Scientific absolute, >99%) at 0 °C. Then, 1.1 eq. conc. HX acid (X = Cl, Br, I) (Sigma-Aldrich hydrochloric acid 37 wt. % in H_2O, 99.999% trace metals basis; Sigma-Aldrich hydrobromic acid, 48 wt. % in H_2O, ≥99.99%, 48%; Sigma-Aldrich hydroiodic acid 57 wt. % in H_2O, distilled, stabilized, 99.95%) was slowly added and the mixture was stirred at 0 °C for 2 h. Afterwards, the solution was allowed to heat up to room temperature and the solvent was removed under vacuum. The product was washed three times with adequate amounts of diethyl ether (Sigma-Aldrich contains 1 ppm BHT as inhibitor, anhydrous, ≥99.7%) and dried under medium vacuum.

Powders of $(4FPEA)_4AgBiX_8$ were synthesized by slowly adding an excess of aq. conc. HX acid (X = Cl, Br, I) (Sigma-Aldrich hydrochloric acid 37 wt. % in H_2O, 99.999% trace metals basis; Sigma-Aldrich hydrobromic acid, 48 wt. % in H_2O, ≥99.99%, 48%; Sigma-Aldrich hydroiodic acid 57 wt. % in H_2O, distilled, stabilized, 99.95%) to 0.5 eq. Ag_2O (Fluka 99%), 0.5 eq. Bi_2O_3 (Alfa-Aesar 99,975 % metals basis) and 4 eq. 4-Fluorophenethylamine (Sigma-Aldrich 99%) under stirring at room temperature for 1 h. The solutions were filtered and the products were washed three times with adequate amounts of diethyl ether (Sigma-Aldrich contains 1 ppm BHT as inhibitor, anhydrous, ≥99.7%) and then dried under medium vacuum.

Single crystals of $(4FPEA)_4AgBiBr_8$ were grown by dissolving the as previously described synthesized powder in $1\,mL$ γ-butyrolactone (GBL) (Sigma-Aldrich ReagentPlus®, ≥99%) in a small vial (V = $1.5\,mL$) which was placed in a bigger vial (V = $25\,mL$) filled with $2\,mL$ diisopropylether (DIPE) (Sigma-Aldrich anhydrous, 99%). By vapour diffusion of the anti-solvent DIPE into the GBL perovskite solution, single crystals were obtained and washed three times with adequate amounts of diethyl ether and dried under medium vacuum.

Single crystals of $(4FPEA)_4AgBiI_8$ were grown by cooling a saturated aqueous HI solution with 1 eq. AgI (Sigma-Aldrich 99%), 1 eq. BiI_3 (TCI anhydrous) and 4 eq. $4FPEAI$ at 3 °C/h from 110 °C to 30 °C. The solution was filtered and the obtained single crystals were washed three times with adequate amounts of diethyl ether and dried under medium

vacuum.

Thin films

The substrates FTO-coated glass, ITO-coated glass and Si-SiO_2 (polished with 300 nm thermally grown SiO_2) wafers were cleaned by ultrasonication for 15 minutes in a solution of acetone, isopropanol and ethanol (1:1:1). Afterwards, the substrates were cleaned for 10 minutes under nitrogen plasma. Stoichiometric amounts of AgX, BiX_3 and 4FPEAX (X = Cl, Br, I) (AgCl Sigma-Aldrich 99%; $BiCl_3$ Sigma-Aldrich >98%; AgBr Alfa-Aesar 99,5%; $BiBr_3$ Sigma-Aldrich >98%; AgI Sigma-Aldrich 99%; BiI_3 (TCI anhydrous >98%) were dissolved in 1-Methyl-2-pyrrolidinone (NMP Sigma-Aldrich anhydrous, 99.5%). Thin films on FTO and ITO were spin coated in a glove box with N_2 atmosphere, from a 0.5 M solution, thin films on Si-SiO_2 wafers were spin coated from a 0.06 M solution. Thin films were spin coated at an initial step of 3000 rpm for 10 s with a second step of 6000 rpm (FTO, ITO) or 8000 rpm (Si-SiO_2) for 50 s. The films were annealed at 100 °C for 3 minutes or 140 °C for 1 minute with a subsequent annealing at 70 °C for 5 minutes to afford a slow cooldown to room temperature.

Photodetectors

Gold contacts were prepared on glass substrates by optical lithography and thermal evaporation followed by a lift-off process. The electrodes are films of Au/Ti with 40/10 nm thickness. The size of the gap between electrodes was 10 μm and the total length was 8 mm, giving an 8×10^{-8} m^2 active area. The noise characterization was done with a larger active area of 0.1 cm^2. Photodetectors were fabricated by doctor blading or drop casting $(4FPEA)_4AgBiX_8$ (X = Br & I) solution in NMP onto pre-patterned finger-structured gold contacts. The devices were then dried at 80 °C for 5 minutes at ambient conditions.

7.5.2 Characterization Techniques

Powder X-ray Diffraction (P-XRD)

P-XRD measurements were carried out on a Stoe Stadi P diffractometer in Debye-Scherrer geometry, operating at 40 kV and 40 mA, using monochromated (Ge(111) single crystal monochromator) Cu-$K_{\alpha 1}$ radiation (λ = 1.5406 Å) and a Dectris Mythen 1k detector.

Thin Film X-ray Diffraction (TF-XRD)

TF-XRD measurements were carried out on a Bruker D8 Discovery diffractometer in Bragg-Brentano geometry, with Ni-filtered Cu-$K_{\alpha 1}$ radiation (λ = 1.5406 Å) and a position-sensitive LynxEye detector.

Single-Crystal X-ray Diffraction (SC-XRD)

SC-XRD were carried out on a Bruker D8 Venture Txs system equipped with a multilayer mirror monochromator and a Mo-K_α rotating anode X-ray tube (λ = 0.71073 Å). The frames were integrated with the Bruker SAINT software package. Data were corrected for absorption effects using the Multi-Scan method (SADABS). The structure was solved and refined using the Bruker Shelxtl Software Package.

Grazing-Incidence Wide Angle X-ray Scattering (GIWAXS)

GIWAXS measurements were carried out on a Anton-Paar Saxspoint 2.0 with a Primux 100 microfocus source with Cu-$K_{\alpha 1}$ radiation (λ = 1.5406 Å) and a Dectris Eiger R 1M 2D Detector.

Scanning Electron Microscopy (SEM) and Energy Dispersive X-ray Spectroscopy (EDX)

SEM and EDX measurements were carried out on a FEI Helios NanoLab G3 UC Dual Beam microscope.

Atomic Force Microscopy (AFM)

AFM measurements were performed under ambient conditions using a Nanoink atomic force microscope with Si n-type tip with a radius of < 10 nm in tapping mode with a scan rate of 0.2 Hz.

First-Principle Calculations Density-Functional Theory (DFT)

First-principle DFT calculations were based on a plane waves basis set and pseudopotentials as implemented in the Quantum Espresso package.[67] Furthermore, the PBE exchange−correlation functional and the Tkatchenko−Scheffler (TS) dispersion scheme were used.[68,69] Latter is necessary to accurately describe the structural properties in low-dimensional perovskite materials.[70] The structures were optimized until all residual forces on the nuclei were below 1.0 x 10^{-3} a.u.. Hereby, following equilibrium unit cell parameters were obtained, all within less than 1% deviation of experimental data:

$(4FPEA)_4AgBiI_8$: a = 8.62, b = 8.75, c = 16.37, α = 98.97, β = 90.12, γ= 90.01
$(4FPEA)_4AgBiBr_8$: a = 7.83, b = 7.62, c = 30.22, α = 90.00, β = 91.87, γ= 90.00
$(4FPEA)_4AgBiCl_8$: a = 8.16, b = 7.78, c = 16.77, α = 90.01, β = 97.38, γ= 90.12
A kinetic energy cutoff of 50 Ry for the wavefunctions and 400 Ry for the charge density was used. For the bromide structure, a minimal, satisfactory converged 2x2x1 k-point grid was utilized for SCF and relaxation calculations because of the large dimension of the system. The iodide and chloride compounds were calculated by using a larger 4x4x1 grid. Furthermore, larger 12x12x3 grids were used for NSCF calculations to accurately describe the projected density of states.

UV-Vis Absorption (UV-Vis)

UV-Vis spectra were taken on a Perkin-Elmer Lambda 1050 spectrometer equipped with a 150 mm integration sphere. Thin films were measured in transmittance and reflectance mode. Powder measurements were measured in reflection mode with a Praying Mantis® diffuse reflection setup.

Photoluminescence (PL)

Photoluminescence-Spectra were measured with a self-built confocal microscope system. The used objective was a Nikon 100x 0.75NA DIC with a working distance of 4 mm. Furthermore, a closed cycle cryostat system (Atto Dry 800, Attocube) with an ultra-short-working-distance option (3 mm from sample to outside) was installed which allows one to control the sample temperature from 5 to 300 K. As Laser-source for excitation a 405 nm pulsed Laser Diode (Pico Quant P-C-405) was used, which has an adjustable repetition rate and a pulse length of 50 to 300 ps, depending on the applied diode voltage. Besides, a Short Pass Filter 450 (Fesh 450 Thorlabs) in the excitation path was installed cleaning the laser spectrum and a Long Pass Filter 490 (Chroma) was used for the detection side. In the detection path, an Avalanche Photo Diode (APD, model MPD PDM, 50 µm detector size) was built in for confocal images and was combined with a Time Correlated Single Photon Counting (TCSPC)-Card (Becker & Hickel) measuring time dependent PL-decays. In addition, a second optical path was implemented with an Andor Shamrock spectrometer SR303i combined with a charged coupled device (CCD) camera (Andor Newton DU920 open electrode) to record spectra.

Photoconductivity (PC)

Photoconductivity was measured by illumination with a tungsten lamp monochromatized through an Acton SP2150 (Princeton Instruments) spectrograph/monochromator.

PC spectra were recorded for light modulated by a mechanical chopper with a frequency of 13 Hz. Bias was applied by a Keithley 236 SMU at 2 V, chosen according to the stability of the dark current. The signal was recorded by a Signal Recovery 7265 DSP lock-in amplifier, which provides as a standard output also the noise voltage or current per bandwidth. The setup was controlled by home-written software in LabView IV.

Optical-pump terahertz-probe spectroscopy

Our optical pump terahertz probe (OPTP) setup has been described in detail previously.[61] Briefly, the OPTP setup used an amplified Ti:sapphire laser system (Spitfire), providing 800-nm emission with 35-fs pulse duration and 5-kHz repetition rate. The fundamental output was used to generate single-cycle THz radiation pulses via the inverse spin Hall effect.[70] THz transmission was measured by using free-space electro-optic (EO) sampling with a 1 mm-thick ZnTe crystal, a Wollaston prism and a pair of balanced photodiodes. Samples for OPTP were deposited onto 2 mm thick z-cut quartz. In the setup, samples were excited by frequency-doubled 400 nm pulses, obtained by second-harmonic generation in a beta-barium-borate (BBO) crystal. During the OPTP measurements, the THz emitter, EO crystal, and samples were kept under vacuum at pressures below 0.1 mbar.

7.5.3 Supplementary Data

Our attempts to synthesize $(PEA)_4AgBiI_8$, $(2PEA)_4AgBiI_8$ and $(3PEA)_4AgBiI_8$ in the same way as for $(4PEA)_4AgBiI_8$ yielded only hybrid bismuth iodides. The resulting crystalline powder is of orange color compared to the red colored $(4PEA)_4AgBiI_8$ and the resulting diffractogram differs greatly from the expected diffractogram that should be close to the standard $n = 1$ double perovskite patterns, this is shown in Figure 7.12. Furthermore, we performed EDX measurements on said powder and confirm the absence of any Ag, only showing the presence of Bi and I as seen in Table 7.1.

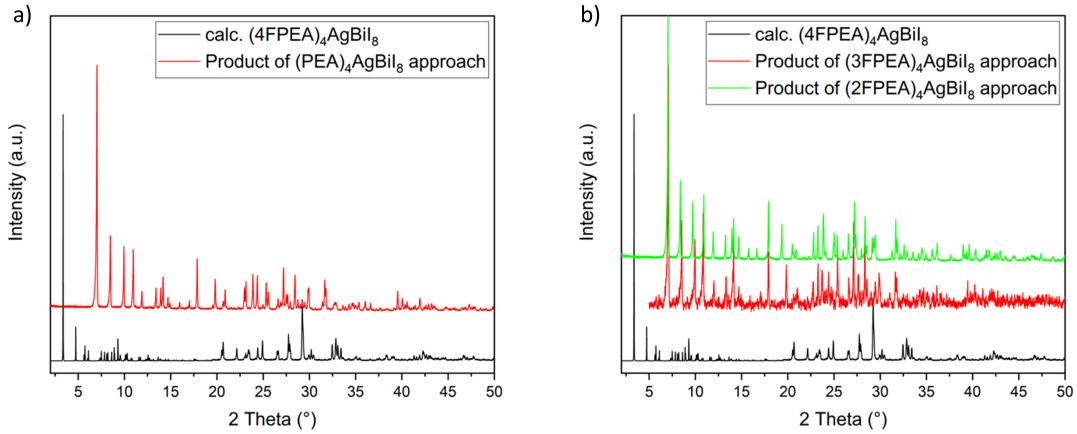

Figure 7.12: Diffractogram of the products of the synthesis approaches for a) $(PEA)_4AgBiI_8$ and $(2FPEA)_4AgBiI_8$ compared to the calculated diffractogram of $(4FPEA)_4AgBiI_8$.

Table 7.1: EDX data for the crystalline products of the synthesis approach for $(PEA)_4AgBiI_8$.

Measurement	Ag (at%)	Bi (at%)	I (at%)	Ratio(Bi:I)
1	-	13.51	86.49	1:6.40
2	-	12.23	87.77	1:7.18
3	-	13.66	86.32	1:6.32
4	-	15.36	84.64	1:5.51
5	-	15.05	84.95	1:5.65
6	-	15.26	84.74	1:5.55

The structure of $(4FPEA)_4AgBiI_8$ has been refined as a 2-component pseudomerohedral

twin (pseudo-monoclinic cell). The twin volume ratio of the two domains refined to 0.75/0.25. Two iodides are slightly disordered, the ratio of site occupation factors refined to 0.97/0.03.

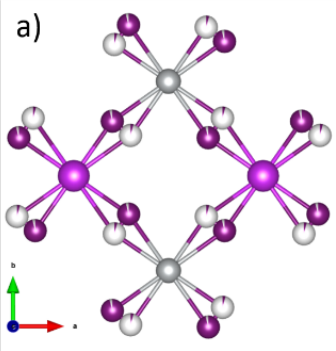

Figure 7.13: Iodide Disorder in the single crystal structure of (4FPEA)4AgBiI8.

The structures $(4FPEA)_4AgBiBr_8$ and $(PEA)_4AgBiBr_8$ display different levels of organic interlayer stacking effects. We note that the structures of $(4FPEA)_4AgBiBr_8$ and $(4FPEA)_4AgBiI_8$ are sufficiently similar (as seen in Figure 7.1) to explain why $(PEA)_4AgBiI_8$ cannot be obtained without additional control of the interactions between layers. By simple comparison of the organic layers in the four shown directions (Figure 7.15), the increased order of the $4FPEA^+$ cations vs. the PEA^+ cations can be observed. When viewed along a, the ring- to-ring stacking for both seems similar, but when viewed along b the twisting of the PEA^+ moiety can be seen distinctly. In Figure 7.15 this is visualized by red lines connecting equal carbon atom positions in $4FPEA^+$ and PEA^+ and a yellow dot/lines displaying the channel formed by the arranged phenyl rings. The aromatic rings of $4FPEA^+$ are stacked in-plane of the organic layer along ab as well as out-of-plane along c, while PEA^+ is only stacked in- plane of the organic layer along ab and not also out-of-plane along c, which is a reason for the stabilizing binding effect between the organic layers. Furthermore, while in-plane stacking of $4FPEA^+$ cations is present in only one direction, as seen when viewed along b (Figure 7.15b)), PEA^+ cations in-plane stacking is present in two directions in an alternating fashion (Figure 7.15b) and d)). This increased out-of-plane stacking effect of the $4FPEA^+$ moieties could be caused by the increased dipole moment of the molecule and/or the fluorine-fluorine attraction, leading to the observed point-symmetric anti stacking of the phenyl-rings (Figure 7.15b) and d)).[46,71] The calculated dipole moment for PEA^+ is 13.47 Debye, whereas for $4PEA^+$ the value increases to 17.50 Debye, visualized in Figure 7.16. We further note that the substitution position of the fluorine atom seems crucial for the stabilizing effect for the 2D hybrid double perovskite iodide. While for lead- and tin-based 2D hybrid perovskites the ortho, meta and para position of the fluorine all yield the desired $n = 1$ 2D hybrid double

perovskite phase, our attempts with $2FPEA^+$ and $3FPEA^+$ only yielded hybrid bismuth iodides (Figure 7.12), confirming that not only sufficient binding effects but also specific geometric requirements of the organic cation are needed to stabilize the silver bismuth iodide system.[72,73] This is best seen in Figure 7.14, where the in-plane stacking of the phenyl rings is observable for both structures in b) and d), but the out of plane organic layer stacking is only seen in $(4FPEA)_4AgBiBr_8$ in a) compared to $(PEA)_4AgBiBr_8$ in c). This difference is displayed more in detail in Figure 7.15, where only the organic part of the structures is shown. Red dotted lines illustrate the stacking positions of layer-to-layer stacking of adjacent phenyl rings and yellow dotted lines illustrate the in-plane stacking of adjacent phenyl rings. It is apparent that the $4FPEA^+$ molecules are arranged orderly in- and out-of-plane, while the PEA^+ molecules are only ordered in-plane. The in-plane stacking is further worse for the PEA molecules, as they stack in an alternating manner, best seen in Figure 7.15b) and d).

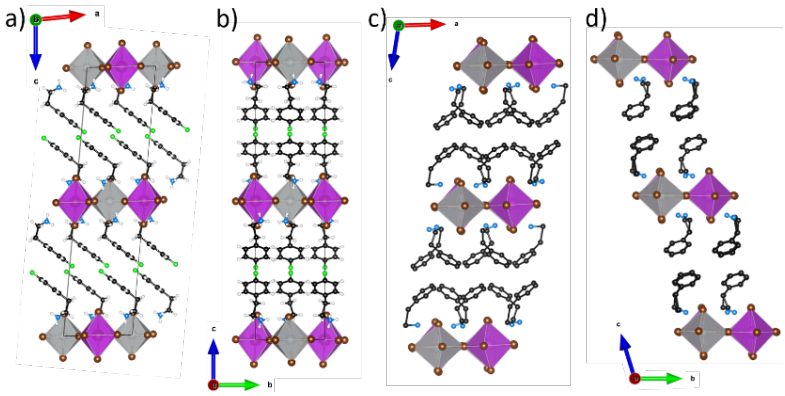

Figure 7.14: Comparison between the crystal structures of a) and b) $(4FPEA)_4AgBiBr_8$ and c) and d) $(PEA)_4AgBiBr_8$ along the b- and a-axis.

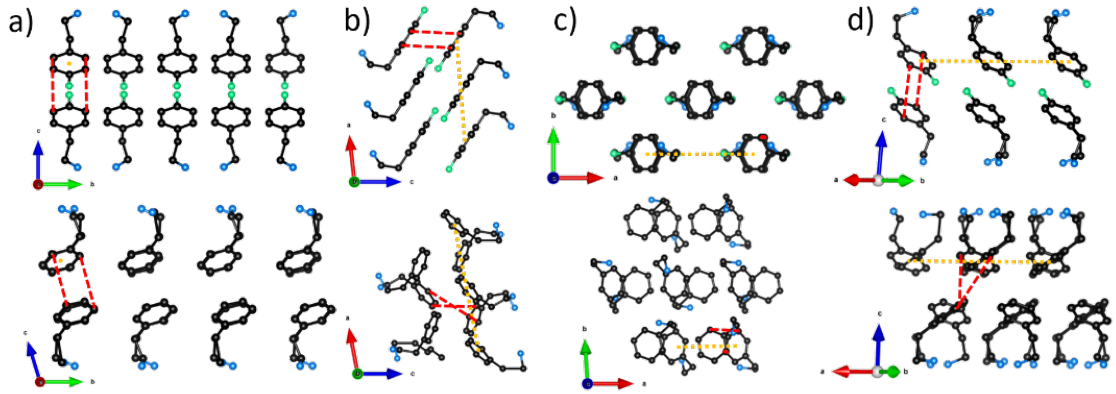

Figure 7.15: Comparison between the organic layers of $(4FPEA)_4AgBiBr_8$ on the top and $(PEA)_4AgBiBr_8$ on the bottom, along different crystallographic axis in a) b) c) and d).

The dipole moment of the cations was calculated by using the Gaussian 16W suite, using DFT and the B3LYP functional in a 6-31G* basis set.[74] The value for PEA^+ is 13.4646 Debye, whereas for $4FPEA^+$ the value increased to 17.4947 Debye. The direction of the dipole moment is visualized in Figure 7.16 as a blue arrow, with the arrow head indicating the positive charged side and the arrow tail indicating the negative charged side. The difference in charge is visualized through an increased length of the arrow in $4FPEA^+$. The increased dipole moment is one of the reasons for the increase in ordered stacking effect for $4FPEA^+$ vs PEA^+, alongside other effects like $\pi - \pi$ stacking and fluorine-fluorine interactions.[71]

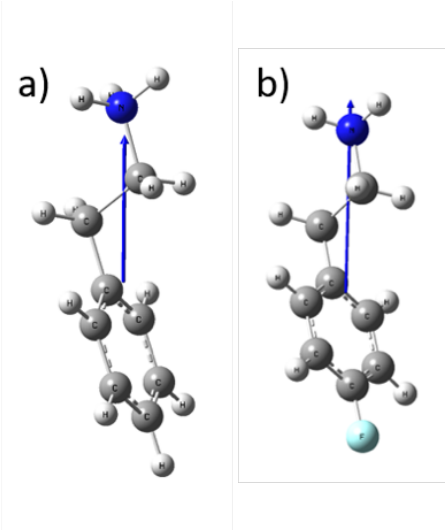

Figure 7.16: Dipole moments of a) PEA^+ and b) $4FPEA^+$ visualized as blue arrows.

The lattice parameters for $(4FPEA)_4AgBiBr_8$ and $(4FPEA)_4AgBiI_8$ were determined through the single crystal structure solution. For $(4FPEA)_4AgBiCl_8$ we performed indexing in EXPO 2014 using the indexing program N-TREOR09 and compared the given solutions with the two solved structures to choose the most plausible parameters.[75] The lattice parameters are given in Table 7.2 and agree well with the powder patterns.

Compound	a (Å)	b (Å)	c (Å)	α (°)	β (°)	γ (°)	V (Å^3)	Space Group
$(4FPEA)_4AgBiCl_8$	8.1741	7.8068	16.7934	90	97.60	90	1062.2	P 1 21 1
$(4FPEA)_4AgBiBr_8$	8.3833	8.1395	32.7693	90	96.120	90	2223.3	P12/n1
$(4FPEA)_4AgBiI_8$	8.6236	8.7470	16.3676	98.973	90.119	90.013	1219.5	P-1

Table 7.2: Lattice parameters for $(4FPEA)_4AgBiX_8$ (X=Cl, Br, I). Parameters for $(4FPEA)_4AgBiBr_8$ and $(4FPEA)_4AgBiI_8$ are obtained from the single crystal structure solution, while parameters for $(4FPEA)_4AgBiCl_8$ were obtained from indexing powder XRD data.

Cross section of $(4FPEA)_4AgBiI_8$ on SiO_2 showing a homogeneous coverage, with $(4FPEA)_4AgBiI_8$ lightest contrast on top, $500\,nm$ thick darker contrast SiO_2 below and a lighter contrast Si on the bottom.

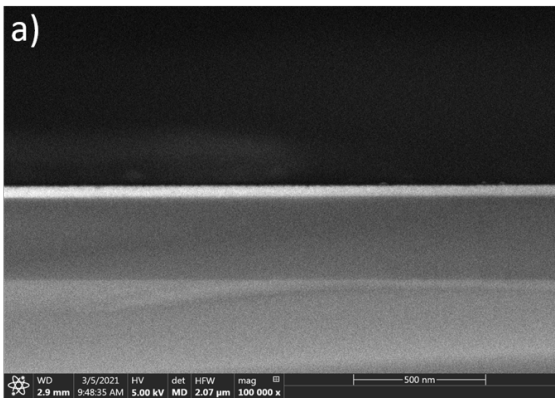

Figure 7.17: Cross section of $(4FPEA)_4AgBiI_8$ on SiO_2.

To confirm the bulk powder products of $(4FPEA)_4AgBiBr_8$ and $(4FPEA)_4AgBiI_8$ we performed a profile refinement in EXPO 2014 employing a Pearson VII profile shape function, background modelling by a Chebyshev polynomial of degree 16 and a refinement of non- structural parameters with the LeBail method.[75] The refinement values R_p and R_{wp} are in good agreement and the biggest deviations can be seen in the difference plots coming from the main reflex between $5 - 6°$ $2\,\theta$, showing a large asymmetric peak shape which is caused by the small angle area and the resulting inaccuracy of the diffractometer. As there are no additional reflexes present in the difference plots or any reflexes missing we conclude the product to be phase pure.

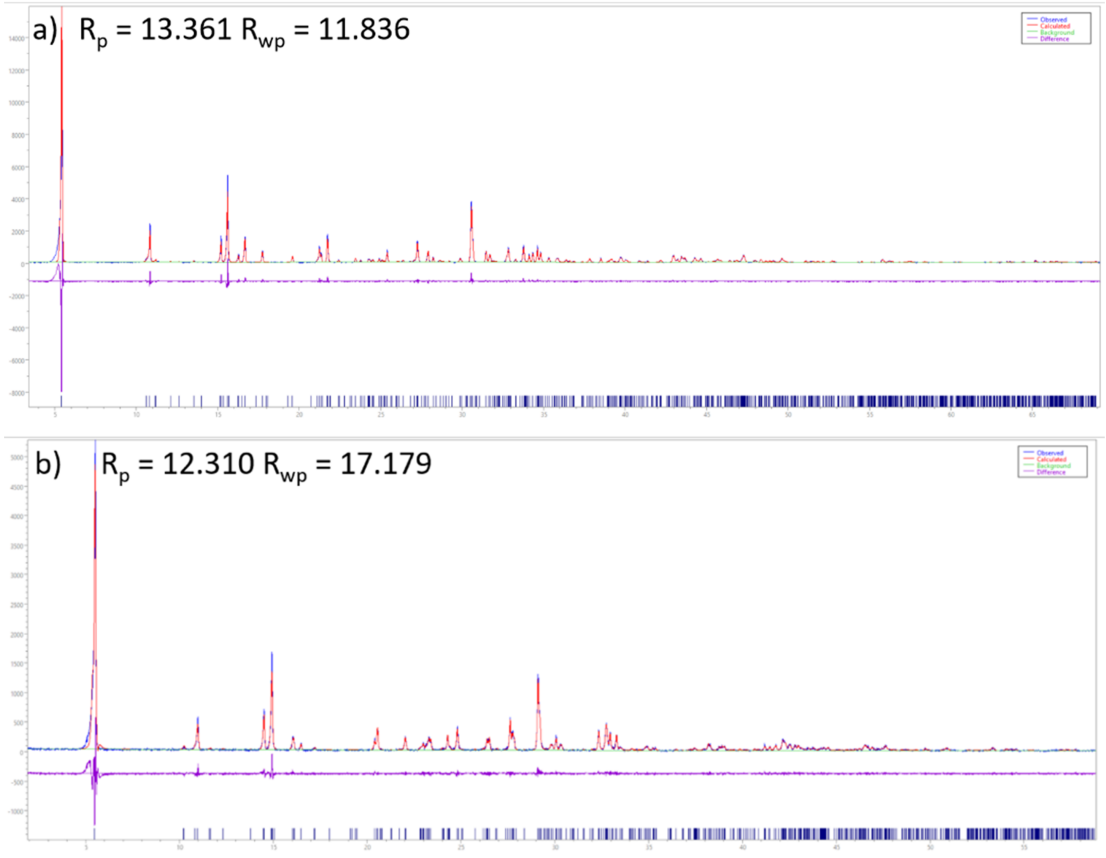

Figure 7.18: Profile Refinements for powder samples of a) $(4FPEA)_4AgBiBr_8$ and b) $(4FPEA)_4AgBiI_8$.

To confirm the elemental composition and purity of the powder and thin films samples, we performed EDX measurements on crystalline powder samples and thin film samples shown in Table 7.3. Since the thin film samples on their respective substrates show an influence of the substrates on the measured signals causing an underestimation of the Ag, we scraped off the thin films from the substrates and measured them separately as powders. All samples agree well with the theoretic stoichiometry and the deviations are in the standard precision limits of the EDX method.

Sample	Ag (at%)	Bi (at%)	Cl (at%)	Ratio (Ag:Bi:X)
Crystal (avg.)	11.94	11.81	76.25	1.01:1:6.46
Thin Film (avg.)	5.86	10.24	83.90	0.57:1:8.19
Powdered Film (avg.)	9.69	12.00	78.32	0.81:1:6.53
	Ag (at%)	Bi (at%)	Br (at%)	
Crystal (avg.)	11.46	10.69	77.84	1.07:1:7.28
Thin Film (avg.)	5.73	9.02	85.26	0.63:1:9.45
Powdered Film (avg.)	12.43	11.14	76.42	1.12:1:6.86
	Ag (at%)	Bi (at%)	I (at%)	
Crystal (avg.)	10.59	10.02	79.40	1.06:1:7.92
Thin Film (avg.)	5.83	9.58	84.58	0.61:1:8.83
Powdered Film (avg.)	11.73	10.14	78.13	1.16:1:7.71

Table 7.3: EDX data for all $(4FPEA)_4AgBiX_8$ (X=Cl, Br, I) in atom% from crystalline samples, thin film samples on ITO substrates and the same thin film samples scraped off and measured in powder form.

AFM images of the substrates show the difference in surface roughness of a) Si-SiO_2 wafer, b) ITO coated-glass and c) FTO-coated glass, which is plotted in Figure 7.19 d) as a line cut across the full length of the substrate. The y-axis zero point was chosen to represent the average height value from the AFM measurement.

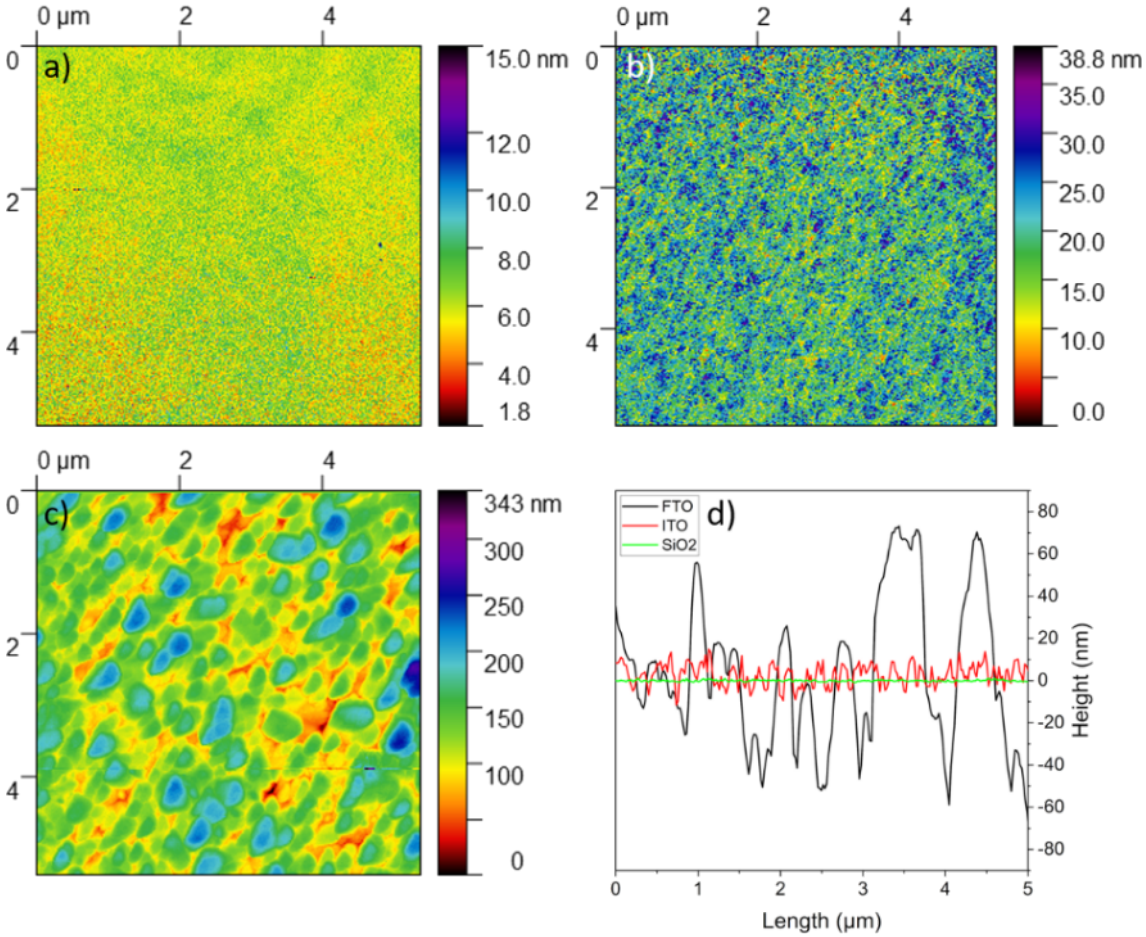

Figure 7.19: atomic force microscopy (AFM) images of substrates a) SiO_2, b) ITO, c) FTO and a line cut of each sample in d).

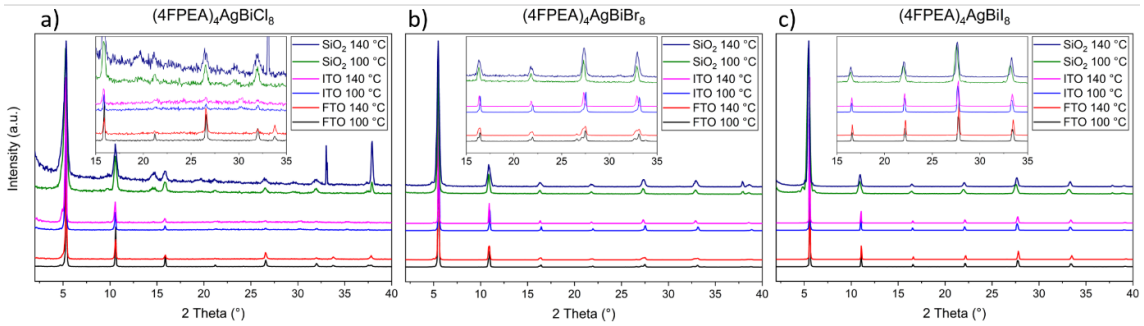

Figure 7.20: XRD patterns of thin films of a) $(4FPEA)_4AgBiCl_8$, b) $(4FPEA)_4AgBiBr_8$ and c) $(4FPEA)_4AgBiI_8$ on substrates FTO, ITO and SiO2 from NMP solution with annealing at 100 °C or 140 °C. The different parameters are indicated in the legends, insets show a magnified view of the 005 reflection.

$(4FPEA)_4AgBiCl_8$: The films of $(4FPEA)_4AgBiCl_8$ on FTO and ITO exhibit similar patterns, albeit with smaller intensities and slightly worse signal-to-noise ratio (S/N) on ITO. The S/N is further worsened on SiO_2, which can mainly be attributed to the film

being thinner compared to the ones on FTO and ITO due to the reduced concentration of the spin coating solution. Additionally, films on SiO_2 show small, additional reflections and the film annealed at $140\,°C$ shows the distinct reflection of the Si substrate at $33°$ 2θ. A broadening of the reflections can be observed for films on SiO_2 compared to the ones on FTO and ITO.

$(4FPEA)_4AgBiBr_8$: Thin films of $(4FPEA)_4AgBiBr_8$ follow the same trends, with two differences. Firstly, the crystallinity, i.e. the S/N under consistent scanning conditions, for all three substrates is better than for the chloride films. Secondly, the thin films on FTO display small additional reflections, best observed in the range from 15 to 35° 2θ. The increased annealing temperature of $140\,°C$ vs. $100\,°C$ for FTO films shows a shift of intensity, increasing the relative intensities of the lower angle reflections, yet the same general reflection positions are seen for both temperatures. This shift is more clearly observed in the thin films on ITO, where for both temperatures distinct, singular reflections are observed. For films annealed at $140\,°C$ the reflections are shifted more clearly towards the lower angle region, while the films annealed at $100\,°C$ have the reflections shifted towards higher angles but also show a remnant of the lower angle reflections (inset of Figure 7.20 b). The films on SiO_2 substrates display the same large broadening, compared to their respective FTO or ITO analogs. For clarity, a magnification of the reflections from 15 to 35° 2θ with the calculated diffractogram of $(4FPEA)_4AgBiBr_8$ is given in Figure 7.21, which shows that the reflection profile is not caused by neighboring reflections, but shows splitting characteristics.

$(4FPEA)_4AgBiI_8$: Thin films of $(4FPEA)_4AgBiI_8$ have the highest S/N and hence presumably the highest degree of crystallinity of the three materials. There are no additional reflections and no reflection splitting, as observed in $(4FPEA)_4AgBiCl_8$ and $(4FPEA)_4AgBiBr_8$. Interestingly, the influence of the annealing temperature is opposite to that of $(4FPEA)_4AgBiBr_8$. With higher temperature the reflections shift towards higher angles compared to the diffractograms of samples annealed at $100\,°C$. This leads to the conclusion that while films of (4FPEA)4AgBiBr8 at $140\,°C$ display increased lattice parameters and tensile stress, films of $(4FPEA)_4AgBiI_8$ show decreased lattice parameters and thus compressive stress. This trend is seen for all three substrates and while again the SiO_2 films show broad reflections, they are also shifted towards higher angles.

Zoom in on the splitting features of $(4FPEA)_4AgBiBr_8$ thin film diffractograms with the calculated diffractogram from the single crystal structure.

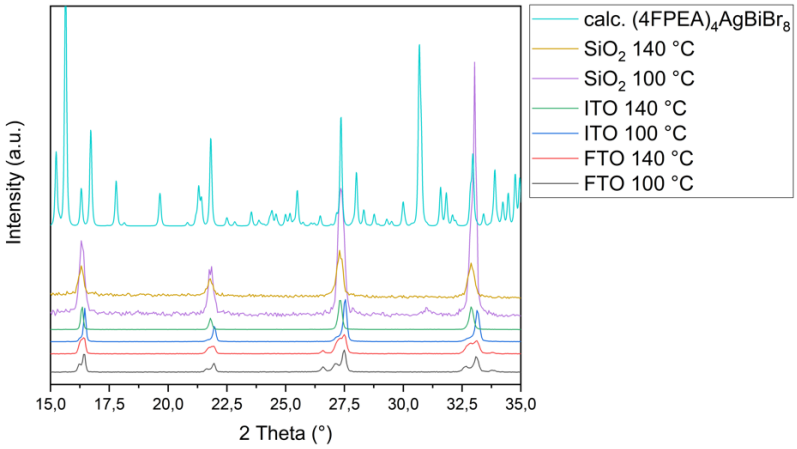

Figure 7.21: XRD zoom in from $15 - 35°$ 2θ of the thin films of $(4FPEA)_4AgBiBr_8$ on all three substrates FTO, ITO and SiO_2 for both annealing temperatures $100\,°C$ or $140\,°C$.

Compound	a (Å)	b (Å)	c (Å)	α (°)	β (°)	γ (°)
$(4FPEA)_4AgBiBr_8$	8.3833	8.1395	32.7693	90	96.120	90
$(4FPEA)_4AgBiBr_8$ - ITO $100\,°C$	8.3797	8.1441	32.8066	90	96.016	90
$(4FPEA)_4AgBiBr_8$ - ITO $140\,°C$	8.3407	8.1666	32.9159	90	96.021	90
$(4FPEA)_4AgBiI_8$	8.6236	8.7470	16.3676	98.973	90.119	90.013
$(4FPEA)_4AgBiI_8$ - ITO $100\,°C$	8.6938	8.7752	16.3885	98.839	90.587	89.684
$(4FPEA)_4AgBiI_8$ - ITO $140\,°C$	8.7153	8.8009	16.3610	98.992	91.025	89.778

Table 7.4: Profile refinements for thin films of $(4FPEA)_4AgBiBr_8$ and $(4FPEA)_4AgBiI_8$ identifying the two phases.

The thin film samples have been probed under varying incident angles from 0.04° - 1.00° to evaluate the degree of orientation throughout the complete depths of the films. The penetration depth of the incident X-ray beam can be estimated by using the relation of refractive properties of the material and the incident angle, as shown in equation 7.1. The index of refraction was calculated in dependence of the X-ray beam energy and the density of the probed material.[76]

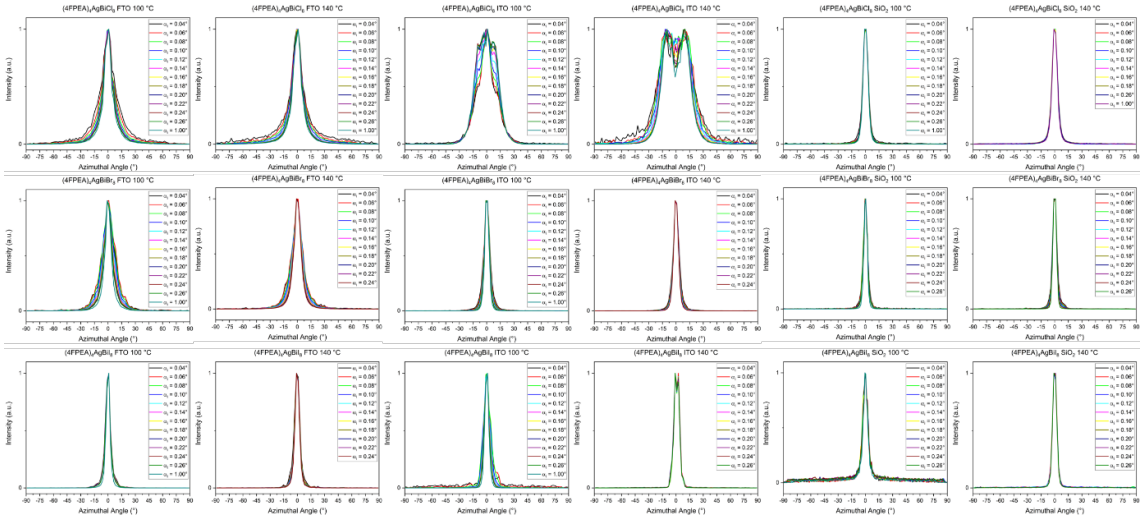

Figure 7.22: Azimuthal cuts of the 001 reflex for all thin films of $(4FPEA)_4AgBiCl_8$, $(4FPEA)_4AgBiBr_8$ and $(4FPEA)_4AgBiI_8$ on FTO, ITO and SiO_2 annealed at 100 °C and 140 °C, measured with incident angles from α_i = 0.04° to 1.00° (parameter in the panels).

All three materials have decreasing FHWMs of χ going from FTO to ITO to SiO_2. Interestingly, while all samples have their maxima at χ = 0°, corresponding to an exclusively horizontal orientation relative the substrate, $(4FPEA)_4AgBiCl_8$ samples on ITO have a slightly tilted horizontal orientation with peak shouldering for 100 °C and peak splitting with maxima for 140 °C, both at χ = 10° and -10°. This small tilting can also be observed in $(4FPEA)_4AgBiI_8$ on ITO at 140 °C, albeit with minimally off-centered maxima at χ = 1° and - 1°. To further probe the degree of orientation, we examined the films at varying incident angles from α_i = 0.04° to 1.00°, to distinguish the surface layers (i.e. several nm) from the complete film depth (i.e. several tens to hundreds nm. The impact of incident angle on penetration depth is further explained in the following).

Equation 7.1 shows the dependence of the penetration depth Λ on the wavenumber k, the X-ray incident angle α_i, the critical angle α_c and the imaginary part of the index of refraction β.

$$\Lambda = \left[\sqrt{2}k \cdot \sqrt{\sqrt{(\alpha_i^2 - \alpha_c^2)^2 + 4\beta^2} - (\alpha_i^2 - \alpha_c^2)}\right]^{-1} \tag{7.1}$$

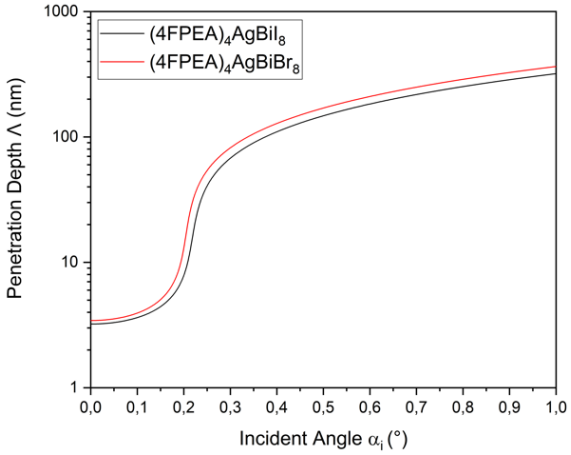

Figure 7.23: Penetration depth of the X-ray beam under grazing incidence as a function of the incident angle for $(4FPEA)_4AgBiBr_8$ and $(4FPEA)_4AgBiI_8$ according to equation (1).

Optical and scanning electron microscope images in Figure 7.24 demonstrating the effect of the increased annealing temperature on the domain size on thin films of $(4FPEA)_4AgBiI_8$ a)+b), $(4FPEA)_4AgBiBr_8$ c)+d) and $(4FPEA)_4AgBiCl_8$ e)+f).

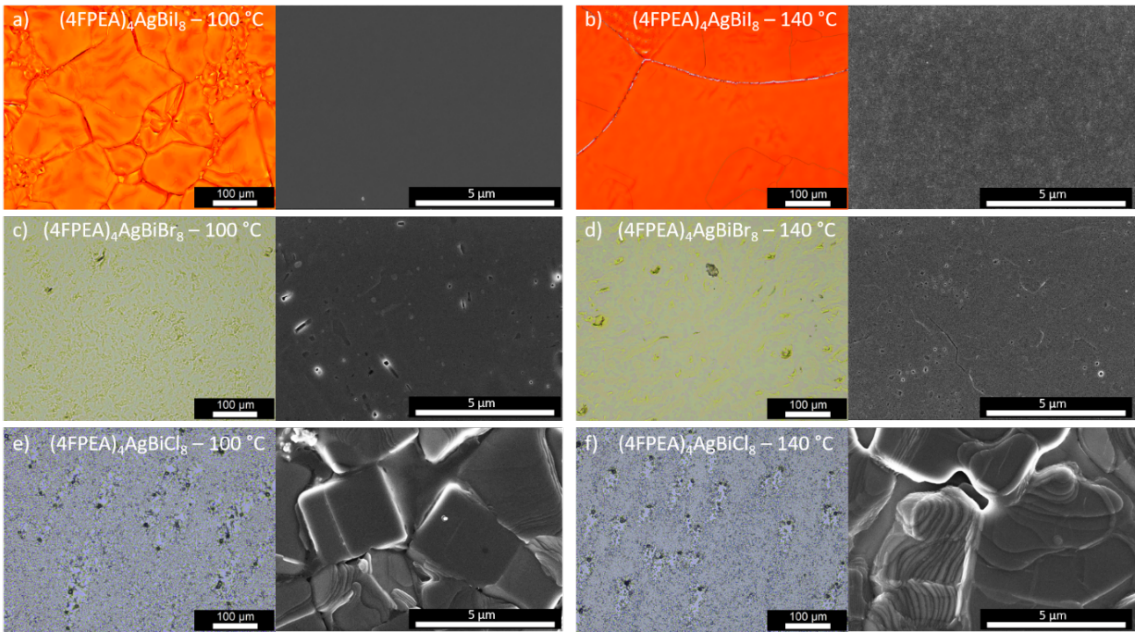

Figure 7.24: Microscope images of thin films spin coated from NMP solution on ITO of $(4FPEA)_4AgBiI_8$ annealed at $100\,°C$ a) and $140\,°C$ b), $(4FPEA)_4AgBiBr_8$ annealed at $100\,°C$ c) and $140\,°C$ d) and $(4FPEA)_4AgBiCl_8$ annealed at $100\,°C$ e) and $140\,°C$ f).

To confirm the crystal phase of our thin films we indexed 2D images of GIWAXS measurements at a sample detector distance of $155.7865\,mm$ and an incident angle of $0.25°$. Representatively, we measured thin film samples on ITO substrates annealed at $140\,°C$ for

a) $(4FPEA)_4AgBiCl_8$, b) ($(4FPEA)_4AgBiBr_8$ and c) $(4FPEA)_4AgBiI_8$ with the lattice parameters shown in Table 7.1 and the indexed 2D images shown in Figure 7.25. Indexing of the GIWAXS data was carried out with the program GIXSGUI.[77] While the diffraction positions of $(00l)$ planes agree well with the calculated positions, the diffraction positions of planes including a and b lattice parameters exhibit a shift indicating a compressed unit cell in a and b. This agrees with the observed lattice compression between thin films and calculated diffractograms in main text Figure 7.2.

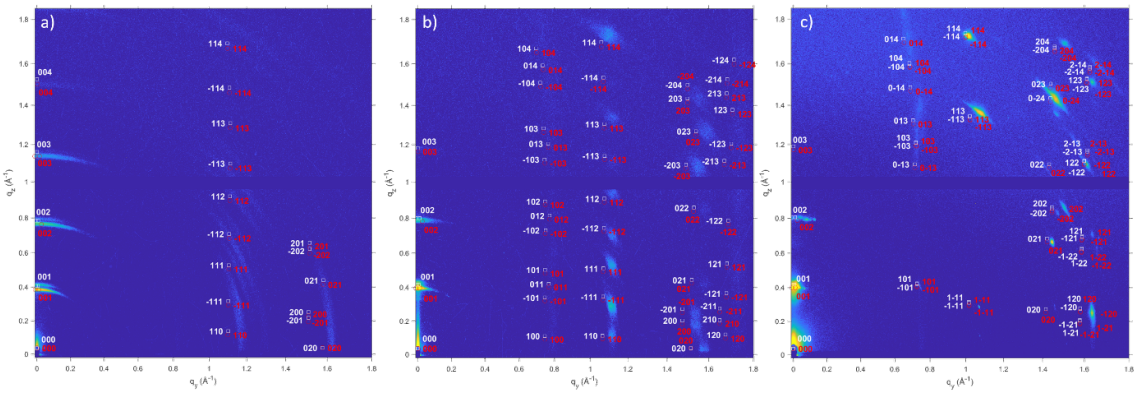

Figure 7.25: GIWAXS 2D images with indexed diffraction positions for a) $(4FPEA)_4AgBiCl_8$, b) $(4FPEA)_4AgBiBr_8$ and c) $(4FPEA)_4AgBiI_8$ thin films on FTO substrates annealed at $140\,°C$.

The optimized synthesis parameters for thin films of $(4FPEA)_4AgBiBr_8$ to yield the same pristine surface morphology as the in the main text shown $(4FPEA)_4AgBiI_8$ thin film, were different by that the spin coating took place under ambient conditions and the initial spin coating step was at 1000 rpm and the second step was at 6000 rpm.

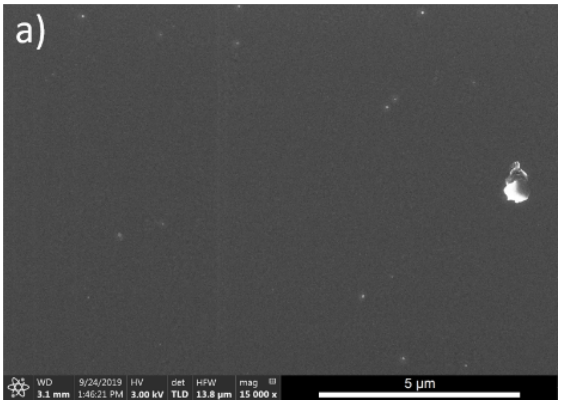

Figure 7.26: Pristine surface morphology from optimized synthesis parameters for $(4FPEA)_4AgBiBr_8$ films on FTO.

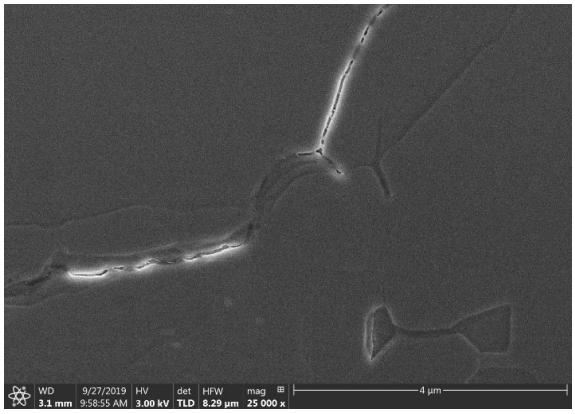

Figure 7.27: XRD zoom in from $15 - 35°$ 2θ of the thin films of $(4FPEA)_4AgBiBr_8$ on all three substrates FTO, ITO and SiO_2 for both annealing temperatures $100\,°C$ or $140\,°C$.

Figure 7.28 shows the indirect nature of the band gap for $(4FPEA)_4AgBiBr_8$ and $(4FPEA)_4AgBiI_8$ if spin-orbit coupling is not considered.

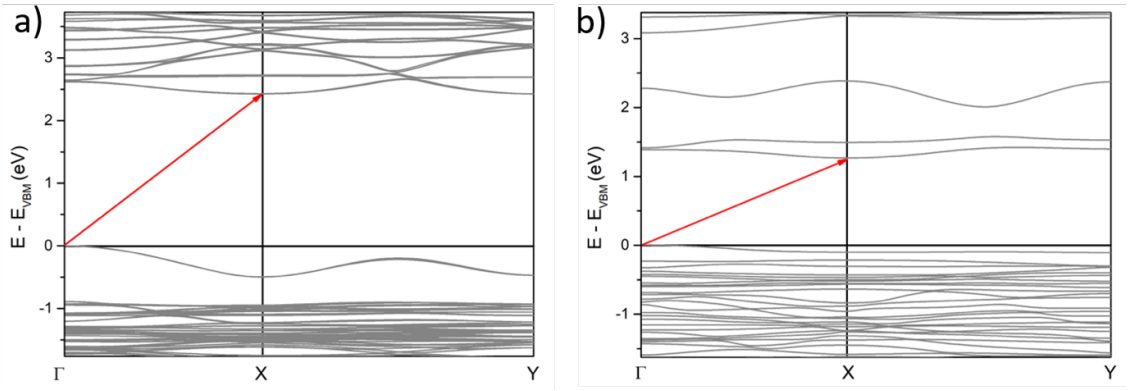

Figure 7.28: Band structures of a) $(4FPEA)_4AgBiBr_8$ and b) $(4FPEA)_4AgBiI_8$ without SOC.

To gather more understanding into the type of quantum well band alignment in these hybrid materials, the partial density of states for organic and inorganic components is depicted in Figure 7.29.

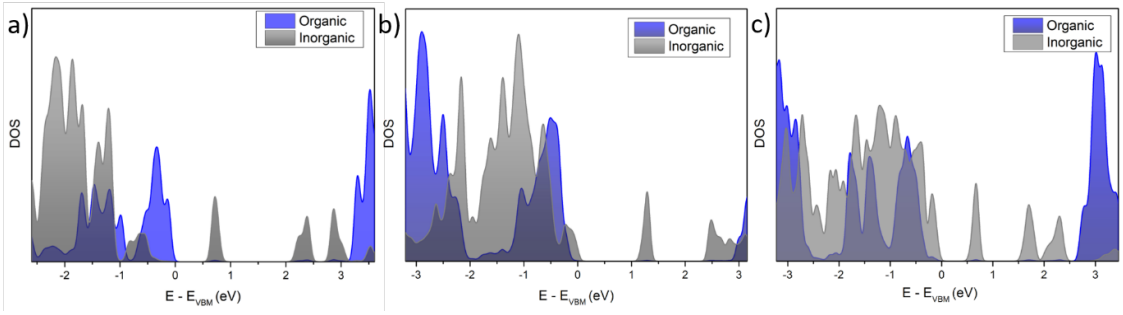

Figure 7.29: Partial DOS for organic and inorganic components for a) $(4FPEA)_4AgBiCl_8$, b) $(4FPEA)_4AgBiBr_8$ and c) $(4FPEA)_4AgBiI_8$.

To approximate the values for the effective masses at the high symmetry point Γ in the calculated band diagrams for the bromide and iodide compounds, a simple parabolic fit function was employed. The curvature values were used to calculate the effective masses as shown in the following equation:

$$m^* = \hbar \left(\frac{\delta^2 E}{\delta k^2} \right)^{-1} \tag{7.2}$$

Where $m*(k)$, $\hbar$, $E(k)$, and k are the effective mass, reduced Planck's constant, energy, and wave vector, respectively. The obtained values are depicted in Table 7.5:

	Bromide	Iodide
Effective masses of electrons $[m_e^*/m_0]$ $(\Gamma - X/\Gamma - Y)$	0.136	0.122
Effective masses of holes $[m_h^*/m_0]$ $(\Gamma - X/\Gamma - Y)$	0.123	0.242

Table 7.5: Effective masses of electrons and holes.

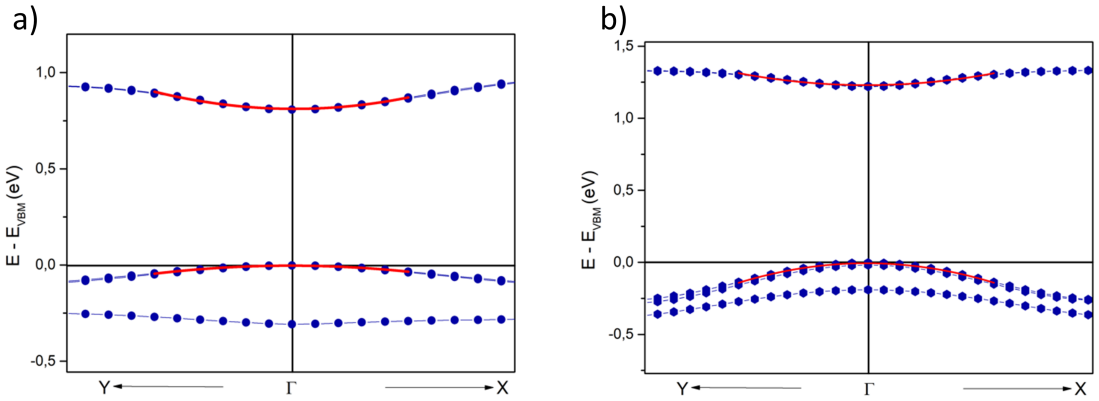

Figure 7.30: $E(k)$ diagrams for $(4FPEA)_4AgBiBr_8$ (left) and $(4FPEA)_4AgBiI_8$ (right).

As expected from the dispersion in the $E(k)$ diagrams, the value for the effective hole mass is much larger for 4FPEAI than for 4FPEABr. The effective electron masses differ by a small amount, also apparent in the band structure plot, with the conduction band being slightly less dispersed for 4FPEABr. We note that the exact prediction of effective mass values requires higher levels of theory, which were not accessible because of the prohibitive system dimensions, but PBE-SOC was also shown to provide satisfactory experimental agreement.[78]

The theoretical absorption spectra were simulated by calculating frequency-dependent complex dielectric functions as implemented in the Quantum espresso epsilon package according to equation 7.3.[79]

$$\alpha(\omega) = \frac{4\pi\omega}{hc}\left[\frac{\sqrt{Re\varepsilon(\omega)^2 + Im\varepsilon(\omega)^2} - Re\varepsilon(\omega)}{2}\right]^{0.5} \tag{7.3}$$

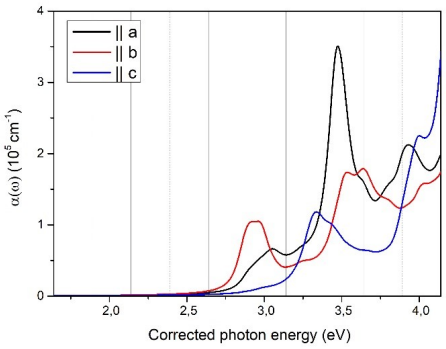

Figure 7.31: Simulated absorption for $(4FPEA)_4AgBiBr_8$ from dielectric response employing the random phase approximation excluding excitonic effects and subtracting the experimental absorption edge.

Employed spectral corrections in equation 7.4, which takes into account the absorption of light reflected from all interfaces, derived by Klahr and Hamann.[80] Here, A_{corr} represents the corrected absorption, while $Tsub$, T_{sam}, R_{sub}, R_{sam} represent the spectral transmittance and reflectance of the substrate and the coated substrate, respectively.

$$A_{corr}(\lambda) = -\log\frac{\frac{T_{sam}(\lambda)}{T_{sub}(\lambda)}}{1 - \frac{R_{sam}(\lambda) - R_{sub}(\lambda)}{T_{sub}(\lambda)^2}} \tag{7.4}$$

Powder samples were measured as diffuse reflectance spectra with a white standard ($BaSO_4$) background.

Zoom in on the powder absorption spectra displaying similar features as the thin film

absorption spectra:

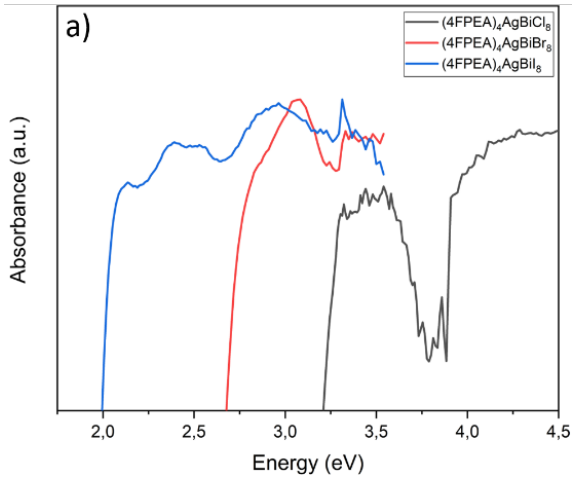

Figure 7.32: Magnification of the absorption features of powder UV-Vis absorbance data for $(4FPEA)_4AgBiCl_8$, $(4FPEA)_4AgBiBr_8$ and $(4FPEA)_4AgBiI_8$.

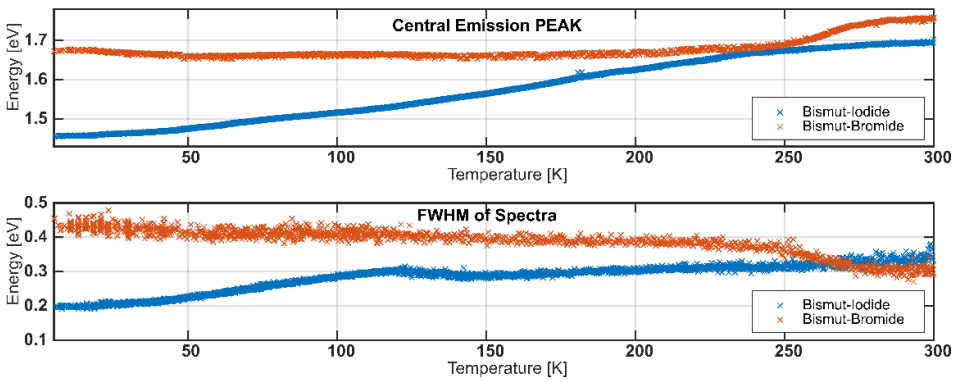

Figure 7.33: Temperature dependent spectral shift of the central emission peak and FWHM of the PL spectra for $(4FPEA)_4AgBiBr_8$ and $(4FPEA)_4AgBiI_8$.

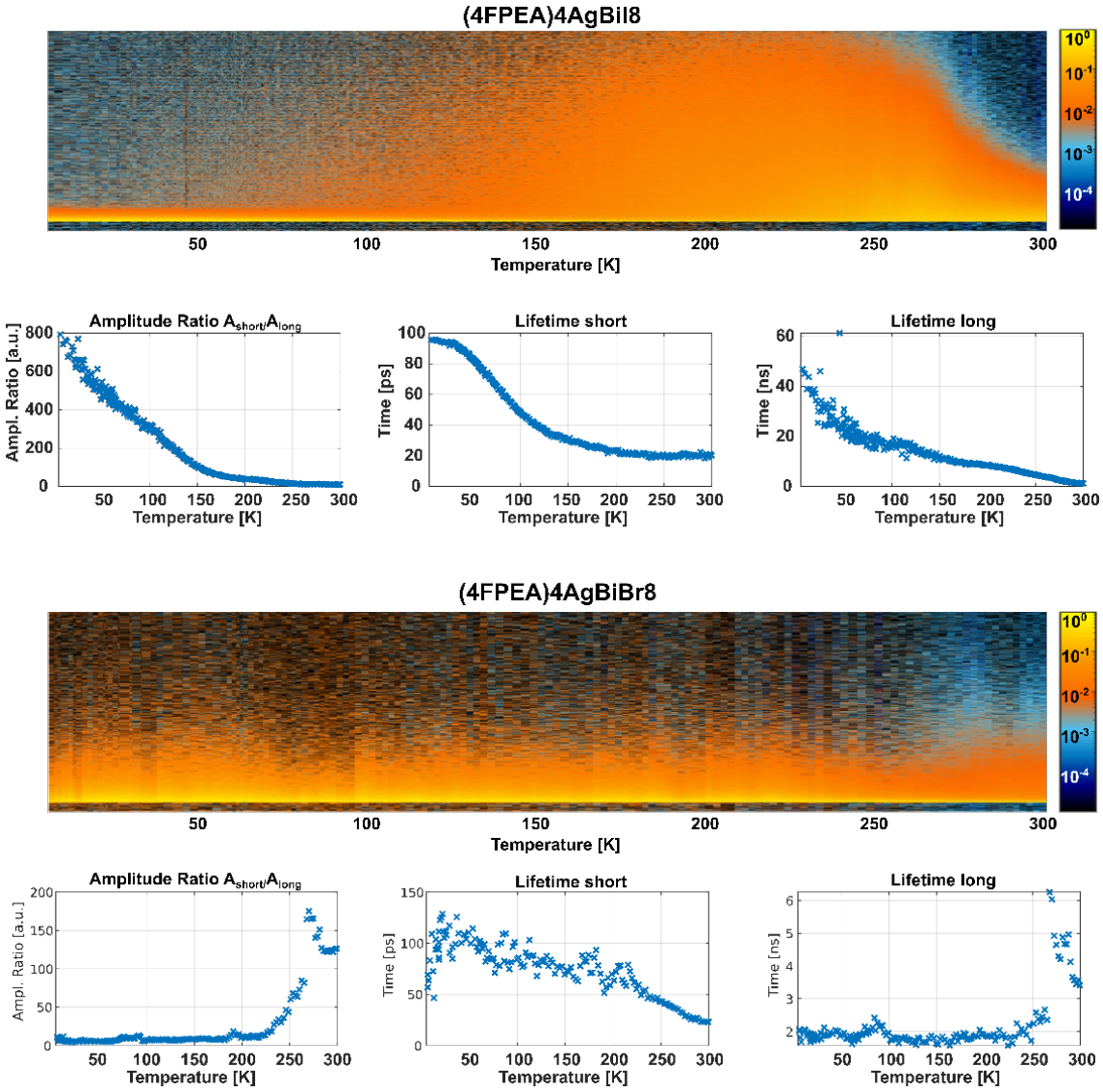

Figure 7.34: Temperature dependent transients and extracted lifetime plots for the short- and long-lived component from a biexponential fitting for $(4FPEA)_4AgBiBr_8$ and $(4FPEA)_4AgBiI_8$.

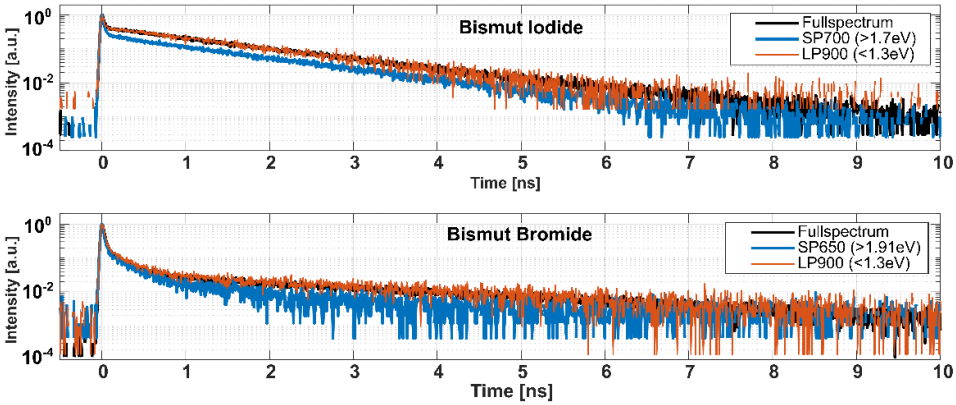

Figure 7.35: Temperature dependent transients and extracted lifetime plots for the short- and long-lived component from a biexponential fitting for $(4FPEA)_4AgBiBr_8$ and $(4FPEA)_4AgBiI_8$.

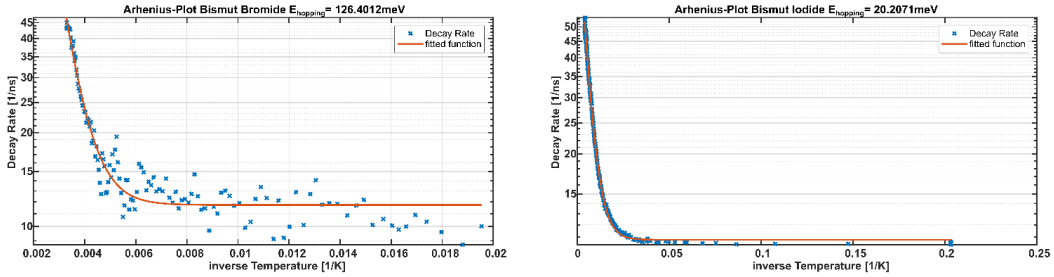

Figure 7.36: Arrhenius plots to extract the activation energy of the proposed hopping barrier for $(4FPEA)_4AgBiBr_8$ and $(4FPEA)_4AgBiI_8$.

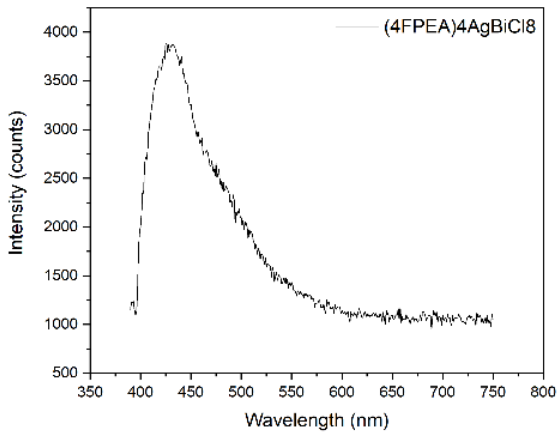

Figure 7.37: Room temperature PL spectrum of $(4FPEA)_4AgBiCl_8$ with excitation wavelength of $375\,\mathrm{nm}$, displaying the same characteristic broad emission as for the bromide and iodide thin films.

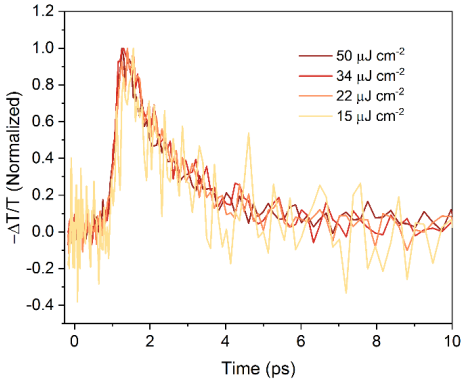

Figure 7.38: Comparison between normalized fluence-dependent OPTP transients for $(4FPEA)_4AgBiI_8$ after $3.1\,eV$ pulsed excitation. Different coloured lines represent different fluences in the range $15\,\mu J\,cm^{-1}$ to $50\,\mu J\,cm^{-1}$.

The charge carrier mobility was determined using the approach developed by Wehrenfennig et al..[57] Furthermore, we fitted the OPTP transient with a two-level mobility model developed by Wright et al. and Buizza et al..[51,59] In the adopted method, we converted the $\frac{\Delta T}{T}$ traces to a photoconductivity signal $\delta\sigma$, which is proportional to the charge-carrier mobility μ and to the charge carrier density n via the equation $\Delta\sigma = en\mu$. For our experimental geometry (i.e. transmission geometry for thin film on a z-qut quartz substrate) the sheet photoconductivity can be approximated to:

$$\Delta\sigma = -\frac{\epsilon_0 c(n_q + n_v)}{d_{film}}\frac{\Delta T}{T} \tag{7.5}$$

where d_{film} is the thickness of the studied film and n_q = 2.13 and n_v = 1 are the refractive indexes of quartz and vacuum, respectively.[81]
Therefore, in order to derive the charge-carrier mobility from the sheet photoconductivity, the photogenerated carrier number N needs to be determined as:

$$N = \phi\frac{E\lambda}{hc}(1 - R_{pump} - T_{pump}) \tag{7.6}$$

Where ϕ is the photon-to-charge branching ratio (i.e. the fraction of generated charges per photons absorbed), E is the excitation energy per pulse, $\epsilon = hc/\lambda$ is the energy of a photon with the wavelength λ, and R_{pump} and T_{pump} are the reflectance and transmittance of the sample at the excitation wavelength. This is converted to the photogenerated charge carrier density n_0 by dividing the film thickness d_{film} and the effective overlap area between THz and pump beam A_{eff}.

The resulting effective mobility can then be expressed as:

$$\phi\mu = -\epsilon_0 c\,(n_q + n_v)\,\frac{A_{eff} hc}{eE\lambda\,(1 - R_{\text{pump}} - T_{\text{pump}})}\left(\frac{\Delta T}{T}\right) \tag{7.7}$$

To better capture the photoconductivity dynamics in silver-bismuth halides, Wright and Buizza developed a two-level mobility model, which describes the charge carrier localization process.[51,59] In this model, the photoconductivity of the material can be described as the sum photoconductivity for two different states with a definite population and mobility: a delocalized state (n_{del}, μ_{del}) and a localized state (n_{loc}, μ_{loc}). The resulting photoconductivity can be expressed as $\Delta\sigma = e(n_{del}\mu_{del} + n_{loc}\mu_{loc})$. In the low excitation fluence regime, where the recombination from the localized state is predominantly monomolecular, the carrier population is described by the set of coupled rate equations:

$$\begin{cases} \frac{dn_{del}}{dt} = -k_{loc} n_{del}(t) \\ \frac{dn_{loc}}{dt} = k_{loc} n_{del}(t) - k_1 n_{loc}(t) \end{cases} \tag{7.8}$$

Here, k_{loc} and k_1 are the localization and monomolecular recombination rates, respectively. As reported in,[51,59] the resulting $\Delta T/T$ signal can be described as:

$$\frac{\Delta T}{T} = -\frac{e n_0 d_{\text{film}}}{\epsilon_0 c\,(n_q + n_v)}\left(\left(\mu_{\text{del}} - \frac{\mu_{\text{loc}}\,k_{\text{loc}}}{k_{\text{loc}} - k_1}\right)e^{-k_{\text{loc}}\,t} + \frac{\mu_{\text{loc}}\,k_{\text{loc}}}{k_{\text{loc}} - k_1}e^{-k_1 t}\right) \tag{7.9}$$

Furthermore, to fit the experimental data reported in Figure 7.10, we convoluted the resulting decay function with a Gaussian function with broadening (representing the instrumental response function) as described in.[51]

Although the responsivity of a photodetector gives a measure of the output signal of the detector for a given optical input signal, it does not give any information about the sensitivity of the device. The sensitivity of the detector can be defined as the minimum detectable optical input power that can be sensed with a signal-to-noise ratio of unity. This power is called the noise-equivalent-power (NEP) of the detector and the detectivity of a detector is the inverse of this noise-equivalent-power. The specific detectivity is denoted D^* and is the detectivity of a photodetector with an area of $1\,\text{cm}^2$ and an electrical bandwidth of $1\,\text{Hz}$, where A is the area of the detector in cm^2. D^* is expressed in units of $\text{cm}\sqrt{\text{Hz}}/\text{W}$.

$$D^* = D\sqrt{A\Delta f} = \sqrt{A\Delta f}\frac{1}{P_{NEP}} \tag{7.10}$$

Active layer		Responsivity A W^{-1}	Specific Detectivity $(Jones)$	Reference
2D $Sn(II)$ based perovskites	$(PEA)_2SnI_4$	16	1.92e11	[82]
	graphene/$(PEA)_2SnI_4$/MoS_2/graphene	121	8.09e9	[83]
	$(PEA)_2SnI_4$	329	2.06e11	[84]
3D $Ag-Bi$ based double perovskites	$Cs_2AgBiBr_6$	7.01	5.66e11	[85]
	$Cs_2AgBiBr_6$/SnO_2 heterojunctions	0.11	2.1e10	[86]
	$Cs_2AgBiBr_6$	0.14	3.29e12	[87]
2D $Ag-Bi$ based double perovskites	$(4FPEA)_4AgBiBr_8$	0.010	6e9	This work
	$(4FPEA)_4AgBiI_8$	0.002	5e8	This work
	((R/S-β-MPA)$_4AgBiI_8$ - microwire array	0.052	3.9e11	[45]
	((R/S-β-MPA)$_4AgBiI_8$ - single crystal	0.000022	1.2e7	[66]

Table 7.6: Summary of related photoconductors.

net formula	C32H44AgBiBr8F4N4
Mr/g mol-1	1516.84
crystal size/mm	0.050 × 0.050 × 0.020
T/K	297.(2)
radiation	MoK_α
diffractometer	'Bruker D8 Venture TXS'
crystal system	monoclinic
space group	'P 1 2/n 1'
a/Å	8.3833(2)
b/Å	8.1395(2)
c/Å	32.7693(7)
α/°	90
β/°	96.1200(10)
γ/°	90
V/Å^3	2223.30(9)
Z	2
calc. density/g cm-3	2.266
μ/mm-1	11.626
absorption correction	Multi-Scan

transmission factor range	0.53–0.80
refls. measured	32609
Rint	0.0451
mean σ(I)/I	0.0439
θ range	2.579–29.129
observed refls.	5392
x, y (weighting scheme)	0, 24.9411
hydrogen refinement	mixed
refls in refinement	5973
parameters	233
restraints	0
R(Fobs)	0.0489
Rw(F2)	0.1302
S	1.239
shift/errormax	0.001
max electron density/e Å-3	1.446
min electron density/e Å-3	-1.333

Table 7.7: Crystallographic data $(4FPEA)_4AgBiBr_8$

net formula	C32H44AgBiF4I8N4
Mr/g mol-1	1892.76
crystal size/mm	0.100 × 0.080 × 0.010
T/K	298.(2)
radiation	MoK_α
diffractometer	'Bruker D8 Venture TXS'
crystal system	triclinic
space group	'P -1'
a/Å	8.6236(6)
b/Å	8.7470(5)
c/Å	16.3676(11)
α/°	98.973(2)
β/°	90.119(2)
γ/°	90.013(2)
V/Å^3	1219.51(14)
Z	1
calc. density/g cm-3	2.577
μ/mm-1	9.109
absorption correction	Multi-Scan
transmission factor range	0.77–0.91
refls. measured	31455
Rint	0.0424
mean σ(I)/I	0.0428
θ range	3.171–30.507
observed refls.	6516
x, y (weighting scheme)	0.0412, 7.1338
hydrogen refinement	mixed

refls in refinement	7455
parameters	241
restraints	0
R(Fobs)	0.0435
Rw(F2)	0.1040
S	1.037
shift/errormax	0.001
max electron density/e Å-3	2.231
min electron density/e Å-3	-1.350

Table 7.8: Crystallographic data $(4\mathrm{FPEA})_4\mathrm{AgBiI}_8$

7.6 REFERENCES

[1] S. D. Stranks, H. J. Snaith, *Nat Nanotechnol* **2015**, *10*, 391–402.

[2] W. Yu, F. Li, L. Yu, M. R. Niazi, Y. Zou, D. Corzo, A. Basu, C. Ma, S. Dey, M. L. Tietze, *Nature communications* **2018**, *9*, 1–10.

[3] L. Yin, H. Wu, W. Pan, B. Yang, P. Li, J. Luo, G. Niu, J. Tang, *Advanced Optical Materials* **2019**, *7*, 1900491.

[4] A. Sadhanala, S. Ahmad, B. Zhao, N. Giesbrecht, P. M. Pearce, F. Deschler, R. L. Hoye, K. C. Gödel, T. Bein, P. Docampo, *Nano letters* **2015**, *15*, 6095–6101.

[5] A. H. Slavney, T. Hu, A. M. Lindenberg, H. I. Karunadasa, *Journal of the American chemical society* **2016**, *138*, 2138–2141.

[6] Y. Zhang, Y. Ma, Y. Wang, X. Zhang, C. Zuo, L. Shen, L. Ding, *Adv Mater* **2021**, *33*, e2006691.

[7] G. Meyer, *Progress in Solid State Chemistry* **1982**, *14*, 141–219.

[8] N. Elliott, L. Pauling, *Journal of the American Chemical Society* **1938**, *60*, 1846–1851.

[9] E. T. McClure, M. R. Ball, W. Windl, P. M. Woodward, *Chemistry of Materials* **2016**, *28*, 1348–1354.

[10] H. C. Sansom, G. Longo, A. D. Wright, L. R. V. Buizza, S. Mahesh, B. Wenger, M. Zanella, M. Abdi-Jalebi, M. J. Pitcher, M. S. Dyer, T. D. Manning, R. H. Friend, L. M. Herz, H. J. Snaith, J. B. Claridge, M. J. Rosseinsky, *J Am Chem Soc* **2021**, *143*, 3983–3992.

[11] Z. Deng, F. Wei, S. Sun, G. Kieslich, A. K. Cheetham, P. D. Bristowe, *Journal of Materials Chemistry A* **2016**, *4*, 12025–12029.

[12] T. T. Tran, J. R. Panella, J. R. Chamorro, J. R. Morey, T. M. McQueen, *Materials Horizons* **2017**, *4*, 688–693.

[13] G. Volonakis, A. A. Haghighirad, R. L. Milot, W. H. Sio, M. R. Filip, B. Wenger, M. B. Johnston, L. M. Herz, H. J. Snaith, F. Giustino, *The journal of physical chemistry letters* **2017**, *8*, 772–778.

[14] B. A. Connor, R.-I. Biega, L. Leppert, H. I. Karunadasa, *Chemical Science* **2020**, DOI 10.1039/d0sc01580f.

[15] M. Roknuzzaman, J. A. Alarco, H. Wang, K. Ostrikov, *Computational Materials Science* **2021**, *186*, DOI 10.1016/j.commatsci.2020.110009.

[16] F. Wei, Z. Deng, S. Sun, F. Xie, G. Kieslich, D. M. Evans, M. A. Carpenter, P. D. Bristowe, A. K. Cheetham, *Materials Horizons* **2016**, *3*, 328–332.

[17] W. Pan, H. Wu, J. Luo, Z. Deng, C. Ge, C. Chen, X. Jiang, W.-J. Yin, G. Niu, L. Zhu, L. Yin, Y. Zhou, Q. Xie, X. Ke, M. Sui, J. Tang, *Nature Photonics* **2017**, *11*, 726–732.

[18] O. A. Lozhkina, A. A. Murashkina, M. S. Elizarov, V. V. Shilovskikh, A. A. Zolotarev, Y. V. Kapitonov, R. Kevorkyants, A. V. Emeline, T. Miyasaka, *Chemical Physics Letters* **2018**, *694*, 18–22.

[19] D. Bartesaghi, A. H. Slavney, M. C. Gelvez-Rueda, B. A. Connor, F. C. Grozema, H. I. Karunadasa, T. J. Savenije, *J Phys Chem C Nanomater Interfaces* **2018**, *122*, 4809–4816.

[20] M. T. Sirtl, F. Ebadi, B. T. Gorkom, P. Ganswindt, R. A. J. Janssen, T. Bein, W. Tress, *Advanced Optical Materials* **2021**, *9*, DOI 10.1002/adom.202100202.

[21] M. T. Sirtl, M. Armer, L. K. Reb, R. Hooijer, P. Dörflinger, M. A. Scheel, K. Tvingstedt, P. Rieder, N. Glück, P. Pandit, et al., *ACS applied energy materials* **2020**, *3*, 11597–11609.

[22] E. Greul, M. L. Petrus, A. Binek, P. Docampo, T. Bein, *Journal of Materials Chemistry A* **2017**, *5*, 19972–19981.

[23] B. A. Connor, L. Leppert, M. D. Smith, J. B. Neaton, H. I. Karunadasa, *J Am Chem Soc* **2018**, *140*, 5235–5240.

[24] X. Wang, K. Li, H. Xu, N. Ali, Y. Wang, Q. Shen, H. Wu, *Chemical Communications* **2020**, DOI 10.1039/d0cc01847c.

[25] M. Pantaler, V. Diez-Cabanes, V. I. Queloz, A. Sutanto, P. A. Schouwink, M. Pastore, I. Garcia-Benito, M. K. Nazeeruddin, D. Beljonne, D. C. Lupascu, et al., *Jacs Au* **2021**, *2*, 136–149.

[26] Y. Li, T. Yang, Z. Xu, X. Liu, X. Huang, S. Han, Y. Liu, M. Li, J. Luo, Z. Sun, *Angew Chem Int Ed Engl* **2020**, *59*, 3429–3433.

[27] L. Mao, S. M. L. Teicher, C. C. Stoumpos, R. M. Kennard, R. A. DeCrescent, G. Wu, J. A. Schuller, M. L. Chabinyc, A. K. Cheetham, R. Seshadri, *J Am Chem Soc* **2019**, *141*, 19099–19109.

[28] A. Walsh, *J Phys Chem C Nanomater Interfaces* **2015**, *119*, 5755–5760.

[29] Z. Xiao, W. Meng, J. Wang, Y. Yan, *ChemSusChem* **2016**, *9*, 2628–2633.

[30] P. Vishnoi, R. Seshadri, A. K. Cheetham, *The Journal of Physical Chemistry C* **2021**, *125*, 11756–11764.

[31] Z. Xu, X. Liu, Y. Li, X. Liu, T. Yang, C. Ji, S. Han, Y. Xu, J. Luo, Z. Sun, *Angewandte Chemie International Edition* **2019**, *58*, 15757–15761.

[32] Y. Yao, B. Kou, Y. Peng, Z. Wu, L. Li, S. Wang, X. Zhang, X. Liu, J. Luo, *Chem Commun (Camb)* **2020**, *56*, 3206–3209.

[33] M. K. Jana, S. M. Janke, D. J. Dirkes, S. Dovletgeldi, C. Liu, X. Qin, K. Gundogdu, W. You, V. Blum, D. B. Mitzi, *J Am Chem Soc* **2019**, *141*, 7955–7964.

[34] F. Zhang, D. H. Kim, H. Lu, J. S. Park, B. W. Larson, J. Hu, L. Gao, C. Xiao, O. G. Reid, X. Chen, Q. Zhao, P. F. Ndione, J. J. Berry, W. You, A. Walsh, M. C. Beard, K. Zhu, *J Am Chem Soc* **2019**, *141*, 5972–5979.

[35] J. Shi, Y. Gao, X. Gao, Y. Zhang, J. Zhang, X. Jing, M. Shao, *Adv Mater* **2019**, *31*, e1901673.

[36] W. Fu, H. Liu, X. Shi, L. Zuo, X. Li, A. K. .-. Jen, *Advanced Functional Materials* **2019**, *29*, 1900221.

[37] D. B. Straus, S. Hurtado Parra, N. Iotov, Q. Zhao, M. R. Gau, P. J. Carroll, J. M. Kikkawa, C. R. Kagan, *ACS Nano* **2020**, *14*, 3621–3629.

[38] Y. Chen, Y. Sun, J. Peng, J. Tang, K. Zheng, Z. Liang, *Adv Mater* **2018**, *30*, DOI 10.1002/adma.201703487.

[39] R. G. Pearson, *Journal of the American Chemical Society* **2002**, *91*, 4947–4955.

[40] J. A. McMillan, *Journal of Inorganic and Nuclear Chemistry* **1960**, *13*, 28–31.

[41] D. B. Mitzi, *Inorg Chem* **2000**, *39*, 6107–13.

[42] L.-Y. Bi, Y.-Q. Hu, M.-Q. Li, T.-L. Hu, H.-L. Zhang, X.-T. Yin, W.-X. Que, M. S. Lassoued, Y.-Z. Zheng, *Journal of Materials Chemistry A* **2019**, *7*, 19662–19667.

[43] M. Li, S. Han, B. Teng, Y. Li, Y. Liu, X. Liu, J. Luo, M. Hong, Z. Sun, *Advanced Optical Materials* **2020**, *8*, DOI 10.1002/adom.202000149.

[44] M. S. Lassoued, L.-Y. Bi, Z. Wu, G. Zhou, Y.-Z. Zheng, *Journal of Materials Chemistry C* **2020**, *8*, 5349–5354.

[45] Y. Zhao, M. Dong, J. Feng, J. Zhao, Y. Guo, Y. Fu, H. Gao, J. Yang, L. Jiang, Y. Wu, *Advanced Optical Materials* **2022**, *10*, 2102227.

[46] F. Schmitz, J. Horn, N. Dengo, A. E. Sedykh, J. Becker, E. Maiworm, P. Bélteky, Á. Kukovecz, S. Gross, F. Lamberti, K. Müller-Buschbaum, D. Schlettwein, D. Meggiolaro, M. Righetto, T. Gatti, *Chemistry of Materials* **2021**, DOI 10.1021/acs.chemmater.1c01182.

[47] E. Brandes, W. Möller, M. Molnárné, T. Schendler, V. Schröder, *Sicherheitstechnische Kenngrößen*, Wirtschaftsverlag NW, Verlag für neue Wissenschaft, **2003**.

[48] J. Su, T. Mou, J. Wen, B. Wang, *The Journal of Physical Chemistry C* **2020**, *124*, 5371–5377.

[49] P. J. Hasnip, K. Refson, M. I. Probert, J. R. Yates, S. J. Clark, C. J. Pickard, *Philos Trans A Math Phys Eng Sci* **2014**, *372*, 20130270.

[50] C. Liu, W. Huhn, K. Z. Du, A. Vazquez-Mayagoitia, D. Dirkes, W. You, Y. Kanai, D. B. Mitzi, V. Blum, *Phys Rev Lett* **2018**, *121*, 146401.

[51] A. D. Wright, L. R. V. Buizza, K. J. Savill, G. Longo, H. J. Snaith, M. B. Johnston, L. M. Herz, *J Phys Chem Lett* **2021**, *12*, 3352–3360.

[52] J. C. Blancon, A. V. Stier, H. Tsai, W. Nie, C. C. Stoumpos, B. Traore, L. Pedesseau, M. Kepenekian, F. Katsutani, G. T. Noe, J. Kono, S. Tretiak, S. A. Crooker, C. Katan, M. G. Kanatzidis, J. J. Crochet, J. Even, A. D. Mohite, *Nat Commun* **2018**, *9*, 2254.

[53] R.-I. Biega, M. R. Filip, L. Leppert, J. B. Neaton, *The journal of physical chemistry letters* **2021**, *12*, 2057–2063.

[54] R. Kentsch, M. Scholz, J. Horn, D. Schlettwein, K. Oum, T. Lenzer, *The Journal of Physical Chemistry C* **2018**, *122*, 25940–25947.

[55] T. Hu, M. D. Smith, E. R. Dohner, M. J. Sher, X. Wu, M. T. Trinh, A. Fisher, J. Corbett, X. Y. Zhu, H. I. Karunadasa, A. M. Lindenberg, *J Phys Chem Lett* **2016**, *7*, 2258–63.

[56] J. A. Steele, P. Puech, M. Keshavarz, R. Yang, S. Banerjee, E. Debroye, C. W. Kim, H. Yuan, N. H. Heo, J. Vanacken, et al., *ACS nano* **2018**, *12*, 8081–8090.

[57] C. Wehrenfennig, G. E. Eperon, M. B. Johnston, H. J. Snaith, L. M. Herz, *Advanced materials* **2014**, *26*, 1584–1589.

[58] M. Righetto, D. Giovanni, S. S. Lim, T. C. Sum, *Applied Physics Reviews* **2021**, *8*, 011318.

[59] L. R. Buizza, A. D. Wright, G. Longo, H. C. Sansom, C. Q. Xia, M. J. Rosseinsky, M. B. Johnston, H. J. Snaith, L. M. Herz, *ACS Energy Letters* **2021**, *6*, 1729–1739.

[60] H. Hempel, T. J. Savenjie, M. Stolterfoht, J. Neu, M. Failla, V. C. Paingad, P. Kužel, E. J. Heilweil, J. A. Spies, M. Schleuning, et al., *Advanced Energy Materials* **2022**, *12*, 2102776.

[61] D. H. Fabini, R. Seshadri, M. G. Kanatzidis, *MRS Bulletin* **2020**, *45*, 467–477.

[62] Z. Xiao, W. Meng, J. Wang, D. B. Mitzi, Y. Yan, *Materials Horizons* **2017**, *4*, 206–216.

[63] M. Li, S. Han, B. Teng, Y. Li, Y. Liu, X. Liu, J. Luo, M. Hong, Z. Sun, *Advanced Optical Materials* **2020**, *8*, 2000149.

[64] L. Zhu, D. Liu, J. Wang, N. Wang, *J Phys Chem Lett* **2020**, DOI 10.1021/acs.jpclett.0c02476.

[65] C. Chen, L. Gao, W. Gao, C. Ge, X. Du, Z. Li, Y. Yang, G. Niu, J. Tang, *Nature communications* **2019**, *10*, 1927.

[66] D. Li, X. Liu, W. Wu, Y. Peng, S. Zhao, L. Li, M. Hong, J. Luo, *Angewandte Chemie* **2021**, *133*, 8496–8499.

[67] J. P. Perdew, K. Burke, M. Ernzerhof, *Physical review letters* **1996**, *77*, 3865.

[68] A. Tkatchenko, M. Scheffler, *Physical review letters* **2009**, *102*, 073005.

[69] R. L. Hoye, P. Schulz, L. T. Schelhas, A. M. Holder, K. H. Stone, J. D. Perkins, D. Vigil-Fowler, S. Siol, D. O. Scanlon, A. Zakutayev, et al., *Chemistry of Materials* **2017**, *29*, 1964–1988.

[70] T. Seifert, S. Jaiswal, U. Martens, J. Hannegan, L. Braun, P. Maldonado, F. Freimuth, A. Kronenberg, J. Henrizi, I. Radu, et al., *Nature photonics* **2016**, *10*, 483–488.

[71] R. J. Baker, P. E. Colavita, D. M. Murphy, J. A. Platts, J. D. Wallis, *J Phys Chem A* **2012**, *116*, 1435–44.

[72] K. Kikuchi, Y. Takeoka, M. Rikukawa, K. Sanui, *Current Applied Physics* **2004**, *4*, 599–602.

[73] J. Hu, I. W. H. Oswald, S. J. Stuard, M. M. Nahid, N. Zhou, O. F. Williams, Z. Guo, L. Yan, H. Hu, Z. Chen, X. Xiao, Y. Lin, Z. Yang, J. Huang, A. M. Moran, H. Ade, J. R. Neilson, W. You, *Nat Commun* **2019**, *10*, 1276.

[74] R. A. Gaussian09, *Inc. Wallingford CT* **2009**, *121*, 150–166.

[75] A. Altomare, M. Camalli, C. Cuocci, C. Giacovazzo, A. Moliterni, R. Rizzi, *Journal of Applied Crystallography* **2009**, *42*, 1197–1202.

[76] B. L. Henke, E. M. Gullikson, J. C. Davis, *Atomic data and nuclear data tables* **1993**, *54*, 181–342.

[77] Z. Jiang, *Journal of Applied Crystallography* **2015**, *48*, 917–926.

[78] J. Yang, P. Zhang, S.-H. Wei, *The journal of physical chemistry letters* **2018**, *9*, 31–35.

[79] P. Giannozzi, S. Baroni, N. Bonini, M. Calandra, R. Car, C. Cavazzoni, D. Ceresoli, G. L. Chiarotti, M. Cococcioni, I. Dabo, et al., *Journal of physics: Condensed matter* **2009**, *21*, 395502.

[80] B. M. Klahr, T. W. Hamann, *The Journal of Physical Chemistry C* **2011**, *115*, 8393–8399.

[81] H. J. Joyce, J. L. Boland, C. L. Davies, S. A. Baig, M. B. Johnston, *Semiconductor Science and Technology* **2016**, *31*, 103003.

[82] L. Qian, Y. Sun, M. Wu, C. Li, D. Xie, L. Ding, G. Shi, *Nanoscale* **2018**, *10*, 6837–6843.

[83] C. Fang, H. Wang, Z. Shen, H. Shen, S. Wang, J. Ma, J. Wang, H. Luo, D. Li, *ACS applied materials & interfaces* **2019**, *11*, 8419–8427.

[84] L. Qian, Y. Sun, M. Sun, Z. Fang, L. Li, D. Xie, C. Li, L. Ding, *Journal of Materials Chemistry C* **2019**, *7*, 5353–5358.

[85] L.-Z. Lei, Z.-F. Shi, Y. Li, Z.-Z. Ma, F. Zhang, T.-T. Xu, Y.-T. Tian, D. Wu, X.-J. Li, G.-T. Du, *Journal of Materials Chemistry C* **2018**, *6*, 7982–7988.

[86] C. Wu, B. Du, W. Luo, Y. Liu, T. Li, D. Wang, X. Guo, H. Ting, Z. Fang, S. Wang, et al., *Advanced Optical Materials* **2018**, *6*, 1800811.

[87] J. Yang, C. Bao, W. Ning, B. Wu, F. Ji, Z. Yan, Y. Tao, J.-M. Liu, T. C. Sum, S. Bai, et al., *Advanced Optical Materials* **2019**, *7*, 1801732.

Conclusion and Outlook 8

In summary, the scope of this thesis was the exploration and study of novel "perovskite-inspired" materials to get insight into the optoelectronic consequences of synthetic modifications like structural conversion, heteroatom alloying and isovalent replacement on the core properties of hybrid perovskite compounds. By tailoring the octahedral framework of the latter, manifold unique material characteristics arise that highlight a vast tunability and multiple possible device applications through simple and inexpensive synthetic techniques.

In the first section, a comparably small modification to the archetype $\mathrm{MAPbI_3}$ structure was undertaken by replacing $\mathrm{Pb^{2+}}$ with $\mathrm{Sb^{3+}}$, resulting in a material with the formal constitution $\mathrm{MASb_{2/3}I_3}$ to account for the trivalent oxidation state. Here, Sb was chosen because of it's isovalent ns^2 electronic configuration to retain the characteristic bonding situation which is seen as fundamental cause for the favorable photovoltaic performance in lead-based materials. While this material exhibited a phase duality with a high-bandgap non-perovskite and a lower bandgap perovskite-related phase, we presented a simple method to form the photovoltaically advantageous polymorph. For this, an acetate precursor was chosen in the thin-film synthesis, which has an intrinsically higher interatomic distance of Sb atoms of about 4.9 Å in comparison to the commonly used $\mathrm{SbI_3}$ with 4.4 Å. This led to a phase-pure synthesis for the lower bandgap phase with a band gap reduction of $120\,\mathrm{meV}$ and a decrease of the exciton binding energy of about $160\,\mathrm{meV}$ in comparison. This material was then employed in prototypical solar cells, exhibiting promising performance with an initial power conversion efficiency of 0.54%. Summing up, this project opened up new pathways for the fabrication of lead-free antimony-based materials which were previously only hardly attainable.

The second section was focused on capitalizing on the above efficient synthesis method by introducing Sn into the same $\mathrm{MASb_{2/3}I_3}$ framework. This was motivated by the high efficiency of $\mathrm{MASnI_3}$-based solar cells, which on the other hand struggle with significant stability and oxidation issues. As we have shown in this work through

experimental and theoretical approaches, Sn was successfully stabilized in this system, leading to mixed-valent $\mathrm{Sn^{2+}}$/$\mathrm{Sn^{4+}}$ clusters on the same positions as Sb, which prevented full oxidation to $\mathrm{Sn^{4+}}$ through charge transfer stabilization between the heterovalent Sn atoms. We furthermore observed a boost in absorption over the whole visible spectrum, which we were able to attribute to additional transitions from $\mathrm{Sn^{2+}}$ to $\mathrm{Sn^{4+}}$ and from occupied Sb to unoccupied Sn states and vice versa. Thus, we were able to show how to dramatically increase the absorption capabilities of $\mathrm{MASb_{2/3}I_3}$ thin films and simultaneously stabilize $\mathrm{Sn^{2+}}$ in this perovskite-related structure.

Next, we introduced a non-perovskite structure with the composition $\mathrm{Cu_xAg_{1-x}Sb_{1-y}Bi_yI_4}$ in the third section in order to study which consequences retaining an octahedral Sb halide coordination outside of the corner-sharing perovskite structure. Here, the crystal structure was based on side-sharing octahedral layers where Cu/Ag/Sb and Bi occupied the same crystallographic positions. Through DFT calculations, we reveal a stable configuration of the formula $\mathrm{AgSbI_4}$. We were able to show a dramatically modified electronic situation with the ns^2 states of $\mathrm{Sb^{3+}}$ completely absent from the valence band. The cationic disorder led to deep states in the band gap with a very low formation energy, which we identified to be intrinsic to this material class. Furthermore, the band gap was revealed to be dependent on Sb/Bi replacement but not on the Cu/Ag ratio. With this knowledge, we managed to tune and improve the performance of thin film solar cells, leading to an optimal ratio of 40% Cu:Ag. Lastly, through omission of white light bias in external quantum efficiency measurements, we showed that the material exhibits an almost doubled photocurrent when working under low-intensity light conditions. Hence, we demonstrated that techniques that were developed for lead-based perovskites are viable also for materials beyond the perovskite lattice and could open up a new application space such as cheap and stable indoor photovoltaics.

In the fourth section, the frontier band characteristics of typical lead-based perovskites were also abandoned but the cubic structure was kept in a double-perovskite approach to study the possibilities of expanding this paradigm beyond ns^2 elements serving as central cations. For this purpose, we synthesized high-quality single crystals of a double perovskite with the formula $\mathrm{Cs_2NaFeCl_6}$. The spin state of $\mathrm{Fe^{3+}}$ was of great interest here, as it could adopt two different values, $+1/2$ or $+5/2$. We demonstrated that the latter is the case through electron paramagnetic resonance analysis and density functional theory calculations. Because this material exhibited an unpaired spin in the d orbitals of Fe, a spin-polarized electronic character was established below the Curie point.

Furthermore, upon cooling these crystals we were able to demonstrate thermochromism without a phase change and strongly excitonic behavior at low temperatures, with an exciton binding energy of only $20\,\mathrm{meV}$ at $80\,\mathrm{K}$. Altogether, these results suggest that double perovskite halide frameworks can be a suitable host for intriguing applications beyond photovoltaics, namely stable thermochromic and magnetic materials as shown here for example.

The last section was concerned with the dimensional reduction of the most widely studied double perovskite, $\mathrm{Cs_2AgBiBr_6}$. This was done to show that by separating the inorganic octahedral slabs with a fluorinated organic spacer cation, not only a band gap change from indirect to direct could be obtained, but also that a phase containing iodine could be stabilized, which was so far not possible for the three-dimensional compound. We were able to fabricate strongly oriented thin films of this material, in which we showed ultrafast charge carrier localization and small-polaron states. With this insight, we could explain the very broad and strongly Stokes-shifted emissive behavior in this class, arising from exciton self-trapping and defect-mediated recombination. All in all, this work gave insight into the design rules for novel, dimensionally reduced lead-free double perovskites, with properties that differ strongly from the three-dimensional parent structure, opening up even more structural and electronic modification routes through the simple introduction of organic spacers into the synthesis.

Concluding, we have established a group of new, easily processable semiconducting compounds and offered some fundamental perspectives into the wide range of optoelectronic properties one can achieve with perovskite-inspired materials and applying them to lead-free materials based on halide-coordinated metal octahedra - be it through structural alteration or heteroatom substitution and more. Although more research should be carried out to become competitive with the extraordinary efficiencies of lead-based perovskite systems in solar cells, a virtually infinite toolbox for simple and efficient material design can be found in the vast field of lead-free perovskite-inspired materials.

Appendix 9

9.1 LIST OF FIGURES

9.2 LIST OF TABLES

9.3 CODE FOR ELLIOTT FITTING

The base code was adapted from this work: V. D'Innocenzo, **2015**. *Photophysics of 3D lead halide perovskite semiconductors: Light absorption and Luminescence*, Politecnico di Milano. This code was expanded in a newer Python framework and a second bandgap absorption was added. Furthermore, a loop was introduced to evaluate multiple datasets automatically.

```
import warnings
warnings.filterwarnings("ignore")
import numpy as np
from numpy import inf
import matplotlib.pyplot as plt
import matplotlib.patches as mpatches
from scipy.integrate import odeint
from scipy.integrate import quad
from scipy.optimize import least_squares
import scipy.optimize as opt
from scipy.interpolate import interp1d
import os

def Elliots_fit(p, a_exp, e, *args):
    Eb, Eg, Eg2, gamma, npc, k, A2 = p

    n = np.linspace(1, 500, 500)

    absex = np.zeros((e.size))

    for i in range(0, e.size):
        expr = 4 * np.pi * (Eb ** (3 / 2)) / (n ** 3) * (1 /
                (np.cosh((e[i] - Eg - Eb / n ** 2) / gamma)))
        S = expr.cumsum(axis=0)
        absex[i] = S[-1]

    abseh = np.zeros((e.size))
    abset = np.zeros((e.size))
```

```
def fun_eh(x, e, gamma, Eb, Eg, npc):
    D = (x - Eg) / Eb
    return (1 / (np.cosh((e - x) / gamma)) * 2 * np.pi
        * np.sqrt(Eb) / (1 - np.exp(-2 * np.pi / (
            np.sqrt(D))))* (1 / (1 - npc * (x - Eg))))

for i in range(0, e.size):
    q = quad(fun_eh, Eg, inf,
             args=(e[i], gamma, Eb, Eg, npc))
    abseh[i] = q[0]

def fun_tan(x, e, gamma, eg2, A2):
    fac = (A2 * gamma) / np.pi
    if e > eg2:
        return fac * (0.5*np.tanh(e - eg2))*
            np.sqrt(e - eg2)/((e - x)**2 + gamma ** 2)
    else:
        return 0

for i in range(0, e.size):
    q = quad(fun_tan, 0.0, np.inf,
             args=(e[i], gamma, Eg2, A2))
    abset[i] = q[0]


abs_sim = np.zeros((e.size))
for i in range(0, e.size):

    abs_sim[i] = (e[i] / Eb ** (3 / 2)) *
        (absex[i] + abseh[i] + abset[i])

if args != ():
    print("Printing␣results")
    np.savetxt("Results_" + filepath[:-4] + ".txt",
        np.c_[e, abs_exp_fit, k *
              abs_sim, abseh, absex, abset],
        header=Eb: {}, Eg1: {}, Eg2: {},
```

```
            gamma: {}, npc: {}, k: {}, A2: {} \n E [eV],
            exp, Fit, Cont, Exc, Tanguy.format(
                p[0], p[1], p[2], p[3], p[4], p[5],
                p[6]))
        plt.plot(e,abs_exp_fit)
        plt.plot(e,k*abs_sim)
        plt.savefig("Results_" + filepath[:-4] + ".jpg")
        plt.close()

    return (abs_sim * k - abs_exp_fit)


path = "."

count = 15
Eb = 0.04
gamma = 0.017
Eg = 2.27
Eg2 = 2.3
npc = -0.31
k = 0.013
A2 = 15.29
p0 = [Eb, Eg, Eg2, gamma, npc, k, A2]

for file in sorted(os.listdir(path)):

    filepath = open(file).name

    print(count)

    data = np.loadtxt(filepath, delimiter=",",
                      skiprows=count)

    count = count + 6
    e_exp = data[:, 0]
    a_exp = np.zeros(e_exp.size)
    a_exp = (data[:, 1] - data[e_exp.size - 1, 1])
```

```
print(e_exp[0])

e = np.linspace(e_exp[e_exp.size-1], e_exp[0], 400)

lower = [0.001, 1.8, 2.0, 0.001, -100., 0, 0]
upper = [0.1, 2.5, 4.0, 0.1, 0., 4., 20.]

f = interp1d(e_exp, a_exp)
abs_exp_fit = f(e)

opt_out = opt.least_squares(Elliots_fit, p0,
            args=(abs_exp_fit, e),
                bounds=[lower, upper],
                method='trf', jac='2-point',
                loss='soft_l1', verbose=1)
p0 = opt_out.x
fitting = Elliots_fit(p0, abs_exp_fit, e, 1)
print(opt_out.x)
```

Publications and Presentations 10

Publications

(1) Weis, A.; Hooijer, R.; Kaiser, W.; Biewald, A.; Dörflinger, P.; Maheu, C.; Arsatiants, O.; Helminger, D.; Dyakonov, V.; Hartschuh, A.; Mosconi, E.; De Angelis, F.; Bein, T. Stability and Performance of (Cu/Ag)-Sb-I "Rudorffite"-Based Thin Films for Photovoltaic Application *in preparation*

(2) Armer, M.*; Dörflinger, P.*; Weis, A.; Büchner, C.; Gottscholl, A.; Höcker, J.; Frank, K.; Nusser, L.; Sirtl, M.T.; Nickel B.; Bein, T.; Dyakonov, V. Low temperature optical properties of novel lead-free $Cs_2NaFeCl_6$ perovskite single crystals. *Advanced Photonics Research* **2023**, 2300017.

(3) Weis, A.; Ganswindt, P.; Kaiser, W.; Illner, H.; Maheu, C.; Glück, N.; Dörflinger, P.; Armer, M.; Dyakonov, V.; Hofmann, J. P.; Mosconi, E.; De Angelis, F.; Bein T. Heterovalent Tin Alloying in Layered $MA_3Sb_2I_9$ Thin Films: Assessing the Origin of Enhanced Absorption and Self-Stabilizing Charge States. *J. Phys. Chem. C* **2022**, 126 (49), 21040–21049.

(4) Sirtl, M. T.; Hooijer, R.; Armer, M.; Ebadi, F. G.; Mohammadi, M.; Maheu, C.; Weis, A.; van Gorkom, B. T.; Häringer, S.; Janssen, R. A. J.; Mayer, T.; Dyakonov, V.; Tress, W.; Bein, T. 2D/3D Hybrid $Cs_2AgBiBr_6$Double Perovskite Solar Cells: Improved Energy Level Alignment for Higher Contact-Selectivity and Large Open Circuit Voltage. *Advanced Energy Materials* **2022**, 12 (7), 2103215.

(5) Hooijer, R.; Weis, A.; Biewald, A.; Sirtl, M. T.; Malburg, J.; Holfeuer, R.; Thamm, S.; Amin, A. A. Y.; Righetto, M.; Hartschuh, A.; Herz, L. M.; Bein, T. Silver-Bismuth Based 2D Double Perovskites $(4FPEA)_4AgBiX_8$ (X = Cl, Br, I): Highly Oriented Thin Films with Large Domain Sizes and Ultrafast Charge-Carrier Localization. *Advanced Optical Materials* **2022**, 10 (14), 2200354.

(6) Buyruk, A.; Blätte, D.; Günther, M.; Scheel, M. A.; Hartmann, N. F.; Döblinger, M.; Weis, A.; Hartschuh, A.; Müller-Buschbaum, P.; Bein, T. 1,10-Phenanthroline as an efficient bifunctional passivating agent for $\mathrm{MAPbI_3}$ perovskite solar cells. *ACS Applied Materials & Interfaces* **2021**, 13 (28), 32894–32905.

(7) Giesbrecht, N.*; Weis, A.*; Bein, T. Formation of stable 2D methylammonium antimony iodide phase for lead-free perovskite-like solar cells. *Journal of Physics: Energy* **2020**, 2 (2), 24007.

(8) Kloß, S. D.; Wandelt, S.; Weis, A.; Schnick, W. Accessing Tetravalent Transition-Metal Nitridophosphates through High-Pressure Metathesis. *Angewandte Chemie International Edition* **2018**, 57 (12), 3192–3195.

(9) Kloß, S. D.; Weis, A.; Wandelt, S.; Schnick, W. High-Pressure Metathesis of the $\mathrm{M_{1-x}PO_{3+4x}N_{1-4x}}$ ($\mathrm{x} \approx 0.05$) and $\mathrm{M_{0.75}PO_4}$ (M = Zr, Hf) Orthophosphates. *Inorganic Chemistry* **2018**, 57 (7), 4164–4170.

*These authors contributed equally to this work

Conference Contributions

(1) HOPV23 - International Conference on Hybrid and Organic Photovoltaics (London) **2023** - *Perovskites and Beyond: Electronic Tunability and Intrinsic Challenges of Novel Lead-Free Antimony-Iodide based Materials.*

(2) Soltech Conference - Solar Technologies go Hybrid (Munich) **2022** - *Heterovalent Tin Alloying in Layered* $\mathrm{MA_3Sb_2I_9}$ *Thin Films: Assessing the Origin of Enhanced Absorption and Self-Stabilizing Charge States.*

(3) e-Conversion Conference (Venice) **2022** - *Heterovalent Tin Alloying in Layered* $\mathrm{MA_3Sb_2I_9}$ *Thin Films: Assessing the Origin of Enhanced Absorption and Self-Stabilizing Charge States.*

(4) HOPV22 - International Conference on Hybrid and Organic Photovoltaics (Valencia) **2022** - *Heterovalent Tin Alloying in Layered* $\mathrm{MA_3Sb_2I_9}$ *Thin Films: Assessing the Origin of Enhanced Absorption and Self-Stabilizing Charge States.*

(5) LMU Soltech Workshop **2020** (online) - *Antimony-based light-absorbing thin film materials beyond the perovskite motif.*

(6) SPP Kickoff Meeting (Potsdam) **2020** - *Lead-Free Perovskites For Photovoltaic Applications*